Stress-Constrained Topology Optimization with Application to the Design of Electrical Machines

Dissertation

zur Erlangung des akademischen Grades
doctor rerum naturalium
(Dr. rer. nat.)
im Fach Mathematik

eingereicht an der
Mathematisch-Naturwissenschaftlichen Fakultät
der Humboldt-Universität zu Berlin

von
M. Sc. Jonas Holley

Präsidentin der Humboldt-Universität zu Berlin
Prof. Dr. Julia von Blumenthal

Dekanin der Mathematisch-Naturwissenschaftlichen Fakultät
Prof. Dr. Caren Tischendorf

Gutachter
Prof. Dr. Michael Hintermüller
Prof. Dr. Dietmar Hömberg
Prof. Dr. Antonio Novotny

Tag der mündlichen Prüfung: 3. Mai 2023

Abstract

In the process of designing a physical object, the mechanical stability under a given load case is an essential requirement in nearly every area of application. Stability can be quantified mathematically by suitable criteria based on the mechanical stress tensor, aiming at the prevention of damage in each point within the physical object. This thesis deals with the development of a framework for the solution of optimal design problems with pointwise stress constraints, where the mechanical behavior is described by a linear elasticity model.

First, a regularization of the optimal design problem is introduced, which comprises a modification of the stress constraints as well as a penalty approach. This perturbation of the original problem represents a central element for the success of a solution method. After analyzing the perturbed problem with respect to the existence of solutions, a line search type gradient descent scheme is developed based on an implicit design representation via a level set function. The core of the optimization method is provided by the topological gradient, which quantifies the effect of an infinitesimal small topological perturbation of a given design on an objective functional. Since the developed approach is a method in function space, the numerical realization is a crucial step towards its practical application. The discretization of the state and adjoint equation provide the basis for developing a finite-dimensional version of the optimization scheme, in particular the topological gradient.

In the last part of the thesis, numerical experiments are conducted in order to assess the performance of the developed algorithm. First, the stress-constrained minimum volume problem for the L-Beam geometry, which is a well-known benchmark example in topology optimization, is addressed. An emphasis is put on examining the effect of the proposed regularization. Afterwards, the multiphysical design of an electrical machine is addressed. In addition to the pointwise constraints on the mechanical stress, the maximization of the mean torque is considered in order to improve the electromagnetic performance of the machine. The success of the numerical tests demonstrate the potential of the developed design method in dealing with real industrial problems.

Zusammenfassung

Während des Designprozesses physischer Gegenstände stellt die mechanische Stabilität in nahezu jedem Anwendungsbereich eine essentielle Anforderung dar. Stabilität kann mittels geeigneter Kriterien, die auf dem mechanischen Spannungstensor basieren, mathematisch quantifiziert werden. Dies dient dem Ziel der Vermeidung von Schädigung in jedem Punkt innerhalb des Gegenstands. Die vorliegende Arbeit behandelt die Entwicklung einer Methode zur Lösung von Designoptimierungsproblemen mit punktweisen Spannungsrestriktionen, wobei das mechanische Verhalten mittels eines linearen Elastizitätsmodells beschrieben wird.
Zunächst wird eine Regularisierung des Optimierungsproblems eingeführt, welche sowohl eine Modifikation der Spannungsrestriktionen, als auch einen Penalty-Ansatz umfasst. Diese Störung des Ausgangsproblems stellt einen zentralen Baustein für den Erfolg einer Lösungsmethode dar. Nach der Analyse des Problems hinsichtlich der Existenz von Lösungen wird ein Gradientenabstiegsverfahren basierend auf einer impliziten Designdarstellung entwickelt. Den Kern des Optimierungsverfahrens stellt der topologische Gradient dar, welcher die Auswirkung einer infinitesimal kleinen topologischen Störung eines gegebenen Designs auf ein Zielfunktional quantifiziert. Da der entwickelte Ansatz eine Methode im Funktionenraum darstellt, ist die numerische Realisierung ein entscheidender Schritt in Richtung der praktischen Anwendung. Die Diskretisierung der Zustandsgleichung und der adjungierten Gleichung bildet die Basis für eine endlich-dimensionale Version des Optimierungsverfahrens.
Im letzten Teil der Arbeit werden numerische Experimente durchgeführt, um die Leistungsfähigkeit des entwickelten Algorithmus zu bewerten. Zunächst wird das Problem des minimalen Volumens unter punktweisen Spannungsrestriktionen anhand der L-Balken Geometrie untersucht. Ein Schwerpunkt wird hierbei auf die Untersuchung der Regularisierung gelegt. Danach wird das multiphysikalische Design einer elektrischen Maschine adressiert. Zusätzlich zu den punktweisen Restriktionen an die mechanischen Spannungen wird die Maximierung des mittleren Drehmoments berücksichtigt, um das elektromagnetische Verhalten der Maschine zu optimieren. Der Erfolg der numerischen Tests demonstriert das Potential der entwickelten Methode in der Behandlung realistischer industrieller Problemstellungen.

Acknowledgements

This thesis is the result of my research, which has been conducted within a cooperation between the Weierstrass Institute for Applied Analysis and Stochastics (WIAS) in Berlin and Robert Bosch GmbH, Corporate Research, located in Renningen. I am indebted to many people who supported me and contributed to this work.
First of all, I want to express my deepest gratitude towards my advisor Prof. Dr. Michael Hintermüller for the opportunity to work in his research group and for introducing me to the field of topology optimization and topological gradients. I am very grateful for his scientific advice, his guidance and the inspiring discussions we had over the past years. Further, I want to thank Prof. Dr. Dietmar Hömberg and Prof. Dr. Antonio Novotny for agreeing to review this thesis.
I am deeply indebted to my supervisors Dr. Adrian Sichau and Dr. Jan-Eric Wurst from Robert Bosch GmbH for the countless discussions, their patience, the valuable lessons in C++ implementation and for proofreading this thesis. Without their moral support during my doctoral studies, especially in times when one step forward felt like two steps backward, I would not have been able to complete my research. In addition, I would like to thank all other colleagues in Renningen for their support and for the pleasant working atmosphere.
Furthermore, I want to thank Moritz Ebeling-Rump and Tobias Kattmann for the many discussions on both mathematical and non-mathematical topics, and for sharing the experience one gains during the time as a PhD student.
In addition, I would like to thank all current and former members of Research Group 8 "Nonsmooth Variational Problems and Operator Equations" for making me feel welcome at WIAS from the first day on.
Moreover, I gratefully acknowledge the financial support from Robert Bosch GmbH and the freedom I was granted during my doctoral studies.
Finally, I want to thank my friends and family, in particular my mother and my father, without whom the completion of this thesis would not have been possible.

Stuttgart, August 2022 *Jonas Holley*

Contents

Notation

$\mathbb{N}$	The set of natural numbers
$\mathbb{R}, \mathbb{R}_0^+$	The real and non-negative real numbers
$\mathbb{R}^d$	The d-dimensional vector space of real numbers
$\mathbb{R}^{d\times d}, \mathbb{R}^{d\times d}_{\text{sym}}$	The vector space of quadratic and symmetric matrices on the real numbers
δ_{ij}	Kronecker delta symbol
$B_r(x)$	Open ball with radius $r > 0$ and center $x \in \mathbb{R}^d$
$x \ll y$	$x \in \mathbb{R}$ is much smaller than $y \in \mathbb{R}$
$\partial\Omega$	Boundary of a set $\Omega \subset \mathbb{R}^d$
$\bar{\Omega}$	Closure of a set $\Omega \subset \mathbb{R}^d$
$\lvert\Omega\rvert$	The d-dimensional Lebesgue measure of a set $\Omega \subset \mathbb{R}^d$
χ_Ω	Characteristic function of a set $\Omega \subset \mathbb{R}^d$
$\operatorname{diam}(\Omega)$	Diameter of a set $\Omega \subset \mathbb{R}^d$
v^T	Transpose of a vector $v \in \mathbb{R}^d$
$v \cdot w$	Inner product of vectors $v, w \in \mathbb{R}^d$
$v \otimes w$	Dyadic product of vectors $v, w \in \mathbb{R}^d$
$\lvert v\rvert$	Euclidean norm of a vector $v \in \mathbb{R}^d$
I	Identity matrix
$A : B$	Frobenius inner product of matrices $A, B \in \mathbb{R}^{d\times d}$
$\operatorname{tr}[A]$	Trace of a matrix $A \in \mathbb{R}^{d\times d}$
$\mathbb{I}$	Fourth-order identity tensor
$\operatorname{span}(v_1, ..., v_N)$	Span of a set of vectors $\{v_1, ..., v_N\}$
$\dim(V)$	Dimension of a space V
$\lVert\cdot\rVert_V$	Norm on a Banach space V
V^*	Dual space of a Banach space V
$\langle\cdot,\cdot\rangle_{V^*,V}$	Duality pairing between V and V^*
$u\lvert_\Omega$	Restriction of a function u to a set Ω
$[\![u]\!]$	Jump of a function u across an interface
n	Outer unit normal vector

∂_n	Normal derivative
∇	Gradient operator as column vector
$\epsilon(u)$	Symmetric gradient of u
div	Divergence operator
curl	Curl operator
$o(\cdot)$	Landau (little-o) asymptotic notation
$O(\cdot)$	Landau (big-O) asymptotic notation
$\to$	Strong convergence
$\rightharpoonup$	Weak convergence
$\subset\subset$	Compactly contained
$C^k(D, \mathbb{R}^m)$	Space of k-times continuously differentiable functions on D with $C^k(D) := C^k(D, \mathbb{R})$
$C^{k,\beta}(D, \mathbb{R}^m)$	Functions in $C^k(D, \mathbb{R}^m)$ whose k-th derivative is Hölder continuous of order $0 < \beta \leq 1$, $C^{k,\beta}(D) := C^{k,\beta}(D, \mathbb{R})$
$L^p(D, \mathbb{R}^m)$	Lebesgue space of p-times integrable functions with $1 \leq p \leq \infty$, $L^p(D) := L^p(D, \mathbb{R})$
$L^p_{\text{loc}}(D, \mathbb{R}^m)$	Lebesgue space of p-times locally integrable functions with $1 \leq p \leq \infty$, $L^p_{\text{loc}}(D) := L^p_{\text{loc}}(D, \mathbb{R})$
$H^{k,p}(D, \mathbb{R}^m)$	Sobolev space of order $k > 0$ with $1 \leq p \leq \infty$, $H^{k,p}(D) := H^{k,p}(D, \mathbb{R})$
a.e.	Almost everywhere

1. Introduction

1.1. Motivation

A fundamental task in the manufacturing process of a physical object, given the knowledge of its basic functionality, is the *determination of its design*. The design, or shape, should be chosen in such a way that the object operates in an optimal way with respect to a priori selected criteria. Until the last century, an iterative and experimental procedure was necessary in order to determine the shape of an object. Based on the experience and intuition of experts, an initial design was chosen for a specific application and improved iteratively by experiments. For several decades, the availability of computers increasingly shifts the design process from the real to the virtual world. In a first major step, the real-world experiments have been replaced by simulations, which are based on physical models. This step has been significant, since it makes the design process less dependent on the expensive and time-consuming construction and testing of prototypes. At this point, the generation of designs still relies on the experience and intuition of experts and solely the design validation is performed virtually. In a natural way, the next major development step addressed the automated generation of suggestions, which is known as *design optimization*. Increasing computational resources on the one hand, as well as advances in mathematical techniques on the other hand, enable more and more the generation of free shapes, which do not rely on an underlying parameterization. This procedure is particularly useful, if the optimal design is non-intuitive or if experience with respect to the given physical object and the chosen design criteria is lacking.
A specific application of design optimization, clarifying the need for sophisticated methods, is the case of *electrical machines*. With the purpose of energy conversion, electrical machines are employed all over the world in nearly every area of everyday's life and industry. Due to this broad use, the optimal design of electrical machines is of utmost importance, especially with regards to energy efficiency. The aim of this design criterion is essentially to keep the energy conversion losses as low as possible. It is crucial to note that a suboptimal design is tantamount to a waste of energy, stressing the need for design optimization methods. The aspect of energy efficiency

is particularly important with regards to the challenge of becoming independent of fossil energy sources, where electrical machines play a key role. Another important aspect is the usage of a minimal amount of material, in particular with regards to rare-earth elements. Consuming as little material as possible is not only necessary for environmental reasons, but also in terms of manufacturing costs.
Besides energy efficiency, additional design criteria from different physical domains need to be taken into account in the design process, resulting in *multiphysical* problems. This is not only the case for electrical machines, but for mainly every real physical object. The complexity of multiphysical design problems manifests itself in a difficulty of using human intuition in the solution process, which emphasizes the necessity of developing modern and automated design methods. Particularly for the case of conflicting criteria, design optimization methods allow to inspire engineers with novel and non-intuitive design ideas. Further, it is fascinating from a mathematicians perspective to be capable of generating innovative designs with having only little expertise in engineering applications.
In practice, an important design criterion is the mechanical stability of a physical object, which needs to be considered for all applications involving the presence of mechanical forces. Employing the concept of failure criteria, mechanical stability is commonly addressed by *stress constraints*. Despite the practical relevance of this problem class, its treatment by design optimization methods is often avoided due to the inherent large number of constraints and the need of keeping a sharp transition between the material phase and void, which is crucial for a reliable and accurate stress assessment of a design. Therefore, the following problem prototype

$$\begin{aligned} \min_{\Omega \in \mathcal{O}} \quad & \mathcal{J}(\Omega) \\ \text{s.t.} \quad & \mathcal{F}[\Omega] \leq \bar{\sigma} \text{ in } \Omega \end{aligned}$$

will be the subject of this thesis, where $\mathcal{O}$ represents the set of admissible designs, $\mathcal{J} : \mathcal{O} \to \mathbb{R}$ is a functional to be minimized and $\bar{\sigma} > 0$ is a maximum admissible stress. Further, given a design $\Omega \in \mathcal{O}$, $\mathcal{F}[\Omega] : \Omega \to \mathbb{R}$ denotes a pointwise failure criterion, which is a function of the stress tensor and quantifies the failure of design Ω with respect to the applied mechanical forces. The problem under consideration falls into the class of problems with *pointwise constraints on the gradient of the state*, which is known to be challenging in the field of optimal control, see [89] and [81], due to a low regularity of the associated Lagrange multipliers involved in the optimality conditions. More precisely, the multipliers and adjoint variables are known to be Borel measures,

or even derivatives of Borel measures, which are difficult to approximate. Problems with a similar mathematical structure arise in various applications, for instance if thermal effects have to be taken into account and the temperature gradients need to be controlled locally.
The development of a design optimization method for solving the generic problem prototype allows to treat specific applications. This thesis demonstrates that topology optimization methods can be applied successfully for the *realistic industrial design* of an electrical machine considering pointwise stress constraints. This is a novelty compared to existing works, see for instance [65], where only the unconstrained case has been addressed and, consequently, mechanical stability can not be guaranteed.

1.2. Topology Optimization

Several different approaches for the solution of design optimization problems have been developed over the past decades. In the following, a brief overview of the established methods is presented. Before we begin with the discussion of different methods, it should be mentioned that the optimization variables are typically chosen as the nodes or elements of a triangulation of the underlying domain. In certain applications, for instance in the case of problems involving local stress constraints, a high resolution of the triangulation is necessary, which leads to a large number of optimization variables. Due to the large-scale nature of design optimization problems, the focus in this section will be on *gradient-based* algorithms. Global optimization techniques, however, can be useful in certain situations, see [125]. For an overview of evolutionary design optimization methods, the reader is referred to the monograph [139]. For approaches based on integer programming, the reader is referred to [132] an the references therein.
The class of *sizing* or *parametric optimization* methods has been developed first for the solution of optimal design problems. Within this approach, the basis geometrical features, more precisely the shape and topology of a design, are fixed a priori. Only a finite, and usually small, number of design parameters are then determined to be optimized. Examples for such parameters are angles between geometrical parts or the thickness of bars. An overview of techniques concerning the latter example, which is known as truss optimization, can be found in the review article [26]. The next step in the solution of optimal design problems has been the class of *shape optimization* methods. While the topology of designs is still fixed for this type of methods, the boundary is allowed to be deformed in a flexible manner. For details on this approach, the reader

is referred to the monographs [129], [76] and [36]. The dependency of optimal designs on the initial shape gave rise to the development of the class of *topology optimization* methods. Within this approach, algorithms are capable of altering the topology of a design throughout the optimization process. Therefore, this class of methods provides the most flexible tool for the solution of optimal design problems. A brief overview of topology optimization approaches, which is based on the review articles [82], [119] and [126], is presented in the following.

The first topology optimization approach, which has been proposed by Bendsøe and Kikuchi in 1988, is the *homogenization method*, see [27]. Instead of considering classical shapes with a sharp transition at the boundary via characteristic functions, generalized shapes with intermediate material densities are allowed. This enlargement of the feasible set of designs is achieved by considering the limits of sequences of classical designs, which can be thought of as composite materials. We mention that these generalized shapes are characterized by the material density distribution as well as a homogenized tensor representing the periodic microstructure of the underlying domain. This tensor describes the material characteristics on a micro scale, such as the shape of holes contained in each cell of the microstructure. For further details regarding the homogenization method, the reader is referred to the monograph [2].

In 1989, Bendsøe introduced the *density method* for topology optimization for the minimum compliance problem subject to a volume constraint, see [25]. The density method relies on the relaxation of the binary variables, describing a distribution of two different materials within a prescribed domain, to intermediate density variables. This step allows the use of standard techniques from continuous optimization in the solution process, whereas only discrete methods are available for binary optimization variables. In contrast to the homogenization method, a penalization of the stiffness tensor is employed for avoiding intermediate densities in the material distribution, which make the physical interpretation as well as the actual manufacturing of designs difficult. Commonly, the *Solid Isotropic Material with Penalization (SIMP)* approach is employed, representing a specific power-law penalization type. The main idea behind this approach is that material with intermediate density contributes only little to the overall stiffness, but has a high price in terms of material consumption. Further details on the density method can be found in the monograph [28].

Another approach for solving optimal design problems is the *level set method*, see [109], which has been proposed by Osher and Santosa in 2001 in the context of topology optimization. In contrast to the density method, this approach relies on a material distribution without intermediate densities. This is achieved by the use of an implicit design representation, provided by a level set function. The evolution of this func-

tion is steered by a velocity field, based on shape sensitivities, in the course of the optimization process. In order to perform modifications of the level set function, a Hamilton-Jacobi equation is used. Note that in practice holes in the design can vanish, but hardly be created by using the level set method, which is simply a consequence of using shape derivatives for guiding the optimization process. The reader is referred to [38] and [6] for further details.
The *phase field method* for topology optimization has been proposed by Bourdin and Chambolle in 2003, see [33]. Like the density method, the phase field approach relies on a material distribution with intermediate densities. However, instead of employing a material penalization scheme, an additional term is added to the objective functional in order to prevent intermediate densities. Commonly, a double well potential is used in the literature. Further details on the phase field method can be found in [30].
Another method for solving optimal design problems, which is chosen in this work, relies on the concept of *topological gradients*. Essentially, this approach provides the sensitivity for the creation of an infinitesimal small topological perturbation within a given design. Therefore, topological gradients allow to explicitly modify the topology of a design in a rigorous and systematic fashion. This approach provides a powerful tool for the solution of the problem class under investigation for several reasons. First, in contrast to the standard level set method and shape optimization approaches, topological gradients allow a maximum design flexibility. Moreover, the use of topological gradients allows to represent a material distribution without intermediate densities. This is particularly important for problems with pointwise stress constraints, since stresses at the boundary of a physical object can be assessed accurately. Since this approach will be used in this thesis and further details are given in Section 4.1, the reader is referred to the monographs [105] and [106] at this point.
Concluding this section, we remark that literature reviews on topology optimization approaches on the specific class of optimal design problems with stress constraints are provided in Section 7.1. Moreover, a review on existing methods for design optimization of an electrical machine is given in Section 8.1.

1.3. Outline of the Thesis

This thesis is concerned with the solution of stress-constrained optimal design problems based on a level set algorithm and the concept of topological gradients. The main contributions of this work are the following:

- A regularization of the original problem, based on an extension of the pointwise

stress constraints, is introduced, which has a stabilizing effect on the numerical scheme.

- We provide a numerical realization of the optimization algorithm, in particular the discretization of the topological gradient, tailored to the class of stress-constrained optimal design problems.

- "Topological derivative-based and level-set methods [...] show tremendous promise, but have not reached the stage of regular industrial applications as yet." We face this gap between academia and industrial practice, observed by Rozvany in the review article [119], by employing the developed approach for the realistic multiphysical design of an electrical machine. Note that there are only a few works addressing industrial applications of the topological derivative method, for instance [43] and [117].

The thesis is organized as follows. In the first part, the formulation and analysis of the optimal design problem is addressed. We begin with stating the original stress-constrained problem in Chapter 2. Motivated by the no-structure problem, an extension of the stress constraints to the air phase, along with a penalty approach, is proposed in Chapter 3. The resulting unconstrained optimal design problem is analyzed with respect to the existence of local minima.
The second part of the thesis addresses a method for the solution of the regularized problem. An essential ingredient of the approach is provided by the topological gradient of the penalty term, which is treated in Chapter 4. This sensitivity serves as the core of a level set-based optimization scheme, which is introduced in Chapter 5. Up to this point, the optimization algorithm is a method in function space. The discretization and numerical realization of the algorithm is discussed in Chapter 6, which is a crucial requirement for its practical implementation.
In the third part, the developed method is investigated by numerical experiments. We begin with examining the effect of the regularization by studying the stress-constrained minimum volume problem in Chapter 7. Observing a stabilizing effect of the regularization on the numerical scheme, we proceed by the multiphysical and stress-constrained design of an electrical machine.

Part I.

Problem Formulation and Analysis

2. Problem Statement

2.1. Elasticity Model

A crucial step in the development of a topology optimization method, which is capable of dealing with stress constraints, is the mathematical description of stresses in a solid body. The basis for stress assessment is a model for the structural mechanical behavior of a solid body under applied forces. Within this thesis, the *linear elasticity problem*, also known *Navier-Lamé equations*, is employed for the mechanical modeling, which is a common procedure in the field of structural analysis and design with local stresses, see for instance [23]. In contrast to the case of plasticity, an elastic body is characterized by the property of changing its shape and size under subjected forces and returning to its initial configuration, if the applied forces stop acting, see [45]. The linearity of the Navier-Lamé equations is based on the assumptions of only *small deformations* occurring in the elastic body and a linear relationship between strains and stresses, known as *Hooke's law*, see [45]. In addition to these assumptions, the material is assumed to be *isotropic* throughout this work and a two-dimensional *plane stress* setting is considered. For a detailed background regarding the Navier-Lamé equations, including a derivation from the full elasticity model, the reader is referred to the monographs [34] and [45].
In shape and topology optimization, a common way of representing the distribution of material and air is the *weak phase approach*, which is also referred to as soft phase or ersatz material approach in literature, see e.g. [5]. Essentially, this approach comprises a generalization from constant to discontinuous material coefficients in the Navier-Lamé equations, resulting in an *interface problem*. Let us consider a bounded Lipschitz domain $D \subset \mathbb{R}^2$ representing the hold-all domain with boundary partitioning $\partial D = \Gamma_D \cup \Gamma_N$, where $\Gamma_D \cap \Gamma_N = \emptyset$ and Γ_D is assumed to be of positive surface measure. The main idea of the weak phase approach is to separate D into an open subset $\Omega \subset D$, representing a solid body, and its complement $D \setminus \Omega$, which represents void. Throughout this work, the sets Ω and $D \setminus \Omega$ will be referred to as *material phase* and *weak phase*, respectively. For a given material distribution Ω, the two different phases are distinguished via a discontinuous coefficient function $\alpha_\Omega : D \to \mathbb{R}$, defined by

$$\alpha_\Omega(x) := \begin{cases} 1, & x \in \Omega, \\ \alpha, & x \in D \setminus \Omega, \end{cases} \tag{2.1}$$

with $0 < \alpha \ll 1$. Due to the assumption of isotropy, the solid body is characterized by a constant elasticity tensor

$$\mathbb{C} = 2\mu\mathbb{I} + \lambda(\mathrm{I} \otimes \mathrm{I}), \tag{2.2}$$

with Lamé constants $\mu, \lambda > 0$, the fourth-order identity tensor $\mathbb{I}$ and $(\mathrm{I} \otimes \mathrm{I})M := \mathrm{tr}[M]I$ for $M \in \mathbb{R}^{d\times d}$ with I denoting the identity matrix. The elasticity tensor within the entire domain D is now defined by

$$\mathbb{C}_\Omega := \alpha_\Omega \mathbb{C}, \tag{2.3}$$

where α_Ω accounts for the given material distribution. For $f \in C^{0,\beta}(D, \mathbb{R}^2)$ with $\beta > 0$, the displacements $u : D \to \mathbb{R}^2$ are a consequence of applied volume forces $f_\Omega : D \to \mathbb{R}^2$, defined by

$$f_\Omega := \alpha_\Omega f, \tag{2.4}$$

as well as traction forces $g \in L^2(\Gamma_N, \mathbb{R}^2)$ and a prescribed displacement $u_D \in L^2(\Gamma_D, \mathbb{R}^2)$ on the boundary, where the space $L^2(\partial D, \mathbb{R}^2)$ denotes the image of the trace operator on $H^1(D, \mathbb{R}^2)$, see [61, p. 258]. Note that the assumption of Hölder continuity of function f will be necessary for the sensitivity analysis in the second part of this thesis.

Remark 2.1. *From a physical point of view, the weak phase $D \setminus \Omega$ behaves similarly to air, since its Lamé coefficients are close to zero due to (2.1). More precisely, the behavior of the weak phase is comparable to foam or a sponge. Note that α must be chosen small enough in order to approximate the behavior of the solid body sufficiently accurately. On the other hand, α should not be chosen too small with regards to numerical algorithms.*

For $\Gamma_I := \partial\Omega$ representing the interface and

$$\epsilon(u) := \frac{1}{2}\left(\nabla u^T + \nabla u\right), \tag{2.5}$$

denoting the *linearized strain tensor*, the behavior of the solid body is modeled via the following transmission problem:

$$-\text{div}\, \mathbb{C}_\Omega \epsilon(u) = f_\Omega, \qquad \text{in } D, \tag{2.6a}$$
$$u = u_D, \qquad \text{on } \Gamma_D, \tag{2.6b}$$
$$\mathbb{C}_\Omega \epsilon(u) \cdot n = g, \qquad \text{on } \Gamma_N, \tag{2.6c}$$
$$[\![u]\!] = 0, \qquad \text{on } \Gamma_I, \tag{2.6d}$$
$$[\![\mathbb{C}_\Omega \epsilon(u) \cdot n]\!] = 0, \qquad \text{on } \Gamma_I. \tag{2.6e}$$

Note that n denotes the outer unit normal vector and $[\![h]\!] := h^+|_{\Gamma_I} - h^-|_{\Gamma_I}$ is the jump of a function h across the interface Γ_I, where h^+ and h^- represent the restrictions of h to the respective subdomains. The weak phase approach is chosen over modeling only the material phase for two reasons. First, different shapes Ω can be represented via a fixed hold-all domain and varying coefficient functions. The main benefit is the possibility of working on a fixed mesh in numerical settings. The second aspect is the option to compute sensitivities for design changes not only in the material phase, but also in air. As a result, optimization algorithms with the capability of removing and adding material can be designed.

2.2. Analysis of the State System

Given the Sobolev space $H^1(D, \mathbb{R}^2)$, we define the subspace

$$\mathcal{V} := \{v \in H^1(D, \mathbb{R}^2) : \gamma(v)|_{\Gamma_D} = 0\}, \tag{2.7}$$

where $\gamma : H^1(D, \mathbb{R}^2) \to L^2(\partial D, \mathbb{R}^2)$ denotes the trace operator, see [61, p. 258] for details. A standard procedure in the analysis of an elliptic partial differential equation is to investigate its *weak formulation*, see [61] for further information. For an open subset $\Omega \subset \mathbb{R}^2$, let us define the bilinear form

$$a_\Omega(v, w) := \int_D \mathbb{C}_\Omega \epsilon(v) : \epsilon(w) dx \tag{2.8}$$

and the linear form

$$l_\Omega(w) := \int_D f_\Omega \cdot w dx + \int_{\Gamma_N} g \cdot w ds \tag{2.9}$$

for functions $v, w \in H^1(D, \mathbb{R}^2)$.

Remark 2.2. *The explicit dependency of the bilinear form a_Ω and the linear form l_Ω on an*

open set Ω reflects the main purpose of this work, which is the computation of optimal designs. While Ω may be considered fixed in this section, it will play the role of an optimization variable in the following section.

The following definition provides the basis for a meaningful notion of solution.

Definition 2.1. *Let an open subset $\Omega \subset D$ be given. A function $u \in H^1(D, \mathbb{R}^2)$ is called a weak solution of the partial differential equation (2.6), if it satisfies*

$$a_\Omega(u, v) = l_\Omega(v), \quad \forall v \in \mathcal{V}, \tag{2.10}$$

and $u|_{\Gamma_D} = u_D$ holds in the trace sense.

The remaining section is devoted to the question, whether a unique weak solution of (2.6) exists. As it is common in the theory of partial differential equations, the Lemma of Lax-Milgram (cf. [61]) from the field of functional analysis is employed to establish existence results. Therefore, we need to verify the assumptions of the Lax-Milgram Lemma by investigating properties of the bilinear form a_Ω and the linear form l_Ω.

Lemma 2.1. *The bilinear form $a_\Omega : \mathcal{V} \times \mathcal{V} \to \mathbb{R}$, defined in (2.8), is coercive and bounded, i.e. there exist constants $c_0, c_1 >$ such that*

$$\begin{aligned} a_\Omega(v, v) &\geq c_0 \|v\|^2_{H^1(D,\mathbb{R}^2)}, \\ |a_\Omega(v, w)| &\leq c_1 \|v\|_{H^1(D,\mathbb{R}^2)} \|w\|_{H^1(D,\mathbb{R}^2)}, \end{aligned}$$

for all $v, w \in H^1(D, \mathbb{R}^2)$.

Proof. The proof is standard and can be found in [22, Corollary 8.1]. We mention that the weak phase parameter α, defined in (2.1), enters the first inequality via the relation $c_0 = \alpha \tilde{c}_0$ for a constant $\tilde{c}_0 > 0$. Hence, the requirement $\alpha > 0$ is essential in order to ensure the coercivity of the bilinear form. □

Lemma 2.2. *The linear form $l_\Omega : \mathcal{V} \to \mathbb{R}$, defined in (2.9), is bounded.*

Proof. The proof is standard and relies on Hölder's inequality and the fact that $\alpha_\Omega \leq 1$ in D. □

Having the two previous lemmas at hand, we are in the position to show existence and uniqueness of a weak solution of the Navier-Lamé equations.

Theorem 2.1 (Existence and Uniqueness)**.** *Let an open subset $\Omega \subset D$ be given and assume the Dirichlet boundary Γ_D to be of positive surface measure. Then, for every $f \in L^2(D, \mathbb{R}^2)$, $g \in L^2(\Gamma_N, \mathbb{R}^2)$ and $u_D \in L^2(\Gamma_D, \mathbb{R}^2)$, there exists a unique solution $u \in H^1(D, \mathbb{R}^2)$ of problem (2.10).*

Proof. The first step is the splitting of u into

$$u = u_0 + \hat{u}, \tag{2.11}$$

with a function $\hat{u} \in H^1(D, \mathbb{R}^2)$, which is assumed to satisfy the condition $\hat{u}|_{\Gamma_D} = u_D$, and a function $u_0 \in \mathcal{V}$, which fulfills the condition $u_0|_{\Gamma_D} = 0$ by definition of $\mathcal{V}$. Based on equation (2.11), a weak solution of (2.6) can be characterized by

$$a_\Omega(u_0, v) = l_\Omega(v) - a_\Omega(\hat{u}, v), \quad \forall v \in \mathcal{V}. \tag{2.12}$$

Note that the splitting of u into a homogeneous and an inhomogeneous part is necessary in order to define the bilinear form a_Ω on the Hilbert space $\mathcal{V}$. This is not the case for the set $\{v \in H^1(D, \mathbb{R}^2) : v|_{\Gamma_D} = u_D\}$ due to the absence of a vector space structure. In Lemma 2.1, it has been shown that the bilinear form $a_\Omega : \mathcal{V} \times \mathcal{V} \to \mathbb{R}$ is coercive and bounded. Further, it is straightforward to see that the linear form

$$\tilde{l}_\Omega(v) := l_\Omega(v) - a_\Omega(\hat{u}, v)$$

is bounded on $\mathcal{V}$ due to the boundedness of a_Ω and l_Ω. Hence, all assumptions of the Lax-Milgram lemma, see for instance [61], are fulfilled, which ensures the existence of a unique solution. □

An essential requirement for formulating the optimal design problem in the following section as well as the topological asymptotic expansion later on is a certain regularity property of the solution $u \in H^1(D, \mathbb{R}^2)$. Due to the discontinuity of the material coefficient (2.1) and potential reentrant corners of the boundary ∂D, we can not expect higher global regularity, see [74] and [93]. However, the assumed Hölder continuity of the volume force guarantees a local regularity property of u.

Lemma 2.3. *Let $\Omega \subset D$ be open and assume $f \in C^{0,\beta}(D, \mathbb{R}^2)$ for $\beta > 0$. Further, let $u \in H^1(D, \mathbb{R}^2)$ be the unique solution of problem (2.10). Then, it holds*

$$u \in C^{2,\beta}(V, \mathbb{R}^2) \tag{2.13}$$

for every open $V \subset\subset D \setminus \partial\Omega$.

Proof. The assertion follows from [93, Theorem 1] and the Sobolev embedding theorem, see for instance [61]. □

2.3. Optimal Design Problem

The goal of this work is the development of a design method focusing on *failure prevention* and *material strength*. Failure occurs in a structure, if the acting forces exceed a certain range. The consequences of this situation are irreversible plastic deformations or the initiation and propagation of cracks. The load a structure can carry depends on the materials it is made of. For more detailed information on the topic of material failure, the reader may refer to [73] or [53].
A commonly used criterion in structural design is the mechanical *compliance* due to its simple mathematical structure, which is introduced in the following.

Definition 2.2. *Let $u \in H^1(D, \mathbb{R}^2)$ be the solution of problem (2.10). The total potential energy*

$$C(u) := \int_D f_\Omega \cdot u dx + \int_{\Gamma_N} g \cdot u ds \tag{2.14}$$

is called compliance.

The compliance is, however, not well suited for designing structures, which need to be fail-safe with respect to a prescribed load case. The reason for this drawback is its *global* nature, whereas actually *local* criteria are necessary. The basis for quantifying failure of a structure is the stress tensor

$$\sigma(u) := \mathbb{C}\epsilon(u), \tag{2.15}$$

where $\mathbb{C}$ is the elasticity tensor, defined in (2.2), and $\epsilon(u)$ represents the strain tensor to displacement u, defined by (2.5). If the stress is below a certain threshold, the *elastic limit* or *stress limit*, the structure does not fail and shows purely elastic behavior. From an application point of view, exceeding the elastic limit typically occurs in regions of local stress concentrations within an elastic structure. This behavior can be observed for instance in the case of loaded solid bodies with sharp reentrant corners.
Safety with respect to failure is formalized mathematically by ensuring that the stress level is below the elastic limit in every point within the structure under consideration. Fundamental for this formalization is the definition of a *failure function*.

Definition 2.3. *Let $\bar{\sigma} > 0$ be given. We call the mapping $F_{\bar{\sigma}} : \mathbb{R}^{2\times 2}_{sym} \to \mathbb{R}^+_0$, defined by*

$$F_{\bar{\sigma}}(\sigma) := f\left(\frac{\sigma}{\bar{\sigma}}\right), \tag{2.16}$$

a failure function to elastic limit $\bar{\sigma}$, if $f : \mathbb{R}^{2\times 2}_{sym} \to \mathbb{R}^{+}_{0}$ has the structure

$$f(\sigma) := \frac{1}{2}\mathbb{D}\sigma : \sigma + d_3 tr[\sigma], \tag{2.17}$$

with a fourth order tensor $\mathbb{D} = d_1\mathbb{I} + d_2 I \otimes I$ and numbers $d_1, d_2, d_3 \in \mathbb{R}$.

We are now in the position to formalize, whether a point x of a structure is within the elastic range or, in other words, if the solid body in x is safe with respect to failure. This is given, if the stress tensor $\sigma = \sigma(x)$ fulfills the inequality

$$F_{\bar{\sigma}}(\sigma) \leq 1, \tag{2.18}$$

for an elastic limit $\bar{\sigma}$ depending on the characteristics of the material under consideration.

Remark 2.3. *The quadratic structure of function f, defined in (2.17), reflects the common procedure of squaring standard failure criteria such as the von Mises criterion or the maximum principal stress criterion. This property facilitates the mathematical treatment of optimal design problems involving stress constraints. For further details regarding specific failure criteria, the reader is referred to [73].*

Before posing the optimal design problem it is necessary to define the feasible set. This decision determines, which classes of designs are allowed within the optimization process. Note that, so far, $\Omega \subset D$ has only been assumed to be open. We choose

$$\mathcal{O} := \{\Omega \subset D : \Omega \text{ open with uniformly Lipschitz continuous boundary}\} \tag{2.19}$$

as feasible set. For the definition of a Lipschitz continuous boundary the reader is referred to [79, Definition 2.4.5]. The elements $\Omega \in \mathcal{O}$ will be called *designs* or *shapes* throughout this work.

Remark 2.4. *The uniform Lipschitz property of designs in $\mathcal{O}$ is chosen in order to establish existence results of local minimizers of the subsequent optimal design problem. More precisely, the Lipschitz property together with a suitably chosen topology ensures the compactness of $\mathcal{O}$. This will be the key for extracting convergent subsequences within a minimizing sequence technique.*

Remark 2.5. *In the definition of the feasible set (2.19), we allow all subsets of the hold-all domain with uniformly Lipschitz continuous boundary. In certain applications, however, additional geometric restrictions may be imposed. Typically, admissible designs are required to be contained in a fixed design domain due to practical restrictions, which will be the case for the applications in the last part of this thesis. We omit this technical detail at this point for the sake of conciseness.*

Let us proceed by posing the optimal design problem. For a given objective functional

$$\mathcal{J} : \mathcal{O} \to \mathbb{R}, \tag{2.20}$$

the stress-constrained problem reads as follows:

$$\begin{aligned} \inf_{\Omega \in \mathcal{O}} \quad & \mathcal{J}(\Omega) && \text{(2.21a)} \\ \text{s.t.} \quad & a_\Omega(u, v) = l_\Omega(v), \quad \forall v \in \mathcal{V}, && \text{(2.21b)} \\ & F_{\bar{\sigma}}(\sigma(u)) \leq 1 \text{ a.e. in } \Omega. && \text{(2.21c)} \end{aligned}$$

Note that a.e. is an abbreviation for the term *almost everywhere*, indicating that the inequality (2.21c) holds in every point within $\Omega \setminus V$, where $V \subset \Omega$ is an arbitrary set of Lebesgue measure zero. We mention that the notion *optimal control problem* will be used equivalently to the term *optimal design problem* throughout this work, indicating that the unknown in problem (2.21) may be interpreted as control variable.

Remark 2.6. *The pointwise stress constraint (2.21c) may be restricted to the part of design Ω, which is contained in a fixed subset of the hold-all domain D. Excluding a certain part from the area, where stress constraints are imposed, can be reasonable for instance in the neighborhood of boundary forces.*

Due to the existence and uniqueness of solutions of the Navier-Lamé system, each design $\Omega \in \mathcal{O}$ can be identified with an associated displacement $u_\Omega \in H^1(D, \mathbb{R}^2)$ for fixed data. This relation is formalized in the following definition.

Definition 2.4. *We call the mapping*

$$S : \mathcal{O} \to H^1(D, \mathbb{R}^2) \tag{2.22}$$

$$\Omega \mapsto u_\Omega, \tag{2.23}$$

which assigns the unique solution u_Ω to a design $\Omega \in \mathcal{O}$, control-to-state operator.

The operator S is called *solution operator* in the context of partial differential equations and *control-to-state operator* in the context of optimal control problems. The stress constraints in (2.21c) can be written in compact form by

$$\mathcal{F}_{\bar{\sigma}}[\Omega](x) := F_{\bar{\sigma}}(\sigma(u_\Omega(x))) \tag{2.24}$$

with $\mathcal{F}_{\bar{\sigma}} : \mathcal{O} \to H^1(D)$. Hence, as it is standard in optimal control theory, see for instance [137] or [89], problem (2.21) can be reduced as follows:

$$\inf_{\Omega \in \mathcal{O}} \quad \mathcal{J}(\Omega) \tag{2.25a}$$

$$\text{s.t.} \quad \mathcal{F}_{\bar{\sigma}}[\Omega] \leq 1 \text{ a.e. in } \Omega. \tag{2.25b}$$

Remark 2.7. *Note that objective functional $\mathcal{J}$ may be dependent on u_Ω, or the solution of an additional partial differential equation, as well. In this case, a structure of the form*

$$\mathcal{J}(\Omega) := J(\Omega, S(\Omega))$$

is typically given.

It is convenient to shift the pointwise stress constraints to the feasible set as follows

$$\mathcal{O}_{\bar{\sigma}} := \{\Omega \in \mathcal{O} : \mathcal{F}_{\bar{\sigma}}[\Omega] \leq 1 \text{ a.e. in } \Omega\}, \tag{2.26}$$

resulting in the following optimal control problem:

$$\inf_{\Omega \in \mathcal{O}_{\bar{\sigma}}} \mathcal{J}(\Omega). \tag{2.27}$$

Clearly every design $\Omega \in \mathcal{O}$ can be classified as either failed or not failed. The set $\mathcal{O}_{\bar{\sigma}} \subset \mathcal{O}$ contains all designs which are classified as not failed, since the pointwise stress constraints are fulfilled. It is important to note that the existence of solutions of optimal control problem (2.25) depends on the choice of $\bar{\sigma}$. If the elastic limit is chosen to small, there might be no design which fulfills the pointwise stress constraints. Consequently, the set $\mathcal{O}_{\bar{\sigma}}$ is empty in this situation.

Remark 2.8. *Note that the pointwise evaluation of stresses in (2.26) within a design $\Omega \in \mathcal{O}$ is a well-defined operation due to the regularity of the state variable. The Hölder continuity of the volume forces f ensures sufficient interior regularity of the state, see (2.13). Moreover, according to [93, Theorem 1], the regularity holds up to the boundary of design Ω, if the boundary is sufficiently regular.*

3. Regularization and Analysis of the Optimal Design Problem

The main focus of this work is the solution of optimal design problem (2.25). A fundamental step towards the development of efficient algorithms is its *regularization*. Essentially, this procedure perturbs problem (2.25) with the aim of replacing it with another problem, which is easier to handle. The regularization of optimal design problem (2.25) in this thesis comprises two steps. First, the set of feasible designs is restricted by extending the stress constraints from the material phase to the entire domain. In a second step, a penalty approach is employed in order to replace the constrained problem by an unconstrained approximation involving a penalty term. Finally, the resulting problem will be analyzed with respect to the *existence of solutions*.

3.1. The No-Structure Problem

A crucial step in the regularization of the generic stress-constrained optimal design problem (2.25) is the modification of the set of feasible designs. Within this section, we will examine the specific case of stress-constrained *volume minimization* in order to motivate this modification. Typically, this problem is formulated as follows in the literature

$$\inf_{\Omega \in \mathcal{O}_{\bar{\sigma}}} \mathcal{J}(\Omega) = \int_D \chi_\Omega dx, \tag{3.1}$$

where the feasible set $\mathcal{O}_{\bar{\sigma}}$ is defined in (2.26). Note that the minimum volume problem will be investigated in more detail in Chapter 7.
It is immediately clear that the empty set $\Omega^* = \emptyset$ is feasible, since, by definition, there are no stress constraints and it is not possible to find another design in $\mathcal{O}$ with less volume. Consequently, problem (3.1) has a trivial and global solution, which is the empty set. In other words, as it has been stated in [126] as one of the major difficulties in stress-constrained topology optimization,

"if one wants to minimize stress, the best structure is no structure."

However, as it is stated in [126], "the 'no structure' problem is often alleviated by combining the stress constraint with an compliance objective or simply ignored". Indeed, to the author's best knowledge, there are no works dealing explicitly with this important aspect of stress-constrained problems. Hence, this work contributes to the understanding and solution of the *no-structure problem*.
Let us proceed by addressing the root of the no-structure problem. Clearly, the trivial solution $\Omega^* = \emptyset$ of problem (3.1) does not make sense from a practical point of view. Consequently, problem (3.1) needs to be modified in an appropriate manner. More precisely, the feasible set needs to be restricted in order to exclude unreasonable designs. Therefore, we aim at identifying a set

$$\tilde{\mathcal{O}}_{\bar{\sigma}} \subset \mathcal{O}_{\bar{\sigma}},$$

containing all physically reasonable designs. A first and straightforward idea might be to exclude solely the empty set from $\mathcal{O}_{\bar{\sigma}}$. This modification, however, does not solve the problem, since creating very little material at the boundary part Γ_{D} or Γ_{N} might solve the minimum volume problem. Instead, it seems to be more reasonable to allow only designs, which connect the boundary parts Γ_{D} and Γ_{N}. This condition ensures that the design part, where the structure is clamped, will be attached to the part, where the boundary force is applied. Therefore, the modified feasible set is chosen as

$$\tilde{\mathcal{O}}_{\bar{\sigma}} = \{\Omega \in \mathcal{O}_{\bar{\sigma}} : \Gamma_{\mathrm{D}} \cup \bar{\Omega} \cup \Gamma_{\mathrm{N}} \text{ is connected}\}, \tag{3.2}$$

revealing that the no-structure problem is rather a *connectivity* problem.

3.2. Extension of Stress Constraints

An essential question at this point is, how the connectivity condition in (3.2) can be realized within a numerical algorithm. In the works [124] and [75], where a stochastic optimization approach is chosen, an explicit connectivity check is performed. In the case of gradient-based optimization algorithms, however, the incorporation of such a mechanism is difficult. Hence, it is necessary to formulate the connectivity condition indirectly via *additional constraints* in the optimal design problem.
In order to identify appropriate constraints, it is important to examine the consequences of a violation of the connectivity condition. Clearly, rather low displacements will

occur at the Dirichlet boundary Γ_D, where the structure is clamped. In contrast, very large displacements will occur at the Neumann boundary Γ_N, where the applied forces are acting. As as result, given the case of a violation of the connectivity condition, very large displacement gradients occur within the weak phase. Summarizing, it can be observed that very large displacements in the material phase and very large stresses in the weak phase occur, if the boundary part Γ_D is detached from Γ_N.
Having the previous considerations in mind, we can immediately identify two different options for imposing additional constraints in order to ensure the connectivity condition. It is straightforward to see that the first option is to impose *displacement constraints within the material phase*. Note that this is indirectly achieved by combining the objective functional with a compliance term, which is a known strategy in literature, see [119]. Assuming the absence of volume forces, the compliance reads

$$C(u_\Omega) = \int_{\Gamma_N} g \cdot u_\Omega ds,$$

where $g : \Gamma_N \to \mathbb{R}^2$ represents the boundary forces and $u_\Omega \in H^1(D, \mathbb{R}^2)$ denotes the displacement field to design Ω. Clearly, in case of a connectivity violation the compliance is larger by several orders of magnitude compared to the connected case. The second option for ensuring connectivity is to impose additional *stress constraints within the weak phase*.
In this thesis, we choose the second option and extend the pointwise stress constraints to the weak phase. The reason for this choice is that the pointwise constraints of the resulting optimal control problem, in contrast to the option of imposing additional displacement constraints, share the same mathematical structure in the material phase and the weak phase. This will be particularly useful in the derivation of the topological gradient, which consequently has the identical structure in both phases.
Hence, we proceed by perturbing the original problem (2.25) by extending the stress constraints to the weak phase as follows:

$$\begin{aligned} \inf_{\Omega \in \mathcal{O}} \quad & \mathcal{J}(\Omega) && \text{(3.3a)} \\ \text{s.t.} \quad & \mathcal{F}_{\bar{\sigma}}[\Omega] \leq 1 \text{ a.e. in } \Omega, && \text{(3.3b)} \\ & \mathcal{F}_{\bar{\sigma}}[\Omega] \leq \mu \text{ a.e. in } D \setminus \bar{\Omega}, && \text{(3.3c)} \end{aligned}$$

where $\mu \geq 1$ acts as scaling coefficient for the elastic limit in the air phase. Note that the purpose of introducing the coefficient μ is the ability to control the trade-off between preventing the connectivity problem on the one hand and obtaining a

reasonably accurate approximation of the original problem (2.25) on the other hand. If μ is chosen too small, for instance $\mu = 1$, the solution of the perturbed problem (3.3) might be quite different from a solution of the original problem (2.25). If, however, μ is chosen much larger than 1, the connectivity of a solution of problem (3.3) might not be achieved. Hence, the choice of coefficient μ is essential, and will be discussed in the following section in more detail. Note that the same elasticity tensor $\mathbb{C}$ is used in the definition of failure criterion $\mathcal{F}_{\bar{\sigma}}$ in both phases. Consequently, the phase difference in the constraints of (3.3) is considered only via the different stress limits.

Remark 3.1. *The feasible set of the perturbed problem (3.3) is a subset of the feasible set of the original problem (2.25), as it has been demanded in the previous section. Moreover, it can be observed that large displacement gradients are not allowed in problem (3.3), if the scaling coefficient of the elastic limit is chosen appropriately. Consequently, the empty set is not a feasible solution of problem (3.3) due to the presence of stress constraints in the weak phase.*

So far, only theoretical aspects with respect to the formulation of stress-constrained optimal design problems have been discussed. The effect of additional stress constraints in the weak phase on the performance of a numerical algorithm, however, is unclear at this point. We will investigate this interesting aspect via numerical experiments in the last part of this thesis.

3.3. Penalty Approach

The second step in the regularization of problem (2.25) consists of tackling the challenges, which are caused by the *pointwise nature of the stress constraints* via a penalty method. The basic idea of this approach is to replace the constrained problem (3.3) by an unconstrained approximation involving a *penalty term*, which is easier to solve. This unconstrained problem represents a key ingredient in this thesis as it will serve as the basis for the development of a numerical solution scheme. In the field of constrained optimization, penalty methods are a commonly used concept, see [104] or [138] for further details. We mention that the Moreau-Yosida regularization is a widely used penalty strategy in the context of optimal control problems with pointwise constraints on the state or its gradient, see for instance [81] and [89].
Let us begin by constructing a penalty term for the approximation of the constrained problem (3.3). In order to distinguish the material phase and the weak phase, two different penalty terms, corresponding to each phase, are introduced. The difference between both terms is in the stress limit, which is given by $\mu \geq 1$ in the weak phase,

and additionally a weighting coefficient $\kappa \geq 0$ for the penalty term in the weak phase. For a *penalty parameter* $\gamma \geq 0$, the resulting problem reads

$$\inf_{\Omega \in \mathcal{O}} \quad \mathcal{J}(\Omega) + \gamma \left[\int_{\Omega} \Phi\left(\mathcal{F}_{\bar{\sigma}}[\Omega](x)\right) dx + \kappa \int_{D \setminus \Omega} \Phi\left(\mu^{-1} \mathcal{F}_{\bar{\sigma}}[\Omega](x)\right) dx \right], \tag{3.4}$$

where the mapping $\Phi : \mathbb{R} \to \mathbb{R}_0^+$, defined by $x \mapsto \max(0, x-1)$, represents a *penalty function*. The underlying idea of minimization problem (3.4) is that the penalty terms contribute to the objective functional, if the constraints are violated, and vanish otherwise. For further details regarding the concept of penalty functions, the reader is referred to [104].

Remark 3.2. *The choice of the penalty parameter γ is a challenging task in practical realizations. On the one hand, it should not be chosen too small in order to ensure that the contribution of the penalty term is significant enough. On the other hand, it should not be chosen too large in order to prevent a domination of the penalty term, which can cause ill-conditioning of problem (2.25), see for instance [104]. A typical way of circumventing these issues is to solve a sequence of problems, where γ is chosen rather small initially. This procedure is commonly referred to as continuation method. The core idea is to increase γ sequentially and use the solution of the previous optimization problem as initial guess. Note that for $\gamma = 0$, the unconstrained problem is recovered.*

An essential and challenging step within the numerical realization of optimization schemes is the selection of parameters. Therefore, aiming at the presence of as few independent parameters as possible in problem (3.4), we proceed with the explicit choice of μ and κ. Regarding the stress limit in the weak phase, we perform a coupling

$$\mu = h(\gamma)$$

between μ and the penalty parameter γ via a continuous and monotonically increasing function $h : \mathbb{R}_0^+ \to \mathbb{R}_0^+$. This coupling between μ and γ is performed in order to ensure the connectivity of designs on the one hand and the approximation of solutions of the original problem (2.25) on the other hand. Let us assume that problem (3.4) is solved via a continuation method, see Remark 3.2, for the subsequent explanation. In the beginning of the continuation procedure, where γ is chosen small, we aim at the connectivity of solutions of problem (3.4). More precisely, the stress limit μ needs to be chosen sufficiently small in order to penalize large displacement gradients in the weak phase and thus guarantee connectivity. Contrarily, in the course of the continuation procedure, where γ is chosen rather large, we aim at approximating solutions of the original problem (2.25). If μ is chosen too small in this situation, local minima of the

original problem might be excluded from the feasible set. Since the connectivity of solutions of the perturbed problem (3.3) is clearly an indispensable requirement, it is important to ensure that h does not grow too fast in the course of the continuation in γ. Therefore, we suggest choices of the function h with at most linear growth, for instance $h(\gamma) = \gamma$ or $h(\gamma) = \sqrt{\gamma}$.
Concerning the coefficient of the penalty term with respect to the weak phase, we choose

$$\kappa = \alpha,$$

where α denotes the weak phase coefficient, see (2.1). This choice is reasonable, since it takes the discrepancy of the elasticity tensor between material and weak phase into account. As a result, the penalty terms in problem (3.4) can be expressed as follows

$$\int_\Omega \Phi\left(\mathcal{F}_{\bar{\sigma}}[\Omega]\right) dx + \alpha \int_{D\setminus\Omega} \Phi\left(h(\gamma)^{-1}\mathcal{F}_{\bar{\sigma}}[\Omega]\right) dx = \int_D \alpha_\Omega \Phi\left(\beta_\Omega^\gamma \mathcal{F}_{\bar{\sigma}}[\Omega]\right) dx,$$

where α_Ω has been defined in (2.1) and the function β_Ω^γ is defined by

$$\beta_\Omega^\gamma(x) := \begin{cases} 1, & x \in \Omega, \\ h(\gamma)^{-1}, & x \in D \setminus \Omega. \end{cases} \tag{3.5}$$

The next step comprises the *approximation* of the non-differentiable *penalty function* Φ in problem (3.4) by a smooth function $\Phi_p : \mathbb{R}_0^+ \to \mathbb{R}_0^+$ with parameter $p > 1$. This approximation is necessary for the topological sensitivity analysis of the penalty term, which will be addressed in the subsequent chapter. As a smooth approximation, we employ the function

$$\Phi_p(x) := (1 + x^p)^{1/p} - 1, \quad p > 1, \tag{3.6}$$

which has been used in different works, see for instance [17] or [49]. A visualization of Φ_p is provided in Figure 3.1 for different choices of the approximation parameter p.

Remark 3.3. *A requirement in the topological sensitivity analysis of the penalty term in problem (3.4) is the regularity property $\Phi_p \in C^{2,\beta}(\mathbb{R}_0^+)$ for $\beta > 0$. Any other approximation of penalty function Φ, which satisfies this property, can be chosen as well.*

Having discussed the approximation of the penalty function Φ, we proceed by stating the following regularized optimal control problem

$$\inf_{\Omega\in\mathcal{O}} \quad \mathcal{J}_\gamma(\Omega) := \mathcal{J}(\Omega) + \gamma \mathcal{P}_\gamma(\Omega), \tag{3.7}$$

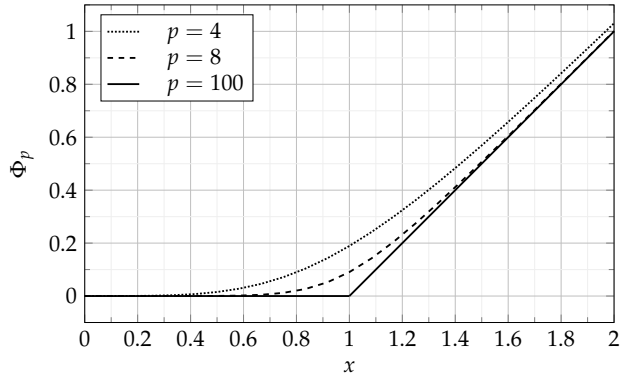

Figure 3.1.: Smooth penalty function Φ_p for different approximation parameters p.

with

$$\mathcal{P}_\gamma(\Omega) := \int_D \alpha_\Omega \Phi_p \left(\beta_\Omega^\gamma \mathcal{F}_{\bar{\sigma}}[\Omega]\right) dx, \tag{3.8}$$

which will play a central role in this thesis.
An essential question, which will be addressed in the last part of this thesis, is how the presence of additional stress constraints in the weak phase affects a numerical optimization scheme. In other words, we are interested in comparing the solution of the original problem (2.25) with the solution of problem (3.3), where additional stress constraints in the weak phase have been introduced. For this purpose, analogously to (3.7), we perform a *regularization of the original problem* (2.25) as follows

$$\inf_{\Omega \in \mathcal{O}} \quad \mathcal{J}(\Omega) + \gamma \mathcal{P}(\Omega), \tag{3.9}$$

where the penalty term is defined by

$$\mathcal{P}(\Omega) := \int_D \chi_\Omega \Phi_p \left(\mathcal{F}_{\bar{\sigma}}[\Omega]\right) dx. \tag{3.10}$$

Note that problem (3.9) can be obtained from (3.4) for $\kappa = 0$.

Remark 3.4. *We mention that the no-structure problem does still occur for the penalized problem (3.9). If we choose the objective functional in (3.9) as the volume term, we obtain the minimization problem*

$$\inf_{\Omega \in \mathcal{O}} \quad \int_D \chi_\Omega dx + \gamma \int_\Omega \Phi_p \left(\mathcal{F}_{\bar{\sigma}}[\Omega]\right) dx,$$

which still has a global minimum at $\Omega^* = \emptyset$ for every $\gamma \geq 0$.

3.4. Existence of Local Minima

Having stated the design problem (2.25) and its regularized version (3.7), the first step towards its solution is the investigation of its theoretical properties. More precisely, the question of *existence of solutions* is of interest as it is a prerequisite for the development of numerical schemes. Therefore, we are interested to answer the following questions: Do both the original problem (2.25) and the perturbed problem (3.7) posses solutions? If this is the case, how are the solutions of both problems related? It is important to mention that, speaking of solutions, we always have local minima in mind. This is a consequence of the non-convex nature of the problems under investigation and an intrinsic property of design optimization problems.
It is known that the question of existence of solutions in the context of shape and topology optimization is a delicate issue, see [79] and [36] for further details. In general, and unless the feasible set and its topology are chosen appropriately, existence of solutions can not be guaranteed. An intuitive example for non-existence in the case of the minimum compliance problem can be found in [79] on page 139, where oscillations of the boundary can be observed. However, there are several options for obtaining existence results concerning objective functional and feasible set, see [36, p. 121]. The first possibility relies on conditions of the objective functional, e.g. a monotonically decreasing functional with respect to the set inclusion. Second, a perimeter term may be added to the objective in order to ensure regularity of feasible shapes. The last option is the restriction of the feasible set by imposing geometric conditions on the shapes.
We follow the last approach and impose a uniform Lipschitz property on each design of the feasible set $\mathcal{O}$, as it has been done in (2.19). Having chosen the feasible set, the choice of a topology on $\mathcal{O}$ remains. This is an important aspect concerning *compactness*, which is of utmost importance for the question of existence of solutions. We mention that the choice of topology is an important and difficult task, since there is no "natural" topology on sets of domains (cf. [79]). Once a topology is selected, a meaningful definition for convergence of domains can be given, which is fundamental for theoretical aspects. In this work, we rely on the convergence in the sense of *Hausdorff* and on the convergence in the sense of *characteristic functions*. While the former is standard and well known, a definition of the latter is given in the following.

Definition 3.1. *Let $L^p_{loc}(\mathbb{R}^d)$ denote the space of locally Lebesgue integrable functions on $\mathbb{R}^d$, see [8, Definition 3.13], and consider a sequence of measurable sets $(E_n)_{n\in\mathbb{N}}$ in $\mathbb{R}^d$. We say that $(E_n)_{n\in\mathbb{N}}$ converges to a measurable set $E \subset \mathbb{R}^d$ in the sense of characteristic functions, if*

$$\chi_{E_n} \to \chi_E \text{ in } L^p_{loc}(\mathbb{R}^d), \forall p \in [1, \infty) \tag{3.11}$$

for $n \to \infty$.

The following compactness theorem will play a central role in the investigation of existence of solutions.

Theorem 3.1 (Compactness of feasible set)**.** *Let* $\mathcal{O}$ *be defined as in (2.19) and consider a sequence* $(\Omega_n)_{n\in\mathbb{N}}$ *in* $\mathcal{O}$*. Then, there exists a shape* $\Omega \in \mathcal{O}$ *and a subsequence* $(\Omega_{n_k})_{k\in\mathbb{N}}$*, which converges to* Ω *in the sense of Hausdorff and in the sense of characteristic functions. Moreover,* $\bar{\Omega}_{n_k}$ *and* $\partial\Omega_{n_k}$ *converge to* $\bar{\Omega}$ *and* $\partial\Omega$*, respectively, in the sense of Hausdorff.*

Proof. A proof can be found in [79, Theorem 2.4.10] on page 56. □

A fundamental aspect for investigating existence of solutions are properties of the control-to-state operator, since stresses depend on the design via the solution of the elasticity problem. The following theorem deals with the *continuity of the control-to-state operator*.

Theorem 3.2 (Continuity of Control-to-State Operator)**.** *Let a topology on* $\mathcal{O}$ *be defined via the convergence in the sense of characteristic functions. Then the control-to-state operator* $S : \mathcal{O} \to H^1(D, \mathbb{R}^2)$*, defined in Definition 2.4, is continuous.*

The proof follows Theorem 1.4.1 and Theorem 1.4.4 from [36] and is provided here for the sake of completeness.

Proof. Let us recall that the state $S(\Omega) = u \in H^1(D, \mathbb{R}^2)$ to design $\Omega \in \mathcal{O}$ is defined as the unique solution of the partial differential equation

$$a_\Omega(u, v) = l_\Omega(v), \quad \forall v \in \mathcal{V}, \tag{3.12}$$

where a_Ω and l_Ω are defined by (2.8) and (2.9), and $\mathcal{V}$ denotes the subspace of $H^1(D, \mathbb{R}^2)$, which has been defined in (2.7). We consider a sequence $(\Omega_n)_{n\in\mathbb{N}} \subset \mathcal{O}$ and a design $\Omega \in \mathcal{O}$ such that $\Omega_n \to \Omega$ if $n \to \infty$, where the convergence is meant in the sense of characteristic functions. For convenience, the corresponding states are abbreviated $u_n := S(\Omega_n)$ and $u := S(\Omega)$. The central equality to be shown is the following:

$$\lim_{n\to\infty} S(\Omega_n) = S(\Omega). \tag{3.13}$$

The Lax-Milgram lemma guarantees the uniform boundedness of the sequence $(u_n)_{n\in\mathbb{N}} \subset H^1(D,\mathbb{R}^2)$, i.e.

$$\|u_n\|_{H^1(D,\mathbb{R}^2)} \leq c, \forall n \in \mathbb{N}, \tag{3.14}$$

for a constant $c > 0$. Since $H^1(D,\mathbb{R}^2)$ is a Hilbert space, a subsequence $(u_{n_k})_{k\in\mathbb{N}} \subset H^1(D,\mathbb{R}^2)$ can be extracted with

$$u_{n_k} \rightharpoonup u^* \text{ in } H^1(D,\mathbb{R}^2) \tag{3.15}$$

and $u^* \in H^1(D,\mathbb{R}^2)$, where (3.15) denotes the weak convergence of the sequence u_{n_k} towards u^*, see [8, Definition 6.1]. Note that the index k will be dropped in the following. The remaining proof consists of two major steps. First, it needs to be shown that $u = u^*$. Second, it must be verified that the convergence in (3.15) is actually strong. We begin proofing the identity $u = u^*$ by showing that the sequence of coefficient functions α_{Ω_n} converges pointwise towards α_Ω, where the coefficient function is defined in (2.1). Since $\Omega_n \to \Omega$ in the sense of characteristic functions, it follows immediately $\chi_{\Omega_n} \to \chi_\Omega$ a.e. in D for $n \to \infty$. Due to the equality $\alpha_\Omega(x) = (1-\alpha)\chi_\Omega(x) + \alpha$, we obtain

$$\alpha_{\Omega_n} \to \alpha_\Omega \text{ a.e. in } D. \tag{3.16}$$

As a result, it follows $\alpha_{\Omega_n}\nabla v \to \alpha_\Omega \nabla v$ a.e. in D for an arbitrary function $v \in H^1(D,\mathbb{R}^2)$. Further, since $\|\alpha_{\Omega_n}\|_{L^\infty(D)} \leq 1$ by definition, we obtain the uniform bound

$$\|\alpha_{\Omega_n}\nabla v\|_{L^2(D,\mathbb{R}^{2\times 2})} \leq \|\nabla v\|_{L^2(D,\mathbb{R}^{2\times 2})}. \tag{3.17}$$

Lebesgue's Theorem yields the convergence

$$\alpha_{\Omega_n}\nabla v \to \alpha_\Omega \nabla v \text{ in } L^2(D,\mathbb{R}^{2\times 2}) \tag{3.18}$$

for $n \to \infty$.
We are now in the position to pass to the limit in the weak formulation of the partial differential equation. Since the weak convergence (3.15) implies $\epsilon(u_n) \rightharpoonup \epsilon(u^*)$, where $\epsilon(v) := \frac{1}{2}\left(\nabla v^T + \nabla v\right)$ denotes the symmetric gradient of a function $v \in H^1(D,\mathbb{R}^2)$, we obtain the following:

$$a_{\Omega_n}(u_n, v) = \int_D \alpha_{\Omega_n}\mathbb{C}\epsilon(v) : \epsilon(u_n)dx \xrightarrow{n\to\infty} \int_D \alpha_\Omega \mathbb{C}\epsilon(v) : \epsilon(u^*)dx = a_\Omega(u^*, v). \tag{3.19}$$

Using similar arguments, the limit passage holds for the linear form as well:

$$l_{\Omega_n}(v) = \int_D \alpha_{\Omega_n} f \cdot v dx + \int_{\Gamma_N} g \cdot v ds \tag{3.20}$$

$$\xrightarrow{n\to\infty} \int_D \alpha_\Omega f \cdot v dx + \int_{\Gamma_N} g \cdot v ds = l_\Omega(v). \tag{3.21}$$

Combining the results yields

$$a_\Omega(u^*, v) = l_\Omega(v), \quad \forall v \in \mathcal{V}, \tag{3.22}$$

which reveals that u^* is actually the unique solution to design Ω, which implies the identity $u = u^*$.
As mentioned before, we proceed by showing that the convergence (3.15) is strong in $H^1(D, \mathbb{R}^2)$. Since the strong convergence $u_n \to u$ in $L^2(D, \mathbb{R}^2)$ follows immediately from the weak convergence in $H^1(D, \mathbb{R}^2)$, it suffices to show

$$\nabla u_n \to \nabla u \text{ in } L^2(D, \mathbb{R}^{2\times 2}) \tag{3.23}$$

for $n \to \infty$. Due to the coercivity of a_{Ω_n}, which has been shown previously in order to apply the lemma of Lax-Milgram, it follows:

$$\begin{aligned} c\|\nabla u_n - \nabla u\|_{L^2}^2 \leq & a_{\Omega_n}(u_n - u, u_n - u) \\ = & \underbrace{a_{\Omega_n}(u_n, u_n - u) - a_\Omega(u, u_n - u)}_{(a)} + \underbrace{a_\Omega(u, u_n - u) - a_{\Omega_n}(u, u_n - u)}_{(b)}. \end{aligned}$$

Further, since $\alpha_{\Omega_n} f \to \alpha_\Omega f$ in $L^2(D, \mathbb{R}^2)$ and $u_n \to u$ in $L^2(D, \mathbb{R}^2)$ we get for the first term:

$$\begin{aligned} (a) &= l_{\Omega_n}(u_n - u) - l_\Omega(u_n - u) \\ &= \int_D (\alpha_{\Omega_n} - \alpha_\Omega) f \cdot (u_n - u) dx \\ &\xrightarrow{n\to\infty} 0. \end{aligned}$$

In the same manner, wo obtain for the second term

$$(b) = \int_D (\alpha_\Omega - \alpha_{\Omega_n}) \mathbb{C}\epsilon(u) : \epsilon(u_n - u) dx \xrightarrow{n\to\infty} 0,$$

which finally shows the strong convergence $\nabla u_n \to \nabla u$ in $L^2(D, \mathbb{R}^{2\times 2})$. □

Having shown continuity of the control-to-state operator S, we address the penalty term (3.8) and investigate its continuity properties. For the subsequent analysis, we introduce the following structure

$$\mathcal{P}_\gamma(\Omega) := P_\gamma(\Omega, u_\Omega) = P_\gamma(\Omega, S(\Omega)), \tag{3.24}$$

where the functional in (3.24) is defined as follows

$$\begin{aligned} P_\gamma : \mathcal{O} \times H^1(D, \mathbb{R}^2) &\to \mathbb{R} \\ (\Omega, u) &\mapsto \int_D j_\Omega\left(\sigma(u)\right) dx, \end{aligned} \tag{3.25}$$

where $\sigma(u) = \mathbb{C}\epsilon(u)$ represents the stress tensor with elasticity tensor $\mathbb{C}$. For $\Omega \in \mathcal{O}$, the density function in (3.25) is defined by

$$\begin{aligned} j_\Omega : \mathbb{R}^{2\times 2} &\to \mathbb{R} \\ d &\mapsto j(d)\chi_\Omega + j^*(d)(1-\chi_\Omega), \end{aligned} \tag{3.26}$$

with functions

$$j(d) := \Phi_p\left(F_{\bar{\sigma}}\left(d\right)\right), \qquad j^*(d) := \alpha\Phi_p\left(h(\gamma)^{-1}F_{\bar{\sigma}}\left(d\right)\right),$$

where α and $h(\gamma)$ are defined in (2.1) and (3.5), respectively and $F_{\bar{\sigma}}$ is the failure function (2.24). We proceed investigating properties of functional P_γ, which will be essential in the existence proof of local minima.

Lemma 3.1. *The functional $P_\gamma : \mathcal{O} \times H^1(D, \mathbb{R}^2) \to \mathbb{R}$, defined in (3.25), is bounded from below and lower semicontinuous.*

Proof. The boundedness from below follows directly from the definition of penalty function Φ_p, which is non-negative. Regarding lower semicontinuity, we consider sequences

$$(\Omega_n)_{n\in\mathbb{N}} \subset \mathcal{O}, \quad (u_n)_{n\in\mathbb{N}} \subset H^1(D, \mathbb{R}^2),$$

with $\Omega_n \xrightarrow{n\to\infty} \Omega$ in the sense of characteristic functions and $u_n \xrightarrow{n\to\infty} u$ in $H^1(D, \mathbb{R}^2)$ with limits $\Omega \in \mathcal{O}$ and $u \in H^1(D, \mathbb{R}^2)$. The linearity of j_Ω in the characteristic function χ_Ω together with the continuity of j and j^* reveals

$$\int_D j_\Omega\left(\sigma(u)\right) dx = \int_D \lim_{n\to\infty} j_{\Omega_n}\left(\sigma(u_n)\right) dx.$$

Since the functions j and j^* are non-negative, we can apply Fatou's Lemma and obtain the inequality

$$\int_D j_\Omega\left(\sigma(u)\right) dx \leq \liminf_{n\to\infty} \int_D j_{\Omega_n}\left(\sigma(u_n)\right) dx,$$

which is precisely the lower semicontinuity of P_γ. □

We are now in the position to proof existence of local minima for the regularized optimal control problem (3.7).

Theorem 3.3. *Let the set $\mathcal{O}$ be defined as in (2.19) and consider a functional $\mathcal{J} : \mathcal{O} \to \mathbb{R}$, which is lower semicontinuous and bounded from below. Furthermore, let the functional $\mathcal{P}_\gamma$ be defined as in (3.8). Then, for $\gamma \in [0, \infty)$, the optimization problem*

$$\min_{\Omega\in\mathcal{O}} \quad \mathcal{J}_\gamma(\Omega) = \mathcal{J}(\Omega) + \gamma\mathcal{P}_\gamma(\Omega)$$

admits at least one solution.

Proof. Since $\mathcal{P}_\gamma$ is bounded from below according to Lemma 3.1, the existence of an infimum of $\mathcal{J}_\gamma$ is guaranteed. Therefore, a minimizing sequence $(\Omega_n)_{n\in\mathbb{N}} \subset \mathcal{O}$ can be chosen:

$$\lim_{n\to\infty} \mathcal{J}_\gamma(\Omega_n) = \inf_{\Omega\in\mathcal{O}} \mathcal{J}_\gamma(\Omega). \tag{3.27}$$

The remaining proof is devoted to the question, whether the infimum is contained in $\mathcal{O}$. Due to the choice of the feasible set $\mathcal{O}$, more precisely the uniform Lipschitz property, Theorem 3.1 ensures the existence of a shape $\Omega^* \in \mathcal{O}$ and a convergent subsequence $(\Omega_{n_k})_{k\in\mathbb{N}}$ such that

$$\Omega_{n_k} \xrightarrow{n\to\infty} \Omega^* \tag{3.28}$$

in the sense of Hausdorff or in the sense of characteristic functions. Hence, the compactness of $\mathcal{O}$ allows to select a candidate for a minimizer.
Due to the continuity of operator S, see Theorem 3.2, and the lower semicontinuity of P_γ, see Lemma 3.1, we obtain the following inequality

$$\begin{aligned}\mathcal{J}_\gamma(\Omega^*) = \mathcal{J}(\Omega^*) + \gamma\mathcal{P}_\gamma(\Omega^*) &\leq \liminf_{n\to\infty} \mathcal{J}(\Omega_n) + \gamma P_\gamma(\Omega_n, S(\Omega_n)) \\ &= \liminf_{n\to\infty} \mathcal{J}_\gamma(\Omega_n) = \inf_{\Omega\in\mathcal{O}} \mathcal{J}_\gamma(\Omega),\end{aligned}$$

which concludes the proof. □

Having shown existence of solutions of the penalized problem (3.7), the next step is the analysis of the constrained problem (2.27).

Theorem 3.4. *Let $\bar{\sigma} > 0$ be given and assume that the set*

$$\mathcal{O}_{\bar{\sigma}} = \{\Omega \in \mathcal{O} : \mathcal{F}_{\bar{\sigma}}[\Omega] \leq 1 \text{ a.e. in } \Omega\}$$

is nonempty. Moreover, consider a functional $\mathcal{J} : \mathcal{O}_{\bar{\sigma}} \to \mathbb{R}$, which is lower semicontinuous and bounded from below. Then the constrained optimal control problem

$$\min_{\Omega\in\mathcal{O}_{\bar{\sigma}}} \mathcal{J}(\Omega)$$

admits at least one solution.

Before we proof the theorem, an example for a nonempty set $\mathcal{O}_{\bar{\sigma}}$ is provided, containing at least one non-trivial element besides the empty set.

Example 3.1. *Assume the hold-all domain $D \subset \mathbb{R}^2$ to be free of geometrical singularities, which is for instance the case, if D has a smooth boundary or is of rectangular shape. Further, setting $\Omega = D$, we obtain*

$$\alpha_\Omega \equiv 1$$

in the entire domain D for the weak phase coefficient, which is defined by (2.1). For sufficiently smooth data of the partial differential equation (2.6), in particular the assumed Hölder continuity $f \in C^{0,\beta}(D, \mathbb{R}^2)$ of the volume forces, we obtain by global regularity $u_\Omega \in C^{2,\beta}(D, \mathbb{R}^2)$, for u_Ω denoting the solution of (2.6). Consequently, the gradient of u_Ω, and thus the stress tensor $\sigma(u_\Omega)$, can be evaluated pointwise and takes finite values within the entire domain D. As a result, we can find a value $0 < \bar{\sigma} < \infty$, which satisfies the inequality

$$\max_{x\in D} \mathcal{F}_{\bar{\sigma}}[\Omega](x) < 1.$$

Clearly, for this choice of the elastic limit $\bar{\sigma}$, we obtain $D \in \mathcal{O}_{\bar{\sigma}}$ by definition (2.26).

The chapter is concluded by the proof of Theorem 3.4.

Proof. Since the functional $\mathcal{J}$ is bounded from below and the feasible set $\mathcal{O}_{\bar{\sigma}}$ is nonempty, we can find a sequence $(\Omega_n)_{n\in\mathbb{N}} \subset \mathcal{O}_{\bar{\sigma}}$ with

$$\lim_{n\to\infty} \mathcal{J}(\Omega_n) = \inf_{\Omega\in\mathcal{O}_{\bar{\sigma}}} \mathcal{J}(\Omega). \tag{3.29}$$

Since $\Omega_n \in \mathcal{O}_{\bar{\sigma}}$ for every $n \in \mathbb{N}$, the inequality

$$\mathcal{F}_{\bar{\sigma}}[\Omega_n] \leq 1 \text{ a.e. in } \Omega_n \tag{3.30}$$

holds by definition. Due to the compactness of $\mathcal{O}$, a subsequence $(\Omega_{n_k})_{k\in\mathbb{N}} \subset \mathcal{O}_{\bar{\sigma}}$ and a shape $\Omega^* \in \mathcal{O}$ can be selected with

$$\Omega_{n_k} \xrightarrow{k\to\infty} \Omega^* \tag{3.31}$$

in the sense of characteristic functions. We drop the index k for the rest of the proof for the sake of readability. Note that the convergence (3.31) implies immediately

$$\chi_{\Omega_n} \xrightarrow{n\to\infty} \chi_{\Omega^*} \text{ a.e. in } D. \tag{3.32}$$

The lower semicontinuity of functional $\mathcal{J}$ implies the inequality

$$\mathcal{J}(\Omega^*) \leq \liminf_{n\to\infty} \mathcal{J}(\Omega_n).$$

The central question in this proof is now, whether $\Omega^* \in \mathcal{O}_{\bar{\sigma}}$ or, in other words, if the inequality

$$\mathcal{F}_{\bar{\sigma}}[\Omega^*] \leq 1 \text{ a.e. in } \Omega^*$$

holds. Essentially, this corresponds to the set $\mathcal{O}_{\bar{\sigma}}$ being closed.
Let us begin by investigating the limit of sequence $(\mathcal{F}_{\bar{\sigma}}[\Omega_n])_{n\in\mathbb{N}}$ and set $u_n := S(\Omega_n)$ and $u^* := S(\Omega^*)$. Due to (3.31) and the continuity of solution operator S, the convergence $u_n \to u^*$ in $H^1(D, \mathbb{R}^2)$ can be inferred for $n \to \infty$. A standard argument shows that $\nabla u_n \to \nabla u^*$ a.e. in D for $n \to \infty$ along a subsequence and thus the convergence

$$\sigma(u_n) \to \sigma(u^*) \text{ a.e. in } D$$

holds. The continuity of the failure function $F_{\bar{\sigma}}$, which is defined in Definition 2.3, implies

$$\mathcal{F}_{\bar{\sigma}}[\Omega_n] \to \mathcal{F}_{\bar{\sigma}}[\Omega^*] \text{ a.e. in } D. \tag{3.33}$$

Note that the convergences (3.32) and (3.33) as well as inequality (3.30) hold only pointwise almost everywhere in D. Therefore, we proceed by choosing an element $x \in \Omega^*$ with the properties

$$\chi_{\Omega_n}(x) \xrightarrow{n\to\infty} \chi_{\Omega^*}(x), \tag{3.34}$$

$$\mathcal{F}_{\bar{\sigma}}[\Omega_n](x) \xrightarrow{n\to\infty} \mathcal{F}_{\bar{\sigma}}[\Omega^*](x), \tag{3.35}$$

as well as the inequality

$$\mathcal{F}_{\bar{\sigma}}[\Omega_n](x) \leq 1, \forall n \geq n_0, \tag{3.36}$$

with a finite number $n_0 \in \mathbb{N}$, which exists due to (3.30) and the convergence (3.34). More precisely, (3.34) implies the existence of $n_0 \in \mathbb{N}$ with $\chi_{\Omega_n}(x) = 1$ for all $n \geq n_0$, since $\chi_{\Omega^*}(x) = 1$ and $\chi_{\Omega_n}(x) \in \{0, 1\}$ for all $n \in \mathbb{N}$ by definition. Consequently, it follows $x \in \Omega_n$ for all $n \geq n_0$.
Due to convergence (3.35) and inequality (3.36) we infer by standard arguments that the limit is bounded as well, more precisely

$$\mathcal{F}_{\bar{\sigma}}[\Omega^*](x) \leq 1. \tag{3.37}$$

Since this procedure holds for almost every $x \in \Omega^*$, inequality (3.37) is valid pointwise almost everywhere in Ω^*, which concludes the proof. □

Part II.

Topology Optimization Method

4. Topological Gradient

4.1. Introduction

The solution of problem (3.7), which falls into the category of optimal design problems, is a challenging subject. As it is the case for many complex problems, there exist various fundamentally different solution approaches. Essentially, two directions can be chosen at this point. The first option is the class of gradient-based optimization approaches, where sensitivities are required for designing an iterative scheme. The second class comprises methods, which do not rely on sensitivity information. Typical approaches are stochastic optimization algorithms (cf. [139]) and integer programming methods, see for example [131]. Note that gradient-free algorithms require descretizing the design domain and hence always fall into the category of first-discretize-then-optimize methods. In this thesis, a gradient-based approach is employed. This is a common choice within the field of optimal design due to the high dimensionality of the solution spaces.

A central ingredient for the development of a gradient-based optimization algorithm is the sensitivity of the objective functional under consideration. The sensitivity, or gradient, is employed as a search direction within a descent scheme, aiming at iteratively decreasing the objective functional. Unlike the case of standard finite-dimensional optimization problems, there is no natural notion of gradients for optimal design problems. This is a consequence of the lack of algebraic structure of the design space, which is the set of all feasible designs. As a result, it is not a priori clear in the context of optimal design, what a *direction* or *perturbation* is. Commonly, two different types of perturbations are considered. The first type is the smooth perturbation of the boundary of a given design, which allows to define the *shape gradient* of an objective functional. We refer the interested reader to the monograph [129] for further details, in particular on the subject of shape sensitivity analysis. The second type is the perturbation of the interior of a given design, which corresponds to the creation of a small hole. This is the basis for the notion of *topological gradients*. Note that this term refers to the change of topology of a design, which goes along with the creation of a hole. It is important to mention that optimization algorithms based on shape sensitivities are not

fully capable of changing the topology of designs. Clearly, this a major drawback since only parts of the design space can be explored by an optimization algorithm based on shape gradients. Therefore, in order to obtain the maximum flexibility of deforming given designs, the concept of topological gradients is employed in this thesis. It has to be mentioned at this point that the topological sensitivity analysis is mathematically more involved as it is the case for shape sensitivities. Consequently, the gain in design flexibility comes at the price of a rather complex and detailed analysis.
The topological gradient has its origin in the pioneering works of Eschenauer et al. (1994) and Schumacher (1995), see [58] and [122], where it has been introduced as bubble method for the special case of linear elasticity and a certain structure of the objective functional. In 1999, the concept was generalized and given a mathematically rigorous framework by Sokołowski and Żochowski, see [127]. Essentially, the topological gradient quantifies the sensitivity of a design-dependent functional with respect to infinitesimal small topological perturbations. The topological gradient is formalized in the subsequent definition, where we follow [72].

Definition 4.1 (Topological Gradient)**.** *Consider a bounded domain $D \subset \mathbb{R}^d$, $d = 2$ or 3, and let $\mathcal{J} : \mathcal{O} \to \mathbb{R}$ be a shape functional on a set $\mathcal{O}$, which contains open sets in D. Consider an open set $\Omega \in \mathcal{O}$ and a point of perturbation $z \in \Omega$. For a fixed open and bounded subset $\omega \subset \mathbb{R}^d$ containing the origin and a radius $\rho > 0$, we define the perturbed set $\Omega_\rho := \Omega \setminus \bar{\omega}_\rho$ with $\omega_\rho := z + \rho\omega$. Let the following asymptotic expansion*

$$\mathcal{J}(\Omega_\rho) = \mathcal{J}(\Omega) + D_T\mathcal{J}[\Omega](z)f(\rho) + o(f(\rho)) \tag{4.1}$$

be satisfied for an arbitrarily small $\rho > 0$ with a function $f(\rho) > 0$, $f(\rho) \to 0$ and $o(f(\rho))/f(\rho) \to 0$ as $\rho \to 0$. The quantity $D_T\mathcal{J}[\Omega](z)$ is called the topological gradient of shape functional $\mathcal{J}$ at design Ω and point of perturbation z.

In the following, a simple example is presented in order to obtain an intuitive understanding for the topological gradient.

Example 4.1. *Let the functional*

$$\mathcal{J}(\Omega) := |\Omega|$$

quantify the volume, i.e. the Lebesgue measure, of a design $\Omega \in \mathcal{O}$. Simple calculations yield the equalities

$$\mathcal{J}(\Omega_\rho) - \mathcal{J}(\Omega) = |\Omega_\rho| - |\Omega| = -|\omega_\rho| = -\rho^d|\omega|,$$

revealing that (4.1) holds with $f(\rho) = |\omega|\rho^d$ and topological gradient

$$D_T\mathcal{J}[\Omega] = -1. \tag{4.2}$$

Note that the topological gradient (4.2) is independent of design Ω as well as the point of perturbation $z \in \Omega$.

The previous example allows to evaluate the objective functional $\mathcal{J}$ immediately. In most applications, however, $\mathcal{J}$ depends on a design Ω via a state variable u_Ω. In these situations, a state equation needs to be solved in order to evaluate objective functional $\mathcal{J}$. A challenging task will be the topological asymptotic analysis for this type of problem. The key, and major difficulty, will be the asymptotic behavior of the topologically perturbed state variable, which represents the solution of an underlying partial differential equation. In other words, the sensitivity of the control-to-state operator has to be investigated in order to obtain the topological gradient.
Two different interpretations of topological perturbations are available in the presence of a state equation. Early works, for instance [127] and [72], considered the creation of holes inside the underlying domain and the specification of boundary data on the boundary of the created hole ω_ρ. In this case, both Dirichlet and Neumann conditions may be imposed, leading to different sensitivities $D_T\mathcal{J}$ in the topological asymptotic expansion (4.1). This case is referred to as *singular perturbation* in [105]. The second case considers perturbations Ω_ρ implicitly via a varying coefficient in the state system, which is defined on a fixed hold-all domain. This situation firstly has been addressed by Amstutz in 2006, see [11], and establishes a link between the singular perturbation approach and works related to the identification of inhomogeneities from measurements, see e.g. [40]. Here, interface conditions have to be included in the state system, accounting for a jump of the coefficient in the differential operator. Instead of interpreting the perturbation of Ω as creation of a hole, this case corresponds to a material inhomogeneity in Ω_ρ. Therefore, a generalization of the perturbed shape

$$\Omega_\rho := \begin{cases} \Omega \setminus \bar{\omega}_\rho, & \text{if } z \in \Omega, \\ \Omega \cup \omega_\rho, & \text{if } z \in D \setminus \bar{\Omega}, \end{cases}$$

depending on the location of the point of perturbation, is possible. This approach is referred to as *configurational perturbation* in [105]. Clearly, there is a connection between singular and configurational perturbations. As mentioned in [105], the topological gradient in the configurational perturbation setting coincides with the sensitivity for

a singular perturbation with a Neumann condition on the boundary of the hole, if the material coefficient in the inclusion ω_ρ tends to zero. In this thesis, we follow the configurational approach. Note that the elasticity model within the configurational approach has been introduced as *weak phase* model in Section 2.1. The advantages of this modeling approach are, as described previously, the possibility of working on a fixed mesh in numerical algorithms as well as the option of designing bi-directional optimization schemes.
Moreover, we note that several generalizations of the topological gradient have been made in the past. In [87], a second order topological expansion has been performed. Further, more general state equations have been addressed compared to the standard case of partial differential equations. In [84] and [86], the cases of a linear complementarity problem and a variational inequality, respectively, have been considered.
The development of topology optimization algorithms relies on the availability of topological gradients in every point within the hold-all domain simultaneously. An efficient way of computing the sensitivities for all points of perturbations at once is offered by the *adjoint method*, which is a standard tool in optimal control theory, see [138] for further details. Essentially, the solution of a linear system, called *adjoint equation*, in addition to the solution of the unperturbed state equation is sufficient for obtaining the full topological gradient.
This chapter is dedicated to the topological asymptotic analysis of a certain class of objective functionals. We will consider stress-based objectives, more precisely functionals depending on the gradient of the displacement, subject to the equations of linear elasticity. In order to provide insights into the development of sensitivities for this class of problems, a short literature review is given in the following.
The majority of works on topological gradients and its application within optimization algorithms for the elasticity case consider solely objectives, which depend on the state. Most commonly used is the mechanical compliance or total potential energy. However, literature gets scarcer for the case of objective functionals, which depend on the gradient of the state. The first work [127] addressing stress-based objective functionals was published by Sokołowski and Żochowski in 1999. Here, quadratic yield criteria have been considered for isotropic material and two space dimensions within the singular perturbation framework. The results of [127] have been extended in two directions. First, an extension to a three-dimensional setting was investigated by Sokołowski and Żochowski in 2001, see [128]. The second direction concerns the application of the topological gradient from [127] in an optimization scheme. This has been examined by Allaire and Jouve in 2008, see [4], using a level set method, coupling shape and topological gradients, for the optimization of stress-based objectives. Further, topological

gradients for a non-quadratic objective, related to the von Mises stress criterion, has been investigated by Amstutz and Novotny in 2010 for the 2D case, isotropic material and the configurational perturbation approach, see [17]. It is important to note that the objective functional from [17] stems from a penalization of pointwise constraints on the gradient of the state. Hence, following a penalty approach, [17] enables the solution of topology optimization problems with local stress constraints. A similar problem, considering a Drucker-Prager type yield criterion instead of a von Mises criterion, has been treated in 2012 by Amstutz et al., see [18]. Both [17] and [18] are mainly based on ideas from Amstutz, published in 2010 in [12]. Here, the topological gradient of a functional, resulting from the penalization of pointwise nonlinear constraints on the gradient of the state, has been investigated for the Laplace equation. Applications of the results regarding the von Mises case [17] have been considered by Lopes and Novotny in 2016, Santos et al. in 2017 and Novotny et al. in 2019, see [99], [120] and [106]. Considering the optimization of compliant mechanisms and multiple load cases, the main difference to [17] is the limit passage in the topological gradient of the artificial material coefficient. In 2013, a quadratic stress-based objective functional has been treated by Schneider and Andrä for anisotropic material, the configurational perturbation approach and a 3D setting, see [121]. It is worth mentioning, that [121] rigorously establishes a link between the topological gradient and results from the field of micromechanics, more precisely Eshelby's Theorem and the elastic moment tensor. The results from [121] have been extended to arbitrary, non-quadratic objectives by Delgado and Bonnet in 2015, see [51]. The techniques for performing the asymptotic expansion in [51] are based on the works from [31] and [7]. To the authors best knowledge, [51] is the most general work on the topological gradient in linear elasticity for objective functionals depending on the gradient of the state. In particular, all previously cited works are contained in [51] as special cases. For this reason, the methods developed in [51] are employed in this thesis.

4.2. Problem Setting

In this section, the problem class under investigation is introduced. We will investigate the topological asymptotic expansion for an *objective functional* of abstract structure, which contains the regularized functional (3.8) as special case. Regarding the *state equation*, a generalization of interface problem (2.10) is performed in terms of spatial dimension and material properties. Moreover, the class of *topology perturbations* will be fixed, which is the basis for identifying the topological gradient.

State Equation

The state system of the optimal control problem under consideration, which is a generalization of the interface problem (2.10), is introduced in the following. We consider a smooth and bounded hold-all domain $D \subset \mathbb{R}^d$ with $d = 2$ or 3, again with boundary partitioning $\partial D = \Gamma_D \cup \Gamma_N$, where $\Gamma_D \cap \Gamma_N = \emptyset$ and Γ_D is assumed to be of positive surface measure. Furthermore an open subset $\Omega \subset D$ is considered, representing a design. As in the previous part of this thesis, the sets Ω and $D \setminus \Omega$ represent two different material phases within the hold-all domain, which are separated by the material interface $\partial\Omega$. Within the domain D, we define the elasticity tensor

$$\mathbb{C}_\Omega := \mathbb{C}^{\text{mat}}\chi_\Omega + \mathbb{C}^{\text{air}}\chi_{D\setminus\Omega} \tag{4.3}$$

for a material distribution Ω with fourth-order tensors $\mathbb{C}^{\text{mat}}$ and $\mathbb{C}^{\text{air}}$, which are required to be positive definite and satisfy the minor and major symmetry properties. Note that a fourth-order tensor $\mathbb{C}$ is positive definite if $A : \mathbb{C}A > 0, \forall A \in \mathbb{R}^{d\times d}, A \neq 0$, satisfies minor symmetries if $M : \mathbb{C}N = M : \mathbb{C}N^T$, $M : \mathbb{C}N = M^T : \mathbb{C}N$ and has the major symmetry property if $M : \mathbb{C}N = N : \mathbb{C}M$ for all $M, N \in \mathbb{R}^{d\times d}$. We mention that the elasticity tensors, in contrast to the previous part, are allowed to be anisotropic. Analogously to Chapter 2, we define the bilinear form

$$a_\Omega(u, v) := \int_D \mathbb{C}_\Omega \epsilon(u) : \epsilon(v) dx \tag{4.4}$$

for $u, v \in H^1(D, \mathbb{R}^d)$. Similarly to the elasticity tensor (4.3), we generalize the volume forces of the elasticity problem as follows

$$f_\Omega := f^{\text{mat}}\chi_\Omega + f^{\text{air}}\chi_{D\setminus\Omega}, \tag{4.5}$$

with functions $f^{\text{mat}}, f^{\text{air}} \in C^{0,\beta}(D, \mathbb{R}^d)$ for $\beta > 0$. Further, given a traction force $g \in L^2(\Gamma_N, \mathbb{R}^d)$, we define the linear form

$$l_\Omega(v) := \int_D f_\Omega \cdot v dx + \int_{\Gamma_N} g \cdot v ds \tag{4.6}$$

for $v \in H^1(D, \mathbb{R}^d)$. Finally, for a prescribed boundary displacement $u_D \in L^2(\Gamma_D, \mathbb{R}^d)$ and the Sobolev space

$$\mathcal{V} := \{v \in H^1(D, \mathbb{R}^d) : v|_{\Gamma_D} = 0\}, \tag{4.7}$$

an element $u \in H^1(D, \mathbb{R}^d)$ is characterized as a solution of the state equation, if the equality

$$a_\Omega(u, v) = l_\Omega(v), \quad \forall v \in \mathcal{V} \tag{4.8}$$

is satisfied and $u|_{\Gamma_D} = u_D$ holds in the trace sense. Since equation (4.8) possesses a unique solution for every open $\Omega \subset D$, we will refer to this solution by u_Ω as in the previous chapter.

Objective Functional

Analogously to the state system, a generalization of the penalty term (3.8) will be introduced in the following. For an open subset $\Omega \subset D$ of the hold-all domain and the corresponding solution $u_\Omega \in H^1(D, \mathbb{R}^d)$ of the state equation (4.8), the objective functional in reduced form

$$\mathcal{J}(\Omega) := J_\Omega(u_\Omega, \epsilon(u_\Omega)) \tag{4.9}$$

with the following structure

$$\begin{aligned} J_\Omega : H^1(D, \mathbb{R}^d) \times L^2(D, \mathbb{R}^{d\times d}) &\to \mathbb{R} \\ (u, e) &\mapsto \int_D j_\Omega(x, u(x), e(x))dx \end{aligned} \tag{4.10}$$

will be considered throughout this chapter. Moreover, the density function in functional (4.10) is defined by

$$j_\Omega := j^{\text{mat}}\chi_\Omega + j^{\text{air}}\chi_{D\setminus\Omega}, \tag{4.11}$$

where the functions $j^{\text{mat}}, j^{\text{air}} : D \times \mathbb{R}^d \times \mathbb{R}^{d\times d} \to \mathbb{R}$ are assumed to be twice differentiable in all their arguments. Further, all second derivatives of j^{mat} and j^{air} are assumed to be in $C^{0,\eta}(D \times \mathbb{R}^d \times \mathbb{R}^{d\times d})$ for $\eta > 0$. Given $v \in H^1(D, \mathbb{R}^d)$ and $h \in L^2(D, \mathbb{R}^{d\times d})$, the partial derivatives of J_Ω are defined as follows:

$$\partial_u J_\Omega(u, e)(v) := \int_D \partial_u j_\Omega(x, u(x), e(x)) \cdot v(x)dx, \tag{4.12}$$

$$\partial_e J_\Omega(u, e)(h) := \int_D \partial_e j_\Omega(x, u(x), e(x)) : h(x)dx. \tag{4.13}$$

Topology Perturbations

We proceed by introducing topological perturbations of a given open subset $\Omega \subset D$. Throughout this chapter, we consider a smooth and bounded domain $\omega \subset \mathbb{R}^d$ containing the origin. Further, let a radius $\rho > 0$ and a point of perturbation $z \in D \setminus \partial\Omega$ be given. We define the scaled and shifted set

$$\omega_\rho := z + \rho\omega \tag{4.14}$$

as well as the perturbed design

$$\Omega_\rho := \begin{cases} \Omega \setminus \bar{\omega}_\rho, & \text{if } z \in \Omega, \\ \Omega \cup \omega_\rho, & \text{if } z \in D \setminus \bar{\Omega}, \end{cases} \tag{4.15}$$

which depends on the location of the point of perturbation. Based on (4.15), the perturbed state equation

$$a_{\Omega_\rho}(u, v) = l_{\Omega_\rho}(v), \forall v \in \mathcal{V}, \tag{4.16}$$

is stated. We will use the following abbreviations

$$\mathbb{C}_\rho := \mathbb{C}_{\Omega_\rho}, \quad a_\rho := a_{\Omega_\rho}, \quad f_\rho := f_{\Omega_\rho}, \quad l_\rho := l_{\Omega_\rho}, \quad u_\rho := u_{\Omega_\rho} \tag{4.17}$$

throughout this chapter for simplicity. Similarly, concerning objective functional (4.10), the quantities

$$j_\rho := j_{\Omega_\rho}, \quad J_\rho := J_{\Omega_\rho} \tag{4.18}$$

are introduced. The difference between the elasticity tensors is defined by

$$\mathbb{C}_\delta := \mathbb{C}^1 - \mathbb{C}^0, \tag{4.19}$$

where the following tensors

$$\mathbb{C}^0 := \begin{cases} \mathbb{C}^{\text{mat}}, & \text{if } z \in \Omega, \\ \mathbb{C}^{\text{air}}, & \text{if } z \in D \setminus \bar{\Omega}, \end{cases} \qquad \mathbb{C}^1 := \begin{cases} \mathbb{C}^{\text{air}}, & \text{if } z \in \Omega, \\ \mathbb{C}^{\text{mat}}, & \text{if } z \in D \setminus \bar{\Omega} \end{cases} \tag{4.20}$$

depend on the point of perturbation $z \in D \setminus \partial\Omega$, more precisely its location within the hold-all domain. Similarly, concerning the volume forces, we define the difference

$$f_\delta := f^1 - f^0, \tag{4.21}$$

where again the following functions

$$f^0 := \begin{cases} f^{\text{mat}}, & \text{if } z \in \Omega, \\ f^{\text{air}}, & \text{if } z \in D \setminus \bar{\Omega}, \end{cases} \qquad f^1 := \begin{cases} f^{\text{air}}, & \text{if } z \in \Omega, \\ f^{\text{mat}}, & \text{if } z \in D \setminus \bar{\Omega} \end{cases} \tag{4.22}$$

contain the dependency on the different material phases. In the same spirit, the difference

$$j_\delta := j^1 - j^0 \tag{4.23}$$

is defined with the functions

$$j^0 := \begin{cases} j^{\text{mat}}, & \text{if } z \in \Omega, \\ j^{\text{air}}, & \text{if } z \in D \setminus \bar{\Omega}, \end{cases} \qquad j^1 := \begin{cases} j^{\text{air}}, & \text{if } z \in \Omega, \\ j^{\text{mat}}, & \text{if } z \in D \setminus \bar{\Omega} \end{cases} \tag{4.24}$$

regarding the density functions in (4.10).

4.3. Asymptotic Analysis of the Perturbed State Variable

The goal of this chapter is the asymptotic expansion of objective functional $\mathcal{J}$, defined by (4.9), with respect to a topological perturbation of a given design Ω. More precisely, for the perturbed design Ω_ρ, defined by (4.15), the main task will be the investigation of the difference

$$\mathcal{J}(\Omega_\rho) - \mathcal{J}(\Omega), \tag{4.25}$$

aiming at identifying the topological gradient. A major challenge within the analysis of (4.25) lies in examining the impact of the topological perturbation on the system dynamics. In particular, we need to analyze the asymptotic behavior of the *perturbed state variable*, which is caused by a topological perturbation of the material distribution. Hence, the asymptotic expansion of the difference

$$u_\rho - u_0, \tag{4.26}$$

where u_ρ is the solution to (4.16), will be the key to the derivation of the topological gradient. Let us begin studying the asymptotic behavior of (4.26) in the following lemma.

Lemma 4.1. *Let u_ρ be the solution of the perturbed state equation (4.16) and let u_0 denote the unperturbed state, i.e. the solution of problem (4.8). Then, the following estimate holds:*

$$\|u_\rho - u_0\|_{H^1(D,\mathbb{R}^d)} = O(\rho^{d/2}). \tag{4.27}$$

Proof. Since u_ρ solves problem (4.16) and u_0 is the solution to (4.8), the identity

$$a_\rho(u_\rho, v) - a_0(u_0, v) = l_\rho(v) - l_0(v), \quad \forall v \in \mathcal{V}$$

holds and it follows immediately:

$$a_\rho(u_\rho - u_0, v) = a_0(u_0, v) - a_\rho(u_0, v) + l_\rho(v) - l_0(v), \quad \forall v \in \mathcal{V}. \tag{4.28}$$

Testing equation (4.28) with $v := u_\rho - u_0$ and employing the triangle inequality yields the following estimate:

$$a_\rho(u_\rho - u_0, u_\rho - u_0) \leq \left| \int_{\omega_\rho} \mathbb{C}_\delta \epsilon(u_0) : \epsilon(u_\rho - u_0) dx \right| + \left| \int_{\omega_\rho} f_\delta \cdot (u_\rho - u_0) dx \right|,$$

where $\mathbb{C}_\delta$ and f_δ have been defined in (4.19) and (4.21), respectively. For ρ small enough and $z \in D \setminus \partial\Omega$ denoting the point of perturbation, the assumed regularity of the volume force (4.5) implies the existence of a number $\eta > 0$ such that $\omega_\rho \subset \overline{B_\eta(z)}$ and

$$\epsilon(u_0)|_{\overline{B_\eta(z)}} \in C^0(\overline{B_\eta(z)}),$$

which yields the existence of a constant

$$c := \max_{x \in \overline{B_\eta(z)}} |\mathbb{C}_\delta \epsilon(u_0(x))| < \infty.$$

Hence, employing Hölder's inequality, the following estimate is obtained:

$$\begin{aligned} \left| \int_{\omega_\rho} \mathbb{C}_\delta \epsilon(u_0) : \epsilon(u_\rho - u_0) dx \right| &\leq \|\mathbb{C}_\delta \epsilon(u_0)\|_{L^2(\omega_\rho)} \|\epsilon(u_\rho - u_0)\|_{L^2(\omega_\rho)} \\ &\leq c|\omega_\rho|^{1/2} \|u_\rho - u_0\|_{H^1(\omega_\rho)}. \end{aligned}$$

Using the continuity of f_δ in a neighborhood of z, a similar estimate can be shown:

$$\left| \int_{\omega_\rho} f_\delta \cdot (u_\rho - u_0) dx \right| \leq \|f_\delta\|_{L^2(\omega_\rho)} \|u_\rho - u_0\|_{L^2(\omega_\rho)} \leq \tilde{c}|\omega_\rho|^{1/2} \|u_\rho - u_0\|_{H^1(\omega_\rho)},$$

where $\tilde{c} > 0$. A combination of the previous inequalities yields the following estimate:

$$a_\rho(u_\rho - u_0, u_\rho - u_0) \leq C|\omega_\rho|^{1/2}\|u_\rho - u_0\|_{H^1(\omega_\rho)} \leq C|\omega_\rho|^{1/2}\|u_\rho - u_0\|_{H^1(D)},$$

with $C > 0$. The coercivity of bilinear form a_ρ, which is precisely the inequality

$$C\|u_\rho - u_0\|^2_{H^1(D)} \leq a_\rho(u_\rho - u_0, u_\rho - u_0),$$

concludes the proof. □

We will see later on, in particular in the proof of Lemma 4.5, that the convergence rate in (4.27) is not sufficient for quantifying the impact of the topological perturbation on the state variable. Therefore, a correction term for $u_\rho - u_0$ is necessary in order to obtain a convergence rate of $o(\rho^{d/2})$ instead of $O(\rho^{d/2})$. Before this correction term is addressed, we need to introduce the following function space on $\mathbb{R}^d$.

Definition 4.2. *For $d \geq 1$, define the space*

$$\tilde{\mathcal{W}} := \left\{ w \in H^1_{loc}(\mathbb{R}^d, \mathbb{R}^d) : \nabla w \in L^2(\mathbb{R}^d, \mathbb{R}^{d\times d}) \right\},$$

with $H^1_{loc}(\mathbb{R}^d, \mathbb{R}^d)$ defined as in [8, Definition 3.13]. The Beppo-Levi space on $\mathbb{R}^d$ is defined as the quotient space

$$\mathcal{W} := \tilde{\mathcal{W}}/\mathbb{R}, \tag{4.29}$$

where all constant functions are factored out.

The following lemma addresses the structure of the Beppo-Levi space. For a proof, the interested reader is referred to [52].

Lemma 4.2. *Let a norm on the space $\mathcal{W}$ be defined by*

$$\|[u]\|_{\mathcal{W}} := \|\nabla u\|_{L^2(\mathbb{R}^d, \mathbb{R}^{d\times d})}, \tag{4.30}$$

where $[u] \in \mathcal{W}$ is an equivalence class and $u \in [u]$ denotes a representative. Then the Beppo-Levi space $\mathcal{W}$, equipped with norm (4.30), is a Hilbert space.

A central component of the correction term for $u_\rho - u_0$ will be the following partial differential equation in weak formulation, which is posed on the entire space $\mathbb{R}^d$

$$\text{Find } v_X \in \mathcal{W}, \quad \int_{\mathbb{R}^d} \mathbb{C}_\omega \epsilon(v_X) : \epsilon(w) dx = -\int_\omega \mathbb{C}_\delta X : \epsilon(w) dx, \quad \forall w \in \mathcal{W}, \tag{4.31}$$

for a given matrix $X \in \mathbb{R}^{d\times d}_{\text{sym}}$, $\mathbb{C}_\delta$ as in (4.19) and

$$\mathbb{C}_\omega := \mathbb{C}^0 \chi_{\mathbb{R}^n \setminus \bar{\omega}} + \mathbb{C}^1 \chi_\omega. \tag{4.32}$$

Remark 4.1. *The partial differential equation (4.31) is known as free space transmission problem in the literature, see for instance the monographs [9] and [10] of Ammari and Kang, where the asymptotic expansion of a topologically perturbed displacement field with applications to the detection of elastic inclusion in structures is addressed.*

Existence and uniqueness of a solution of problem (4.31) is guaranteed by the subsequent lemma.

Lemma 4.3. *For every $X \in \mathbb{R}^{d\times d}_{sym}$, there exists a unique solution $v_X \in \mathcal{W}$ of the free space transmission problem (4.31).*

Proof. The claim follows from the Lax-Milgram Lemma together with Lemma 4.2 and the coercivity of the elasticity tensors $\mathbb{C}^0, \mathbb{C}^1$. □

Let us proceed with the construction of an approximation of $u_\rho - u_0$. For $x \in \mathbb{R}^d$ and $\rho > 0$, we define

$$G_\rho(x) := \rho v_X \left(\frac{x - z}{\rho} \right), \tag{4.33}$$

where v_X denotes the solution of (4.31) with $X := \epsilon(u_0(z))$.

Lemma 4.4. *Let u_ρ be the solution of the perturbed state equation (4.16) and let u_0 denote the unperturbed state, i.e. the solution of problem (4.8). Further, let $G_\rho \in \mathcal{W}$ be defined in (4.33). Then, the following estimate holds:*

$$\|u_\rho - u_0 - G_\rho\|_{H^1(D,\mathbb{R}^d)} = o(\rho^{d/2}). \tag{4.34}$$

Proof. A proof can be found in [50]. □

Remark 4.2. *Estimate (4.34) shows that the perturbed state variable behaves approximately as*

$$u_\rho - u_0 \approx G_\rho \tag{4.35}$$

for small $\rho > 0$ with asymptotic growth rate $o(\rho^{d/2})$. For this reason, (4.33) is usually referred to as leading contribution of the inner approximation of $u_\rho - u_0$ in the literature, see for instance [7] and [51].

We proceed with the introduction of the *elastic moment tensor*, which is an essential ingredient for quantifying the perturbation of the state variable with respect to topological perturbations of the underlying material distribution.

Definition 4.3 (Elastic Moment Tensor)**.** *Let $X \in \mathbb{R}^{d\times d}_{sym}$ be given and let $v_X \in \mathcal{W}$ denote the solution to the free space transmission problem (4.31). The fourth-order tensor $\mathbb{E}$, defined by*

$$\mathbb{E}X := \int_\omega \mathbb{C}_\delta \left(X + \epsilon(v_X)\right) dx, \tag{4.36}$$

is called the elastic moment tensor.

As in the case of the free space transmission problem, the monographs of Ammari and Kang, see [9] and [10], provide a solid background on properties of the elastic moment tensor for isotropic material. The following asymptotic expansion will turn out to be crucial in the analysis of objective functional (4.9) and connects the perturbed state u_ρ with the elastic moment tensor $\mathbb{E}$.

Lemma 4.5. *For any vector field $w \in C^2(U, \mathbb{R}^d)$, where $U \subset D$ is a neighborhood of $z \in D$, the asymptotic expansion*

$$\int_{\omega_\rho} \mathbb{C}_\delta \epsilon(u_\rho) : \epsilon(w) dx = \rho^d \mathbb{E}\epsilon(u_0(z)) : \epsilon(w(z)) + o(\rho^d) \tag{4.37}$$

holds for arbitrarily small $\rho > 0$, where the elastic moment tensor $\mathbb{E}$ is defined in (4.36).

Proof. We begin by splitting the left hand side of (4.37) as follows

$$\int_{\omega_\rho} \mathbb{C}_\delta \epsilon(u_\rho) : \epsilon(w) dx = \int_{\omega_\rho} \mathbb{C}_\delta \epsilon(u_0 + G_\rho) : \epsilon(w) dx + \int_{\omega_\rho} \mathbb{C}_\delta \epsilon(u_\rho - u_0 - G_\rho) : \epsilon(w) dx, \tag{4.38}$$

with G_ρ defined in (4.33) and set $X := \epsilon(u_0(z))$. Concerning the first term in (4.38), the following identities hold

$$\begin{aligned}\int_{\omega_\rho} \mathbb{C}_\delta \epsilon(u_0 + G_\rho) : \epsilon(w) dx &= \int_{\omega_\rho} \mathbb{C}_\delta (X + \epsilon(G_\rho)) : \epsilon(w(z)) dx + o(\rho^d) \\ &= \rho^d \epsilon(w(z)) : \int_\omega \mathbb{C}_\delta (X + \epsilon(v_X)) dy + o(\rho^d) \\ &= \rho^d \epsilon(w(z)) : \mathbb{E}X + o(\rho^d),\end{aligned} \tag{4.39}$$

where the regularity of u_0 and w at z as well as a standard integral transformation have been used. Regarding the second term in (4.38), we obtain the following estimate by applying Hölder's inequality:

$$\int_{\omega_\rho} \mathbb{C}_\delta \epsilon(u_\rho - u_0 - G_\rho) : \epsilon(w) dx \leq c \|\epsilon(w)\|_{L^2(\omega_\rho)} \|\epsilon(u_\rho - u_0 - G_\rho)\|_{L^2(\omega_\rho)}.$$

Due to estimate (4.34) and the inequality

$$\|\epsilon(w)\|_{L^2(\omega_\rho)} \leq c\rho^{d/2},$$

it follows

$$\int_{\omega_\rho} \mathbb{C}_\delta \epsilon(u_\rho - u_0 - G_\rho) : \epsilon(w) dx = o(\rho^d), \tag{4.40}$$

which concludes the proof. □

Note that the elastic moment tensor arises naturally in (4.39) within the preceding proof. Furthermore, it can be noticed that (4.40) acts as remainder within (4.38), revealing the importance of the inner approximation G_ρ.

Sensitivity of the Control-to-State Operator

Let us take a different perspective at this point and employ the preceding results for investigating differentiability properties of the control-to-state operator

$$\begin{aligned} S : \mathcal{O} &\to H^1(D, \mathbb{R}^d) \\ \Omega &\mapsto u_\Omega, \end{aligned}$$

which has been introduced in Definition 2.4. In Theorem 3.2 of the previous chapter, continuity of the control-to-state operator S with respect to convergence in the sense of Hausdorff or in the sense of characteristic functions has already been shown. The question of differentiability and a sensitivity of operator S arises naturally at this point. As it has been pointed out in the introduction of this chapter, it is a priori not clear what a direction, and hence a sensitivity, in the context of optimal design problems actually is. Clearly, a meaningful notion of directions relies on the type of perturbations of a given design Ω. Within this chapter, the class of topological perturbations, see the previous section for details, has been chosen in order to define the topological gradient. For a point of perturbation $z \in D \setminus \partial\Omega$, a sequence of perturbed designs is given by $(\Omega_\rho)_{\rho>0}$. The following lemma shows that this sequence converges towards the unperturbed design Ω in the sense of characteristic functions.

Lemma 4.6. *Let a design $\Omega \in \mathcal{O}$, a radius $\rho > 0$ and a point of perturbation $z \in D \setminus \partial\Omega$ be given. Further, let the perturbed design Ω_ρ be defined as in (4.15). Then, it holds*

$$\Omega_\rho \xrightarrow{\rho \to 0} \Omega$$

in the sense of characteristic functions.

Proof. Assume $p \in [1, \infty)$. Elementary calculations and the definition of the perturbed design (4.15) show

$$\|\chi_{\Omega_\rho} - \chi_\Omega\|^p_{L^p(D)} = \int_D |\chi_{\Omega_\rho} - \chi_\Omega|^p dx = \int_{\omega_\rho} 1 dx = |\omega_\rho| \xrightarrow{\rho \to 0} 0,$$

which proofs the claim. □

The preceding lemma, together with Theorem 3.2, reveals that the mapping

$$\rho \mapsto u_\rho = S(\Omega_\rho) \tag{4.41}$$

is continuous. Note that this is reflected in estimate (4.27), which states that

$$\left\| u_\rho - u_0 \right\|_{H^1(D, \mathbb{R}^d)} \xrightarrow{\rho \to 0} 0.$$

Let us go a step further and examine the differentiability of (4.41) by analyzing the asymptotic behavior of the mapping

$$\rho \mapsto \frac{S(\Omega_\rho) - S(\Omega)}{\rho^{d/2}} \tag{4.42}$$

where a limit is guaranteed by (4.27). For the candidate

$$\rho \mapsto \frac{G_\rho}{\rho^{d/2}}, \tag{4.43}$$

where G_ρ is defined by (4.33), estimate (4.34) implies immediately

$$\left\| \frac{u_\rho - u_0}{\rho^{d/2}} - \frac{G_\rho}{\rho^{d/2}} \right\|_{H^1(D, \mathbb{R}^d)} \xrightarrow{\rho \to 0} 0.$$

Consequently, we observe the asymptotic behavior

$$\frac{S(\Omega_\rho) - S(\Omega)}{\rho^{d/2}} \approx \frac{G_\rho}{\rho^{d/2}}$$

for small $\rho > 0$.

4.4. Topological Asymptotic Expansion of the Objective Functional

Having investigated the asymptotic behavior of the perturbed state variable in the previous section, we continue with the topological asymptotic expansion of the objective functional (4.9). Before stating the main theorem, the *adjoint equation*

$$\text{Find } p \in \mathcal{V}, \quad a_\Omega(v,p) = \partial_u J_\Omega(u_\Omega, \epsilon(u_\Omega))(v) + \partial_e J_\Omega(u_\Omega, \epsilon(u_\Omega))(\epsilon(v)) \quad \forall v \in \mathcal{V}, \tag{4.44}$$

is introduced with u_Ω denoting the solution of (4.8), $\mathcal{V}$ defined in (4.7) and J_Ω the functional (4.10) with its partial derivatives defined by (4.12) and (4.13). It is straightforward to verify that the right hand side of equation (4.44) defines a bounded linear form. Hence, the lemma of Lax-Milgram ensures the existence of a unique solution of (4.44), which will be denoted by $p_\Omega \in \mathcal{V}$ and referred to as *adjoint state*.

Theorem 4.1. *Let an objective functional $\mathcal{J}$ of type (4.9), an open set $\Omega \subset D$, a smooth and bounded domain $\omega \subset \mathbb{R}^d$ containing the origin and a point of perturbation $z \in D \setminus \partial\Omega$ be given. Further, let $u_\Omega \in H^1(D, \mathbb{R}^d)$ denote the solution of the state equation (4.8) as well as $p_\Omega \in \mathcal{V}$ the solution of the adjoint equation (4.44). Assume that there exist $\delta > 0$ and $\beta > 0$ such that $u_\Omega, p_\Omega \in C^{2,\beta}(B_\delta(z))$ and abbreviate $u := u_\Omega(z), p := p_\Omega(z)$. Furthermore, let v_X denote the solution of (4.31) for $X = \epsilon(u_\Omega(z))$, $\mathbb{E}$ the elastic moment (4.36) and let j_δ and f_δ be defined by (4.23) and (4.21), respectively. Then, functional $\mathcal{J}$ allows an asymptotic expansion of the form (4.1) with $f(\rho) = \rho^d$. Moreover, the topological gradient of $\mathcal{J}$ is given by the following expression*

$$\begin{aligned} D_T\mathcal{J}[\Omega](z) =& |\omega| j_\delta(z, u, \epsilon(u)) + |\omega| f_\delta(z) \cdot p - \mathbb{E}\epsilon(u) : \epsilon(p) \\ &+ \partial_e j_\delta(z, u, \epsilon(u)) : \int_\omega \epsilon(v_X) dx \\ &+ \int_{\mathbb{R}^d \setminus \omega} \mathcal{G}^0(z, \epsilon(v_X)) dx + \int_\omega \mathcal{G}^1(z, \epsilon(v_X)) dx, \end{aligned} \tag{4.45}$$

where the functions $\mathcal{G}^i : \mathbb{R}^d \times \mathbb{R}^{d\times d} \to \mathbb{R}$, for $i \in \{0, 1\}$, are defined by

$$\mathcal{G}^i(z,h) := j^i(z, u, \epsilon(u) + h) - j^i(z, u, \epsilon(u)) - \partial_e j^i(z, u, \epsilon(u)) : h. \tag{4.46}$$

The proof of Theorem 4.1 is based on the analysis of the difference $\mathcal{J}(\Omega_\rho) - \mathcal{J}(\Omega)$.

First, we rewrite the difference in the following form:

$$
\begin{aligned}
&\mathcal{J}(\Omega_\rho) - \mathcal{J}(\Omega) \\
=&J_\rho(u_0, \epsilon(u_0)) - J_0(u_0, \epsilon(u_0)) && (4.47)\\
+&J_\rho(u_\rho, \epsilon(u_\rho)) - J_\rho(u_0, \epsilon(u_\rho)) - \partial_u J_\rho(u_0, \epsilon(u_0))(u_\rho - u_0) && (4.48)\\
+&J_\rho(u_0, \epsilon(u_\rho)) - J_\rho(u_0, \epsilon(u_0)) - \partial_e J_\rho(u_0, \epsilon(u_0))(\epsilon(u_\rho - u_0)) && (4.49)\\
+&\partial_u J_\rho(u_0, \epsilon(u_0))(u_\rho - u_0) + \partial_e J_\rho(u_0, \epsilon(u_0))(\epsilon(u_\rho - u_0)). && (4.50)
\end{aligned}
$$

In the following lemmas, we will analyze each term of the preceding equation separately. As a result, we can observe how each term contributes to the topological gradient (4.45).

Lemma 4.7. *Let the assumptions of Theorem 4.1 be satisfied. Further, let the perturbed objective functional J_ρ be defined by (4.18). Then, the following asymptotic expansion holds:*

$$J_\rho(u_0, \epsilon(u_0)) - J_0(u_0, \epsilon(u_0)) = \rho^d |\omega| j_\delta(z, u_0(z), \epsilon(u_0(z))) + o(\rho^d).$$

Proof. The proof is straightforward and can be found in [50]. □

Lemma 4.8. *Let the assumptions of Theorem 4.1 be satisfied. Further, let the perturbed objective functional J_ρ be defined by (4.18) and let $u_\rho \in H^1(D, \mathbb{R}^d)$ denote the perturbed state variable, i.e. the solution to problem (4.16). Then, the following asymptotic expansion holds:*

$$J_\rho(u_\rho, \epsilon(u_\rho)) - J_\rho(u_0, \epsilon(u_\rho)) - \partial_u J_\rho(u_0, \epsilon(u_0))(u_\rho - u_0) = o(\rho^d).$$

Proof. A proof can be found in [50]. □

Lemma 4.9. *Let the assumptions of Theorem 4.1 be satisfied. Further, let the perturbed objective functional J_ρ be defined by (4.18) and let $u_\rho \in H^1(D, \mathbb{R}^d)$ denote the perturbed state variable, i.e. the solution to problem (4.16). Then, the asymptotic expansion*

$$
\begin{aligned}
&J_\rho(u_0, \epsilon(u_\rho)) - J_\rho(u_0, \epsilon(u_0)) - \partial_e J_\rho(u_0, \epsilon(u_0))(\epsilon(u_\rho - u_0)) \\
=&\rho^d \left[\int_{\mathbb{R}^d \setminus \omega} \mathcal{G}^0(z, \epsilon(v_X)) dx + \int_\omega \mathcal{G}^1(z, \epsilon(v_X)) dx \right] + o(\rho^d),
\end{aligned}
$$

holds, where $\mathcal{G}^0, \mathcal{G}^1$ are defined in (4.46) and v_X is the solution of problem (4.31) with $X = \epsilon(u_0(z))$.

Proof. A proof can be found in [50]. □

Lemma 4.10. *Let the assumptions of Theorem 4.1 be satisfied. Further, let the perturbed objective functional J_ρ be defined by (4.18) and let $u_\rho \in H^1(D, \mathbb{R}^d)$ denote the perturbed state variable, i.e. the solution to problem (4.16). Moreover, let $p_0 \in \mathcal{V}$ denote the adjoint state, i.e. the solution of problem (4.44). Then, the asymptotic expansion*

$$\begin{aligned}
&\partial_u J_\rho(u_0, \epsilon(u_0))(u_\rho - u_0) + \partial_e J_\rho(u_0, \epsilon(u_0))(\epsilon(u_\rho - u_0)) \\
=&\rho^d \left[|\omega| f_\delta(z) \cdot p_0(z) - \mathbb{E}\epsilon(u_0(z)) : \epsilon(p_0(z)) + \partial_e j_\delta(z, u_0(z), \epsilon(u_0(z))) : \int_\omega \epsilon(v_X) dx \right] \\
&+ o(\rho^d)
\end{aligned}$$

holds, where $\mathbb{E}$ denotes the elastic moment tensor, defined by (4.36), and v_X is the solution of problem (4.31).

Proof. We begin the proof by splitting the expression in Lemma 4.10 into two parts as follows:

$$\begin{aligned}
&\partial_u J_\rho(u_0, \epsilon(u_0))(u_\rho - u_0) + \partial_e J_\rho(u_0, \epsilon(u_0))(\epsilon(u_\rho - u_0)) \\
=&\partial_u J_0(u_0, \epsilon(u_0))(u_\rho - u_0) + \partial_e J_0(u_0, \epsilon(u_0))(\epsilon(u_\rho - u_0)) && (4.51) \\
+&\partial_u [J_\rho - J_0](u_0, \epsilon(u_0))(u_\rho - u_0) + \partial_e [J_\rho - J_0](u_0, \epsilon(u_0))(\epsilon(u_\rho - u_0)). && (4.52)
\end{aligned}$$

Let us examine the term (4.51) first. The definition of the adjoint equation (4.44) yields immediately

$$\partial_u J_0(u_0, \epsilon(u_0))(u_\rho - u_0) + \partial_e J_0(u_0, \epsilon(u_0))(\epsilon(u_\rho - u_0)) = a_0(u_\rho - u_0, p_0),$$

where $a_0 := a_\Omega$ is an abbreviation for the unperturbed bilinear form. Further, by subtracting the unperturbed state equation (4.8) from the perturbed problem (4.16), the following identity is obtained:

$$a_\rho(u_\rho - u_0, w) = (l_\rho - l_0)(w) - (a_\rho - a_0)(u_0, w), \forall w \in \mathcal{V}. \tag{4.53}$$

Straightforward calculations, equality (4.53) and the asymptotic expansion (4.37) reveal the following identities:

$$
\begin{aligned}
&a_0(u_\rho - u_0, p_0) \\
=&a_\rho(u_\rho - u_0, p_0) - \int_{\omega_\rho} \mathbb{C}_\delta \epsilon(u_\rho - u_0) : \epsilon(p_0) dx \\
=&(l_\rho - l_0)(p_0) - (a_\rho - a_0)(u_0, p_0) - \int_{\omega_\rho} \mathbb{C}_\delta \epsilon(u_\rho - u_0) : \epsilon(p_0) dx \\
=&(l_\rho - l_0)(p_0) - \int_{\omega_\rho} \mathbb{C}_\delta \epsilon(u_\rho) : \epsilon(p_0) dx \\
=&\rho^d |\omega| f_\delta(z) \cdot p_0(z) - \rho^d \mathbb{E}\epsilon(u_0(z)) : \epsilon(p_0(z)) + o(\rho^d),
\end{aligned}
$$

which shows the asymptotic behavior of the term (4.51). Expression (4.52) can be treated as in [51]. □

Remark 4.3. *It is interesting to note that the topological gradient (4.45) simplifies significantly, if the objective functional (4.10) depends solely on the state, not on its gradient. More precisely, let us assume the objective functional to be of the following structure*

$$J_\Omega(u) := \int_D j_\Omega(x, u(x)) dx.$$

This structure is given in many applications, for example in the case of a compliance type functional. It can be observed that the topological gradient (4.45) in this situation becomes

$$D_T \mathcal{J}[\Omega](z) = |\omega| j_\delta(z, u_\Omega(z)) + |\omega| f_\delta(z) \cdot p_\Omega(z) - \mathbb{E}\epsilon(u_\Omega(z)) : \epsilon(p_\Omega(z)). \tag{4.54}$$

This expression is particularly interesting with regards to the numerical computation of the topological gradient. The only non-trivial part in (4.54) is the elastic moment tensor $\mathbb{E}$, which can be represented in closed form in certain cases. The analytical computation of tensor $\mathbb{E}$ will be investigated in the subsequent section.

4.5. Representation of the Topological Gradient in Closed Form

In the previous section, the topological asymptotic expansion of the objective functional (4.9) has been performed and its topological gradient (4.45) derived. An essential part of formula (4.45) is the solution $v_X \in \mathcal{W}$ of the free space transmission problem (4.31). Note that also the elastic moment tensor $\mathbb{E}$, defined in (4.36), depends on v_X.

Therefore, regarding the practical computation of the topological gradient, it remains to investigate how v_X can be represented analytically. First, we recall the free space transmission problem (4.31) with $X \in \mathbb{R}^{d\times d}_{\text{sym}}$ for the reader's convenience

$$\text{Find } v_X \in \mathcal{W}, \quad \int_{\mathbb{R}^d} \mathbb{C}_\omega \epsilon(v_X) : \epsilon(w) dx = -\int_\omega \mathbb{C}_\delta X : \epsilon(w) dx, \quad \forall w \in \mathcal{W},$$

where $\mathcal{W}$ denotes the Beppo-Levi space (4.29) and $\mathbb{C}_\omega$ and $\mathbb{C}_\delta$ are defined by (4.32) and (4.19), respectively.

Eshelby's Inhomogeneity and Inclusion Problem

In (4.33), we employed the solution v_X of the free space transmission problem (4.31) for the construction of the inner approximation of the perturbed state variable. Besides the topological asymptotic analysis of shape functionals, (4.31) plays an important role in the field of *micromechanics* where it is known as *Eshelby's inhomogeneity problem* (cf. [103]). Due to its central importance, several approaches for the solution of the inhomogeneity problem have been developed in the past decades. We will make use of these results in order to obtain an analytic expression for the solution v_X of (4.31) under certain assumptions regarding the shape of ω and the properties of the elasticity tensors.
As a first step, we introduce an additional problem, which is known as *Eshelby's inclusion problem* for given constant *eigenstrain* $\tau \in \mathbb{R}^{d\times d}_{\text{sym}}$:

$$\text{Find } v^\tau \in \mathcal{W}, \quad \int_{\mathbb{R}^d} \mathbb{C}^0 \epsilon(v^\tau) : \epsilon(w) dx = \int_\omega \mathbb{C}^0 \tau : \epsilon(w) dx, \quad \forall w \in \mathcal{W}. \tag{4.55}$$

In the literature, the solution of (4.55) is often referred to as *Eshelby's solution*. A brief note on the physical intuition behind the term eigenstrain is given in the following remark.

Remark 4.4. *The term eigenstrain has been coined by T. Mura (cf. [103]). From a physical point of view, it refers to strains in infinite bodies, which are not caused by external forces. A typical example of eigenstrains is thermal expansion. Here, a part ω of the considered body is subjected to temperature changes. If ω wasn't surrounded by material, the change in temperature would result in a change of the displacement field. Since ω is part of an infinite body, however, internal stresses are generated.*

It can be observed that the inhomogeneity problem (4.31) and the inclusion problem (4.55) are of a similar structure, but have certain differences. The subsequent remark deals with the differences from a physical point of view.

Remark 4.5 (Inclusion and Inhomogeneity)**.** *It is common in micromechanics to distinguish between inclusions and inhomogeneities, see for instance [103] or [59]. A part ω of a body under consideration is called inclusion, if the entire body consists of homogeneous material and an eigenstrain is applied within ω. In contrast, a part ω is referred to as inhomogeneity, if the material properties within ω differ from those of the remaining body.*

The basic idea of the following procedure is now to investigate the solution of problem (4.55), which has several useful properties, and to connect it with the solution of Eshelby's inhomogeneity problem. First, the existence of a solution of the inclusion problem needs to be examined.

Lemma 4.11. *For any eigenstrain $\tau \in \mathbb{R}^{d\times d}_{sym}$, Eshelby's inclusion problem (4.55) possesses a unique solution. Moreover, the solution operator*

$$\tau \mapsto v^\tau \tag{4.56}$$

is a linear mapping.

Proof. Existence and uniqueness of a solution can be shown in a standard fashion by application of the Lax-Milgram theorem. The linearity of mapping (4.56) follows immediately from the fact that the right hand side of problem (4.55) is linear in τ. □

Inclusions of Ellipsoidal Shape

Having introduced the inclusion problem (4.55), we proceed investigating its solution v^τ as well as the connection to the inhomogeneity problem (4.31). An important step towards an explicit formula for v^τ is the restriction of the inclusion ω. For this purpose, we assume the inclusion to be of *ellipsoidal shape* from now on, which is a central requirement in the subsequent theorem. Note that the elasticity tensors $\mathbb{C}^0$ and $\mathbb{C}^1$ are allowed to be anisotropic at this point. Together with the linearity of mapping (4.56), the following statements concerning Eshelby's inclusion problem can be formulated.

Theorem 4.2 (Eshelby's theorem)**.** *Assume the inclusion ω to be an ellipsoid for $d = 3$ and an ellipse for $d = 2$. Let further an arbitrary eigenstrain $\tau \in \mathbb{R}^{d\times d}_{sym}$ be given and let v^τ denote the solution of the inclusion problem (4.55). Then, there exists a mapping $\mathbb{S} : \mathbb{R}^d \to \mathcal{L}(\mathbb{R}^{d\times d}_{sym})$, called Eshelby tensor, such that*

$$\epsilon(v^\tau)(x) = \mathbb{S}(x)\tau, \quad \forall x \in \mathbb{R}^d \backslash \partial\omega, \tag{4.57}$$

with

$$\mathbb{S}(x) := \begin{cases} \mathbb{S}^{int}, & x \in \omega, \\ \mathbb{S}^{ext}(x), & x \in \mathbb{R}^d \backslash \bar{\omega}, \end{cases} \tag{4.58}$$

where $\mathbb{S}^{int}$ is a constant tensor.

Proof. A proof has been given in the publications of Eshelby, see [59] and [60] for isotropic material. For the anisotropic case, we refer the reader to [103]. □

The importance of Theorem 4.2, which was proven by Eshelby in his pioneering work [59], lies in the insight that the strain of v^τ is constant inside an inclusion of ellipsoidal shape. The tensors $\mathbb{S}^{\text{int}}$ and $\mathbb{S}^{\text{ext}}$ in (4.58) are called *interior* and *exterior Eshelby tensor*, respectively.

Remark 4.6. *Note that the solution of Eshelby's inclusion problem (4.55) is entirely determined by the elasticity tensor $\mathbb{C}^0$ as well as the inclusion ω. Consequently, Eshelby's tensor $\mathbb{S}$ encodes the properties of the background material and the shape of the inclusion.*

The following result links Eshelby's inhomogeneity problem to the inclusion problem. As a consequence, identity (4.57) from Eshelby's theorem can be employed for the solution of the inhomogeneity problem.

Theorem 4.3 (Equivalent inclusion method)**.** *Let the inhomogeneity ω be an ellipsoid for $d = 3$ and an ellipse for $d = 2$ and consider an arbitrary matrix $X \in \mathbb{R}^{d\times d}_{sym}$. Then, the fourth order tensor $\mathbb{C}_\delta^{-1}(\mathbb{C}^0 + \mathbb{C}_\delta \mathbb{S}^{int})$ is invertible. Further, the solution of Eshelby's inclusion problem (4.55) is related to the solution of Eshelby's inhomogeneity problem (4.31) by the identity*

$$v_X = v^\tau, \tag{4.59}$$

where

$$\tau = -(\mathbb{C}^0 + \mathbb{C}_\delta \mathbb{S}^{int})^{-1} \mathbb{C}_\delta X.$$

The equivalent inclusion method goes back to J. Eshelby, see [59]. A recent proof can be found in [121], which is repeated here for convenience.

Proof. Starting from problem (4.55) with the unique solution $v^\tau \in \mathcal{W}$, we obtain the identity

$$\int_{\mathbb{R}^d} \mathbb{C}^0 \epsilon(v^\tau) : \epsilon(w) dx = \int_\omega \mathbb{C}^0 \tau : \epsilon(w) dx \pm \int_\omega \mathbb{C}^1 \epsilon(v^\tau) : \epsilon(w) dx, \quad \forall w \in \mathcal{W}.$$

Rearranging terms and utilizing (4.57) yields

$$\int_{\mathbb{R}^d} \mathbb{C}_\omega \epsilon(v^\tau) : \epsilon(w) dx = \int_\omega (\mathbb{C}^0 + \mathbb{C}_\delta \mathbb{S}^{\text{int}})\tau : \epsilon(w) dx, \quad \forall w \in \mathcal{W},$$

revealing the equality

$$v^\tau = v_X \tag{4.60}$$

with $X := -\mathbb{C}_\delta^{-1}(\mathbb{C}^0 + \mathbb{C}_\delta \mathbb{S}^{\text{int}})\tau$. It remains to show that $\mathbb{C}_\delta^{-1}(\mathbb{C}^0 + \mathbb{C}_\delta \mathbb{S}^{\text{int}})$ is invertible or, in other words, that the mapping

$$\tau \mapsto \mathbb{C}_\delta^{-1}(\mathbb{C}^0 + \mathbb{C}_\delta \mathbb{S}^{\text{int}})\tau \tag{4.61}$$

is bijective. Since (4.61) maps between the same finite-dimensional space, that is $\mathbb{R}^{d\times d}_{\text{sym}}$, it suffices to show that (4.61) is injective. Let us therefore assume that $\mathbb{C}_\delta^{-1}(\mathbb{C}^0 + \mathbb{C}_\delta \mathbb{S}^{\text{int}})\tau = 0$ holds. Due to the linearity of the mapping $X \mapsto v_X$, the equality $v_X = 0$ follows immediately. Further, due to (4.60), we obtain $v^\tau = 0$. The linearity of (4.56) finally implies $\tau = 0$. □

Using the results above, we arrive at an expression for the strain of the solution of Eshelby's inhomogeneity problem in closed form.

Corollary 4.1. *Assume ω and X to be defined as in the previous theorem and let v_X be the solution of Eshelby's inhomogeneity problem (4.31). Then, the identity*

$$\epsilon(v_X)(x) = -\mathbb{S}(x)(\mathbb{C}^0 + \mathbb{C}_\delta \mathbb{S}^{int})^{-1}\mathbb{C}_\delta X \tag{4.62}$$

holds for all $x \in \mathbb{R}^d \backslash \partial\omega$, where $\mathbb{S}$ is defined in (4.58).

Proof. The statement follows immediately from the application of the equivalent inclusion method (4.59) and Eshelby's theorem (4.57). □

In the same manner, an analytical expression for the elastic moment tensor (4.36) is found.

Corollary 4.2. *Let ω be as in the previous theorem. Then, the elastic moment tensor $\mathbb{E}$ is of the following form:*

$$\mathbb{E} = |\omega|\mathbb{C}^0(\mathbb{C}^0 + \mathbb{C}_\delta \mathbb{S}^{int})^{-1}\mathbb{C}_\delta. \tag{4.63}$$

Proof. Let $X \in \mathbb{R}^{d\times d}_{\text{sym}}$ be arbitrary. Since the elastic moment tensor $\mathbb{E}$ is defined as an integral over ω in (4.36) and $\epsilon(v_X)$ is constant inside ω according to (4.62), we obtain the following identity:

$$\mathbb{E}X = |\omega|\left[\mathbb{C}_\delta - \mathbb{C}_\delta \mathbb{S}^{\text{int}}(\mathbb{C}^0 + \mathbb{C}_\delta \mathbb{S}^{\text{int}})^{-1}\mathbb{C}_\delta\right] X.$$

Further, we observe

$$\mathbb{C}_\delta \mathbb{S}^{\text{int}} = (\mathbb{C}^0 + \mathbb{C}_\delta \mathbb{S}^{\text{int}}) - \mathbb{C}^0 \Longleftrightarrow \mathbb{C}_\delta \mathbb{S}^{\text{int}}(\mathbb{C}^0 + \mathbb{C}_\delta \mathbb{S}^{\text{int}})^{-1} = \mathbb{I} - \mathbb{C}^0(\mathbb{C}^0 + \mathbb{C}_\delta \mathbb{S}^{\text{int}})^{-1},$$

which concludes the proof. □

Isotropic Material and Circular Inhomogeneity

The derived analytical expressions reveal that both the solution of the inhomogeneity problem (4.31), as well as the elastic moment tensor (4.36), depend only on the elasticity tensors and Eshelby's tensor (4.58). Consequently, the computation of Eshelby's tensors needs to be investigated at this point. In the general case of anisotropic material, expressions in closed form for the tensors $\mathbb{S}^{\text{int}}$ and $\mathbb{S}^{\text{ext}}$ are not available. Instead, numerical procedures have to be employed in practical realizations, see [103] and [50]. If the material tensors $\mathbb{C}^0$ and $\mathbb{C}^1$ are *isotropic*, however, analytic expressions for $\mathbb{S}^{\text{int}}$ and $\mathbb{S}^{\text{ext}}$ can be found. These formulas have first been provided by Eshelby in [59] and [60]. Although expressions in closed form are available if the inhomogeneity is of ellipsoidal shape, we restrict the setting at this point to a *circular inhomogeneity*. The reason for this restriction is the fact that the resulting formulas for $\mathbb{S}^{\text{int}}$ and $\mathbb{S}^{\text{ext}}$ become simpler, which is particularly convenient when it comes to the practical realization. Moreover, the simple case of circular inhomogeneities is sufficient in the context of topology optimization algorithms based on topological gradients. Since the model problem in this thesis is posed in the two-dimensional space, we will omit the formulas for the three-dimensional case at this point. However, we remark that the corresponding formulas can be found in [121].

Lemma 4.12. *Let $\omega = B_1(0) \subset \mathbb{R}^2$ and assume the elasticity tensor $\mathbb{C}^0$ of the background material to be isotropic with Poisson's ratio $\nu = \frac{\lambda_0}{2(\lambda_0+\mu_0)}$. Then, the interior Eshelby tensor $\mathbb{S}^{int}$ can be represented in closed form by*

$$\mathbb{S}^{int} = \frac{3 - 4\bar{\nu}}{4(1-\bar{\nu})}\mathbb{I} + \frac{4\bar{\nu} - 1}{8(1-\bar{\nu})} I \otimes I, \tag{4.64}$$

with

$$\bar{\nu} := \begin{cases} \nu, & \textit{(plane strain assumption)}, \\ \frac{\nu}{1+\nu}, & \textit{(plane stress assumption)}. \end{cases} \tag{4.65}$$

Moreover, let $x \in \mathbb{R}^2 \backslash \bar{\omega}$ *and set* $\rho := \frac{1}{|x|}, \bar{x} := \rho x$. *For* $T \in \mathbb{R}^{2\times 2}_{sym}$, *the exterior Eshelby tensor can be written in closed form as follows*

$$\begin{aligned} \mathbb{S}^{ext}(x)T = \frac{\rho^2}{8(1-\bar{\nu})}\Big[&(\rho^2 + 4\bar{\nu} - 2)tr[T]\mathbb{I} + 2(\rho^2 - 4\bar{\nu} + 2)T \\ &+ 4(1-\rho^2)T\bar{x}\cdot\bar{x}\mathbb{I} + 4(1 - 2\bar{\nu} - \rho^2)tr[T]\bar{x}\odot\bar{x} \\ &+ 16(\bar{\nu} - \rho^2)\bar{x}\odot T\bar{x} + 8(3\rho^2 - 2)\bar{x}\cdot T\bar{x}\bar{x}\odot\bar{x}\Big], \end{aligned} \tag{4.66}$$

with

$$y \odot z := \frac{1}{2}(y \otimes z + z \otimes y),$$

for $y, z \in \mathbb{R}^2$.

Proof. Proofs of the identities (4.64) and (4.66) are available in the literature, see for instance [103] and [97]. □

As stated in (4.65), the plane strain and plane stress case needs to be distinguished in the computation of Eshelby's tensors. Clearly, this is necessary regarding the elasticity tensor as well.

Remark 4.7. *In plane elasticity, i.e. in the two dimensional case, the conversion of elastic moduli needs to be handled carefully. More precisely, it has to be distinguished between plane strain and plane stress assumptions in the Lamé coefficients* μ, λ, *which determine the elasticity tensor*

$$\mathbb{C} = 2\mu\mathbb{I} + \lambda I \otimes I$$

in the presence of isotropic material. In the plane strain case, the connection between the Lamé coefficients (μ, λ) *and* (E, ν), *where* E *denotes Young's modulus and* ν *represents Poisson's ratio, is given as follows:*

$$\mu = \frac{E}{2(1+\nu)}, \quad \lambda = \frac{\nu E}{(1+\nu)(1-2\nu)}.$$

Conversely, in the plane stress case, the following relations hold:

$$\mu = \frac{E}{2(1+\nu)}, \quad \lambda = \frac{\nu E}{1-\nu^2}.$$

Note that the formulas for the general 3D case coincide with the 2D plan strain case. Further details on the difference between plane strain and plane stress assumptions can be found in [47].

Having a formula in closed form for the interior Eshelby tensor at hand, see (4.64), the elastic moment tensor can be computed analytically as well.

Corollary 4.3. *Assume $\omega = B_1(0) \subset \mathbb{R}^2$. Further, let the elasticity tensors of the background material $\mathbb{C}^0$ and the inhomogeneity $\mathbb{C}^1$ be isotropic, i.e.*

$$\mathbb{C}^0 = 2\mu_0 \mathbb{I} + \lambda_0 I \otimes I, \quad \mathbb{C}^1 = 2\mu_1 \mathbb{I} + \lambda_1 I \otimes I,$$

and assume

$$\frac{\mu_1}{\mu_0} = \frac{\lambda_1}{\lambda_0} := r.$$

Then, the elastic moment tensor (4.36) is given by

$$\mathbb{E} = |\omega| \mathbb{C}^0 \mathbb{P}, \tag{4.67}$$

where

$$\mathbb{P} := \frac{(r-1)(k+1)}{2(kr+1)} \left[2\mathbb{I} + \frac{(r-1)(k-2)}{k+2r-1} I \otimes I \right]$$

and

$$k := \frac{3\mu_0 + \lambda_0}{\mu_0 + \lambda_0}.$$

Proof. Due to the formula (4.63), it suffices to show

$$(\mathbb{C}^0 + \mathbb{C}_\delta \mathbb{S}^{\text{int}})^{-1} \mathbb{C}_\delta = \mathbb{P}.$$

The first step is to verify the identity

$$(\mathbb{C}^0 + \mathbb{C}_\delta \mathbb{S}^{\text{int}})^{-1} \mathbb{C}_\delta = \frac{b_\delta}{b_0 + b_\delta t} \mathbb{I} + \frac{1}{2} \left[\frac{a_\delta}{a_0 + a_\delta s} - \frac{b_\delta}{b_0 + b_\delta t} \right] \mathrm{I} \otimes \mathrm{I}$$

with

$$\begin{aligned} a_\delta &:= a_1 - a_0, & a_0 &:= \lambda_0 + \mu_0, & a_1 &:= \lambda_1 + \mu_1, \\ b_\delta &:= b_1 - b_0, & b_0 &:= \mu_0, & b_1 &:= \mu_1, \end{aligned}$$

and

$$s := \frac{2}{k+1}, \quad t := \frac{k}{k+1},$$

where the formula (4.64) for the interior Eshelby tensor is used. In a second step, straightforward calculations reveal the equalities

$$\frac{b_\delta}{b_0 + b_\delta t} = \frac{(r-1)(k+1)}{kr+1}, \quad \frac{1}{2}\left[\frac{a_\delta}{a_0 + a_\delta s} - \frac{b_\delta}{b_0 + b_\delta t}\right] = \frac{(r-1)^2(k-2)(k+1)}{2(kr+1)(k+2r-1)},$$

which conclude the proof. □

Remark 4.8. *It is worth mentioning that (4.67) coincides with the formula for the elastic moment tensor $\mathcal{P}_{\omega,r}$ in [11, p. 98], which in turn has been checked to be identical with the elastic moment tensor of Ammari and Kang in [9] and [10].*

Remark 4.9. *It can be observed in (4.64) and (4.67) that the isotropy of the elasticity tensors is inherited to the interior Eshelby tensor $\mathbb{S}^{int}$ as well as the elastic moment tensor $\mathbb{E}$.*

5. Topology Optimization Scheme

5.1. Introduction

This chapter addresses the solution of optimization problem (3.7), introduced in the beginning of this thesis, by means of a numerical algorithm. For this purpose, we consider the generic topology optimization problem

$$\min_{\Omega \in \mathcal{O}} \mathcal{J}(\Omega), \tag{5.1}$$

where $\mathcal{J} : \mathcal{O} \to \mathbb{R}$ is a shape functional on a set of admissible designs $\mathcal{O} \subset \mathcal{P}(D)$, which are contained in the power set of a Lipschitz domain $D \subset \mathbb{R}^2$. In order to solve the minimization problem (5.1), a descent scheme is employed. The core of the presented method is the topological gradient, see (4.1), serving as a descent direction in the iterative algorithm. Since the topological gradient is not a gradient in the classical sense, but rather a directional derivative, the selection of appropriate optimization algorithms is not straightforward. This issue will be discussed in more detail later on. Let us assume for this chapter that the topological gradient of objective functional $\mathcal{J}$ exists for every design $\Omega \in \mathcal{O}$ and every point of perturbation within $D \setminus \partial\Omega$. The essential question arises at this point, how it can be used for topology optimization or, in other words, how it can be used to solve optimization problem (5.1). Two fundamentally different approaches are available in the literature, which are described briefly in the following.

The first approach is an extension of a shape optimization scheme. The field of shape optimization addresses the minimization of shape functionals over a set of designs with fixed topology. Hence, the admissible set is smaller compared to the admissible set in the topology optimization case, where different topologies are allowed. A common approach for the solution of shape optimization problems consists in a descent scheme, where a descent direction is provided by shape sensitivities. These objects are a measure for the sensitivity of a shape functional with respect to smooth boundary perturbations of a given design Ω. For details on shape optimization, we refer the reader to the monograph [129] by Sokołowski and Zolésio. One approach within the

field of shape optimization is the level set method, based on the works of Osher and Sethian, see [108] and [123]. Fundamental for this method is the implicit representation of a given design $\Omega \in \mathcal{O}$ by a *level set function* $\psi : D \to \mathbb{R}$ via

$$\Omega = \{x \in D : \psi(x) > 0\}, \quad D \backslash \bar{\Omega} = \{x \in D : \psi(x) < 0\}.$$

The basic idea of the level set method is to control the evolution of the level set function ψ by a Hamilton-Jacobi equation (cf. [123]) in a fictitious time, corresponding to the iterations of an optimization algorithm. The velocity field in the Hamilton-Jacobi equation involves shape sensitivities, which are thus responsible for steering the evolution of ψ. The shape sensitivities can be of different type. Allaire et al. investigated the level set method using shape gradients, see [6]. Furthermore, approaches involving second order shape information, known as shape Hessians, have been examined by Hintermüller and Ring, see [88].
Numerical realizations have demonstrated that the level set method using shape sensitivities is capable of solving the shape optimization problem satisfactorily. However, topological changes of the generated designs can still decrease the value of the objective functional. The reason for this is that the algorithm is not capable of performing topological changes. Thus, the topology of the designs, generated by the level set algorithm, is highly dependent on the initial topology. This observation is not surprising, considering the fact that only shape sensitivities are used in the optimization scheme. In practice, the merging of holes is possible with the level set method. The creation of new holes, at least for the two dimensional case, is impossible, see [6].
As a consequence of this observation, it becomes clear that a mechanism for topological changes needs to be incorporated in the level set method. More precisely, the algorithm has to be designed in such a way that a design after convergence is stationary in a certain topological sense. The appropriate tool for this task has been discovered to be provided by the topological gradient. An extension of the level set method using shape sensitivities by the topological gradient has been investigated by Burger et al. in [37] and Allaire et al. in [3]. The main idea of these approaches consists in choosing an initial design, applying the level set method using shape sensitivities and assessing a topological stationarity measure of the resulting design. The stationarity measure is based on the topological gradient and will be discussed in more detail later on. If the design is not topologically stationary, a change of topology is performed by the creation of small holes. The locations of these holes are chosen according to the minimal values of the topological gradient. Different strategies concerning the number of created holes may be employed, where either one or several holes are created simultaneously. This

procedure is repeated as long as topological changes decrease the objective functional. Further, the topological gradient as a tool for automatized initialization prior to shape optimization has been addressed by Hintermüller and Laurain in [83] and [85].
Besides the extension of the level set method with shape sensitivities, a second algorithm, using topological gradients only, is available in the literature. Different variants have been proposed by Hintermüller in [80] and Amstutz and Andrä in [14]. Both works rely, as in the previously presented method, on an implicit description of a design $\Omega \in \mathcal{O}$ by a level set function ψ. In contrast to the previously described scheme, this algorithm requires solely topological sensitivities. An advantage over the first approach is therefore that the shape sensitivity analysis of objective functional $\mathcal{J}$ becomes obsolete. It is important to notice that, even though this approach is referred to as level set algorithm in the literature, it is fundamentally different from the standard level set method from shape optimization. While in the case of shape optimization, the evolution of the level set function is controlled by a Hamilton-Jacobi equation, a fixed-point equation is employed in the topology optimization case. The second algorithm, using only topological sensitivities, is chosen for solving the topology problem at hand in this work. The reader, interested in the analysis of the algorithm, is referred to [13].

5.2. Level Set Algorithm

The following definition is essential for the development of a topology optimization algorithm and addresses the implicit representation of an arbitrary design via a level set function.

Definition 5.1 (Level set function)**.** *Let a design $\Omega \in \mathcal{O}$ be given. The level set function $\psi \in C^0(D)$ associated to Ω is defined implicitly by the following relations:*

$$\Omega = \{x \in D : \psi(x) > 0\}, \quad D \backslash \bar{\Omega} = \{x \in D : \psi(x) < 0\}. \tag{5.2}$$

As every design $\Omega \in \mathcal{O}$ can be represented by a level set function $\psi = \psi_\Omega \in C^0(D)$, we can formulate the optimal design problem (5.1) with the level set function as optimization variable. Introducing the functional $\bar{\mathcal{J}} : C^0(D) \to \mathbb{R}$, which is defined by the relation $\bar{\mathcal{J}}(\psi_\Omega) = \mathcal{J}(\Omega)$, we can formulate the minimization problem (5.1) as follows:

$$\min_{\psi \in C^0(D)} \bar{\mathcal{J}}(\psi).$$

Having the development of a numerical optimization algorithm for the solution of (5.1) in mind, the determination of a *descent direction* is a central task. The base for this quantity will be provided by the topological gradient, which has been introduced in the previous chapter, see Definition 4.1. Given a material distribution $\Omega \in \mathcal{O}$, we recall that the topological gradient $D_T\mathcal{J}[\Omega] : D \setminus \partial\Omega \to \mathbb{R}$ indicates, if a change of topology decreases the objective functional. This is the case for a point of perturbation $z \in D \setminus \partial\Omega$, if $D_T\mathcal{J}[\Omega](z) < 0$ holds true. Within this chapter, we assume the topological gradient to be continuous in the material phase Ω as well as the weak phase $D \setminus \bar{\Omega}$, which allows the pointwise evaluation in both phases. In the following, we distinguish two cases:

1. Assume $z \in \Omega$. According to definition (5.2), property $\psi(z) > 0$ holds true. In order to change the topology in z, the sign of the level set function ψ has to be reversed in a neighbourhood of z. As we assumed $D_T\mathcal{J}[\Omega](z) < 0$, the change of topology can be achieved by adding a multiple of $D_T\mathcal{J}[\Omega]$ to ψ. Note that this situation corresponds to the creation of a weak component in the hard phase Ω.

2. Assume $z \in D\setminus\bar{\Omega}$, i.e. $\psi(z) < 0$. In this case, a positive quantity needs to be added to the level set function in order to reverse the sign of ψ in a neighbourhood of z. As $D_T\mathcal{J}[\Omega](z) < 0$, a multiple of $-D_T\mathcal{J}[\Omega]$ is a possible choice. The interpretation of this case is the insertion of a hard component in the soft phase.

These observations motivate the following definition.

Definition 5.2 (Topological descent direction)**.** *Let the level set function $\psi \in C^0(D)$ associated to a design $\Omega \in \mathcal{O}$ be given and consider the topological gradient $D_T\mathcal{J}[\Omega]$ of the shape functional $\mathcal{J} : \mathcal{O} \to \mathbb{R}$. The topological descent direction $g_\psi : D \setminus \partial\Omega \to \mathbb{R}$ is defined as follows for every $x \in D \setminus \partial\Omega$:*

$$g_\psi(x) := \begin{cases} D_T\mathcal{J}[\Omega](x), & \psi(x) > 0, \\ -D_T\mathcal{J}[\Omega](x), & \psi(x) < 0. \end{cases} \tag{5.3}$$

Remark 5.1. *Note that the topological descent direction is not defined explicitly on the interface $\partial\Omega$ between hard and weak phase in (5.3). In numerical realizations, however, explicit values are determined via gradient filtering. This issue will be discussed in the subsequent chapter.*

In the following, optimality conditions regarding the topological gradient are discussed.

Definition 5.3. *Consider a shape functional $\mathcal{J} : \mathcal{O} \to \mathbb{R}$. A design $\Omega \in \mathcal{O}$ is called stationary in the topological sense, if the property*

$$D_T\mathcal{J}[\Omega](x) > 0 \tag{5.4}$$

holds for all $x \in D \setminus \partial\Omega$.

It is important to notice at this point that stationarity in the topological sense can not be expressed via a vanishing gradient, as it is the case in standard theory of continuous optimization. The reason for this is that the topological gradient is not a gradient in the classical sense. As definition (5.4) indicates, it corresponds to the notion of directional derivatives. The direction in this situation is Ω_ρ, the design Ω perturbed at z with radius $\rho > 0$ small enough. Since the direction Ω_ρ, characterized by the point of perturbation z, is an intrinsic part of the topological gradient, it is impossible to isolate an object, behaving like a gradient from the theory of continuous optimization. Note that this is a fundamental difference to the field of shape gradients. Here, a shape gradient, independent of a direction can be isolated. This result regarding the shape gradient is known as structure theorem, details can be found in [129].

Remark 5.2. *The stationarity condition (5.4) provides a sufficient local optimality criterion. If the property (5.4) is weakened to*

$$D_T\mathcal{J}[\Omega](x) \geq 0,$$

a necessary local optimality criterion is obtained.

The following result provides an equivalent characterization of stationarity in the topological sense.

Lemma 5.1. *Let the level set function* $\psi \in C^0(D)$ *associated to a design* $\Omega \in \mathcal{O}$ *be given and consider the topological descent direction* $g_\psi : D \setminus \partial\Omega \to \mathbb{R}$. *The design* Ω *is stationary, if and only if the equation*

$$sign[g_\psi(x)] = sign[\psi(x)] \tag{5.5}$$

holds for all $x \in D\setminus\partial\Omega$.

Proof. The assertion follows immediately from (5.4), the definition of the level set function (5.2) and the topological descent direction (5.3). □

Corollary 5.1. *Assume that there exists* $c > 0$, *such that the following equation*

$$\psi(x) = c \cdot g_\psi(x) \tag{5.6}$$

holds for all $x \in D \setminus \partial\Omega$. *Then,* Ω *is a stationary design.*

Having different characterizations of stationarity of a design $\Omega \in \mathcal{O}$ or, equivalently, of the associated level set function $\psi \in C^0(D)$ at hand, the construction of an algorithm for the solution of (5.1) is investigated. First, we observe that the level set function $c\psi$ represents the design $\Omega \in \mathcal{O}$, independent of the choice of $c > 0$. In order to prevent the level set function to take large values, and thus aiming at numerical stability, the following condition is imposed

$$\|\psi\|_{L^2(D)} = 1, \tag{5.7}$$

where the L^2-norm is employed. As a consequence, the stationarity condition (5.6) can be written equivalently by the equation

$$\psi(x) = \frac{g_\psi(x)}{\|g_\psi\|_{L^2(D)}}, \tag{5.8}$$

which is required to hold for all $x \in D \backslash \partial\Omega$.

The next step is the construction of an update scheme for the iterative solution of the optimal design problem (5.1), aiming at the stationarity condition (5.8). Therefore, given an index $i \in \mathbb{N}$, we consider a current iterate $\psi_i \in C^0(D)$ with the topological descent direction g_{ψ_i} and assume $\|\psi_i\|_{L^2(D)} = 1$. The aim is now the construction of an update ψ_{i+1} based on the level set function ψ_i and the descent direction g_{ψ_i}, which is again required to fulfill the equality $\|\psi_{i+1}\|_{L^2(D)} = 1$ due to (5.7). Since the main intention regarding the update step is to achieve a decrease of the objective functional, i.e. $\bar{\mathcal{J}}(\psi_{i+1}) < \bar{\mathcal{J}}(\psi_i)$, we construct ψ_{i+1} by adding a multiple of g_{ψ_i} to the current iterate ψ_i. Note that the topological descent direction has been introduced for exactly this purpose, see the discussion in the beginning of this section. Hence, we define the update of the current level set function as follows

$$\psi_{i+1} := \alpha_i \psi_i + \beta_i \frac{g_{\psi_i}}{\|g_{\psi_i}\|_{L^2(D)}},$$

with coefficients $\alpha_i, \beta_i \in \mathbb{R}_0^+$ controlling the trade-off between current level set function and descent direction. Within an iterative scheme, the coefficients α_i and β_i need to be chosen appropriately in order to obtain a decrease of the objective functional. Based on a parameter $\kappa_i \in (0, 1]$ and the angle

$$\theta_i := \arccos\left[\frac{(\psi_i, g_{\psi_i})_{L^2(D)}}{\|g_{\psi_i}\|_{L^2(D)}}\right] \tag{5.9}$$

between the level set function ψ_i and the descent direction g_{ψ_i}, we set the coefficients

as follows

$$\alpha_i := \frac{\sin((1-\kappa_i)\theta_i)}{\sin(\theta_i)}, \qquad \beta_i := \frac{\sin(\kappa_i\theta_i)}{\sin(\theta_i)}, \tag{5.10}$$

which guarantees the required property $\|\psi_{i+1}\|_{L^2(D)} = 1$. For details regarding the derivation of α_i and β_i using the rules of trigonometry, we refer the reader to [14] or [62]. Employing (5.10), we obtain the following update scheme

$$\psi_{i+1} = \frac{1}{\sin(\theta_i)} \left[\sin((1-\kappa_i)\theta_i)\psi_i + \sin(\kappa_i\theta_i) \frac{g_{\psi_i}}{\|g_{\psi_i}\|_{L^2(D)}} \right], \tag{5.11}$$

where κ_i can be interpreted as a line search parameter. Note that θ_i vanishes, if the optimality condition (5.8) is satisfied. Hence, θ_i can be used as a stationarity criterion in the topology optimization algorithm. The resulting algorithm can be interpreted as a descent scheme, where g_ψ provides a descent direction, and is sketched in Algorithm 5.1.

Algorithm 5.1: Level set-based topology optimization algorithm

Input: Initial design Ω_0, tolerance ϵ_θ
Output: Solution Ω^* of topology optimization problem (5.1)

Generate initial level set function ψ_0 from Ω_0
Compute the descent direction g_{ψ_0} according to (5.3)
Compute the angle θ_0 according to (5.9)
Set $i \leftarrow 0$
while $\theta_i \geq \epsilon_\theta$ **do**
    Set $\kappa \leftarrow 1, \psi_{\text{temp}} \leftarrow \psi_i, \mathcal{J}_{\text{temp}} \leftarrow \bar{\mathcal{J}}(\psi_i)$
    while $\mathcal{J}_{temp} \geq \bar{\mathcal{J}}(\psi_i)$ **do**
        Update: $\psi_{\text{temp}} = \frac{1}{\sin(\theta_i)} \left[\sin((1-\kappa)\theta_i)\psi_i + \sin(\kappa\theta_i) \frac{g_{\psi_i}}{\|g_{\psi_i}\|_{L^2(D)}} \right]$
        Objective evaluation: $\mathcal{J}_{\text{temp}} \leftarrow \bar{\mathcal{J}}(\psi_{\text{temp}})$
        Step reduction: $\kappa \leftarrow \frac{\kappa}{2}$
    Set $\psi_{i+1} \leftarrow \psi_{\text{temp}}$
    Compute the descent direction $g_{\psi_{i+1}}$ according to (5.3)
    Compute the angle θ_{i+1} according to (5.9)
    Set $i \leftarrow i + 1$;
Reconstruct design Ω^* from level set function ψ_i
return Ω^*

The update scheme (5.11) can be derived alternatively via an ordinary differential equation, which is discussed in the following remark.

Remark 5.3. *Let us introduce a fictitious optimization time $t \geq 0$, corresponding to a continuous version of a discrete iteration index. Further, let us replace the level set function $\psi(x)$ by $\psi(t,x)$ and analogously the descent direction $g_\psi(x)$ by $g_\psi(t,x)$. Since g_ψ is an indicator for topological stationarity, a natural choice of controlling the dynamics of ψ is the following ordinary differential equation:*

$$\psi(0,\cdot) = \psi_0, \qquad \frac{\partial \psi}{\partial t} = g_\psi, \ \forall t > 0, \tag{5.12}$$

where ψ_0 represents the initial design. Note that a requirement for (5.12) to settle in a stationary state is $\frac{\partial \psi}{\partial t} = 0$. This is the case, if g_ψ vanishes. However, this condition contradicts property (5.4). For this reason, the ordinary differential equation (5.12) is extended by

$$\frac{\partial \psi}{\partial t} = g_\psi - \frac{(\psi, g_\psi)}{\|\psi\|^2}\psi, \tag{5.13}$$

where the right hand side is the orthogonal projection of g_ψ on the orthogonal complement of ψ. It can be verified that the level set function in (5.13) has unitary norm for every $t \geq 0$. Moreover, if the right hand side of (5.13) vanishes, the stationarity condition (5.6) is fulfilled, see [14]. An explicit Euler scheme on the unit sphere for (5.13) leads to the update regime (5.11).

We mention that two assumptions concerning the problem setting have been made in this chapter. First, the hold-all domain D has been assumed to be a subset of the two-dimensional space. Second, the distribution of precisely two materials has been addressed. The following remark deals with the generalization of these restrictions.

Remark 5.4. *Algorithm 5.1 can be generalized straightforwardly to the three-dimensional case, if the corresponding topological gradient is available. For one iteration, this has been done by Gangl and Sturm in [71]. Moreover, the level set algorithm can be extended in order to optimize the distribution of more than two materials. For details regarding this topic, the interested reader is referred to [66] and [118].*

6. Numerical Realization

6.1. Introduction

The aim of this chapter is the *numerical solution* of the regularized optimal design problem (3.7) using the level set algorithm from the previous chapter. Since the numerical solution comprises replacing the infinite-dimensional problem by a finite-dimensional approximation, all objects involved in the optimization scheme are required in discrete form. Therefore, the discretization of the *level set function* (5.2), the *topological descent direction* (5.3) and the *objective functional* in (3.7) will be the subject of investigation within this chapter.
Before we begin with the discretization of all relevant objects, the main ideas regarding the numerical realization will be sketched. In particular, the relation between the *infinite-dimensional problem* and its *discrete counterpart* will be discussed briefly. Further, the specific content of this chapter with regards to this greater context will be clarified. Let us denote the set of admissible continuous designs by $\mathcal{O}$ as in (2.19) and let us refer to the set of *discrete designs* by $\mathcal{O}_h$ for a discretization parameter $h > 0$. The exact definition of a discrete design will be omitted here for the sake of simplicity and stated later on. It may be useful for the intuition, however, to think of discrete designs as sets with a piecewise linear boundary, which is bound to a triangulation of the underlying hold-all domain. Let us consider a sequence of discrete designs

$$(\Omega_h)_{h>0}, \tag{6.1}$$

with $\Omega_h \in \mathcal{O}_h$ denoting a solution of the finite-dimensional approximation of problem (3.7). Note that sequence (6.1) is generated by a numerical algorithm in a practical setting. The existence of solutions to the discrete design problems is assumed at this point, which is reasonable since existence for the continuous case has been addressed in Chapter 3 and properties of infinite-dimensional objects are typically inherited to the discrete case. A question, which arises naturally at this point, is whether sequence (6.1) converges towards a continuous design for a vanishing discretization parameter. In other words, one might ask if there exists a design $\Omega^* \in \mathcal{O}$ with

$$\Omega_h \to \Omega^*, \text{ if } h \to 0 \tag{6.2}$$

for an appropriately chosen norm. A crucial task, provided that convergence (6.2) holds, is to identify properties of design Ω^*. The most important question at this point is probably, whether Ω^* is a local minimum of the continuous optimal design problem (3.7). This property is clearly a requirement for the design of a numerical optimization scheme. An important aspect within these considerations is the limiting behavior of the associated discrete states $u_h \in \mathcal{V}_h$, where $\mathcal{V}_h$ denotes the discrete state space for discretization parameter $h > 0$. Note that a discrete design Ω_h and discrete state u_h are connected via the equation

$$a_{\Omega_h}(u_h, v_h) = l_{\Omega_h}(v_h), \quad \forall v_h \in \mathcal{V}_h, \tag{6.3}$$

which is the discrete variant of state equation (2.10). The reader, who is familiar with the *finite element method*, will have noticed that the bilinear form and linear form in (6.3) are not constant, but vary with Ω_h. This situation is commonly known as variational crime, see for instance [35]. It should be mentioned that these considerations are classical questions from the field of numerical analysis.

The preceding considerations show that the numerical realization comprises several complex aspects concerning theory as well as practice. Since the investigation of all different questions exceeds the scope of this thesis, we will not examine the limiting behavior (6.2) of a sequence of discrete designs (6.1) for a vanishing mesh size. Instead, the scope of this chapter is the *practical algorithmic computation* of a discrete solution for a fixed discretization parameter. This is a crucial step towards the numerical experiments, which will be conducted and discussed in the following chapters. We mention at this point that, to the author's best knowledge, there are no works available dealing explicitly with the numerical realization of algorithms for solving stress-constrained topology optimization problems. Since this aspect is crucial for a practical realization, in particular for the presence of pointwise stress constraints, this chapter aims at closing this gap in the literature.

We will begin by discussing the numerical solution of the involved partial differential equations, which are the direct and adjoint state equations. This is a fundamental step in the evaluation of the objective functional as well as the computation of the topological descent direction. The major focus at this point will be the assembly process and the discrete elasticity tensor, especially with regards to the presence of stress constraints. Having the discrete direct and adjoint state at hand, we can address the discretization of all objects which appear directly in the optimization algorithm.

In this step, the computation of the topological gradient will turn out to be crucial. Further, we discuss several aspects concerning the practical implementation of the developed method within an object-oriented framework on a computer.

6.2. Numerical Solution of Interface Problems

An essential part of the gradient-based algorithm for solving optimal design problem (3.7) is a numerical scheme for the solution of the involved partial differential equations. The problems to be solved are the *state equation* (2.10) and the *adjoint equation* (4.44), which form the basis for the computation of the objective functional as well as the topological gradient. In this section, we address the discretization of both problems as well as the assembly of the resulting discrete systems via the *finite element method*. The case of mesh elements, which are intersected by the material interface, will be of particular interest. For a thorough background on the numerical solution of partial differential equations with the finite element method, the reader is referred to the monographs [34], [35] and [46]. Let us assume within this chapter that the hold-all domain $D \subset \mathbb{R}^2$ is a polygonal Lipschitz domain and $\mathcal{T}_h$ an admissible triangulation of D, see [34, Definition 5.1] for details.

Remark 6.1. *It is essential for an admissible triangulation that the underlying domain is of polygonal shape. Clearly, this assumption is unrealistic when it comes to real-world applications, for instance in the case of an electrical machine. Note that the polygonal domain D may be imagined as an approximation of a real geometry, facilitating the mathematical treatment. For details on the finite element method regarding domains with non-polygonal boundaries, we refer the reader to [34] or [22].*

Finite Element Approach

We choose the vector-valued finite element space of second order

$$\mathcal{V}_h := \mathcal{S}^2(\mathcal{T}_h)^2 := \{v \in C^0(D, \mathbb{R}^2) : v|_T \in \mathbb{P}_2(T, \mathbb{R}^2), \forall T \in \mathcal{T}_h\} \tag{6.4}$$

as a finite-dimensional conformal approximation of the Sobolev space $\mathcal{V} := H^1(D, \mathbb{R}^2)$ with nodal basis $\{\phi_1, ..., \phi_M\}$, where $M := \dim \mathcal{V}_h$. For the definition of the nodal basis of a Lagrangian finite element space, we refer the reader to [34, Definition 5.5].

Remark 6.2. *The choice of second order finite elements is a common procedure in structural engineering and provides an excellent trade-off between accuracy and computational effort, in particular with regards to stress analysis.*

We will consider an arbitrary design $\Omega \in \mathcal{O}$, representing the material distribution within the hold-all domain D, throughout this section in order to discuss the discretization of the relevant interface problems. Note that we explicitly choose a continuous design for the sake of generality, since the set of discrete designs, which will be introduced in the subsequent section, is contained in the set of continuous designs $\mathcal{O}$. Nevertheless, in the numerical realization of the level set algorithm, the state and adjoint equation will of course be solved with respect to a given discrete design. We mention at this point that the discretization of a design, which represents the control variable of problem (3.7), and the state are not necessarily related and can be chosen independently. The *discrete state*

$$u_h = \sum_{i=1}^{M} U_i \phi_i \in \mathcal{V}_h,$$

with scalars $U_i \in \mathbb{R}, i = 1, ..., M$, denotes the unique solution of the following system of linear equations

$$\sum_{i=1}^{M} U_i a_\Omega(\phi_i, \phi_j) = a_\Omega(u_h, \phi_j) = l_\Omega(\phi_j), \quad 1 \leq j \leq M, \tag{6.5}$$

where the bilinear form a_Ω and the linear form l_Ω have been defined in (2.8) and (2.9), respectively.

Remark 6.3. *Note that the discretization of the state equation (2.10) is addressed in (6.5). Regarding the following discussion, the adjoint equation (4.44) may be considered just as well by replacing the linear form l_Ω by the corresponding right hand side of (4.44), where transposing the bilinear form $a_\Omega(\cdot, \cdot)$ in (6.5) is not necessary due to the symmetry of the elasticity tensor.*

This system of linear equations can be represented equivalently by

$$A_\Omega U = b_\Omega, \tag{6.6}$$

with vector $U = (U_1, ..., U_M)^T \in \mathbb{R}^M$, *stiffness matrix* $A_\Omega \in \mathbb{R}^{M \times M}$, defined by

$$A_\Omega^{ij} := a_\Omega(\phi_i, \phi_j), \quad 1 \leq i, j \leq M, \tag{6.7}$$

and *load vector* $b_\Omega \in \mathbb{R}^M$, which is defined similarly by

$$b_\Omega^j := l_\Omega(\phi_j), \quad 1 \leq j \leq M. \tag{6.8}$$

It can be observed immediately that the solution of the *discrete system* (6.5) is equivalent to the solution of the system of linear equations (6.6) in $\mathbb{R}^M$. Concerning techniques for the solution of the discrete system, in particular the advantages of direct and indirect solvers, the reader is referred to [34].

Accuracy of Discrete Approximations

Let us proceed by focusing on the *assembly* process of stiffness matrix A_Ω for $\Omega \in \mathcal{O}$ with *interface* $\Gamma := \partial\Omega$. Note that the assembly of the load vector b_Ω follows the same procedure. For $1 \leq i, j \leq M$, the corresponding entry of the stiffness matrix reads

$$A_\Omega^{ij} = a_\Omega(\phi_i, \phi_j) = \int_D \mathbb{C}_\Omega \epsilon(\phi_i) : \epsilon(\phi_j) dx = \sum_{T \in \mathcal{T}_h} \int_T \mathbb{C}_\Omega \epsilon(\phi_i) : \epsilon(\phi_j) dx, \tag{6.9}$$

where the elasticity tensor is defined by

$$\mathbb{C}_\Omega = \mathbb{C}^0 \chi_\Omega + \mathbb{C}^1 \chi_{D \setminus \Omega}. \tag{6.10}$$

It can be observed on the discrete level that, given a quadrature rule $\{(w_p, x_p)\}_{p=1}^P$ on T with weights $w_p \in \mathbb{R}$ and integration points $x_p \in \mathbb{R}^2$ for $1 \leq p \leq P$, an approximation of the corresponding summand in (6.9) reads

$$\int_T \mathbb{C}_\Omega \epsilon(\phi_i) : \epsilon(\phi_j) dx \approx \sum_{p=1}^P w_p \mathbb{C}_\Omega(x_p) \epsilon(\phi_i(x_p)) : \epsilon(\phi_j(x_p)). \tag{6.11}$$

If a mesh element $T \in \mathcal{T}_h$ is entirely occupied by phase Ω or its complement $D \setminus \Omega$, the assembly on T is straightforward due to the smoothness of $\mathbb{C}^0$ and $\mathbb{C}^1$. If, however, T is *intersected by the interface* Γ, we have to face the discontinuity of $\mathbb{C}_\Omega$ on T. The assignment of values of the material coefficient $\mathbb{C}_\Omega$ in this situation will be the subject of the following discussion. An example of an intersected element is provided in Figure 6.1.

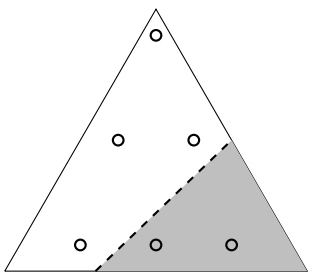

Figure 6.1.: Intersected triangle T with interface Γ and six quadrature points.

First, the effect of a discontinuous material coefficient within the interior of a mesh element on a numerical algorithm needs to be clarified. Essentially, the answer is in the *accuracy* of approximations of the continuous state variable, being generated by a numerical scheme. In order to specify this thought, we consider the solution of the continuous problem (2.10), which is denoted by $u \in \mathcal{V}$, as well as the discrete state $u_h \in \mathcal{V}_h$, which is the solution of the discrete problem (6.5). A key question at this point is, given a discretization parameter $h > 0$, how close the discrete solution u_h is to the exact solution u or, formulated slightly different, how small parameter h needs to be chosen in order to achieve a certain approximation accuracy.

Remark 6.4. *Note that the term accuracy in this context is to be understood as the convergence rate* $\|u - u_h\| = O(h^\alpha)$ *of sequence* $(u_h)_h$ *for a vanishing discretization parameter* $h > 0$ *and exponent* $\alpha > 0$*. Clearly, this convergence rate is determined by the specific choice of the numerical scheme, which is employed for generating the discrete solutions* $u_h \in \mathcal{V}_h$*, where parameter* h *refers to the mesh size of the underlying triangulation.*

Let us assume for a moment that the material coefficient is *globally smooth* in the entire domain D and the discrete solution belongs to $u_h \in \mathcal{S}^k(\mathcal{T}_h)^2$ for $k \geq 1$. In this case, standard finite element theory, see for instance [34, Theorem 6.4], offers the a priori estimate

$$\|u - u_h\|_{\mathcal{V}} = O(h^k), \tag{6.12}$$

if the solution u belongs to the space $H^{k+1}(D, \mathbb{R}^2)$. Consequently, the convergence rate of the approximative solutions is determined by the regularity of the true solution and can be improved by increasing the order $k \in \mathbb{N}$ of the finite element space.
This estimate, however, is not valid in the case of interface problems with *intersected mesh elements*. Indeed, the a priori estimate

$$\|u - u_h\|_{\mathcal{V}} = O(h^{1/2}), \tag{6.13}$$

holds in this situation, see for instance [20]. The most interesting implication of this estimate is probably that the convergence rate of a standard finite element scheme can not be improved by increasing the polynomial degree k. It is important to note that this problem does not occur, if the interface Γ is resolved by the mesh $\mathcal{T}_h$, see [21]. This is the case, if the interface is aligned with the mesh faces and there is no occurrence of intersected elements.

Strategies for the Assignment of Material Coefficients

Having the convergence rates (6.12) and (6.13) in mind, we come back to the assignment of material coefficients on intersected elements within the assembly of the stiffness matrix. We will discuss several assignment strategies with a major focus on an accurate stress computation within the optimization algorithm, which is of utmost importance for obtaining realistic results in the subsequent chapters. Essentially, there are three options for dealing with the discontinuity of the material coefficient, if the triangulation as well as the basis of the finite element space are assumed to be *constant*. We will briefly introduce and describe the three options in the following and discuss the effect on the stress constraints afterwards.

1. **Assignment based on element centroid**
   The first option is to assign an intersected element entirely to one of the two material phases based on the position of its centroid. This procedure has been performed in [65] within a topology optimization scheme based on a level set approach. Note that this strategy leads to a jagged interface. A visualization of this assignment strategy is provided by the left graphic in Figure 6.2.

2. **Harmonic averaging**
   The second option consists in an averaging of the material coefficient on intersected elements. This strategy is by far the most common choice in the field of level set-based design optimization, see for instance [6] and [14], offering the advantage of optimal convergence rates of finite element approximations, see [63]. Unfortunately, this procedure is not physically reasonable in every situation. For the class of fluid-structure-interaction problems for instance, the averaging of the material coefficient corresponds to the mixing of fluid and solid. We refer to the middle graphic in Figure 6.2 for an illustration.

3. **Discontinuous material coefficient**
   The third strategy is to perform the assembly in a standard fashion, accepting the discontinuity of the elasticity tensor and hence the low convergence rate of finite element approximations. This assignment strategy is visualized by the right graphic in Figure 6.2.

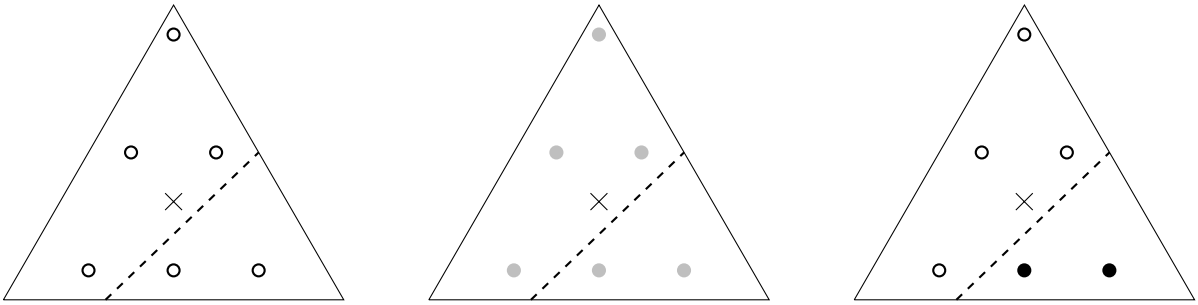

Figure 6.2.: Material assignment strategies for intersected element. Left: Assignment based on element centroid. Middle: Harmonic averaging. Right: Discontinuous material coefficient.

Having the three options for material assignment at hand, the question arises, which one should be chosen within an algorithm for the solution of an optimal design problem with *stress constraints*. First, let us recall that the aim of incorporating stress constraints into the optimal control problem is the prevention of material failure. In other words, stress constraints are used to quantify, and thus be able to control, material failure. Further, it is known that in many situations failure occurs initially at the boundary of a loaded structure and propagates into the interior. An example for this phenomenon is crack initiation and propagation, see the discussion in Section 2.3 for further details. Consequently, as the boundary of the loaded structure is represented by the interface Γ in this work, it is important to guarantee an accurate stress computation in this area. In the following, the different strategies of material assignment are assessed with respect to the computation of stresses at the interface. Note that the same elasticity tensor is employed within the partial differential equation and the computation of stresses in a postprocessing step.

As mentioned above, one has to face a jagged interface if the *first material assignment strategy* is chosen. This procedure, stemming essentially from a manipulation of the interface, leads to artificial stress peaks at the interface. Consequently, a reasonable design might be rejected within the update step of the optimization algorithm due to a jagged distortion of the interface.

In contrast, the *second strategy* may lead to unrealistic low stresses in intersected elements. This is a consequence of the averaging procedure and the weak phase approach, which has been described in Section 2.1. As a result, a design in this situation can be accepted by the update regime of the optimization algorithm, although its true stress values at the interface are much larger than predicted.

As a result, the *assembly in standard fashion* is selected in this thesis. Being aware of the convergence rate (6.13) of an finite element approximation, this procedure is chosen

due to its comparable accurate stress computation. The low convergence rate will be taken into account in the numerical experiments by choosing an appropriately fine triangulation.
It is important to note that the different strategies above have been developed under the premise of a fixed *triangulation* and a fixed *basis of the finite element space*. Of course, methods with optimal convergence rates are available if either the triangulation or the basis of the finite element space are allowed to be modified in order to resolve the interface. Several approaches for the numerical solution of interface problems have been developed in the past and will be summarized in the following. First, the category of *fitted methods* will be described briefly. All approaches in this category rely on a mesh modification during the numerical solution of interface problems. One approach to deal with moving interfaces, which is widely used in shape optimization, consists of manipulating a given mesh by moving its vertices. This method is commonly referred to as *mesh morphing* in the literature. Further approaches are the local mesh refinement at the interface as well as the generation of a completely new mesh, which a priori resolves the interface. Moreover, several approaches have been proposed for numerically treating interface problems by the modification of the basis of finite element spaces. These approaches are summarized under the category of *unfitted methods*. The *extended finite element method* relies on the enrichment of the finite element space by additional basis functions, see e.g. [24]. Originally, the extended finite element method has been developed for the numerical investigation of crack propagation within the field of elasticity. A similar approach is provided by the *immersed finite element method*. In contrast to the extended finite element method, the number of basis functions is kept constant and the existing basis functions with support at the interface are modified. We refer the reader to [98] for details. Another approach has been developed in [64] in the context of fluid-structure interaction. This method relies on a local adaptation of the finite element space in an implicit parametric way for a mesh consisting of quadrilaterals. Note that this approach has been modified for the case of triangles and applied in the context of shape and topology optimization in [65].

6.3. Discrete Optimization Algorithm

Having discussed the approximation of the direct and adjoint state, the next step is the numerical computation of the level set function, the topological gradient and the objective functional.

Discrete Designs

Since the *level set function* is the basis for computing the descent direction and evaluating the objective functional, its discretization will be discussed first. Note that the relation between designs and level set functions has been introduced in (5.2) in the previous chapter. The space

$$\mathcal{W}_h := \mathcal{S}^1(\mathcal{T}_h), \tag{6.14}$$

where $\mathcal{T}_h$ is the same triangulation as in the previous section, is chosen for the discretization of the level set function. Hence, the discrete state and the level set function share the identical triangulation. Due to the polynomial order of the space $\mathcal{W}_h$, the interface

$$\Gamma_h = \{x \in D : \psi_h(x) = 0\}$$

of a *discrete level set function* $\psi_h \in \mathcal{W}_h$ is a polygonal chain. More precisely, the interface is continuous across edges and a line segment on every intersected mesh element.

Remark 6.5. *It is important to see that space (6.14) is not a priori determined for the discretization of the space of level set functions, but is chosen explicitly at this point. The first reason for choosing (6.14) is the global continuity of functions $\psi_h \in \mathcal{W}_h$, which is necessary for defining a meaningful interface. Moreover, the polynomial degree is chosen as low as possible in order to reduce the computational burden in a practical implementation. Note that the values of the level set function on the nodes of space $\mathcal{W}_h$, which coincide in this situation with the vertices $\mathcal{N}_h$ of mesh $\mathcal{T}_h$, are the optimization variables of the level set algorithm. Lastly, an interface consisting of line segments can be resolved by a local mesh refinement using standard elements.*

For any discrete level set function $\psi_h \in \mathcal{W}_h$, the associated discrete design $\Omega_h \subset D$ is determined as in the continuous setting by

$$\Omega_h = \{x \in D : \psi_h(x) > 0\}. \tag{6.15}$$

Consequently, the set of *discrete designs* can be defined as follows

$$\mathcal{O}_h := \{\Omega_h \subset D : \exists \psi_h \in \mathcal{W}_h \text{ with } \Omega_h = \psi_h^+\}, \tag{6.16}$$

where $\psi_h^+ := \{x \in D : \psi_h(x) > 0\}$.

Remark 6.6. *Note that the set $\mathcal{O}_h$ is contained in the set of continuous designs $\mathcal{O}$ if the*

uniform Lipschitz property in (2.19) is satisfied. It can be verified that this property is given, if the angle of interface Γ_h is bounded away from zero on each intersected edge. As it can be observed in (6.16), we did not incorporate such a condition in the definition of $\mathcal{O}_h$. We recall at this point that the Lipschitz property in the continuous case has been necessary for guaranteeing compactness of $\mathcal{O}$ and certain effects, such as boundary oscillations, may occur for the limit of a sequence in $\mathcal{O}$. Since we did not observe any negative effects in the numerical experiments, however, the incorporation of a condition concerning the Lipschitz property has not been necessary. We mention at this point that the use of a fixed triangulation within the optimization process prevents oscillations of the boundary.

Discontinuity of Topological Descent Direction

For the remaining section, we consider an arbitrary objective functional $\mathcal{J} : \mathcal{O} \to \mathbb{R}$, which allows a topological asymptotic expansion as defined in Definition 4.1. In the optimization algorithm, which has been introduced in the previous chapter, the *topological descent direction* is responsible for generating updates of the level set function. The descent direction $g_\psi : D \setminus \partial\Omega \to \mathbb{R}$ is repeated in the following for convenience

$$g_\psi(x) = \begin{cases} D_T\mathcal{J}[\Omega](x), & \psi(x) > 0, \\ -D_T\mathcal{J}[\Omega](x), & \psi(x) < 0, \end{cases}$$

where $\psi : D \to \mathbb{R}$ is the level set function and $D_T\mathcal{J}[\Omega] : D \setminus \partial\Omega \to \mathbb{R}$ denotes the topological gradient of objective functional $\mathcal{J}$, which has been specified in Definition 4.1. We proceed with the discretization of the topological descent direction, which is an essential step in the realization of the level set-based optimization scheme. The first aspect to be addressed is the choice of a suitable discrete space for the descent direction. This choice is determined by the discrete space of the level set function, since the DOF vectors need to be added within the update step of the optimization scheme. Consequently, the discrete descent direction needs to be an element of the space $\mathcal{W}_h$, as it is the case for the level set function. The central task is therefore to define the values of the discrete descent direction at the nodes of the first order finite element space $\mathcal{W}_h$, which coincide with the mesh vertices.
Let us recall that the gradient of the direct and adjoint state form the basis of the topological gradient, see for example expression (4.45) for the stress-based objective functional (4.9). Further, the computation of the discrete state $u_h \in \mathcal{V}_h$ and the discrete adjoint state $p_h \in \mathcal{V}_h$ have been addressed in the previous section. It can be observed immediately that the gradient of the discrete state belongs to the space

$$\nabla u_h \in \{w \in L^2(D, \mathbb{R}^{2\times 2}) : w|_T \in \mathbb{P}_1(T, \mathbb{R}^{2\times 2}), \forall T \in \mathcal{T}_h\},$$

which holds analogously for the discrete adjoint state. Hence, we can see that the global continuity gets lost with differentiation in the case of standard Lagrange finite element functions. Consequently, the discontinuity of ∇u_h and ∇p_h at mesh vertices and edges needs to be taken into account in the computation of the discrete descent direction at mesh vertices. Fundamental for the definition of a discrete descent direction is the observation that smoothness of the direct and adjoint state is given in the interior of mesh elements. Therefore, the central question at this point is the following: How can the discrete topological descent direction at a mesh vertex be defined based on information of values in the interior of the surrounding mesh elements?
Interestingly, this question is of importance in the postprocessing of certain quantities, for instance strains and stresses, in finite element software as well. The step of obtaining a continuous version of the discontinuous gradient ∇w_h, where $w_h \in \mathcal{S}^k(\mathcal{T}_h)^2$ describes the displacement field, is commonly referred to as *gradient recovery* in the context of finite elements. The reader is referred to [142] for details concerning the practical realization and to [1] for a rather theoretical background. Note that the continuity of strains and stresses is necessary for a reasonable visualization. The procedure for gradient recovery usually comprises the following steps. First, the order of the Lagrange finite element space for the field quantity w_h is chosen, which determines the set of mesh nodes uniquely. Second, the values of the gradient ∇w_h on each node is computed based on the values of the gradient within the neighborhood of the node. Third, the total function can be computed, and hence visualized, by interpolation in the chosen finite element space. Clearly, the second step is crucial and determines the quality of the recovered gradient. Moreover, this step can be performed in various manners and is not determined a priori. A simple and straightforward strategy, which is proposed in the literature, see for instance [142], is the evaluation of ∇w_h in the node of interest on each neighboring element and an averaging over all values. Note that for polynomial orders $k > 1$, this procedure is only necessary for nodes, which are located on the boundary of mesh elements. This strategy provides the first approach for the investigation in this chapter.

Strategies for Discretization of Topological Descent Direction

Let us come back to the discretization of the topological descent direction and formalize the setting appropriately in order to formulate the computation strategies. We consider

a vertex $z \in \mathcal{N}_h$ and the surrounding element patch $\mathcal{P}_z = \{T_1^z, ..., T_M^z\} \subset \mathcal{T}_h$. As mentioned previously, the first strategy evaluates the descent direction in vertex z on each patch element and averages over the computed values. For given discrete level set function $\psi_h \in \mathcal{W}_h$, the discrete descent direction $g_{h,1} \in \mathcal{W}_h$ in vertex z is defined as follows

$$g_{h,1}(z) := \frac{1}{M} \sum_{i=1}^{M} g_{\psi_h}|_{T_i}(z), \tag{6.17}$$

where g_{ψ_h} is defined as above, see (5.3).
Let us continue by proposing a second strategy for the recovery of the discrete descent direction. The main motivation behind the introduction of a second computation strategy is the exploitation of information in a neighborhood of vertex $z \in \mathcal{N}$. Note that so far, solely values of g_{ψ_h} in vertex z have been used. Essentially, we propose to select a set of sampling points $\{x_1^i, ...x_P^i\}$ on each element T_i^z for $1 \leq i \leq M$ and average over all patch elements and all sampling points within those elements. The discrete descent direction $g_{h,2}$ in this situation is defined as follows in vertex z:

$$g_{h,2}(z) := \frac{1}{MP} \sum_{i=1}^{M} \sum_{p=1}^{P} g_{\psi_h}(x_p^i). \tag{6.18}$$

Remark 6.7. *The averaging process in (6.17) and (6.18) can be interpreted as a filter for the discrete descent direction. Definition (6.18) can be generalized straightforwardly by averaging over all sampling points within a given filter radius $R > 0$, instead of averaging over the sampling points within the neighboring element patch.*

The practical implementation of a numerical scheme requires the consideration of its computational cost. This aspect is addressed in the following remark for both proposed strategies.

Remark 6.8. *It can be observed that only one evaluation per element of the descent direction g_{ψ_h} is necessary in (6.17). In contrast, the topological descent direction needs to be evaluated in each sampling point within an element in the case of strategy (6.18). Note that the number of sampling points $P > 1$ needs to be chosen carefully in order to keep the computational effort in a reasonable order. This is particularly important in the case of stress-based objectives due to the numerical integration, which needs to be performed in each evaluation of the topological gradient (4.45).*

An important aspect in the comparison of strategy (6.17) and (6.18) is the consideration of the interface Γ_h in the computation of the descent direction. To be more precise,

let us consider the situation of an element patch surrounding vertex $z \in \mathcal{N}_h$, which is intersected by the interface. This setting is visualized in the Figure 6.3.

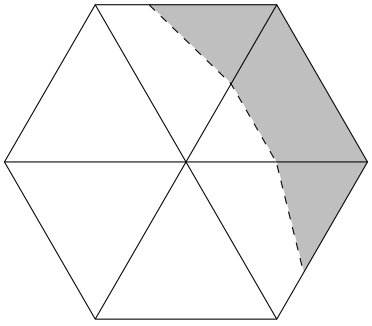

Figure 6.3.: Element patch surrounding vertex $z \in \mathcal{N}_h$, which is intersected by Γ_h.

It is straightforward to see that the first recovery strategy (6.17) is not affected by the presence or absence of the interface Γ_h in element patch $\mathcal{P}_z$. In the second recovery strategy (6.18) however, the change of material phases is considered via the sign manipulation of the topological gradient in (5.3). Intuitively spoken, the information about the interface Γ_h being close to vertex z is encoded in strategy (6.18). The difference between the two recovery strategies is visualized in Figure 6.4.

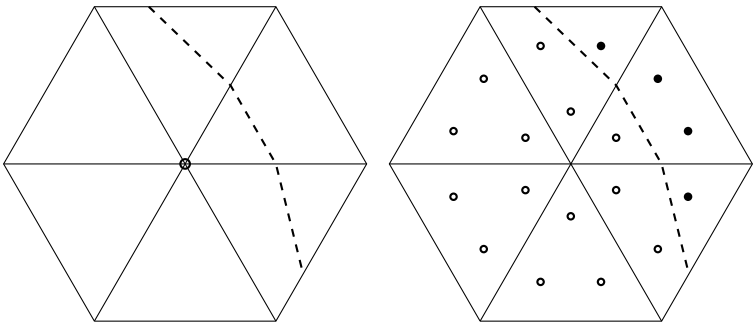

Figure 6.4.: Comparison of recovery strategies for discrete descent direction in vertex $z \in \mathcal{N}_h$. Left: Strategy (6.17). Right: Strategy (6.18).

The influence of the gradient recovery strategy has been studied via numerical experiments and the results are visualized in Figure 6.5. We consider the well-known *minimum compliance minimization* under a volume constraint

$$\begin{aligned} \min_{\Omega \in \mathcal{O}} \quad & \mathcal{C}(\Omega) = \int_{\Gamma_N} g \cdot u_\Omega dS \\ \text{s.t.} \quad & \int_D \chi_\Omega dx \leq V, \end{aligned} \tag{6.19}$$

where the compliance has been introduced in (2.14), u_Ω denotes the solution of the

state system (2.10) and $V > 0$ is the volume bound. Note that we study the minimum compliance problem instead of problems with stress constraints at this point, since the results allow a clear demonstration of the main effects concerning the gradient recovery strategy. At the end of this section, however, we will discuss the different strategies with regards to problems involving stress constraints. Regarding the experiments, we chose the L-Beam geometry as geometrical domain and the absence of volume forces. The iterates in Figure 6.5 have been generated using the level set-based optimization scheme from the previous chapter, where the topological gradient of the compliance term is provided by (4.54).

Two major effects can be observed in Figure 6.5. First, recovery strategy (6.17) leads to the presence of various small and *isolated material parts*, as it can be seen in the case of iteration eight and ten. This effect is present during the optimization procedure and vanishes, if the algorithm is close to convergence. In contrast, the designs generated by recovery strategy (6.18) are less affected by small and isolated parts. For iteration eight, a large isolated material part can be observed. From iteration ten on, however, the designs are connected. The second major effect concerns the *smoothness of the interface*. Clearly, a higher degree of smoothness can be observed in case of recovery strategy (6.18). The achieved smoothness is particularly impressive for the final iteration. Note that both observed effects are closely linked to the previously discussed capability of the employed recovery strategy in detecting the interface.

Most importantly for the aim of this thesis, however, is the observation that only recovery strategy (6.18) is successful in the presence of local *stress constraints*. Numerical tests have shown that the optimization algorithm stops after a few iterations, if strategy (6.17) is used for the discretization of the topological descent direction. A possible explanation for this observation is the importance of a smooth interface in the presence of local stress constraints. As a result of the preceding studies, all numerical experiments in the following chapters will be conducted with recovery strategy (6.18). We mention that a different strategy for gradient recovery, which might be interesting to investigate for the solution of problems involving stress constraints, has been proposed in [15].

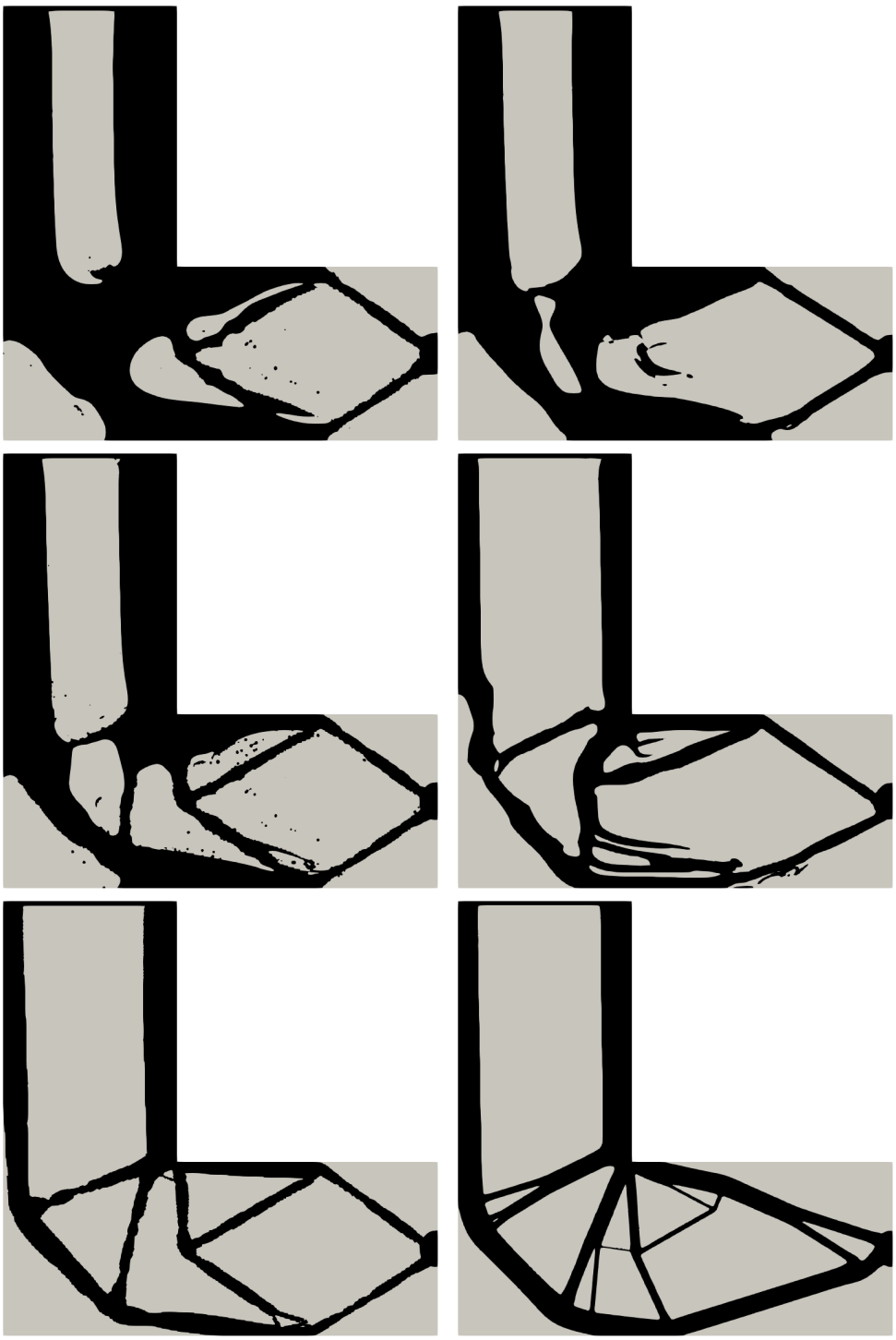

Figure 6.5.: Effect of gradient recovery strategies for iterations 8, 10 and 52. Left: First option. Right: Second strategy.

6.4. Implementation Remarks

This section provides useful hints concerning an efficient implementation, in particular with regards to the topological gradient (4.45).

Tensor Construction

The first aspect to be considered is the handling of isotropic fourth-order tensors, which are introduced rigorously in the following definition.

Definition 6.1. *A fourth-order tensor $\mathbb{A}$ is called isotropic, if there exist $a_1, a_2 \in \mathbb{R}$ such that the identity*

$$\mathbb{A} = a_1 \mathbb{I} + a_2 I \otimes I$$

holds with $\mathbb{I}$ denoting the fourth-order identity tensor and $(I \otimes I)M := tr[M]I$ for a matrix $M \in \mathbb{R}^{d\times d}$.

We assume the case of isotropic material and an inhomogeneity of circular shape in order to exploit the closed form expressions, which have been derived in Section 4.5. In particular, we are interested in implementing the elastic moment tensor

$$\mathbb{E}M = |\omega|\mathbb{C}^0(\mathbb{C}^0 + \mathbb{C}_\delta \mathbb{S}^{\text{int}})^{-1}\mathbb{C}_\delta M,$$

with a matrix $M \in \mathbb{R}^{d\times d}_{\text{sym}}$, as well as the term

$$\epsilon(v_X)(x) = -\mathbb{S}(x)(\mathbb{C}^0 + \mathbb{C}_\delta \mathbb{S}^{\text{int}})^{-1}\mathbb{C}_\delta X,$$

with a matrix $X \in \mathbb{R}^{d\times d}_{\text{sym}}$, which is the strain of the solution of problem (4.31). Note that Eshelby's tensor $\mathbb{S}$ is given in (4.58) in abstract form.
Due to the assumed material isotropy and the circular inhomogeneity, Eshelby's tensor $\mathbb{S}$ can be stated in closed form, see (4.64) and (4.66). Consequently, the expressions above can be entirely computed in closed form prior to the implementation. This has been already done for the elastic moment tensor in (4.67). Note that this is the case for most publications as well, see for example [17] and [99].
The reader, who is experienced in software development and practical implementation of algorithms, will have noticed how error-prone this procedure can get. Therefore, despite the possibility of calculating the elastic moment tensor and the solution of the free space transmission problem by hand, we recommend a different procedure at this point. An elegant way is the separation of *tensor representation* and *algebraic operations*

on the set of isotropic tensors within an object-oriented framework.
The basic idea is quite simple and natural. In a first step, the isotropic fourth-order tensors $\mathbb{C}^0, \mathbb{C}^1$ and $\mathbb{S}^{\text{int}}$ need to be initialized. Note that every isotropic tensor is entirely determined by two real numbers by definition. The required objects $\mathbb{E}$ and $\epsilon(v_X)$ are then constructed by applying algebraic operations, more precisely addition, multiplication and inversion, on these tensors. It should be mentioned at this point that the exterior Eshelby tensor $\mathbb{S}^{\text{ext}}$ requires special treatment, as it is not representable as isotropic tensor in standard form, see (4.66).
In the following, the two required classes are described briefly. First, a class representing isotropic tensors of fourth order needs to be implemented. Each instance of this class is initialized by two doubles $a_1, a_2 \in \mathbb{R}$. In order to facilitate the algebraic operations, which will be part of the second class, a conversion of isotropic tensors to a different representation is assigned to the first class. For this purpose, we introduce the isotropic fourth-order tensors

$$\mathbb{J} := \frac{1}{d}\mathrm{I} \otimes \mathrm{I}, \quad \mathbb{K} := \mathbb{I} - \mathbb{J}, \tag{6.20}$$

where $d \in \mathbb{N}$ denotes the spatial dimension.

Remark 6.9. *Given a matrix $M \in \mathbb{R}^{d\times d}$, the decomposition*

$$M = \mathbb{J}M + \mathbb{K}M$$

can always be performed by definition of $\mathbb{J}$ and $\mathbb{K}$. Note that $\mathbb{J}M$ is usually referred to as volumetric part and $\mathbb{K}M$ is known as the deviatoric part of M.

The following lemma provides rules for the conversion between different tensor representations.

Proposition 6.1. *Let an isotropic tensor*

$$\mathbb{A} = a_1\mathbb{I} + a_2 I \otimes I$$

be given with $a_1, a_2 \in \mathbb{R}$. Using the tensors $\mathbb{J}$ and $\mathbb{K}$, $\mathbb{A}$ can be represented as follows:

$$\mathbb{A} = (da_2 + a_1)\mathbb{J} + a_1\mathbb{K}. \tag{6.21}$$

Conversely, an isotropic tensor

$$\mathbb{B} = b_1\mathbb{J} + b_2\mathbb{K}$$

can be represented in standard form as follows:

$$\mathbb{B} = b_2\mathbb{I} + \frac{b_1 - b_2}{d} I \otimes I. \tag{6.22}$$

Proof. The identity (6.21) follows from basis algebraic rules

$$\begin{aligned}\mathbb{A} &= a_1\mathbb{I} + a_2\mathrm{I}\otimes\mathrm{I} = a_1\mathbb{I} + a_2 d\mathbb{J} + a_1\mathbb{J} - a_1\mathbb{J} \\ &= a_1(\mathbb{I} - \mathbb{J}) + a_1\mathbb{J} + a_2 d\mathbb{J} = a_1\mathbb{K} + (a_1 + a_2 d)\mathbb{J},\end{aligned}$$

as it is the case for equality (6.22):

$$\mathbb{B} = b_1\mathbb{J} + b_2\mathbb{K} = b_1\mathbb{J} + b_2\mathbb{I} - b_2\mathbb{J} = b_2\mathbb{I} + (b_1 - b_2)\mathbb{J} = b_2\mathbb{I} + \frac{b_1 - b_2}{d}\mathrm{I}\otimes\mathrm{I}.$$

□

The second class is in charge of performing algebraic operations on the set of fourth-order isotropic tensors. Essentially, this class contains routines for addition, multiplication and inversion of isotropic tensors. It is convenient within the multiplication and inversion routines to use the internal conversions (6.21) and (6.22) between different representations of isotropic tensors. The advantage of converting an isotropic tensor to the representation based on the tensors $\mathbb{J}, \mathbb{K}$ is the simplicity regarding algebraic manipulations. In the following, several auxiliary statements concerning $\mathbb{J}$ and $\mathbb{K}$ are provided.

Lemma 6.1. *Let the isotropic fourth-order tensors $\mathbb{J}$ and $\mathbb{K}$ be defined by (6.20). The following equalities hold:*

$$\mathbb{J}\mathbb{J} = \mathbb{J}, \quad \mathbb{K}\mathbb{K} = \mathbb{K}, \quad \mathbb{J}\mathbb{K} = \mathbb{K}\mathbb{J} = 0. \tag{6.23}$$

Proof. Let $M \in \mathbb{R}^{d\times d}$ be given. Regarding the first equality in (6.23), we obtain

$$\mathbb{J}\mathbb{J}M = \frac{1}{d^2}(\mathrm{I}\otimes\mathrm{I})(\mathrm{I}\otimes\mathrm{I})M = \frac{1}{d^2}(\mathrm{I}\otimes\mathrm{I})\mathrm{tr}[M]I = \frac{1}{d^2}\mathrm{tr}[M]\mathrm{tr}[I]I = \frac{1}{d}\mathrm{tr}[M]I = \mathbb{J}M,$$

where $\mathrm{tr}[I] = d$ has been employed. Concerning the second identity in (6.23), we observe

$$\mathbb{K}\mathbb{K}M = (\mathbb{I} - \mathbb{J})(\mathbb{I} - \mathbb{J})M = \mathbb{I}\mathbb{I}M - \mathbb{I}\mathbb{J}M - \mathbb{J}\mathbb{I}M + \mathbb{J}\mathbb{J}M = (\mathbb{I} - \mathbb{J})M = \mathbb{K}M,$$

where the previously shown equality $\mathbb{J}\mathbb{J} = \mathbb{J}$ has been used. The third identity in (6.23) follows straightforwardly from applying $\mathbb{J}\mathbb{J} = \mathbb{J}$. □

The following statements provide useful rules regarding the multiplication and inversion of isotropic tensors.

Proposition 6.2 (Multiplication of isotropic fourth-order tensors)**.** *Let two isotropic fourth-order tensors*

$$\mathbb{A} = a_1\mathbb{J} + a_2\mathbb{K}, \qquad \mathbb{B} = b_1\mathbb{J} + b_2\mathbb{K}$$

be given with $a_1, a_2, b_1, b_2 \in \mathbb{R}$*. The following identity holds:*

$$\mathbb{A}\mathbb{B} = \mathbb{B}\mathbb{A} = a_1b_1\mathbb{J} + a_2b_2\mathbb{K}.$$

Proof. The claim follows from

$$\begin{aligned}&\mathbb{A}\mathbb{B}\\ =&(a_1\mathbb{J} + a_2\mathbb{K})(b_1\mathbb{J} + b_2\mathbb{K}) = a_1b_1\mathbb{J}\mathbb{J} + a_1b_2\mathbb{J}\mathbb{K} + a_2b_1\mathbb{K}\mathbb{J} + a_2b_2\mathbb{K}\mathbb{K} = a_1b_1\mathbb{J} + a_2b_2\mathbb{K},\end{aligned}$$

where the identities in (6.23) have been employed. □

Corollary 6.1 (Inversion of isotropic fourth-order tensors)**.** *Let an isotropic tensor*

$$\mathbb{A} = a_1\mathbb{J} + a_2\mathbb{K}$$

be given with $a_1, a_2 \in \mathbb{R}$*. If* $a_1 \neq 0$ *and* $a_2 \neq 0$*, the inverse* $\mathbb{A}^{-1}$ *of* $\mathbb{A}$ *exists and reads as follows:*

$$\mathbb{A}^{-1} = a_1^{-1}\mathbb{J} + a_2^{-1}\mathbb{K}.$$

Numerical Integration

The term

$$\int_{\mathbb{R}^2\setminus\omega} \mathcal{G}^0(z, \epsilon(v_X(x)))dx \tag{6.24}$$

in the topological gradient, see (4.45), requires special attention due to its unbounded area of integration. In particular, a numerical scheme is necessary in order to approximate the integral (6.24). Two aspects are important to notice at this point. First, the

strain of the solution of the free space transmission problem $\epsilon(v_X)$ is not constant outside the unit circle ω. This, in contrast, is the case for points inside ω. Second, it should be mentioned that the integral (6.24) takes a finite value. This is a consequence of $\epsilon(v_X)$ having a fast enough decay at infinity, which becomes clear by the exterior Eshelby tensor $\mathbb{S}^{\text{ext}}$, see (4.66).
A natural step towards the computation of integral (6.24) is the transformation of its area of integration. Let us denote the integrand by

$$f(x) := \mathcal{G}^0(z, \epsilon(v_X(x)))$$

for convenience. In a first step, a change from Cartesian to polar coordinates is performed:

$$\int_{\mathbb{R}^2\setminus\omega} f(x)dx = \int_0^{2\pi}\int_1^{\infty} rf(r\cos\theta, r\sin\theta)drd\theta.$$

Furthermore, the interval $[1,\infty]$ is substituted by the finite set $[0,1]$ as follows

$$\int_0^{2\pi}\int_1^{\infty} rf(r\cos\theta, r\sin\theta)drd\theta = \int_0^1 \frac{1}{r^3}\int_0^{2\pi} f(r^{-1}\cos\theta, r^{-1}\sin\theta)d\theta dr,$$

and we obtain finally

$$\int_{\mathbb{R}^2\setminus\omega} f(x)dx = \int_{[0,1]^2} \frac{2\pi}{r^3} f(r^{-1}\cos(2\pi\theta), r^{-1}\sin(2\pi\theta))d\theta dr, \tag{6.25}$$

which allows to use a quadrature rule on the unit square $[0,1]\times[0,1]$ for the numerical integration.
The next step is to ask for a numerical scheme in order to approximate integral (6.25). Tests have shown that different 1D quadrature rules for radius and angle perform best. More precisely, a Gauss quadrature for the radius and a composite trapezium rule, i.e. a Newton-Cotes quadrature, for the angle show excellent performance. For details regarding 1D quadrature rules, we refer the reader to [133]. Denoting the Gauss quadrature points and weights by

$$(r_i)_{i=1}^N \subset [0,1], \quad (w_i^r)_{i=1}^N,$$

and the Newton-Cotes points and weights

$$(\theta_j)_{j=1}^M \subset [0,1], \quad (w_j^\theta)_{j=1}^M,$$

we obtain the two-dimensional quadrature rule

$$\int_0^1 \int_0^1 \tilde{f}(\theta, r) d\theta dr \approx \sum_{i=1}^{N} \sum_{j=1}^{M} w_i^r w_j^\theta \tilde{f}(r_i, \theta_j) \tag{6.26}$$

for $\tilde{f}(r, \theta) := \frac{2\pi}{r^3} f(r^{-1}\cos(2\pi\theta), r^{-1}\sin(2\pi\theta))$.

Exact Integration for Quadratic Objective Functionals

Due to the complicated structure of the topological gradient (4.45) for stress-based functionals, a practical implementation is error-prone and needs to be handled carefully. An important step within the implementation is the validation of the topological gradient using finite differences, which will be explained in more detail later on.
A step, which is recommended prior to the validation of the full gradient, is the validation of integral (6.24) for two reasons. First, the integrand in (6.24) involves the exterior Eshelby tensor $\mathbb{S}^{\text{ext}}$, see (4.66), which is rather complicated and needs to be hard coded. Second, the numerical integration routine, which has been described previously, needs to be assessed. It is important to notice at this point that the accuracy in computing integral (6.24) determines the quality of gradient (4.45).
The strategy in validating the unbounded integral is to consider a special class of objectives, more precisely quadratic objective functionals, and to derive a closed formula of integral (6.24). This analytical expression allows then the comparison with the result of the numerical integration routine. Let us consider a quadratic integrand

$$j^0(d) := \frac{1}{2}\mathbb{B}d : d,$$

with an isotropic tensor $\mathbb{B}$ for an arbitrary symmetric matrix $d \in \mathbb{R}^{2\times 2}_{\text{sym}}$. Furthermore, let the elasticity tensors be defined by

$$\mathbb{C}^i := \alpha_i \mathbb{C}, \quad i \in \{0, 1\},$$

with constants $\alpha_0, \alpha_1 \in \mathbb{R}$. Then, we see that the integrand in (6.24) becomes

$$\mathcal{G}^0(z, d) = j^0(\epsilon(u(z)) + d) - j^0(\epsilon(u(z))) - \partial_d j^0(\epsilon(u(z))) : d = j^0(d).$$

Moreover, due to equality (4.62), we obtain the following identity:

$$\int_{\mathbb{R}^2\setminus\omega} \mathcal{G}^0(z, \epsilon(v_X(x)))dx = \int_{\mathbb{R}^2\setminus\omega} j^0(\mathbb{S}^{\text{ext}}(x)[\mathbb{C}^0 + \mathbb{C}_\delta \mathbb{S}^{\text{int}}]^{-1}\mathbb{C}_\delta X)dx.$$

For the case of a Mises stress criterion, i.e. $\mathbb{B} = \mathbb{C}\mathbb{C}\tilde{\mathbb{B}}$ with

$$\tilde{\mathbb{B}} := 3\mathbb{I} - \mathrm{I} \otimes \mathrm{I},$$

it has been shown in [17] that

$$\begin{aligned}
&\int_{\mathbb{R}^2 \setminus \omega} j^0(\mathbb{S}^{\mathrm{ext}}(x)[\mathbb{C}^0 + \mathbb{C}_\delta \mathbb{S}^{\mathrm{int}}]^{-1}\mathbb{C}_\delta X)dx \\
=&\frac{\pi}{\beta^2}\left[5(2\mathbb{C}X : \mathbb{C}X - \mathrm{tr}[\mathbb{C}X]^2) + 3\left(\frac{1+\eta\alpha}{1+\zeta\alpha}\right)^2 \mathrm{tr}[\mathbb{C}X]^2\right],
\end{aligned}$$

with the following real numbers:

$$\alpha := \frac{\alpha_1}{\alpha_0}, \quad \eta := \frac{3-\nu}{1+\nu}, \quad \zeta := \frac{1+\nu}{1-\nu}, \quad \beta := \frac{\alpha_1 - \alpha_0}{\eta\alpha_1 + \alpha_0}.$$

Part III.

Numerical Experiments and Applications

7. Volume Minimization under Local Stress Constraints

7.1. Introduction

The aim of this chapter is the application of the previously developed level set-based optimization method, relying on the topological gradient (4.45), to the solution of the minimum volume problem under local stress constraints

$$\min_{\Omega \in \mathcal{O}} \quad \mathcal{J}(\Omega) = \int_D \chi_\Omega dx \tag{7.1a}$$

$$\text{s.t.} \quad \mathcal{F}_{\bar{\sigma}}[\Omega] \leq 1 \text{ a.e. in } \Omega, \tag{7.1b}$$

where the set of feasible designs $\mathcal{O}$ is chosen as in (2.19) and the failure function $\mathcal{F}_{\bar{\sigma}}$ is defined in (2.24).
Investigating problem (7.1) is a natural first step towards the solution of more complex optimal design problems with stress constraints. The reasons for this choice are threefold: First, there is no partial differential equation involved in objective functional (7.1a) representing the volume. As a result, the computational cost of evaluating objective functional (7.1a) and its topological gradient is low. Additionally, the topological gradient possesses a very simple structure. The second reason is the ease of intuitive interpretation of numerical solutions. More precisely, it is possible to decide immediately, whether a solution to the minimum volume problem is physically reasonable or not. Note that this is not the case for every problem, especially for the case of problems involving multiphysical phenomena, which will be discussed in the subsequent chapter. Third, the majority of works dealing with stress constraints consider the minimum volume problem. Consequently, the success and performance of the developed approach can be compared to existing results, which have been achieved using fundamentally different methods. Nevertheless, let us keep in mind at this point that the case of volume minimization is just a first step and the aim of this thesis is the

realistic design optimization of an electrical machine under stress constraints.
In the following, a brief literature review on existing works concerning design optimization methods for the minimum volume problem with local stress constraints is given. Note that only gradient-based methods are considered. For approaches based on integer programming techniques, we refer to [134] and the references therein. An intensively studied approach within the field of topology optimization is the class of *density-based methods* including the well-known SIMP and RAMP method, see for instance [28] or [126]. We recall that the main idea of density-based methods consists in allowing intermediate densities for the design representation, which makes the resulting optimization problems accessible to standard mathematical programming techniques. The first approach for treating stress-constrained problems within the class of density-based methods has been proposed by Duysinx and Bendsøe (1998), see [55]. An emphasis is put on the investigation and discussion of suitable models for local stresses, in particular for intermediate densities. Further, a so-called ϵ-relaxation (cf. [42]) is applied in order to resolve the singularity phenomenon, which is inherent to density-based methods for stress-constrained problems and will be described briefly below. Moreover, the local stress constraints are treated immediately, without the use of a penalty approach or similar techniques. In Le et al. (2009), a different model for describing the local stresses has been chosen, see [96]. The advantage of this choice is an immediate prevention of the singularity problem. Furthermore, the maximum norm on the stresses, which corresponds to a local stress constraint imposed on the entire domain, is approximated by the p-norm. Technical extensions of the numerical scheme, which are referred to as normalization and regional clustering, are necessary in order to obtain a reasonable approximation of the maximum stress value. The latest approach for solving stress-constrained problems within the class of density-based methods has been proposed by Salazar de Troya and Tortorelli (2018), see [49] as well as [48] for further details. In contrast to [96], a penalty approach has been chosen in order to tackle the large number of stress constraints. Moreover, adaptive mesh refinement is employed within the optimization algorithm in order to achieve a more accurate stress assessment, particularly with regards to intermediate densities. Concerning the class of *homogenization methods*, one approach for solving the stress-constrained minimum volume problem has been proposed by Allaire et al. (2004), see [5]. However, the minimization of a global stress-based criterion with quadratic structure has been addressed instead of the case of local stress constraints. Another well-known approach in topology optimization is the *phase-field method*, see for instance [30] or [33]. The solution of the stress-constrained minimum volume problem using the phase-field method has been addressed by Burger and Stainko (2006), see [39] and [130]. A refor-

mulation and relaxation of the local stress constraints is performed, which results in purely linear constraints. This approach offers the advantage of a uniform constraint qualification, which is not the case for the ϵ-relaxation technique. Furthermore, several works dealing with the *level set method* and *shape gradients* are available. Note that the level set method in this context is not the algorithm from Chapter 5, but relies on a Hamilton-Jacobi equation in the spirit of [108] instead. The first approach within this class has been proposed by Allaire and Jouve (2008), see [4]. As in [5], not the case of local stress constraints is investigated, but the minimization of a stress-based criterion. In [56], Emmendoerfer and Fancello (2014) proposed a method based on a reformulation of the stress constraints and an augmented Lagrangian approach. This method has been extended in [57] by employing a reaction-diffusion equation instead of a Hamilton-Jacobi equation. Another approach has been presented by Picelli et al. (2018), see [114] and [115]. Here, a stress aggregation using the p-norm approach has been chosen in combination with several technical numerical extensions as in [96]. The last class of methods addresses the application of the *topological gradient* applied within the level set-based algorithm, which has been described in Chapter 5. Amstutz and Novotny (2010) proposed the first approach for solving stress-constrained problems involving the topological gradient, see [17]. Fundamental in this work is the use of a penalty approach as well as a weighted combination of the resulting penalty term and the compliance. Moreover, the topological gradient of the stress-based penalty term is derived for a von Mises stress criterion. In [18], Amstutz et al. (2012) extended the work of [17] to a Drucker-Prager stress constraint.

The method, which is chosen for the solution of optimal design problems with stress constraints in this thesis is based on a level set representation and the topological gradient. In the following, the reasons for the choice of this approach are described. In particular, it will be discussed why this approach is chosen over the various different methods. Let us begin with all approaches, which allow intermediate densities in the design variables. These are the density-based methods, the homogenization method and the phase-field method. One main drawback of these methods in the solution of stress-constrained problems is clearly the difficulty of assessing stresses in regions with intermediate densities. More precisely, the question arises how the stress can be defined physically reasonable in this case. Further, the lack of a clear design boundary makes the reliable stress computation difficult. The second major drawback of approaches involving intermediate densities is the so-called singularity problem. This phenomenon is described in [41] for truss optimization problems and in [55] for density-based topology optimization problems. Essentially, the singularity phenomenon refers to the effect of optimal solutions being located in degenerated

parts of the design space. This is a consequence of the fact that the stress in a bar of a truss structure tends to a finite, non-zero value if the diameter of the bar tends to zero. The same effect holds for the stress in a mesh element within a density-based approach, if the density tends to zero. It has been observed and discussed, see [41] and [55], that optimization algorithms are unable to approximate these optimal solutions in a reliable way due to a lack of constraint qualification. Instead, the obtained numerical solutions often show very thin bars or elements of low density, respectively. As a consequence, the optimal design problem needs to be perturbed in a certain manner, which is not a priori clear.

All methods, which rely on the level set method and shape gradients do not allow intermediate densities and are thus not affected of the previously described problems. It is clear, however, that the shape gradient does not allow for topological changes of the design in an automatic fashion. Therefore, the approach involving the topological gradient combined with the level set-based optimization scheme is an excellent choice for the treatment of stress-constrained problems.

There are three major challenges in the treatment of optimal design problems involving local stress constraints. The first difficulty is the *large number of constraints* and hence the computational complexity, which is simply caused by the local nature of stress constraints. This difficulty is tackled with a penalty approach in this thesis, see Section 3.2. The second challenge is an *accurate and reliable stress assessment*, in particular at the boundary of a design. This difficulty is caused by the highly nonlinear behavior of local stresses with respect to design perturbations (cf. [96], [49]). Intuitively speaking, small variations of a given design often result in large changes of the local stresses. Note that this is not the case for many other, especially global, criteria such as the mechanical compliance of a structure. We face this difficulty with a level set-based design representation, which results in a sharp material interface and hence a clear design boundary. Further, the recovery strategy in the discretization of the topological gradient ensures a certain smoothness of the interface, see the previous chapter for details. The third challenge is the *formulation* of the minimum volume problem with stress constraints. As it has been mentioned in [126] and explained in Section 3.2, a trivial and global solution of problem (7.1) is the empty set. Therefore, a regularization is crucial in order to obtain reasonable results. The choice of this regularization is the main concern of this chapter and will be investigated by numerical experiments.

The starting point and basis for the investigation of an appropriate regularization of problem (7.1) is the work of Amstutz and Novotny (2010), see [17]. Two different perturbations of the original stress-constrained minimum volume problem have been performed in their work. First, a penalty approach has been applied in order to

approximate the original problem by another one involving a penalty term. Second, the objective functional, consisting of the volume and the penalty term, is extended by the mechanical compliance. Clearly, both perturbations are introduced in order to overcome the challenge of posing the minimum volume problem in a physically reasonable manner. However, several important aspects remain unanswered. In the construction of the stress-based penalty term in [17], an extension of the stress constraints to the entire domain is performed. Note that this step corresponds to a perturbation of the set of feasible designs. It remains unclear, however, what the effect of this extension really is and if it is necessary. Moreover, the compliance term is added to the original problem without further explanations. Investigating the necessity of the compliance term is of particular interest with regards to practical applications, since it changes the resulting solution drastically. Let us keep in mind at this point, that the aim of this thesis is to design an electrical machine in terms of efficiency. Clearly, the extension of the optimal design problem by a compliance term affects the electromagnetic performance and thus the efficiency of the resulting optimal design. In addition to the investigation of these questions, a modified penalty term compared to [17] is proposed in this thesis. While the penalty parameter in [17] is solely used as a weighting coefficient, it is additionally coupled with the stress limit in the air phase, see Section 3.2 for a detailed explanation. The main idea behind this modification is that the regularized problem tends towards the original problem for large penalty parameters.

7.2. Optimal Design Problem and Topological Gradient

The purpose of this section is to state the optimal design problems, which will be investigated by numerical experiments in the subsequent section and provide the necessary mathematical setting. Aiming at the comparison of the regularized optimal design problem (3.7) with problem (3.9), where stresses are only considered in the material phase, the state system as well as the failure criterion will be stated in the following. Moreover, we will apply Theorem 4.1 for the derivation of the topological gradient, which is of central importance for the optimization scheme.

Optimal Design Problem

The *state system* of the stress-constrained minimum volume problem is represented by the elasticity equation (2.10) in weak formulation. Aiming at conducting numerical experiments in the following, we need to select specific data within the generic system

(2.10). Throughout this chapter, we assume homogeneous Dirichlet data as well as the absence of volume forces. Note that these choices are made for comparability with existing works on the solution of the stress-constrained minimum volume problem. Hence, the state $u_\Omega \in \mathcal{V}$ to design $\Omega \in \mathcal{O}$ is the unique solution of the following problem:

$$\int_D \mathbb{C}_\Omega \epsilon(u_\Omega) : \epsilon(v) dx = \int_{\Gamma_N} g \cdot v ds, \quad \forall v \in \mathcal{V}, \tag{7.2}$$

where the elasticity tensor $\mathbb{C}_\Omega$ is defined by (2.3), $g \in L^2(\Gamma_N, \mathbb{R}^2)$ and

$$\mathcal{V} = \{v \in H^1(D, \mathbb{R}^2) : \gamma(v)|_{\Gamma_D} = 0\}$$

denotes the Sobolev space with homogeneous Dirichlet data.
We proceed by selecting a specific *failure criterion*, which forms the basis for defining the pointwise stress constraints. Throughout this chapter, for a given elastic limit $\bar{\sigma} > 0$, we consider the *von Mises* criterion

$$S_{vm}(\sigma) \leq \bar{\sigma}, \tag{7.3}$$

where the von Mises stress is defined by

$$S_{vm}(\sigma) := \sqrt{\frac{1}{2}\mathbb{D}\sigma : \sigma}, \tag{7.4}$$

with the fourth-order tensor $\mathbb{D} := 3\mathbb{I} - \mathrm{I} \otimes \mathrm{I}$.

Remark 7.1. *The von Mises criterion is employed for quantifying failure in ductile materials, for instance metal or steel. From a physical perspective, (7.3) states that yielding, and thus inelastic deformation, begins when the strain energy density of distortion reaches the critical value $\bar{\sigma}$. Therefore, (7.3) is also known as maximum distortion criterion. Further information regarding the von Mises criterion and the comparison to different failure criteria can be found in [53] and [73].*

Remark 7.2. *We choose the von Mises criterion within this chapter for the sake of comparability. Typically, algorithms for solving the stress-constrained minimum volume problem are benchmarked with respect to the L-Beam geometry, which will be introduced in the subsequent section, and the von Mises criterion, see for instance [55], [17] and [49].*

In order to match the framework from Part I, we need to square inequality (7.3) and obtain

$$f(\sigma) := \frac{1}{2}\mathbb{D}\sigma : \sigma \leq \bar{\sigma}^2,$$

which fits into the definition of failure function (2.17). Analogously to (2.24), we set

$$\mathcal{F}_{\bar{\sigma}}[\Omega] = F_{\bar{\sigma}}(\sigma(u_\Omega)) = \frac{1}{\bar{\sigma}^2} f(\sigma(u_\Omega)) \tag{7.5}$$

for a design $\Omega \in \mathcal{O}$ and the associated state $u_\Omega \in \mathcal{V}$. Based on the failure function (7.5) in reduced form, we can formulate the minimum volume problem with pointwise stress constraints as in (2.25), where the objective functional

$$\mathcal{J}(\Omega) := \int_D \chi_\Omega dx \tag{7.6}$$

is chosen as the volume of Ω.

Within this chapter, a major focus is directed towards investigating the effect of additional *stress constraints in the weak phase*, which have been introduced in Section 3.2. Therefore, we will compare the numerical solution of the regularized optimal design problem (3.7) and its counterpart (3.9), where stresses are only considered in the material phase, in the subsequent section. For the sake of readability, we recall both problems under investigation. Given a penalty parameter $\gamma > 0$, the regularized problem (3.7) reads

$$\min_{\Omega \in \mathcal{O}} \quad \mathcal{J}(\Omega) + \gamma \mathcal{P}_\gamma(\Omega), \tag{7.7}$$

with the penalty term

$$\mathcal{P}_\gamma(\Omega) = \int_D \alpha_\Omega \Phi_p \left(\beta_\Omega^\gamma \mathcal{F}_{\bar{\sigma}}[\Omega]\right) dx, \tag{7.8}$$

where α_Ω and β_Ω^γ have been defined in (2.1) and (3.5), respectively, and the penalty function Φ_p is defined by (3.6). In contrast, considering solely stresses in the material phase, problem (3.9) reads

$$\min_{\Omega \in \mathcal{O}} \quad \mathcal{J}(\Omega) + \gamma \mathcal{P}(\Omega), \tag{7.9}$$

with the penalty term

$$\mathcal{P}(\Omega) = \int_D \chi_\Omega \Phi_p \left(\mathcal{F}_{\bar{\sigma}}[\Omega]\right) dx. \tag{7.10}$$

Before we turn to the topological gradient with respect to both optimal design problems, the *existence of local minima* needs to be guaranteed. It is straightforward to verify that the functional (7.6) is bounded from below and continuous, where convergence of sets is understood in the sense of characteristic functions, see Definition 3.1. Hence,

the application of Theorem 3.3 ensures the existence of solutions for (7.7) and (7.9).

Topological Gradient

Having specified the optimal design problems under investigation, we proceed with deriving the topological gradient of the associated objective functionals. Essentially, this step comprises the application of Theorem 4.1 to the previously defined penalty terms (7.8) and (7.10). Since the structure of both penalty terms is similar, we will treat only problem (7.7) in detail. The difference to penalty term (7.10) is stated briefly within a remark.
For the presentation of the topological gradient, we consider a design $\Omega \in \mathcal{O}$, a point of perturbation $z \in D \setminus \partial\Omega$ and the circular inhomogeneity $\omega = B_1(0)$. Due to the linearity of the differential operation associated to the topological gradient, we observe that

$$D_T\mathcal{J}[\Omega](z) + \gamma D_T\mathcal{P}_\gamma[\Omega](z) \tag{7.11}$$

is equal to the topological gradient of the objective functional in (7.7) at design Ω and point of perturbation z. As shown in Example 4.1, the topological gradient for the volume functional reads as follows:

$$D_T\mathcal{J}[\Omega](z) = \begin{cases} -1, & z \in \Omega, \\ 1, & z \in D \setminus \bar{\Omega}. \end{cases}$$

Further, the topological gradient of the penalty term $\mathcal{P}_\gamma$ can be obtained by applying Theorem 4.1. In a first step, we observe that penalty term (7.8) is a special case of the generic objective functional (4.9). In order to match the structure of objective (4.9), we denote the penalty term (7.8) as follows

$$\mathcal{P}_\gamma(\Omega) = P_\Omega(\epsilon(u_\Omega)) = \int_D j_\Omega(\epsilon(u_\Omega))dx, \tag{7.12}$$

with density function $j_\Omega = j^{\text{mat}}\chi_\Omega + j^{\text{air}}\chi_{D\setminus\Omega}$ as in (4.11) and

$$j^{\text{mat}}(d) := \Phi_p(F_{\bar{\sigma}}(\mathbb{C}d)), \qquad j^{\text{air}}(d) := \alpha\Phi_p(h(\gamma)^{-1}F_{\bar{\sigma}}(\mathbb{C}d)).$$

for $d \in \mathbb{R}^{2\times 2}$.

Remark 7.3. *The only difference for penalty term (7.10) is the definition of the density function $j^{air}(d) := 0$ in the weak phase.*

Moreover, the *adjoint state* $p_\Omega \in \mathcal{V}$ for penalty term (7.8) to given state $u_\Omega \in \mathcal{V}$ is the unique solution to

$$a_\Omega(v, p_\Omega) = \partial_e P_\Omega(\epsilon(u_\Omega))(\epsilon(v)) \quad \forall v \in \mathcal{V}, \tag{7.13}$$

which is the adjoint equation (4.44) for the given specific setting. Note that the bilinear form $a_\Omega(\cdot,\cdot)$ has been defined in (2.8).
We proceed by *verifying* the *assumptions* of Theorem 4.1. Due to the volume forces in (7.2), which are constantly zero, the state u_Ω is smooth in a neighborhood of the point of perturbation z. As a result, and due to the smoothness of penalty function (3.6), the right hand side of the adjoint equation (7.13) is locally smooth. Hence, by elliptic regularity, the assumption regarding the adjoint state p_Ω is satisfied as well in a neighborhood of the point of perturbation.
Hence, abbreviating the pointwise evaluation of the strain of the direct and adjoint state by $U := \epsilon(u_\Omega(z)), P := \epsilon(p_\Omega(z))$, the application of Theorem 4.1 yields

$$\begin{aligned} D_T\mathcal{P}_\gamma[\Omega](z) =& \pi j_\delta(U) - \mathbb{E}U : P + \pi \nabla j_\delta(U) : \epsilon(v_X(0)) \\ &+ \int_{\mathbb{R}^2\setminus\omega} \mathcal{G}^0(z, \epsilon(v_X))dx + \int_\omega \mathcal{G}^1(z, \epsilon(v_X))dx, \end{aligned} \tag{7.14}$$

where j_δ has been defined in (4.23), $\mathbb{E}$ is the elastic moment tensor (4.36), v_X denotes the solution of problem (4.31) and $\mathcal{G}^0, \mathcal{G}^1$ are defined as in (4.46).
Furthermore, since the case of *isotropic elasticity tensors* and a *circular inclusion* ω is considered, tensor $\mathbb{E}$ and function $\epsilon(v_X)$ can be stated in closed form. Similar to the density function in (7.12), we set

$$\mathbb{C}_\Omega = \mathbb{C}^{\text{mat}}\chi_\Omega + \mathbb{C}^{\text{air}}\chi_{D\setminus\Omega},$$

with

$$\mathbb{C}^{\text{mat}} := \mathbb{C}, \qquad \mathbb{C}^{\text{air}} := \alpha\mathbb{C},$$

where $\mathbb{C}$ is defined as in (2.1) and $\alpha > 0$ is the weak phase parameter (2.1) in the elasticity model. Defining the difference between the elasticity tensors $\mathbb{C}_\delta$ as in (4.19), we obtain

$$\epsilon(v_X)(x) = -\mathbb{S}(x)(\mathbb{C}^0 + \mathbb{C}_\delta\mathbb{S}^{\text{int}})^{-1}\mathbb{C}_\delta X,$$

see (4.62), as well as the following formula

$$\mathbb{E} = |\omega|\mathbb{C}^0(\mathbb{C}^0 + \mathbb{C}_\delta \mathbb{S}^{\text{int}})^{-1}\mathbb{C}_\delta$$

for the elastic moment tensor, see (4.63). The corresponding formulas for the Eshelby tensor $\mathbb{S}$, cf. (4.58), in the case of isotropic material are stated in (4.64) and (4.66).

7.3. Numerical Experiments

In this section, experiments are conducted in order to investigate the numerical solution of optimal design problem (7.9) as well as problem (7.7), where the pointwise stress constraints are extended to the entire hold-all domain. The experimental procedure comprises two major steps. First, the topological gradient of both problems is validated by examining the finite differences with respect to a decreasing radius of the inclusion. This step is necessary in order to verify that the topological gradient, as well as its implementation, is correct. Note that this step is crucial due to the high complexity of the topological gradient. Second, after having validated the topological gradients, the level set-based optimization scheme from Chapter 5 is applied for examining the numerical solution of both optimal design problems. The central insights will be summarized briefly in observation environments.

Throughout this section, we investigate the numerical algorithm for the case of the L-beam example, which is visualized in Figure 7.1. The L-beam is commonly studied in order to assess the performance of numerical schemes for the solution of the minimum volume problem with pointwise stress constraints, see [126]. We chose the length of the vertical and horizontal beams as 2.5 m and the width as 1 m. Further, the structure is clamped at the top and a vertical load of 50 N/m is applied over the load region of length 0.02 m around the coordinate (2.5, 0.5), which results in an applied force of 1 N. In the vicinity of the load region and the boundary, where the L-beam is clamped no design changes are allowed. More precisely, a strip with height 0.02 m at the top and a half circle with radius 0.1 m around the point (2.5, 0.5) are defined as non-design area. Note that this area is necessary in order to prevent that the load regions become disconnected from the main structure in the course of the optimization procedure. Concerning the material properties of the L-beam, a Young's modulus of $E = 1$ MPa and a Poisson's ratio of $\nu = 0.3$ are chosen together with a weak phase parameter of $\alpha = 10^{-3}$. These parameters are usually chosen for the L-Beam example in literature, see for instance [17], [96] and [49], which allows comparing the results of different works. Note that this choice of parameters is purely academic and does not aim at modeling real materials.

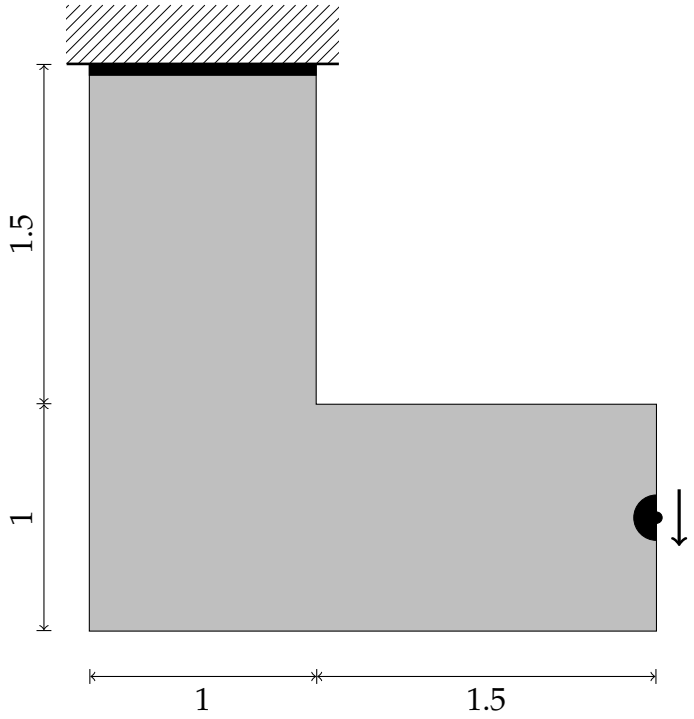

Figure 7.1.: Geometry of L-beam with design area in gray and non-design area in black.

Validation of the Topological Gradient

We begin the numerical experiments by validating the topological gradients for different scenarios in a fixed point of perturbation $z \in D \setminus \partial\Omega$, where $\Omega \subset D$ represents the material distribution in the unperturbed configuration. The validation is performed for both penalty terms (7.8) and (7.10). Moreover, we distinguish the creation of a hole within the material phase and, vice versa, the creation of material within the air phase. In the former case, where $z \in \Omega$, we choose the unperturbed material distribution as $\Omega = D$, which means that the entire domain is filled by material. In the latter case, where $z \in D \setminus \bar{\Omega}$, we choose domain D to be entirely occupied by air except for small subsets in the vicinity of the load regions, which are visualized as black domains in Figure 7.2. Note that distinguishing the location of z is crucial since the topological gradient for both material and air as background phase is necessary for the successful application of the level set-based optimization scheme. All combinations of both penalty terms and both cases regarding the point of perturbation z are investigated, which results in *four different scenarios*.
The validation procedure is straightforward and will be sketched exemplarily in the

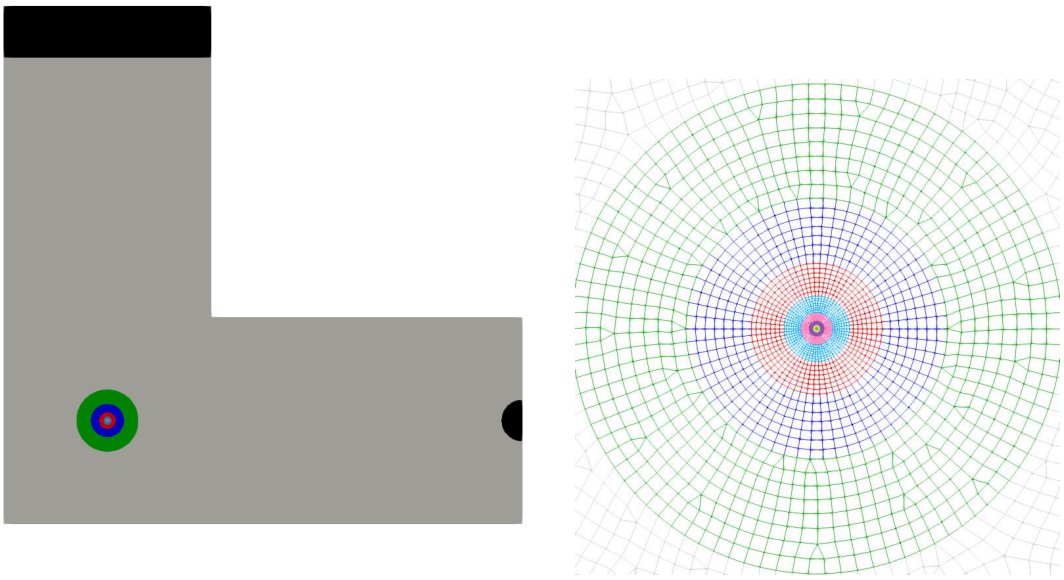

Figure 7.2.: Sketch of geometrical setup containing holes with center z for gradient validation (left) and zoom to meshed hole area (right).

following for penalty term $\mathcal{P}$, defined by (7.10). First, for radius $\rho > 0$ and the perturbed material configuration $\Omega_\rho \subset D$ defined by (4.15), we recall the topological asymptotic expansion (4.1) of functional $\mathcal{P}$

$$\mathcal{P}(\Omega_\rho) = \mathcal{P}(\Omega) + D_T\mathcal{P}[\Omega](z)\rho^2 + o(\rho^2),$$

which is guaranteed by Theorem 4.1 with topological gradient $D_T\mathcal{P}[\Omega]$, stated in (7.14). Based on the asymptotic expansion, we define the *finite difference*

$$\Delta\mathcal{P}[\Omega](z,\rho) := \frac{\mathcal{P}(\Omega_\rho) - \mathcal{P}(\Omega)}{\rho^2} \tag{7.15}$$

in order to obtain direct approximations of the topological gradient at point z. Then, the error measure for assessing the discrepancy between the topological gradient and the finite differences is chosen as follows

$$e(\rho) := \frac{|\Delta\mathcal{P}[\Omega](z,\rho) - D_T\mathcal{P}[\Omega](z)|}{|D_T\mathcal{P}[\Omega](z)|}, \tag{7.16}$$

where a normalization by the value of the topological gradient is used for the purpose of comparability between the different scenarios.
The validation setup for the L-beam comprises a total number of 8 holes with decreasing radii and is illustrated in Figure 7.2 together with a picture of the meshed area around

the point of perturbation. We chose the different hole radii in decreasing order as 160, 80, 40, 20, 10, 5, 2.5 and 1.25 mm. In the numerical simulations, a stress limit of $\bar{\sigma} = 3$ Pa is chosen, which is below the stress value at the point of perturbation. This choice has been made in order to guarantee that all terms in the topological gradient (7.14) are positive and hence taken into account in the validation. Moreover, in the case of penalty term (7.8) we chose the coefficient $h(\gamma) = 1$ for simplicity.

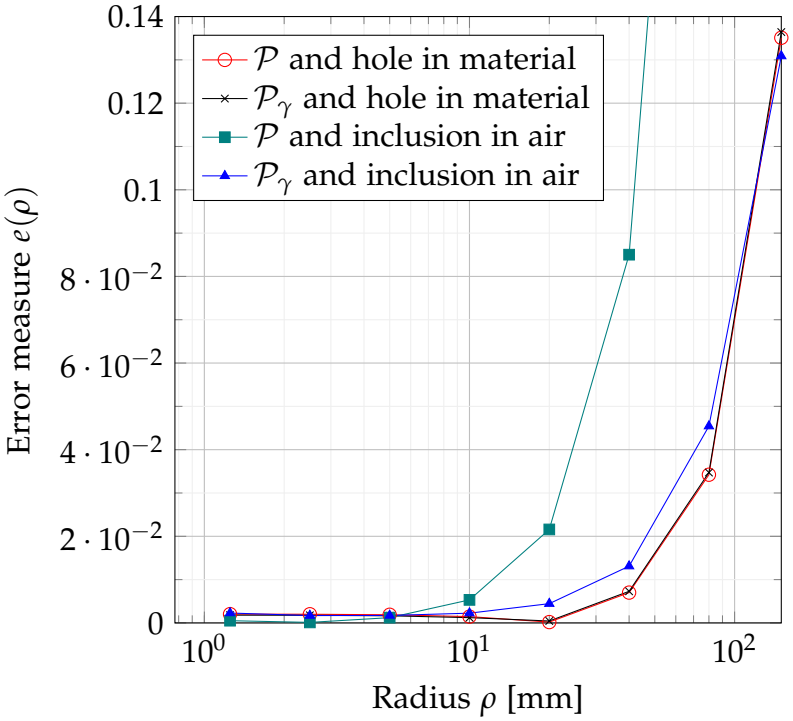

Figure 7.3.: Results of gradient validation for eight different radii.

The validation results are plotted in Figure 7.3. It can be observed that the error measure is close to 10^{-3} for a sufficiently small radius in all different scenarios, showing that the topological gradients as well as their implementations are correct. Furthermore, it is interesting to compare the values of the topological gradient for the different scenarios. In the case of *creating a hole* within the material phase, the values $D_T\mathcal{P}[\Omega](z) = 30.41$ and $D_T\mathcal{P}_\gamma[\Omega](z) = 30.48$ are obtained, which shows a high accordance between both penalty terms. In contrast, for the case of *creating a material inclusion* within the air phase, we obtain the values $D_T\mathcal{P}[\Omega](z) = 0.72$ and $D_T\mathcal{P}_\gamma[\Omega](z) = -2773.85$. Note that a discrepancy in the case of material creation is not surprising, since the dominating part of domain D is occupied by air, where the penalty terms (7.10) and (7.8) differ by definition.
The most interesting observation at this point, however, is that the topological gradients

have different signs, and thus differ *qualitatively*, in the case of material creation. The implication of this situation is of particular importance for the optimization scheme from Chapter 5. If penalty term (7.10) is employed for the optimization process, the topological gradient takes a positive value in z. As it has been discussed in Chapter 5, design changes near the point of perturbation z will not be performed within the optimization algorithm. If, however, penalty term (7.8) is employed, the topological gradient is negative at the point of perturbation z. Consequently, the optimization scheme will perform a design change near z as it decreases the value of the objective functional. This observation indicates, that the solution of problem (7.7), where the penalty term $\mathcal{P}_\gamma$ is employed, might differ significantly from the solution of problem (7.9).

Observation 7.1. *The topological gradient of penalty term (7.8) differs qualitatively from the topological gradient of penalty term (7.10) for a point of perturbation within the weak phase. This discrepancy is of particular importance for the design evolution within the level set-based optimization scheme.*

Optimization Setup

Before the numerical solution of problems (7.7) and (7.9) is addressed, the *setup* and *parameters* regarding the optimization algorithm need to be fixed. The area, where the stress constraints are enforced, is chosen to be identical with the design area, which is represented by the gray domain in Figure 7.1. This choice is reasonable, since the high stresses near loads are unavoidable and should not be taken into account for the stress assessment. Further, the initial design for the optimization scheme is chosen to be the entire domain in all experiments within this chapter. For the following numerical experiments, a stress limit of $\bar{\sigma} = 60$ Pa is chosen and the parameter, which controls the approximation accuracy of the penalty function (3.6) is set to $p = 50$. Concerning the numerical integration, which needs to be performed within the evaluation of topological gradient (7.14), we chose $N = 30$ and $M = 60$ integration points for the discretization of the radius and the angle, respectively. For the details on the numerical integration, we refer to Section 6.4, in particular to quadrature rule (6.26). In the optimization algorithm from Chapter 5, we set the initial line search parameter to $\kappa_0 = 1$ and update a current parameter κ by $\kappa/2$.
We use the number of vertices, where the topological gradient of the total objective functional is negative as a *convergence measure* instead of the angle θ between level set function and descent direction, see (5.9). More precisely, the convergence measure is defined as

$$\epsilon_c := \frac{|\{n \in \mathcal{N}_h : D_T \mathcal{P}[\Omega](n) < 0\}|}{|\mathcal{N}_h|}, \tag{7.17}$$

where $\mathcal{N}_h$ is the set of mesh vertices. The optimization algorithm is terminated, if ϵ_c is below a chosen threshold. Note that this is a discrete variant of the stationarity criterion (5.4). We chose to employ convergence measure (7.17) instead of (5.9), since it behaves more robust in the numerical solution of the stress-constrained minimum volume problem. Additionally, the algorithm is terminated, if a decrease of the objective functional has not been achieved after 20 step reductions within the line search scheme. Note that this number has been determined heuristically and is based on the experience from numerical tests.

Before proceeding with the presentation of the numerical results, the necessary details concerning the *continuation strategy* of penalty parameter γ are given. First, we recall that in problem (7.9), parameter γ simply acts as a weighting coefficient for the penalty term. In problem (7.7), however, γ additionally serves for scaling the stress limit in the weak phase. The main idea of a continuation strategy within a penalty approach is to solve a sequence of optimization problems, where the penalty parameter is increased gradually and the solution of the previous problem is used as an initial guess for the current problem. Within this procedure, a strategy for tuning the penalty parameter needs to be selected. On the one hand, the penalty parameter should not be chosen too low in order to respect the constraints. On the other hand, it should not be chosen too large, which typically leads to convergence problems. For details on the penalty approach and the continuation method, we refer to the discussion in Section 3.3. For the following experiments, we employ

$$h(\gamma) := \frac{\gamma}{\gamma_0} \tag{7.18}$$

as coefficient function in the penalty term (7.8), where γ_0 represents the initial penalty parameter. Note that a reasonable choice of function h can not be determined a priori and is therefore based on the experience from numerical tests.

Effect of Stress Constraints in the Weak Phase

We begin the presentation of the experimental results by comparing the numerical solution of problem (7.9) and (7.7) for a fixed penalty parameter. We chose $\gamma_0 = 1000$ and $\gamma_0 = 10$ for the solution of problem (7.9) and (7.7), respectively. Note that the difference in the order of magnitude is necessary due to the different penalty terms. In

Figure 7.4, the optimization history of both problems is visualized. Moreover, Figure 7.5 shows the designs in the final iteration.

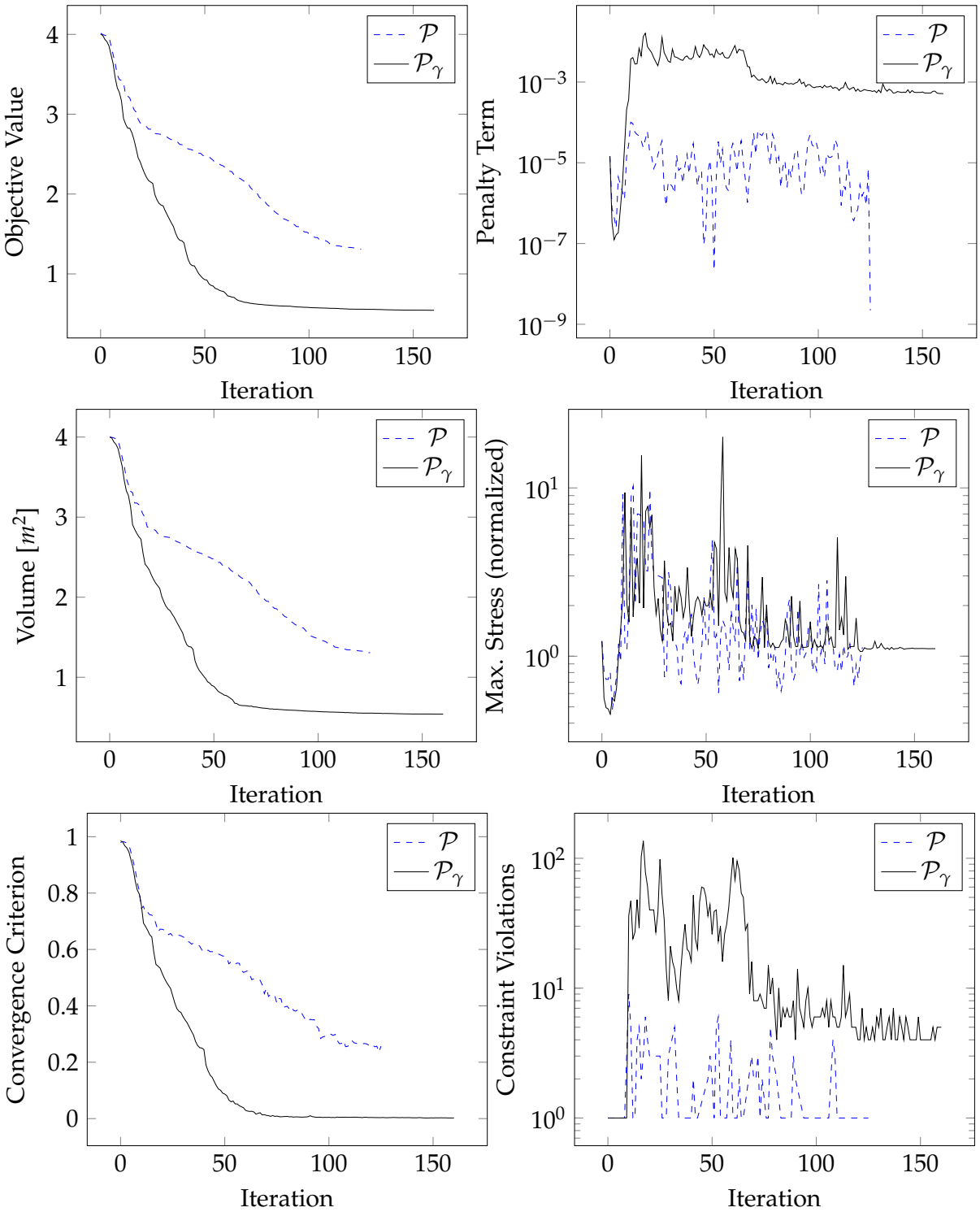

Figure 7.4.: Optimization history for the solution of problems (7.9) and (7.7).

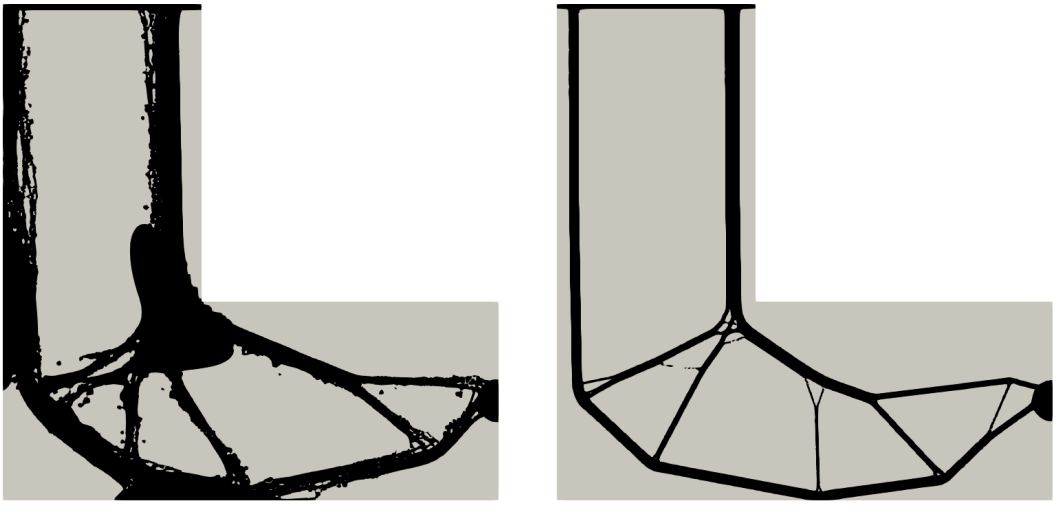

Figure 7.5.: Designs in final iteration for fixed parameter γ. Left: Result for problem (7.9) with constraints only in material phase. Right: Result for problem (7.7) with constraints in entire domain.

In the case of problem (7.9), where stress constraints are imposed only in the material phase, it can be observed that the optimization scheme does not converge. The algorithm terminates after 126 iterations with $\epsilon_c = 0.26$. This is clearly reflected in the design of the final iteration, see Figure 7.5, which shows perforations and small isolated parts. Nevertheless, it can be stated that the topological gradient directs the algorithm to a plausible structure due to the availability of information regarding the local stresses. In the case of problem (7.7), with stress constraints imposed in both material and air phases, the optimization algorithm converges and behaves differently compared to the previously discussed case. More precisely, the algorithm terminates after 161 iterations with $\epsilon_c = 2.23 \times 10^{-3}$. Further, the volume and the penalty term begin to settle after 65 iterations, see Figure 7.4. Concerning the maximum normalized stress and the number of constraint violations in the material phase, we can observe large fluctuations. This is simply a consequence of the highly nonlinear behavior of pointwise stress constraints, where small design changes result in large stress variations. Summarizing, a stabilizing effect on the numerical scheme can be observed, if the pointwise stress constraints are extended to the entire computational domain. Moreover, the choice of penalty parameter γ turns out to be simpler for the case of problem (7.7), where stress constraints are present in both phases. The numerical algorithm can be observed to be successful for a rather large interval of penalty parameters. In the case of problem (7.9), however, the choice of γ is a quite delicate task. Only values of γ within a very small interval lead to results, which tend

towards a plausible structure. Based on the previous observations and the excellent results for the extension of the stress constraints to the entire domain, we will focus on the solution of problem (7.7) for the remainder of this chapter. Hence, problem (7.9) will not be investigated further, since it does not lead to satisfactory results.
We continue with several details concerning the numerical solution of problem (7.7).

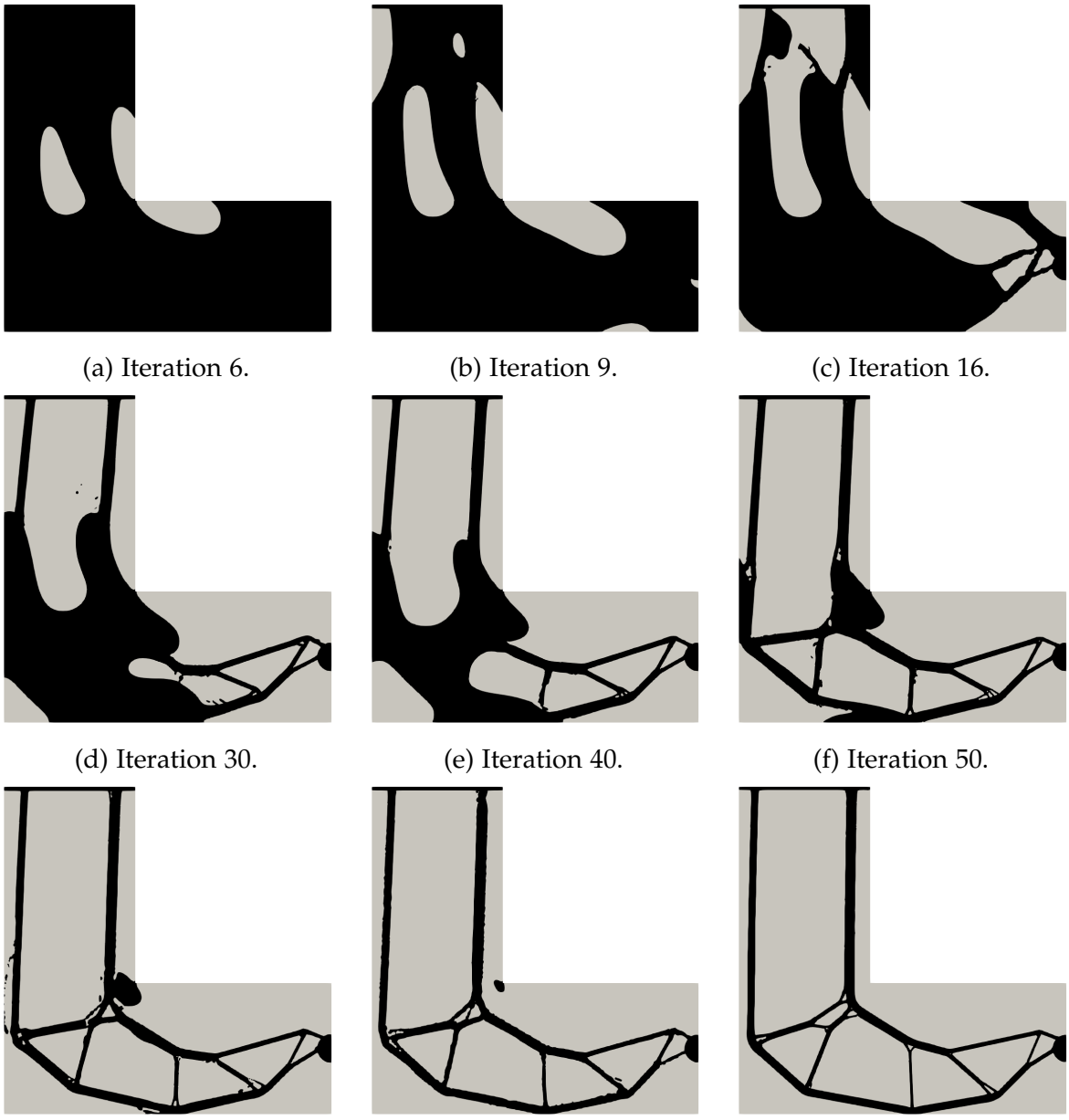

(a) Iteration 6. (b) Iteration 9. (c) Iteration 16.

(d) Iteration 30. (e) Iteration 40. (f) Iteration 50.

(g) Iteration 59. (h) Iteration 62. (i) Iteration 80.

Figure 7.6.: Design evolution for the numerical solution of problem (7.7) with stress constraints in the entire domain.

In Figure 7.6, the designs at nine iterations are depicted. First, we remark that the design evolution behaves quite slowly compared to the minimum compliance problem, which will be discussed later on for the sake of comparability. Second, it can be observed that the algorithm removes material in regions of low stresses first, for instance at the left upper corner of the L-beam. In contrast, the design in areas with large stress values, for instance the area around the reentrant corner, is altered rather at the end of the optimization process. Lastly, and probably most interesting, we observe that the area containing the stress singularity at the reentrant corner is isolated in the course of the optimization and completely removed after the isolation has been carried out.

Observation 7.2. *The regularized problem (7.8), which comprises an extension of the pointwise stress constraints to the weak phase, is solved successfully by the level set algorithm. Since this is not the case for problem (7.10), a stabilizing effect of the additional stress constraints on the numerical scheme can be stated.*

Observation 7.3. *The optimal design problem (7.7), which comprises a volume term and the stress-based penalty term, was solved successfully. This result reveals that an additional compliance term, which is commonly employed for preventing the no-structure problem (cf. [119]), is not necessary for solving the stress-constrained minimum volume problem.*

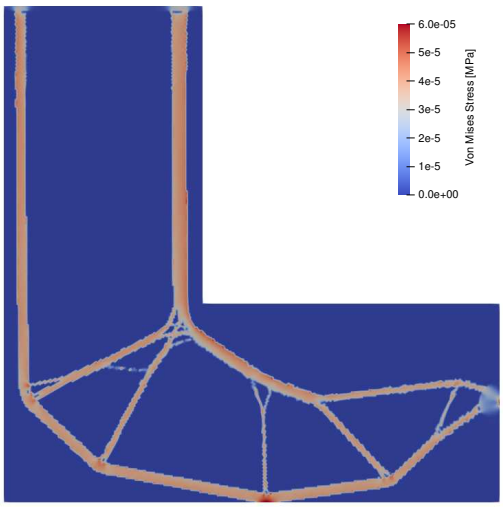

Figure 7.7.: Von Mises stress field for design in Figure 7.5 (prior to continuation in γ).

Continuation in Penalty Parameter

At this point, it is crucial to examine the local stresses in the final iteration in order to assess the success of the numerical scheme. In particular, it needs to be verified if

the pointwise stress constraints are satisfied. In Figure 7.7, we can observe constraint violations in five different vertices, all of them located at the lowest design part with a maximum von Mises stress of 66.5 Pa.
Although this is already a very good result and close to the desired solution, we are interested in obtaining designs, which do fulfill the imposed constraints. Therefore, we proceed by investigating the continuation in penalty parameter γ. By increasing γ successively, we aim at adapting the design in Figure 7.5 such that the stress constraints are satisfied. Continuing from the design in Figure 7.5, we chose the sequence of penalty parameters $5 \times 10^2, 5 \times 10^3, 7.5 \times 10^3, 2 \times 10^4, 5 \times 10^5$. Note that this choice is a result of several experiments. However, a strategy for determining values of γ in an automated fashion can be developed, as it is typically done within penalty approaches.

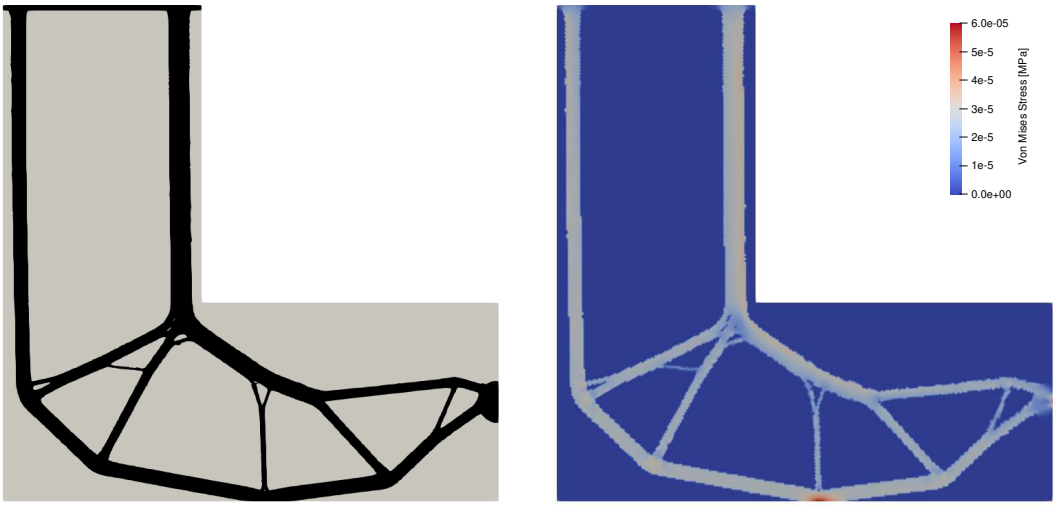

Figure 7.8.: Design (left) and corresponding stress field (right) after continuation in penalty parameter γ.

In Figure 7.8, the effects of the continuation in γ become clear immediately. Compared to the result in Figure 7.5, we can observe that the design becomes thicker in general, but is qualitatively unchanged. More precisely, the volume is increased from $0.54\,\mathrm{m}^2$ to $0.75\,\mathrm{m}^2$. This change in the design leads to the desired constraint satisfaction with a maximum pointwise von Mises stress of 59.6 Pa and a vanished penalty term. Note that the penalty term vanishes due to coefficient $h(\gamma)$, which scales the stress limit in the weak phase. If we choose $h(\gamma) = 1$, the penalty term can be observed to be positive, even if the stress constraints in the material phase are satisfied. As a result, the optimization algorithm continues enforcing the design, even if the pointwise constraints in the material phase are already satisfied due to the presence of artificial stress constraints in air. Preventing this behavior by choosing $h(\gamma)$ as in (7.18) is an

important aspect in order to guarantee that only as much material as necessary is used.

Observation 7.4. *The continuation in γ leads to an enforcement of the design, which has been obtained by an optimization procedure with fixed initial penalty parameter, until the pointwise constraints are satisfied and the penalty term vanishes. During the process of continuation, the initial design remains qualitatively unchanged.*

Stress Verification

An important aspect concerning the result of the continuation in γ (cf. Figure 7.8) is a realistic stress assessment. Let us recall that all experiments are conducted on a fixed mesh, which results in intersections of the interface and mesh elements in the course of the optimization. As discussed in the previous chapter, these intersections lead to a loss of accuracy in the finite element approximation of the displacement field, in particular at the interface of the level set function. Additionally, it is unclear a priori what the impact of the weak phase on the stresses actually is.

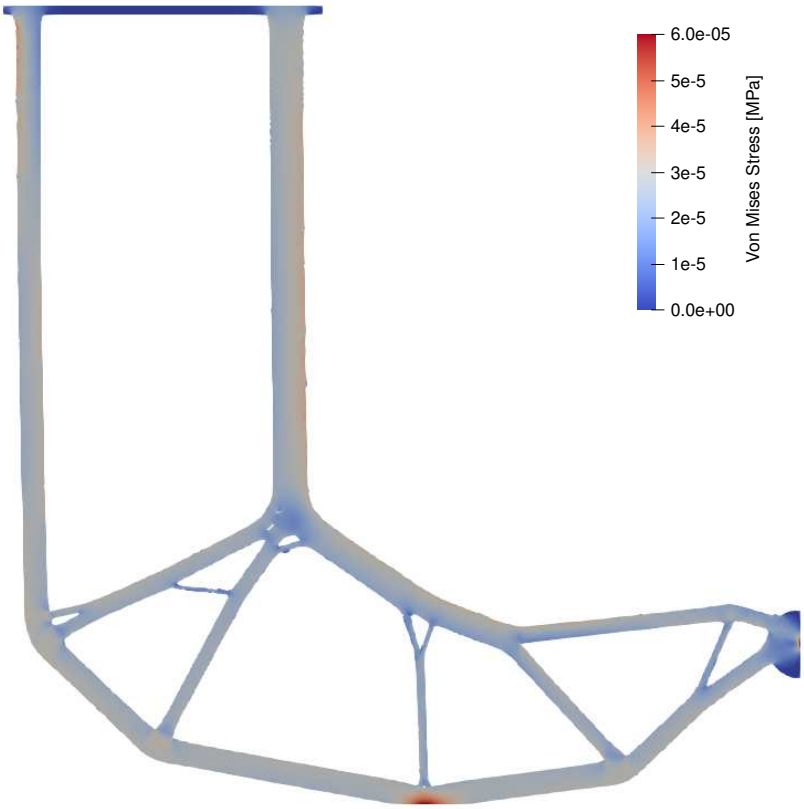

Figure 7.9.: Stress verification with fitted mesh and removed weak phase.

Therefore, we need to address the question, how the von Mises stress field behaves, if the weak phase is deleted and the material phase is meshed properly. Only after these

adaptations, the stress analysis will be sufficiently reliable for modeling the actual manufactured component realistically. The adaptations are performed by extracting the material phase based on the level set description and employing a reasonably fine and fitted mesh. The result of the stress analysis is shown in Figure 7.9, where the stress field of the material phase is visualized. It can be observed that the stress constraint is violated only in two vertices at the lowest part of the design with a maximum von Mises stress of 61.9 Pa. Note that this very satisfactory result has been achieved without any postprocessing of the level set function.

Comparison with Minimum Compliance Design

The last aspect within this section addresses the comparison of the obtained stress design with the solution of the commonly studied minimum compliance problem, which has been stated in (6.19). For the purpose of comparability, we set the volume bound V in the minimum compliance problem to exactly the volume of the obtained stress design. In Figure 7.10, the design as well as the corresponding stress field are shown for the minimum compliance problem.

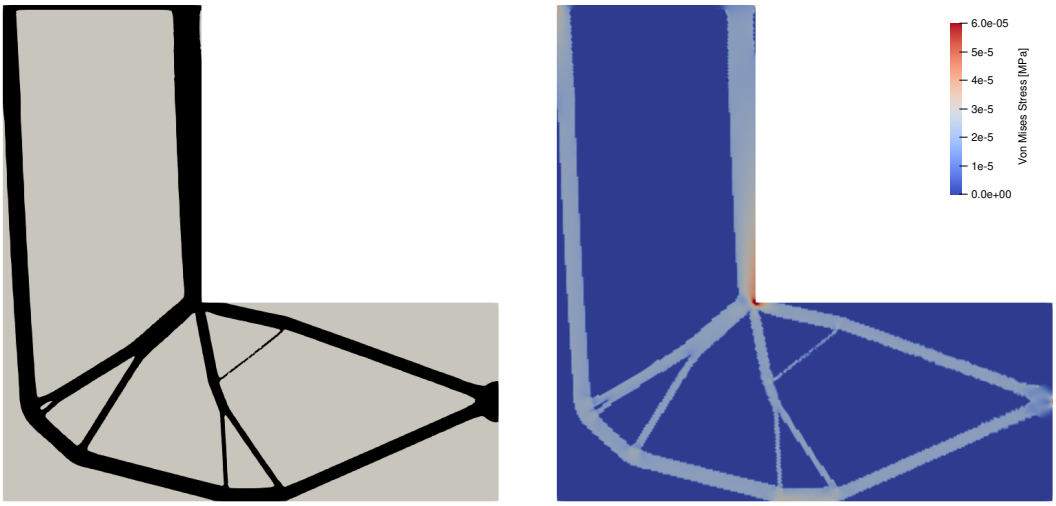

Figure 7.10.: Design (left) and stress field (right) for minimum compliance problem.

We can observe clear differences in the design compared to the solution of the stress-constrained minimum volume problem, see Figure 7.8. Most prominent, the stress concentration at the reentrant corner with a maximum von Mises stress of 136.2 Pa is present in this experiment. This observation shows the necessity of incorporating stress constraints for certain applications. Additionally, a large variation of the stress level can be observed.

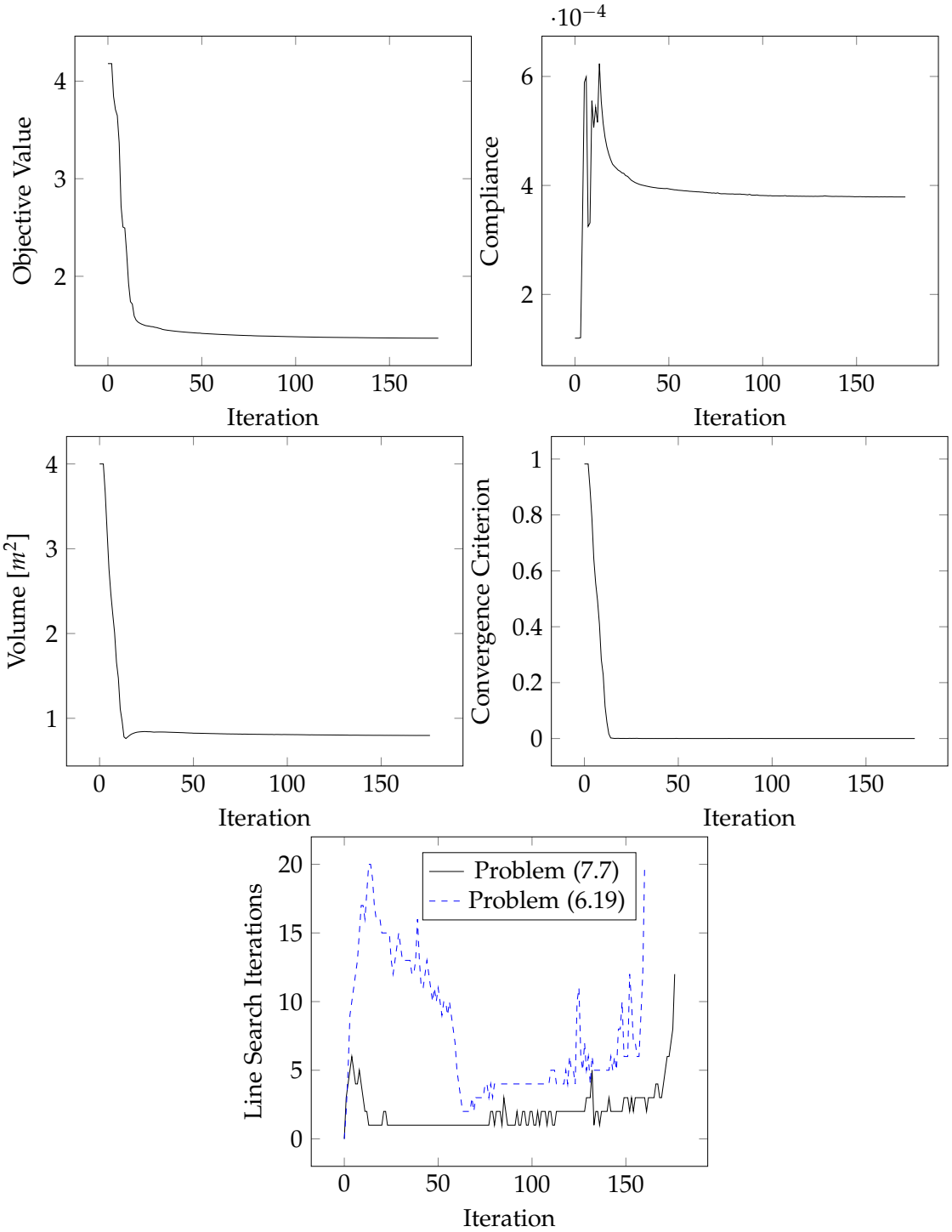

Figure 7.11.: Optimization history for the solution of the minimum compliance problem.

In contrast, the stress level is more homogeneous in the entire design for the case of the stress design. Clearly, the algorithm is capable to design the structure in such a manner

that the stresses are distributed over the structure. In Figure 7.11, the optimization history for the minimum compliance problem is shown. It can be observed that the algorithm approximates a local minimum much faster than for the previously investigated minimum volume problems with stress constraints. Indeed, the volume stabilizes after 20 iterations and only minor design changes are performed afterwards. The reason for this difference is that large steps in the algorithm are possible, since the compliance is less sensitive to design changes than the stress field. For the stress-constrained problems, however, small step sizes are necessary in order to be able to control the stress levels appropriately. This difference in the step size can be observed in the last plot of Figure 7.11, where the line search iterations for both problems are shown. Clearly, a much larger number of step reductions within the line search is necessary for the case of the minimum volume problem with stress constraints.

7.4. Discussion

Having reported on the numerical experiments in the previous section, the results will be summarized briefly in the following. First, the topological gradient of both penalty terms under investigation, more precisely (7.8) and (7.10), have been validated. This has been done for the creation of a hole in the material phase as well as for the inclusion of material in the weak phase. The examination of both cases is crucial since the optimization algorithm relies on the sensitivities for both cases. An interesting observation is the qualitative discrepancy of the topological gradient for both penalty terms in the case of an inclusion of material in the weak phase. This suggests that the design evolution will differ significantly during the optimization procedure for both penalty terms. The subsequent step addressed the numerical solution of problem (7.9) and (7.7) with the level set-based optimization scheme. For problem (7.9), where the penalty term is constructed as an integral over the material phase, it could be observed that the optimization algorithm does not converge. Moreover, the design in the final iteration shows a large number of perforations and small isolated material parts. Nonetheless, the rough shape of the evolving structure shows the characteristic features of a typical stress design. In this sense, the minimization of problem (7.9) seems not to be completely unreasonable, despite the problem of the trivial and global solution being the empty set. We proceeded by examining the numerical solution of problem (7.7), where the stress constraints have been extended to the entire computational domain. This regularization has been introduced in order to overcome the no-structure problem. It could be observed that a penalty term of this type leads

to a convergent optimization algorithm, which is capable of satisfying the pointwise stress constraints. Consequently, it can be concluded that the extension of the stress constraints is sufficient for alleviating the no-structure problem. In particular, a further regularization with a compliance term is not necessary for the solution of the minimum volume problem. A crucial part of the optimization method is the continuation in penalty parameter γ in order to generate designs which fulfill precisely the pointwise stress constraints. Moreover, we could observe that the incorporation of the coefficient function $h(\gamma)$ in problem (7.7) leads to a vanishing penalty term for the specific choice (7.18), if the stress constraints in material are satisfied. The resulting effect is that the algorithm terminates, as soon as the pointwise constraints are fulfilled and no unnecessary material is used. Moreover, function $h(\gamma)$ allows to connect problem (7.7) with the original minimum volume problem with pointwise stress constraints in the material phase. While a small parameter γ is necessary in the beginning of the optimization procedure in order to guarantee convergence, large values for γ lead to vanishing constraints in the air phase. Consequently, the original problem is approximated successfully for large penalty parameters. Finally, the stresses for the obtained design have been checked in a more precise and realistic simulation. Essentially, the mesh has been fitted to the design boundary in order to remove intersected mesh elements and the weak phase has been deleted. The stress analysis shows high accordance with the predicted stress values and only a minor constraint violation in two vertices could be observed.

After having summarized the results of the numerical experiments, the main findings compared to Amstutz and Novotny (2010), see [17], are stated. Note that their work has been one of the starting points for the research, which has been conducted in this thesis. First, novel insights concerning the no-structure problem are gained by investigating the regularization of the original stress-constrained minimum volume problem. It could be shown that an extension of the pointwise constraints to the weak phase is a crucial step in order to obtain a convergent numerical scheme. Note that we had to address the topological gradient of a large class of penalty terms in order to be able to solve problem (7.9). Further, the incorporation of a compliance term in the optimal design problem is not necessary for solving the stress-constrained minimum volume problem. Second, we modified the penalty term by introducing the coefficient function $h(\gamma)$. This modification has the effect of a vanishing penalty term, if the stress constraints are fulfilled in the material phase. Consequently, combined with a continuation method in the penalty parameter γ, the function $h(\gamma)$ ensures that the original problem with pointwise stress constraints in the material phase is approximated by the regularized problem (7.7).

The aim of this thesis is a method for the solution of generic stress-constrained optimal design problems, where the minimum volume problem is only a special case. Therefore, the question arises, if the regularizing effect of the stress constraint extension to the air phase is limited to the minimum volume problem or holds for different problems as well. We will investigate this question in the following chapter, where the multiphysical design of an electrical machine under pointwise stress constraints is addressed.

8. Multiphysical Design of an Electrical Machine

8.1. Introduction

In the previous chapter, the solution of the minimum volume problem with pointwise stress constraints for the L-beam geometry, which is a standard benchmark problem in stress-constrained topology optimization, has been investigated. In this chapter, we turn towards a more challenging problem, which has, to the author's best knowledge, not been addressed in literature so far. The problem under investigation is the multiphysical design of the rotor of an electrical machine. More precisely, the aim is to maximize the average torque of the machine, which is an electromagnetic quantity, subject to pointwise constraints on the first principal stress in the rotor, which is a quantity from the domain of structural mechanics and can be used to assess the mechanical stability of the rotor in operation mode. The purpose of this chapter is twofold. First, the developed method is employed for the solution of a real industrial problem with relevance to practitioners and engineers. This is particularly important, since, in contrast to the widely used SIMP method, the application of topological gradients seems to be mostly restricted to academic problems so far. To the author's best knowledge, only the works [43] and [117] address industrial applications of topological gradients. Second, the regularizing effect of stress constraints in the air phase will be examined for the case of torque maximization. In particular, it will be investigated, whether the regularization has a stabilizing effect on the numerical scheme, as it has been observed in the previous chapter for the stress-constrained minimum volume problem and the L-beam geometry.

Before the optimal design problem is formulated, a short overview of the existing literature on shape and topology optimization for electrical machines is given. Note that only sensitivity-based approaches are considered in the following. One of the earliest works dealing with topology optimization for electrical machines has been published by Takahashi et al. in 2010, see [135], which uses the *ON/OFF method*. This approach has been introduced in [107] and relies on discrete sensitivities and a

heuristic optimization scheme. In [135], the minimization of the torque ripple, which is a term from engineering and describes undesirable periodic fluctuations of the torque, as well as the case of average torque maximization have been addressed. In [68], Gangl and Langer (2012) employed the ON/OFF method for the minimization of a criterion, which is related to the smooth rotation of the rotor of a permanent synchronous machine. The concept of *shape derivatives* has been employed for the optimization of an electrical machine by Gangl et al. in 2015, see [69], where the objective is again related to the smoothness of the rotation of the rotor. Another approach based on shape derivatives and isogeometric analysis can be found in [102], where Merkel et al. (2021) considered the minimization of the total harmonic distortion of an interior permanent magnet synchronous machine. In 2012, Choi et al. considered the rotor pole design of an electrical machine using the *phase field method*, see [44]. Further, the *SIMP approach* has been employed by Kuci et al. (2019) for the torque ripple minimization of an interior permanent magnet synchronous machine, see [95]. Gangl et al. (2016) used the concept of *topological gradients* for the minimization of an electromagnetic objective functional, see [65] and [67].

We remark at this point that all existing works take solely electromagnetic quantities into account. To the author's best knowledge, multiphysical shape or topology optimization has not been addressed so far for the design of electrical machines. The consideration of multiphysical effects, however, is crucial for obtaining *realistic* machine designs due to a well known conflict between electromagnetic and mechanical criteria, see for instance [100] or [136]. This conflict between electromagnetics and structural mechanics is meant in the sense that certain design features, which are favorable for one domain, have a negative effect on the performance with respect to the other domain. This challenge in the design process of electrical machines highlights the practical relevance of topology optimization and demonstrates the actual potential of the developed method.

Let us clarify briefly, which aspects of the design of an electrical machine are novel compared to the stress-constrained minimum volume problem. First, a *nonlinear system dynamic* needs to be taken into account in order to model the electromagnetic behavior of the machine. This nonlinearity in the state system, which is a simplified version of Maxwell's equations, is caused by the nonlinear behavior of magnetic fields in ferromagnetic material. The consequence of the nonlinear state system is a challenging and computationally expensive objective evaluation and sensitivity computation. Further, as it has been mentioned previously, the maximization of the average torque subject to local stress constraints is a *multiphysical* design problem. In contrast to the minimum volume problem, obtained solutions might not be intuitively plausible anymore due to

the previously mentioned conflict between electromagnetic and structural mechanical design criteria. This aspect comprises the chance of generating novel, and up to now unknown, design ideas.
The structure within this chapter is chosen as follows. First, the electromagnetic and structural mechanical modeling of electrical machines is addressed. Based on the derived physical models and quantities, the optimal design problem is formulated. Since the obtained problem matches the framework from the first chapters, the developed methods can be applied. As in the case of volume minimization, we will investigate existence of local minima of the optimal control problem and derive its topological gradient. Numerical experiments are conducted in order to investigate the performance of the numerical scheme for the design of a permanent magnet synchronous machine. In particular, the choice of the penalty term will be examined and discussed.

8.2. Modeling of Permanent Magnet Synchronous Machines

A first and fundamental step towards designing an electrical machine is understanding and describing its essential *physical functionality*. Therefore, in this section, we will provide an overview of the most common types of electrical machines and explain the functionality of the important class of permanent magnet synchronous machines (PMSM), which will be considered throughout this chapter, in more detail. Further, an electromagnetic model as well as a structural mechanical model for describing the behavior of the considered machine type will be derived and discussed.
Electrical machines fall into the category of *electromechanical energy converters*, see for instance the monograph [29]. If electrical energy is converted to mechanical energy, a machine is called an electric motor and, in case of conversion from mechanical energy to electrical energy, a machine is referred to as electric generator. Electrical machines can be categorized as either *rotating* or *linear*, depending on the type of mechanical movement in operation mode. For the rotating case, a machine consists of a fixed part, which is commonly referred to as stator, and a rotating inner part, which is called rotor. Essentially, magnetic fields of certain types are generated in the stator as well as the rotor and the interaction between both fields is used for generating a mechanical rotation of the rotor. We will discuss the operation principle of a specific type of rotating machines in more detail below. Further, the class of *synchronous machines* is distinguished from induction machines, which are of *asynchronous* type. The former class, in contrast to induction machines, is characterized by a synchronous rotation of

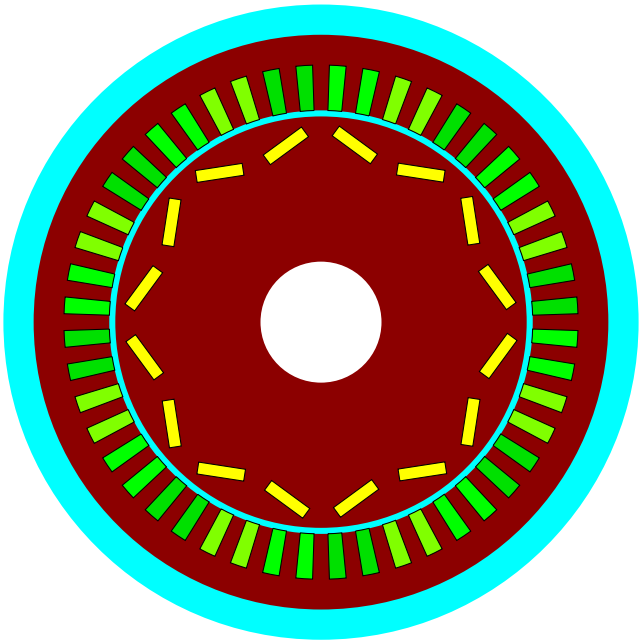

Figure 8.1.: 2D cross-section of an interior PMSM. The stator consists of iron (brown) and coils (green) and is separated by the airgap (blue) from the rotor, which consists of iron and magnets (yellow).

the rotor and the rotating magnetic field of the stator. An important subcategory of these machines is the class of *permanent magnet synchronous machines*, where the rotor contains permanent magnets in order to generate a constant magnetic field. In contrast to reluctance machines or hysteresis machines, this type offers the advantages of high power densities and efficiency, see for instance [78] or [136]. Concerning the rotor arrangement, the permanent magnets can be either buried in the interior of the rotor or mounted on its surface. The class of *interior permanent magnet synchronous machines*, in contrast to the surface-mounted type, has the advantage of high torques and low cost, see [54] and [91]. A sketch of the two-dimensional cross-section of an interior permanent magnet synchronous machine, which will be considered throughout this chapter, is visualized in Figure 8.1.

The magnet arrangement for an interior PMSM is a delicate task and has a significant impact on the performance of the machine. The specific size and location of the magnets in Figure 8.1 is known as *V-shape* in engineering, referring to the constellation of two neighboring magnets. It has been demonstrated in [78] that the V-shape, in contrast to different arrangements, "has the broadest area of high efficiency and, thus, the best energy consumption in a mixed driving scenario of a small battery electric vehicle". This property makes the V-shaped interior PMSM an ideal candidate for the experiments within this chapter. We mention that the exact parameters regarding

magnet size, position and angle within the V-shape arrangement are not fixed a priori, but need to be chosen for the given problem at hand. In case of the machine in Figure 8.1, these parameters are the result of a parametric *multi-objective optimization* with respect to criteria from different physical domains.
Besides the previously mentioned positive properties of interior permanent magnet synchronous machines, which are high power density, high torque and overall efficiency, there are of course less favorable characteristics compared to different machines types. The probably most severe disadvantage of an interior PMSM is the *low mechanical robustness* of the rotor caused by centrifugal forces in operating mode, for instance [91] and [77]. This lack of mechanical stability is a consequence of the specific arrangement of steel and permanent magnets within the rotor and will be discussed in more detail later on. Note that the mechanical robustness is a very important aspect, since it affects directly the maximum allowable rotational speed of the machine. We highlight at this point that our approach tackles this well-known challenge in the design of an interior PMSM by considering the mechanical stresses.
We proceed by explaining the basic functionality of a permanent magnet synchronous machine in more detail. The stator, which is the outer part in Figure 8.1, is fixed and consists of a steel core as well as electromagnetic coils, which are typically made of copper. The purpose of these coils is the generation of a *rotating magnetic field*, which is realized by supplying an alternating current flow of the same amplitude and frequency to each coil. We recall from the theory of electromagnetism that an alternating current flow in a coil induces an alternating magnetic flux density, see for instance [29]. Choosing a suitable phase difference for the alternating currents of the different coils and taking the spatial distribution of the coils into account, the interaction of the sinusoidal magnetic flux densities results in a rotating stator field. In Figure 8.1, the phase difference between the coils is visualized via three different types of green. The illustration indicates that the current flow in all coils of the same color is identical and a phase shift of 120° characterizes the differences between two coils of different colors. Note that machines involving stators of this type are commonly referred to as three-phase machines. We mention at this point that in many applications, in particular if the current source is a battery, an inverter is necessary for transforming direct to alternating currents. Furthermore, the rotor of a PMSM consists of a steel core and permanent magnets, which create a *constant magnetic field*. For a suitable arrangement of the permanent magnets, the interaction between the constant rotor field and the rotating magnetic field, induced by the stator, results in a mechanical rotation of the rotor. This rotational force can be transferred to other mechanical devices via the rotor shaft, which is attached to the rotor and located in its center.

The goal of the remaining section is to derive a model for describing the behavior of a permanent magnet synchronous machine. Instead of modeling the entire three-dimensional object, we will consider only a *two-dimensional cross section*. This is a common procedure in the modeling process of a PMSM and provides a very good trade-off between model accuracy and computational complexity. We will see later on that the model assumptions, which allow the reduction of dimensions, are reasonable. Moreover, *two physical domains* will be taken into account in the modeling process. First, the electromagnetic behavior, more precisely the magnetic field, is a quantity of interest. Second, the structural mechanical behavior will be considered by the displacement field. Note that displacements occur due to centrifugal forces in the rotor, which are caused by mechanical rotation. The ultimate goal is to define the torque of the electrical machine and the principal stress in the rotor in order to formulate an optimal design problem, which will be addressed in the following section. Note that more than the two mentioned physical domains need to be considered in practice. Taking acoustic effects into account is important in the design of electrical machines in order to prevent undesirable sounds, especially at high rotational speeds. Moreover, thermal effects are usually considered in the design process in order to keep heating of certain machine parts as low as possible and prevent material damage. However, it is known from engineering experience that the consideration of only electromagnetic and structural mechanical effects provides a sufficiently accurate approximation of the real machine for obtaining a first realistic design. We specify that a realistic design in this context has to be understood as manufacturable and mechanically robust, which allows to actually manufacture the designed machine for testing purposes. A modification of the design with respect to thermal and acoustic effects, however, is of course necessary in order to obtain a machine for everyday use. Additionally, we will assume a *constant rotational speed* of the permanent magnet synchronous machine. This assumption covers an important operation case of electrical machines and allows to employ stationary models. Note that the consideration of variable rotational speeds, which results in instationary and hence more complex models, is of interest for describing the starting phase or speed variations of a machine.

Electromagnetics

Let us begin with modeling the electromagnetic behavior of a permanent magnet synchronous machine. In the following, several simplifications of Maxwell's equations will be conducted and the necessary assumptions discussed, which results in the *magnetostatic problem*.

Electromagnetic phenomena are modeled by Maxwell's equations, which describe the relation between electric and magnetic fields (cf. [90] or [92]):

$$\operatorname{curl} \boldsymbol{H} = \boldsymbol{J} + \frac{\partial \boldsymbol{D}}{\partial t}, \tag{8.1}$$

$$\operatorname{curl} \boldsymbol{E} = -\frac{\partial \boldsymbol{B}}{\partial t}, \tag{8.2}$$

$$\operatorname{div} \boldsymbol{B} = 0, \tag{8.3}$$

$$\operatorname{div} \boldsymbol{D} = \rho. \tag{8.4}$$

The quantities in the system of partial differential equations (8.1) - (8.4) are called the magnetic field intensity $\boldsymbol{H}$, the magnetic flux density $\boldsymbol{B}$, the electric field intensity $\boldsymbol{E}$, the electric flux density $\boldsymbol{D}$, the electric current density $\boldsymbol{J}$ and the electric charge density ρ. Note that all objects in Maxwell's equations depend on a point in space $x \in \mathbb{R}^3$ and time $t \in \mathbb{R}_0^+$.
The equations (8.1) - (8.4) are connected via material laws, which are formalized by the following constitutive relations

$$\boldsymbol{B} = \mu \boldsymbol{H} + \boldsymbol{M}, \tag{8.5}$$

$$\boldsymbol{D} = \epsilon \boldsymbol{E} + \boldsymbol{P}, \tag{8.6}$$

$$\boldsymbol{J} = \sigma \boldsymbol{E} + \boldsymbol{J}_e, \tag{8.7}$$

where $\boldsymbol{M}$ denotes the magnetization, $\boldsymbol{P}$ represents the electric polarization and $\boldsymbol{J}_e$ is an impressed current density. In general, the magnetic permeability μ, the electric permittivity ϵ and the conductivity σ are matrices depending nonlinearly on $\boldsymbol{H}$ and $\boldsymbol{E}$. For the rest of this chapter, however, we assume *isotropic* material behavior such that these matrices become scalar quantities. Furthermore, we *neglect hysteresis effects* in all involved materials. It is common to describe the relation between $\boldsymbol{H}$ and $\boldsymbol{B}$ by the reciprocal of the magnetic permeability, which is called the magnetic reluctivity ν, implying the equation

$$\boldsymbol{H} = \nu(\boldsymbol{B} - \boldsymbol{M}). \tag{8.8}$$

In certain materials, such as air, copper or permanent magnets, the reluctivity ν takes constants values. In ferromagnetic materials, however, $\nu = \nu(|\boldsymbol{B}|)$ is a nonlinear function of the magnitude of the magnetic flux density $\boldsymbol{B}$. Details regarding this

function will be provided later on.
It is a common procedure in the modeling of electrical machines to consider the low-frequency case of electromagnetism, see for instance [94], which allows to *neglect displacement currents* compared to the current density:

$$\left|\frac{\partial \boldsymbol{D}}{\partial t}\right| \ll |\boldsymbol{J}|.$$

In this situation, equation (8.4) decouples from the other equations. Further, since the magnetic flux density is divergence free according to (8.3), a *magnetic vector potential* $\boldsymbol{A}$ exists such that

$$\boldsymbol{B} = \operatorname{curl} \boldsymbol{A}, \tag{8.9}$$

where the vector potential $\boldsymbol{A}$ is unique up to a gradient field. Moreover, due to the assumption of a constant rotational speed, all quantities in Maxwell's equations can be assumed as *time-independent*. These assumptions, together with the equations (8.1), (8.2), (8.5) and (8.7) yield the vector potential formulation of the magnetostatic problem:

$$\operatorname{curl}\left[\nu(|\operatorname{curl} \boldsymbol{A}|)\operatorname{curl} \boldsymbol{A}\right] = \boldsymbol{J}_e + \operatorname{curl}\left[\nu \boldsymbol{M}\right]. \tag{8.10}$$

In order to complete the partial differential equation (8.10) by suitable boundary conditions, an underlying bounded Lipschitz domain $D \subset \mathbb{R}^3$ is introduced, which represents the three-dimensional permanent magnet synchronous machine. We assume the boundary of D to consist of two parts Γ_B and Γ_H with $\partial D = \overline{\Gamma}_B \cup \overline{\Gamma}_H$ and $\Gamma_B \cap \Gamma_H = \emptyset$. With n denoting the outer unit normal vector to ∂D, the following boundary conditions are chosen (cf. [111]):

$$\boldsymbol{B} \cdot n = 0, \quad \text{on} \quad \Gamma_B, \tag{8.11}$$

$$\boldsymbol{H} \times n = 0, \quad \text{on} \quad \Gamma_H. \tag{8.12}$$

We mention that condition (8.11) ensures the normal component of the flux density $\boldsymbol{B}$ to vanish on Γ_B and condition (8.12) guarantees the tangential component of the field intensity $\boldsymbol{H}$ to vanish on Γ_H. Moreover, additional properties concerning $\boldsymbol{B}$ and $\boldsymbol{H}$ need to be specified in the presence of different materials, which leads to discontinuities of the reluctivity function. Denoting Γ_I the material interfaces within D, the following interface conditions are imposed (cf. [111])

$$[\![\boldsymbol{B}\cdot n]\!]=0,\quad [\![\boldsymbol{H}\times n]\!]=0\quad \text{on } \Gamma_I, \tag{8.13}$$

where $[\![f]\!]$ represents the jump of a function f across the interface Γ_I.
The last step in the simplification of Maxwell's equation is the reduction of (8.10) to a *two-dimensional* problem. This procedure can be applied under several assumptions and aims at reducing the computational cost within numerical computations by considering only a two-dimensional cross-section of the actual three-dimensional object. The first assumption concerns the underlying domain and requires the geometrical structure

$$D = D^{\mathrm{em}}\times(-l,l),$$

with $l \gg \operatorname{diam}(D^{\mathrm{em}})$, where the superscript in $D^{\mathrm{em}}\subset\mathbb{R}^2$ refers to the physical domain of electromagnetics. Second, the following assumptions regarding the structure of $\boldsymbol{H}, \boldsymbol{M}$ and $\boldsymbol{J}_e$ are made

$$\boldsymbol{J}_e=\begin{pmatrix}0\\0\\J_3(x_1,x_2)\end{pmatrix},\quad \boldsymbol{H}=\begin{pmatrix}H_1(x_1,x_2)\\H_2(x_1,x_2)\\0\end{pmatrix},\quad \boldsymbol{M}=\begin{pmatrix}M_1(x_1,x_2)\\M_2(x_1,x_2)\\0\end{pmatrix}, \tag{8.14}$$

for $(x_1,x_2)\in D^{\mathrm{em}}$. It results immediately from the equations (8.8) and (8.9) that the magnetic vector potential is of the form

$$\boldsymbol{A}=\begin{pmatrix}0\\0\\A_3(x_1,x_2)\end{pmatrix}. \tag{8.15}$$

Introducing the abbreviations $u := A_3$, $M^{\perp} := (-M_2, M_1)^T$ and observing the identities

$$\boldsymbol{B}\cdot n = \nabla u\cdot\tau,\qquad \boldsymbol{H}\times n = \nu(x,|\nabla u|)\nabla u\cdot n,$$

with the tangential unit vector τ, we obtain the *two-dimensional magnetostatic problem*:

$$
\begin{aligned}
-\operatorname{div}\left[\nu(x,|\nabla u|)\nabla u\right] &= J_3 - \operatorname{div}\left[\nu M^{\perp}\right], && \text{in } D^{\mathrm{em}}, && \text{(8.16a)}\\
u &= 0, && \text{on } \Gamma_D, && \text{(8.16b)}\\
\nu(x,|\nabla u|)\nabla u \cdot n &= 0, && \text{on } \Gamma_N, && \text{(8.16c)}\\
[\![u]\!] &= 0, && \text{on } \Gamma_I, && \text{(8.16d)}\\
[\![\nu(x,|\nabla u|)\nabla u \cdot n]\!] &= 0, && \text{on } \Gamma_I. && \text{(8.16e)}
\end{aligned}
$$

It is important to note that a solution of the magnetostatic problem (8.16) describes the magnetic field for one *fixed rotor position* or one fixed point in time, respectively. For a given fixed rotor position, the current density J_3 takes a constant value within each coil and vanishes in the remaining domain. If the rotor position is varied, these values need to be updated in order to account for the sinusoidal shape of the currents. Note that the rotating magnetic field in the stator can be influenced by adapting the current density. Further, the magnetization M of the permanent magnets in the rotor, which is not affected by changes of the rotor position, is constant within each magnet and vanishes otherwise.
We proceed by introducing a subdivision of the two-dimensional domain D^{em} in order to take different materials into account. First, we divide D^{em} into two subdomains $\Omega^{\mathrm{d}} \subset D^{\mathrm{em}}$ and $\Omega^{\mathrm{n}} \subset D^{\mathrm{em}}$ with $\Omega^{\mathrm{d}} \cap \Omega^{\mathrm{n}} = \emptyset$ as follows

$$\overline{D^{\mathrm{em}}} = \overline{\Omega^{\mathrm{d}}} \cup \overline{\Omega^{\mathrm{n}}}.$$

We will consider changes of the material distribution solely within the *design domain* Ω^{d} and keep the material distribution fixed within the *no-design domain* Ω^{n}. Moreover, we will allow only two materials, namely ferromagnetic material and air, within the design domain. Hence, for a given material distribution, we can further split the design domain as follows

$$\Omega^{\mathrm{d}} = \Omega \cup \left(\Omega^{\mathrm{d}} \setminus \Omega\right),$$

where Ω denotes the ferromagnetic part and $\Omega^{\mathrm{d}} \setminus \Omega$ refers to the subset of Ω^{d}, which is occupied by air. We mention that Ω will serve as optimization variable in the optimal design problem, which will be introduced in the subsequent section. Regarding the no-design domain Ω^{n}, where the material distribution is fixed, we allow for more than two different materials. More precisely, we introduce the subdomains $\Omega_{\mathrm{f}}, \Omega_{\mathrm{a}}, \Omega_{\mathrm{c}}, \Omega_{\mathrm{m}} \subset D^{\mathrm{em}}$ with the following relation

$$\overline{D^{\mathrm{em}}} = \overline{\Omega_{\mathrm{f}}} \cup \overline{\Omega_{\mathrm{a}}} \cup \overline{\Omega_{\mathrm{c}}} \cup \overline{\Omega_{\mathrm{m}}}$$

in order to represent the parts of the no-design domain, which are occupied by ferromagnetic material, air, copper and magnets. The geometrical setup along with the material distribution is depicted in Figure 8.2. Note that we consider only a 45°-segment of the cross-section in all numerical computations due to the periodicity of coils and permanent magnets in the machine arrangement, see Figure 8.1.

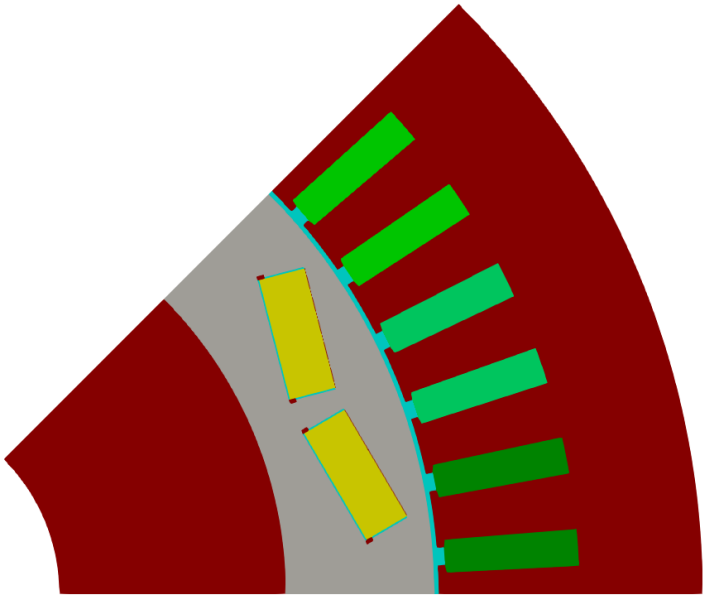

Figure 8.2.: Hold-all domain of the electromagnetic model (45°-segment of PMSM cross-section) with ferromagnetic material in rotor and stator (brown), coils (green), permanent magnets (yellow), the airgap between rotor and stator (blue) and the design domain (gray).

Based on the subdivision of D^{em}, we specify the reluctivity function by

$$\nu_\Omega(x, |\nabla u^{\mathrm{em}}|) := \begin{cases} \hat{\nu}(|\nabla u^{\mathrm{em}}|), & x \in \Omega_{\mathrm{f}} \cup \Omega, \\ \nu_0, & x \in D^{\mathrm{em}} \setminus (\Omega \cup \Omega_{\mathrm{f}}), \end{cases} \tag{8.17}$$

where the subscript in ν_Ω is chosen in order to clarify the dependency on design $\Omega \subset \Omega^{\mathrm{d}}$. The constant ν_0 characterizes the reluctivity in air, copper and the permanent magnets.

Remark 8.1. *Note that the actual reluctivity coefficient of copper and magnet differ from the constant ν_0. However, since the realistic reluctivity constants are close to ν_0, we omit the*

distinction at this point for the sake of readability. In all numerical experiments, which will be presented within this chapter, we employed the realistic constants.

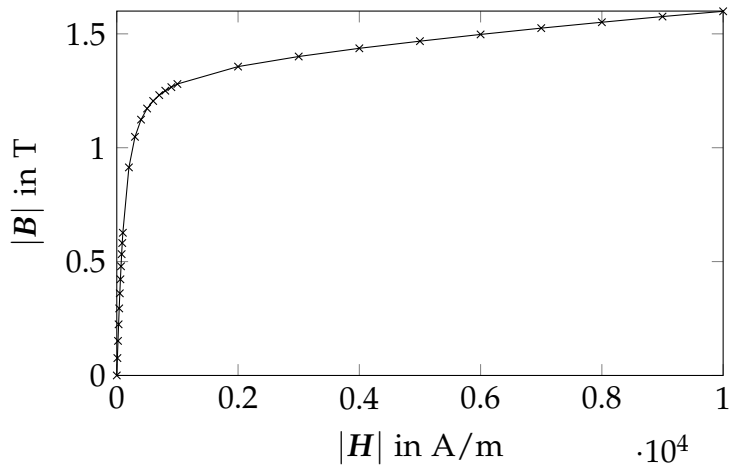

Figure 8.3.: *B*-*H*-curve of ferromagnetic material (Courtesy of Robert Bosch GmbH).

In ferromagnetic material, the reluctivity is characterized by the nonlinear function $\hat{\nu}$. Usually, $\hat{\nu}$ is described via a so-called *B*-*H*-curve, relating the flux density $\boldsymbol{B}$ and the field intensity $\boldsymbol{H}$. According to the constitutive relations of Maxwell's equations, assuming the absence of permanent magnetization, these quantities are connected by the equation

$$\boldsymbol{B} = \mu(|\boldsymbol{H}|)\boldsymbol{H},$$

where μ denotes the magnetic permeability. This relation can be described by a function $f : \mathbb{R}_0^+ \to \mathbb{R}_0^+$, defined by

$$f(|\boldsymbol{H}|) = |\boldsymbol{B}|,$$

which is precisely the previously mentioned *B*-*H*-curve. Note that the relation between the function f and reluctivity $\hat{\nu}$ is given by

$$\hat{\nu}(s) := \frac{f^{-1}(s)}{s}, \tag{8.18}$$

for $s \in \mathbb{R}_0^+$. The specific *B*-*H*-curve, which has been used for the numerical experiments within this chapter, is shown in Figure 8.3. For further details on *B*-*H*-curves, in particular the aspect of interpolation from measured data points, the reader is referred to [112].
Having modeled the behavior of the magnetic field in (8.16), we proceed by defining

the torque of an electrical machine at a fixed rotor position. First, given $r_{\min}, r_{\max} > 0$, an additional domain $\Omega_g := \{x \in \mathbb{R}^2 : r_{\min} < \|x\| < r_{\max}\} \subset \Omega_a$ is introduced, which represents the air gap between rotor and stator. This area is particularly important in the generation of mechanical forces. For a given magnetic field u^{em}, the torque of the electrical machine (cf. [19]) is defined by the functional

$$T(u^{\text{em}}) := \int_0^{2\pi} \int_{r_{\min}}^{r_{\max}} U_P(r,\varphi)^T M_T(r,\varphi) U_P(r,\varphi) dr d\varphi, \tag{8.19}$$

with the abbreviation

$$U_P(r,\varphi) := \nabla u^{\text{em}}(r\cos(\varphi), r\sin(\varphi)),$$

and the matrix M_T defined by

$$M_T(r,\varphi) := r\frac{\nu_0}{r_{\max} - r_{\min}} \begin{pmatrix} \sin(\varphi)\cos(\varphi) & \sin(\varphi)^2 \\ -\cos(\varphi)^2 & -\sin(\varphi)\cos(\varphi) \end{pmatrix},$$

where ν_0 is the reluctivity in air. Furthermore, we define the derivative of T at u^{em} in direction of v as follows:

$$\partial_u T(u^{\text{em}})(v) := 2\int_0^{2\pi} \int_{r_{\min}}^{r_{\max}} U_P(r,\varphi)^T M_T(r,\varphi) V_P(r,\varphi) dr d\varphi, \tag{8.20}$$

where $V_P(r,\varphi) := \nabla v(r\cos(\varphi), r\sin(\varphi))$. Definition (8.19) is based on the observation, that the torque can be computed by a line integral over a circular ring within the air gap. While this quantity is independent of the radius of the circular ring if u^{em} is given exactly, it varies for numerical approximations of u^{em}. For this reason, the torque is averaged over the whole cross sectional area of the air gap, leading to more reliable results in practical simulations. This approach is known as eggshell method, coined by the shape of the air gap. Further details can be found in [19, p. 56].

Structural Mechanics

Having stated and discussed the electromagnetic model for describing the behavior of a permanent magnet synchronous machine, we proceed with the structural mechanical model. Here, the quantity of interest is the mechanical displacement within the electrical machine, again at constant rotational speed. Displacements, and therefore mechanical stresses, occur solely in the rotor area due to centrifugal forces, which are caused by rotation. Since the mechanical behavior at constant speed does not change with the rotor position, all mechanical quantities are independent of the rotor angle.

As in the case of the electromagnetic model, we begin with choosing a two-dimensional *hold-all domain* $D^{\mathrm{sm}} \subset \mathbb{R}^2$, where the superscript refers to the physical domain of structural mechanics. Since mechanical forces are present only within certain parts of the machine, more precisely the rotor area, we require D^{sm} to be entirely contained in the hold-all domain of the electromagnetic model and choose $D^{\mathrm{sm}} \subset D^{\mathrm{em}}$. In addition, we exclude the permanent magnet area from the hold-all domain, since the magnets are not critical with respect to material failure and will be fixed throughout the optimization process. Further, we choose the design domain to be entirely contained in the hold-all domain, which means $\Omega^{\mathrm{d}} \subset D^{\mathrm{sm}}$. The remaining part of D^{sm}, which will not be altered in the course of the optimization, is assumed to be composed of steel only. The hold-all domain of the structural mechanical model is depicted in Figure 8.4.

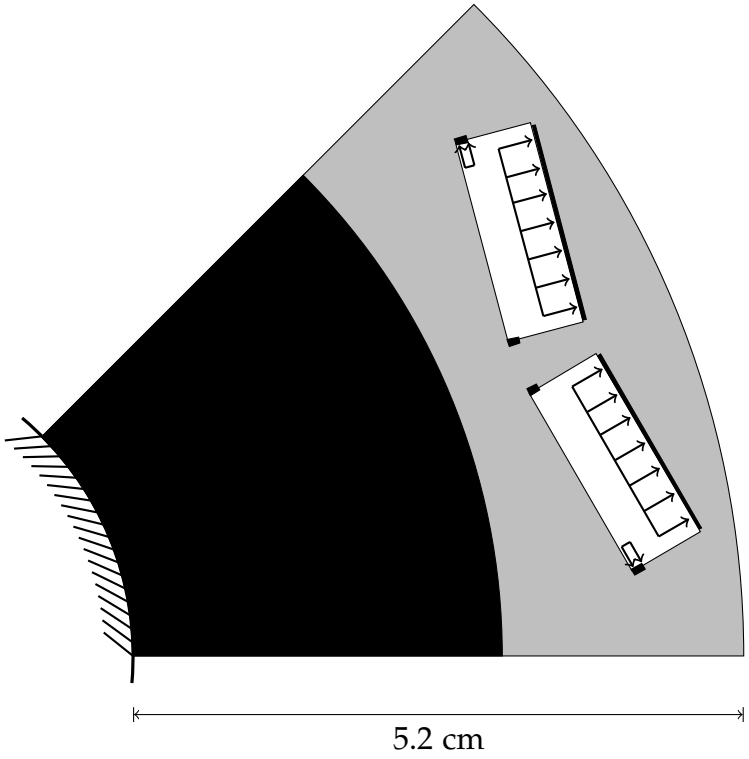

Figure 8.4.: Hold-all domain of the mechanical model (45°-segment of rotor cross-section excluding permanent magnets) with non-design area (black) containing steel only and design area Ω^{d} (gray).

It can be observed in Figure 8.4 that certain areas of D^{sm} are part of the *design domain* Ω^{d}, whereas the material distribution in other parts will not be allowed to change during the optimization process. Let us clarify briefly, why the distribution of design area and non-design area has been chosen in this manner. As it will be explained in more detail below, mechanical boundary forces are acting on the shaft hole, which

is represented by the inner boundary, as well as on the magnet boundaries due to replacement loads. It is precisely the vicinity of these boundaries, which is chosen as non-design area in order to guarantee a physically reasonable setup throughout the optimization process. Clearly, the boundary data needs to be modified if the material distribution of the corresponding boundary is changed, which is an undesired step within the optimization. Note that the small iron bars on the inner and outer sides of the permanent magnets are known as noses in engineering and chosen here as non-design domain in order to obtain realistic results. The practical purpose of the noses is to fix the magnets and ensure that they will stay in place if the machine operates. Furthermore, a rather large non-design domain around the shaft has been chosen in order to keep the computational effort, more precisely the computation of the topological gradient, in a reasonable order of magnitude. We mention that this area has not been chosen arbitrarily, but is based on experience from numerical tests revealing that design alterations do not occur in this region for the chosen criteria from the domains of electromagnetics and structural mechanics.
The plane stress equations of linear elasticity (2.6) are chosen for modeling the structural mechanical behavior of a two-dimensional cross section of the rotor. Note that the *assumption of linearity* is justified, since only small displacements occur in the rotor up to a certain rotational speed. Furthermore, the *plane stress assumption* within the reduction of dimensions is valid, if the axial dimension of the rotor is much smaller than the diameter of a two-dimensional cross section. Although this assumption seems to be false at first sight, it actually holds due to the manufacturing process of the machine. More precisely, the rotor is composed of many thin metal sheets of uniform thickness between 0.2 mm and 0.5 mm, called lamellas in engineering, which are pressed together during the production process. Therefore, the computational cross section can be thought of as one iron sheet, where the plane stress assumption is valid. Note that this manufacturing technique, which is based on stamping the desired rotor shape from a thin metal sheet, is advantageous in terms of design flexibility compared to the standard procedure of milling or casting the entire rotor from a single metal block. In particular, the stamping process enables to manufacture a large class of designs, which may not be manufacturable by standard techniques. We emphasize at this point the strength of topology optimization for finding novel rotor designs, which can actually be manufactured in mass production. Having verified the model assumptions, we state the plane stress equations of linear elasticity again for the sake of convenience and refer to (2.6) for detailed explanations:

$$
\begin{aligned}
-\operatorname{div} \mathbb{C}_\Omega \epsilon(u^{\mathrm{sm}}) &= f_\Omega, && \text{in } D^{\mathrm{sm}}, && (8.21a)\\
u^{\mathrm{sm}} &= u_D, && \text{on } \Gamma_D, && (8.21b)\\
\mathbb{C}_\Omega \epsilon(u^{\mathrm{sm}}) \cdot n &= g, && \text{on } \Gamma_N, && (8.21c)\\
[\![u^{\mathrm{sm}}]\!] &= 0, && \text{on } \Gamma_I, && (8.21d)\\
[\![\mathbb{C}_\Omega \epsilon(u^{\mathrm{sm}}) \cdot n]\!] &= 0, && \text{on } \Gamma_I. && (8.21e)
\end{aligned}
$$

In interface problem (8.21), the unknown $u^{\mathrm{sm}} : D^{\mathrm{sm}} \to \mathbb{R}^2$ represents the displacement field. Further, analogously to Section 2.1, the elasticity tensor depends on the design Ω and is defined by

$$\mathbb{C}_\Omega := \alpha_\Omega \mathbb{C},$$

where the weak phase coefficient function is defined by

$$\alpha_\Omega(x) := \begin{cases} 1, & x \in \Omega \cup \left(D^{\mathrm{sm}} \setminus \Omega^{\mathrm{d}}\right), \\ \alpha, & x \in \Omega^{\mathrm{d}} \setminus \Omega, \end{cases}$$

with $\alpha \ll 1$. For details regarding (8.21), in particular the elasticity tensor $\mathbb{C}$ or the weak phase approach, the reader is referred to Section 2.1.
We proceed by explaining the data in interface problem (8.21), which represent the applied forces in the rotor of the electrical machine in operating mode. Due to the rotation at constant speed $\omega > 0$, *centrifugal forces* $f : D^{\mathrm{sm}} \to \mathbb{R}^2$, defined by

$$f(x) := \rho \omega^2 x, \tag{8.22}$$

are acting as volume forces within the entire rotor domain, where ρ denotes the density of iron. Additionally, *constant displacements* $u_D : \Gamma_D \to \mathbb{R}^2$ are prescribed on the boundary of the shaft hole, see Figure 8.4 for details. This deformation is a consequence of the manufacturing process, where the shaft is pressed into the shaft hole in order to attach both components to each other. Note that a cooling of the shaft is performed in practice prior to this assembly step in order to decrease the shaft size. Once the shaft has revolved to its normal state, this step results in a safe assembly of both components, which is particularly important with regards to high speed applications. On the remaining part of the boundary, which is Γ_N, *Neumann conditions* are imposed. Taking the excluded permanent magnets into account, $g : \Gamma_N \to \mathbb{R}^2$ contributes as replacement load with additional centrifugal forces on the exterior magnet cavities and

vanishes on the remaining boundary part.
Having modeled the behavior of the mechanical displacements in the rotor, we proceed by defining a suitable *failure criterion*. The purpose of a failure criterion, which is a function of the stress tensor, is to quantify material failure and ensure mechanical stability of the machine in the design process. We refer to Section 2.3 for further details on this aspect. Throughout this chapter, the maximum principal stress criterion, also known as Rankine criterion (cf. [73]), is chosen for quantifying material failure. The first principal stress $S_{\mathrm{p}} : \mathbb{R}^{2\times 2} \to \mathbb{R}$, which is the first eigenvalue of a given stress tensor $\sigma \in \mathbb{R}^{2\times 2}$, is defined as follows:

$$S_{\mathrm{p}}(\sigma) := \frac{\sigma_{11}+\sigma_{22}}{2} + \sqrt{\left(\frac{\sigma_{11}-\sigma_{22}}{2}\right)^2 + \sigma_{12}^2}. \tag{8.23}$$

In the following section, the first principal stress will serve as the basis for defining the local stress constraints in the optimal design problem.

8.3. Optimal Design Problem

In the previous section, the electromagnetic torque and the mechanical principal stress for a permanent magnet synchronous machine have been derived based on physical models. The aim of this section is the formulation of an optimal design problem, which relies on these quantities. In a first step, the partial different equations will be analyzed with regards to existence and uniqueness. Based on these considerations, solution operators can be defined, which allows the reduction of the objectives. As a result, an optimal design problem is obtained, which fits into framework of Section 2.3. In particular, the structure of problem (2.25) is obtained, enabling the application of the developed solution methods. Finally, the existence of local minima of the optimal design problem is examined.

Electromagnetics

We begin by analyzing the weak formulation of the magnetostatic problem (8.16). A function $u^{\mathrm{em}} \in H_0^1(D^{\mathrm{em}})$ is a weak solution of the partial different equation (8.16), if it solves

$$\int_{D^{\mathrm{em}}} \mathcal{A}_\Omega(x, \nabla u^{\mathrm{em}}) \cdot \nabla v dx = \langle F, v\rangle \qquad \forall v \in H_0^1(D^{\mathrm{em}}), \tag{8.24}$$

where

$$\mathcal{A}_\Omega(x, \nabla u^{\mathrm{em}}) := \nu_\Omega(x, |\nabla u^{\mathrm{em}}|)\nabla u^{\mathrm{em}}, \tag{8.25}$$

and the right hand side is defined by

$$\langle F, v\rangle := \int_{D^{\mathrm{em}}} J_3 v + \nu_{\mathrm{m}} M^{\perp} \cdot \nabla v dx.$$

Further, for

$$a(y) := \hat{\nu}(|y|)y, \quad y \in \mathbb{R}^2,$$

with its Jacobian

$$\partial_u a(y) := \begin{cases} \hat{\nu}(|y|)I + \frac{\hat{\nu}'(|y|)}{|y|} y \otimes y, & y \neq (0,0)^T, \\ \hat{\nu}(|y|)I, & y = (0,0)^T, \end{cases} \tag{8.26}$$

we define the derivative of $\mathcal{A}_\Omega$ as follows:

$$\partial_u \mathcal{A}_\Omega(x, \nabla u^{\mathrm{em}}) := \begin{cases} \partial_u a(\nabla u^{\mathrm{em}}), & z \in \Omega, \\ \nu_0 I, & z \in \Omega^{\mathrm{d}} \setminus \bar{\Omega}. \end{cases} \tag{8.27}$$

The following theorem ensures the existence of a unique solution of (8.24) under certain conditions on the reluctivity function in ferromagnetic material.

Theorem 8.1. *Assume that there exist constants $\underline{\nu}, \overline{\nu} > 0$, such that the reluctivity function $\hat{\nu} : \mathbb{R}_0^+ \to \mathbb{R}^+$, defined in (8.17), satisfies the following conditions:*

$$(\hat{\nu}(s)s - \hat{\nu}(t)t)(s-t) \geq \underline{\nu}(s-t)^2, \qquad \forall s, t \in \mathbb{R}_0^+, \tag{8.28}$$

$$|\hat{\nu}(s)s - \hat{\nu}(t)t| \leq \overline{\nu}|s-t|, \qquad \forall s, t \in \mathbb{R}_0^+. \tag{8.29}$$

Then, there exist a unique solution $u^{em} \in H_0^1(D^{em})$ of problem (8.24) and there exists a constant $c > 0$ such that the following estimate holds:

$$\|u^{em}\|_{H_0^1(D^{em})} \leq c \|F\|_{H^{-1}(D^{em})}. \tag{8.30}$$

Proof. A detailed proof is given in [110], which is sketched briefly in the following. Conditions (8.28) and (8.29) are precisely the definitions of strong monotonicity and Lipschitz continuity of the mapping $s \mapsto \hat{\nu}(s)s$. Consequently, the operator $A_\Omega : H_0^1(D^{\mathrm{em}}) \to (H_0^1(D^{\mathrm{em}}))^*$, which is defined by $\langle A_\Omega w, v\rangle := \int_{D^{\mathrm{em}}} \mathcal{A}_\Omega(x, \nabla w) \cdot \nabla v dx$, is strongly monotone and Lipschitz continuous, see [110]. The theorem of Zarantonello,

which is a nonlinear version of the Lax-Milgram lemma, ensures the existence of a unique solution as well as estimate (8.30). A proof of the theorem of Zarantonello can be found in [140]. □

Remark 8.2. *Conditions (8.28) and (8.29) can be guaranteed by imposing conditions on the B-H-curve f, which is particularly convenient for practical applications. The requirements regarding B-H-curve f can be found in [112].*

Analogously to (2.22) in the elasticity case, Theorem 8.1 allows to define a solution operator

$$S^{\mathrm{em}} : \mathcal{O} \to H_0^1(D^{\mathrm{em}}) \tag{8.31}$$

$$\Omega \mapsto u_\Omega^{\mathrm{em}}, \tag{8.32}$$

which associates the unique solution u_Ω^{em} to a design $\Omega \in \mathcal{O}$. Consequently, we can reduce the torque functional $T : H_0^1(D^{\mathrm{em}}) \to \mathbb{R}$, which has been defined in (8.19), as follows:

$$\mathcal{T}(\Omega) := T(u_\Omega^{\mathrm{em}}). \tag{8.33}$$

In order to introduce the average torque for one rotor rotation of the electrical machine, a finite set of angles

$$\{\varphi_1, ..., \varphi_N\} \subset [0, 2\pi) \tag{8.34}$$

is introduced, representing the rotor positions. Further, the torque at a given angle $\varphi \in [0, 2\pi)$ is defined by

$$\mathcal{T}_\varphi(\Omega) := T(u_{\Omega,\varphi}^{\mathrm{em}}), \tag{8.35}$$

where $u_{\Omega,\varphi}^{\mathrm{em}} \in H_0^1(D^{\mathrm{em}})$ denotes the unique solution of (8.24) associated to design $\Omega \in \mathcal{O}$ and rotor angle φ. Clearly, the data in problem (8.24) needs to be modified in order to account for changes in the rotor angle. The values of the reluctivity ν_Ω and the magnetization M remains unchanged, solely the spatial rotation needs to be taken into account. In the case of the current density J_3, the values need to be modified in order to obtain a sinusoidal current shape in the coils. Based on the set of angles (8.34) and the reduced functional (8.35), the average torque for design $\Omega \in \mathcal{O}$ is defined by

$$\mathcal{J}(\Omega) := -\frac{1}{N}\sum_{i=1}^{N} \mathcal{T}_{\varphi_i}(\Omega), \tag{8.36}$$

representing an approximation of the average torque for one continuous rotation. Note the negative sign in (8.36), which has been added in order to account for the fact that the torque is intended to be maximized in the optimization.

Remark 8.3. *The average torque has been chosen as objective functional for the optimal control problem, as it aims at maximizing the torque of the permanent magnet synchronous machine for a given amount of electrical energy. However, we could have chosen a different objective functional without any impact on the theory, which will be introduced subsequently. An objective, which is related to the smoothness of the rotation, can be found in [65].*

Structural Mechanics

The analysis of elasticity problem (8.21) has already been treated in Section 2.2. The existence of a unique solution $u^{\mathrm{sm}} \in H^1(D^{\mathrm{sm}}, \mathbb{R}^2)$ of the weak formulation (2.10) is ensured by Theorem 2.1, where the weak phase coefficient needs to fulfill the condition $\alpha > 0$. Consequently, we can define a solution operator

$$\begin{aligned} S^{\mathrm{sm}} : \mathcal{O} &\to H^1(D^{\mathrm{sm}}, \mathbb{R}^2) \\ \Omega &\mapsto u^{\mathrm{sm}}_{\Omega}, \end{aligned}$$

which assigns a design $\Omega \in \mathcal{O}$ to the associated displacement. As for the generic failure function (2.24), a reduced principal stress field $\mathcal{S}_{\mathrm{p}}[\Omega] : D^{\mathrm{sm}} \to \mathbb{R}$ is defined by

$$\mathcal{S}_{\mathrm{p}}[\Omega](x) := S_{\mathrm{p}}(\sigma(u^{\mathrm{sm}}_{\Omega}(x))), \tag{8.37}$$

where the first principal stress has been defined in (8.23).

Problem Formulation

Having defined the average torque functional (8.36) and the principal stress field (8.37) in reduced form, we are in the position to formulate the optimal design problem. Given a stress limit $\bar{\sigma} > 0$ and the set of feasible designs

$$\mathcal{O} := \{\Omega \subset \Omega^{\mathrm{d}} : \Omega \text{ open with uniformly Lipschitz continuous boundary}\}, \tag{8.38}$$

the optimal design problem reads as follows:

$$\min_{\Omega \in \mathcal{O}} \quad \mathcal{J}(\Omega) \tag{8.39a}$$

$$\text{s.t.} \quad \mathcal{S}_p[\Omega] \leq \bar{\sigma} \text{ a.e. in } \Omega. \tag{8.39b}$$

Comparing problem (8.39) with the generic stress-constrained optimal design problem (2.25), we can observe that the constraint (8.39b) does not match with the constraint structure in the generic problem (2.25). More precisely, the first principal stress (8.23) is not of quadratic structure as it is the case for a failure function (2.17). Therefore, in order to obtain a problem, which fits into the generic framework, we will characterize the constraint in (8.39) equivalently. First, we observe for $\sigma \in \mathbb{R}^{2\times 2}$ that the inequality

$$S_{\mathrm{p}}(\sigma) \leq \bar{\sigma}, \tag{8.40}$$

where S_{p} is defined in (8.23), can be expressed equivalently by means of the two inequalities

$$\left(\frac{\sigma_{11} - \sigma_{22}}{2}\right)^2 + \sigma_{12}^2 \leq \left(\bar{\sigma} - \frac{\sigma_{11} + \sigma_{22}}{2}\right)^2, \tag{8.41}$$

$$\frac{\sigma_{11} + \sigma_{22}}{2} \leq \bar{\sigma}, \tag{8.42}$$

and define the functions

$$f^1(\sigma) := \frac{1}{2}\mathbb{D}\sigma : \sigma + \mathrm{tr}[\sigma], \qquad f^2(\sigma) := \frac{1}{2}\mathrm{tr}[\sigma],$$

with $\mathbb{D} := \mathbb{I} - \mathrm{I} \otimes \mathrm{I}$. Hence, analogously to the definition of failure function (2.16), the inequalities (8.41) and (8.42) can be expressed in the form

$$F^1_{\bar{\sigma}}(\sigma) \leq 1,$$
$$F^2_{\bar{\sigma}}(\sigma) \leq 1,$$

with $F^i_{\bar{\sigma}}(\sigma) := f^i(\bar{\sigma}^{-1}\sigma)$ for $i = 1, 2$. Finally, by setting $\mathcal{F}^i_{\bar{\sigma}}[\Omega] := F^i_{\bar{\sigma}}(\sigma(u^{\mathrm{sm}}_\Omega))$, the optimal control problem (8.39) can be formulated equivalently as follows

$$\min_{\Omega \in \mathcal{O}} \quad \mathcal{J}(\Omega) \tag{8.43a}$$

$$\text{s.t.} \quad \mathcal{F}^1_{\bar{\sigma}}[\Omega] \leq 1 \text{ a.e. in } \Omega, \tag{8.43b}$$

$$\mathcal{F}^2_{\bar{\sigma}}[\Omega] \leq 1 \text{ a.e. in } \Omega, \tag{8.43c}$$

where the structure of the constraints matches with the failure function (2.16). Analogously to Section 3.2, the stress constraints (8.43b) and (8.43c) are extended to the entire domain and a penalty approach is performed. Therefore, we obtain the regularized optimal design problem

$$\min_{\Omega \in \mathcal{O}} \quad \mathcal{J}_\gamma(\Omega) := \mathcal{J}(\Omega) + \gamma \mathcal{P}_1(\Omega) + \gamma \mathcal{P}_2(\Omega), \tag{8.44}$$

where the penalty terms are defined by

$$\mathcal{P}_i(\Omega) := \int_{D^{\text{sm}}} \alpha_\Omega \Phi_p \left(\beta^\gamma_\Omega \mathcal{F}^i_{\bar{\sigma}}[\Omega] \right) dx, \tag{8.45}$$

for $i = 1, 2$.

Existence of Local Minima

Before we proceed by deriving the topological gradient of the regularized problem (8.44), we need to ensure the existence of local minima. The framework for this task is provided by Theorem 3.3, where continuity and boundedness from below has been assumed for the generic functional $\mathcal{J}$. Within this chapter, the objective is the reduced torque functional

$$\mathcal{J}(\Omega) = -\frac{1}{N} \sum_{i=1}^{N} \mathcal{T}_{\varphi_i}(\Omega) = -\frac{1}{N} \sum_{i=1}^{N} T(u^{\text{em}}_{\Omega,\varphi_i}),$$

see (8.36). It can be observed immediately that functional $T : H^1_0(D^{\text{em}}) \to \mathbb{R}$, defined by (8.19), is continuous. The essential question at this point is therefore, whether the solution $u^{\text{em}}_{\Omega,\varphi}$ of the magnetostatic problem is continuous in $\Omega \in \mathcal{O}$. Clearly, this property is equivalent to the continuity of the solution operator of the magnetostatic problem $S^{\text{em}} : \mathcal{O} \to H^1_0(D^{\text{em}})$, defined by (8.31). The following proposition ensures the continuity of operator S^{em} under mild assumptions concerning the regularity of solutions of the magnetostatic problem.

Proposition 8.1. *Assume that there exists $\epsilon > 0$, such that the operator $S^{em} : \mathcal{O} \to H_0^1(D^{em})$, defined by (8.31), satisfies*

$$\|S^{em}(\Omega)\|_{H^{1+\epsilon}(D^{em})\cap H_0^1(D^{em})} \leq c, \qquad \forall\, \Omega \in \mathcal{O},$$

where the constant $c > 0$ depends only on the domain D^{em} and the data of problem (8.24). Then, the solution operator S^{em} is continuous.

Proof. A proof is given in Proposition 3.3 in [69]. □

Before we proceed, the global regularity assumption $u_\Omega^{\mathrm{em}} \in H^{1+\epsilon}(D^{\mathrm{em}})$ for $\epsilon > 0$ in Proposition 8.1 is discussed. It is known that the regularity of solutions of interface problems is determined by the right hand side, the boundary of the underlying domain and the shape of the subdomains with respect to the different material phases, see [93] or [113]. Since the data in problem (8.24) as well as the boundary of D^{em} are sufficiently smooth, the limiting factor in the given case is clearly the shape of the subdomains or, in other words, the smoothness of the interface. In [113], the global $H^{1+\epsilon}$-regularity is shown under certain assumptions regarding the interface. Hence, we mention at this point that the required conditions regarding the interface might be a limitation in certain situations.

Remark 8.4. *As in Section 3.4 on the existence of solutions for the generic stress-constrained optimal design problem, convergence in $\mathcal{O}$ is to be understood in the sense of Hausdorff or in the sense of characteristic functions.*

The continuity of T together with Proposition 8.1 ensures the continuity of objective functional $\mathcal{J}$. Moreover, the boundedness from below of objective $\mathcal{J}$ follows immediately from the estimate

$$\|S^{\mathrm{em}}(\Omega)\|_{H_0^1(D^{\mathrm{em}})} = \|u_\Omega^{\mathrm{em}}\|_{H_0^1(D^{\mathrm{em}})} \leq c\,\|F\|_{H^{-1}(D^{\mathrm{em}})}, \qquad \forall\, \Omega \in \mathcal{O},$$

see (8.30).

Remark 8.5. *Note that functional F represents the right hand side of the magnetostatic equation (8.24) and contains the current density as well as the magnetization. The interpretation of estimate (8.30) with respect to $\mathcal{J}$ is therefore simply that the amount of torque, i.e. mechanical energy, is determined by the amount of electrical energy, which is provided to the machine.*

The following theorem addresses the existence of solutions for the regularized optimal design problem (8.44).

Theorem 8.2. *Let the feasible set $\mathcal{O}$ be defined as in (8.38) and consider the functional $\mathcal{J} : \mathcal{O} \to \mathbb{R}$, defined by (8.36). Further, let $\mathcal{P}_1$ and $\mathcal{P}_2$ be defined as in (8.45). Then, for a penalty parameter $\gamma \geq 0$, the optimal design problem (8.44)*

$$\min_{\Omega \in \mathcal{O}} \quad \mathcal{J}_\gamma(\Omega) = \mathcal{J}(\Omega) + \gamma \mathcal{P}_1(\Omega) + \gamma \mathcal{P}_2(\Omega)$$

admits at least one solution.

Proof. Lemma 3.1 ensures the boundedness from below as well as the lower semicontinuity of the penalty terms $\mathcal{P}_1$ and $\mathcal{P}_2$. In Proposition 8.1, the continuity of the control-to-state operator (8.31) has been shown. Together with the continuity of the torque functional T, which has been defined in (8.19), the continuity of $\mathcal{J}$ follows. Since a continuous functional is lower semicontinuous by definition and due to the boundedness from below of objective functional $\mathcal{J}$, the assumptions of Theorem 3.3 are satisfied and we obtain the existence of a local minimum for problem (8.44). □

8.4. Topological Gradient

In the previous section, the regularized optimal design problem (8.44) has been formulated. Aiming at its numerical solution, the topological gradient of the objective functional $\mathcal{J}_\gamma$ will be derived in this section. We will derive the topological gradient according to definition (4.1) with $f(\rho) = \rho^2$. In a first step, we observe that the equality

$$D_T \mathcal{J}_\gamma[\Omega] = D_T \mathcal{J}[\Omega] + \gamma D_T \mathcal{P}_1[\Omega] + \gamma D_T \mathcal{P}_2[\Omega] \tag{8.46}$$

holds due to linearity of the corresponding differential operator. The different terms in (8.46) will be treated separately in the following.

Electromagnetics

The topological gradient of the average torque functional

$$D_T \mathcal{J}[\Omega] = -\frac{1}{N} \sum_{i=1}^{N} D_T \mathcal{T}_{\varphi_i}[\Omega]$$

will be treated first. For the sake of conciseness, we will derive the topological gradient for a fixed rotor position and drop the angle in the following. Hence, we are interested in a formula for the topological gradient

$$D_T\mathcal{T}[\Omega] = D_T\left[T(S^{\mathrm{em}}(\Omega))\right], \tag{8.47}$$

where the functional T has been defined in (8.19) and the solution operator S^{em} is given in (8.31).

Remark 8.6. *In contrast to the solution operator S^{sm} of the elasticity equation (2.10), S^{em} comprises the nonlinearity of the magnetostatic equation (8.24). This leads to a challenging derivation of the topological gradient of (8.47), which is reflected in its complex mathematical structure.*

The topological gradient for functionals of type (8.47) has been derived in [70], as well as in [71] for the three-dimensional case. Hence, we will solely state the results in this thesis and refer to [70] and [71] for the derivation and further details. Before the topological gradient is stated, several objects need to be introduced.
The *adjoint state* $p^{\mathrm{em}} \in H_0^1(D^{\mathrm{em}})$ to functional (8.33) is the solution of the equation

$$\int_{D^{\mathrm{em}}} \partial_u \mathcal{A}_\Omega(x, \nabla u_\Omega^{\mathrm{em}}) \nabla\varphi \cdot \nabla p^{\mathrm{em}} dx = -\partial_u T(u^{\mathrm{em}})(\varphi), \quad \forall \varphi \in H_0^1(D^{\mathrm{em}}), \tag{8.48}$$

where the derivatives of $\mathcal{A}_\Omega$ and T have been defined in (8.27) and (8.20), respectively, and $u_\Omega^{\mathrm{em}} \in H_0^1(D^{\mathrm{em}})$ is the unique solution of problem (8.24). The existence and uniqueness of a solution of problem (8.48) can be proven in a standard fashion by applying the Lax-Milgram Theorem. For a given design $\Omega \in \mathcal{O}$, we will denote the unique solution of the adjoint equation (8.48) by $p_\Omega^{\mathrm{em}} \in H_0^1(D^{\mathrm{em}})$. At this point, the abbreviations

$$U := \nabla u_\Omega^{\mathrm{em}}(z), \qquad P := \nabla p_\Omega^{\mathrm{em}}(z) \tag{8.49}$$

are set for convenience. Further, we introduce the functions

$$a_0(y) := \begin{cases} \hat{\nu}(|y|)y, & z \in \Omega, \\ \nu_0 y, & z \in \Omega^{\mathrm{d}} \setminus \bar{\Omega}, \end{cases} \qquad a_1(y) := \begin{cases} \nu_0 y, & z \in \Omega, \\ \hat{\nu}(|y|)y, & z \in \Omega^{\mathrm{d}} \setminus \bar{\Omega}, \end{cases}$$

depending on the location of $z \in \Omega^{\mathrm{d}} \setminus \partial\Omega$, which represents the point of topological perturbation. We will need a_0 and a_1 in order to distinguish between the phases Ω and $\Omega^{\mathrm{d}} \setminus \Omega$ in the topological gradient. Moreover, the operator

$$\mathcal{A}_\omega(x, y) := \begin{cases} a_1(y), & x \in \omega, \\ a_0(y), & x \in \mathbb{R}^2 \setminus \omega, \end{cases} \tag{8.50}$$

on the entire space $\mathbb{R}^2$ is defined. Based on the previous definitions, the *variation of the direct state* $H \in BL(\mathbb{R}^2)$ is introduced as the solution of

$$\int_{\mathbb{R}^2} [\mathcal{A}_\omega(x, \nabla H + U) - \mathcal{A}_\omega(x, U)] \cdot \nabla \varphi dx = -\int_\omega [a_1(U) - a_0(U)] \cdot \nabla \varphi dx, \tag{8.51}$$

$\forall \varphi \in BL(\mathbb{R}^2)$, where $BL(\mathbb{R}^2)$ denotes the Beppo-Levi space, see [70]. Similarly, we introduce the *variation of the adjoint state* $K \in BL(\mathbb{R}^2)$ as the solution of the following equation:

$$\int_{\mathbb{R}^2} \partial_u \mathcal{A}_\omega(x, U) \nabla \varphi \cdot \nabla K dx = -\int_\omega [\partial_u a_1(U) - \partial_u a_0(U)] \nabla \varphi \cdot P dx, \tag{8.52}$$

$\forall \varphi \in BL(\mathbb{R}^2)$, where the derivatives $\partial_u \mathcal{A}_\omega$ and $\partial_u a_1, \partial_u a_2$ are defined analogously to (8.27) and (8.26), respectively. Note that both (8.51) and (8.52) possess a unique solution, which has been proven in [70]. We are now in the position to give a formula for the topological gradient (8.47), which requires certain regularity assumptions of the direct and adjoint state as well as additional assumptions concerning the reluctivity function. The topological gradient (8.47) is presented in the following theorem.

Theorem 8.3. *Let a design $\Omega \in \mathcal{O}$, an open and bounded set $\omega \subset \mathbb{R}^2$ containing the origin and a point of perturbation $z \in \Omega^d \setminus \partial\Omega$ be given. Assume that the reluctivity function $\hat{\nu}$, defined in (8.17), satisfies condition (8.28) and (8.29). Moreover, assume that $\hat{\nu} \in C^2(\mathbb{R}_0^+)$, $\hat{\nu}'(0) = 0$ and that there is a constant $c > 0$ such that $\hat{\nu}'(s) \leq c$ and $\hat{\nu}'' \leq c$ for all $s \in \mathbb{R}_0^+$. Further, let $u_\Omega^{em} \in H_0^1(D^{em})$ denote the solution of problem (8.24) and let $p_\Omega^{em} \in H_0^1(D^{em})$ denote the solution of the adjoint problem (8.48) and let $U, P \in \mathbb{R}^{2\times 2}$ be defined as in (8.49). Assume that $u_\Omega^{em} \in C^{1,\alpha}(\overline{B_\delta(z)})$, $p_\Omega^{em} \in C^1(\overline{B_\delta(z)})$ for some $\delta > 0$ and $0 < \alpha < 1$ and $\nabla p_\Omega^{em} \in L^\infty(D^{em}, \mathbb{R}^2)$. Then the topological gradient of objective functional (8.47) at design Ω and point of perturbation z reads as follows*

$$D_T \mathcal{T}[\Omega](z) = [a_1(U) - a_0(U)] \cdot \int_\omega P + \nabla K dx \tag{8.53}$$

$$+ \int_{\mathbb{R}^2} [\mathcal{A}_\omega(x, \nabla H + U) - \mathcal{A}_\omega(x, U) - \partial_u \mathcal{A}_\omega(x, U)(\nabla H)] \cdot (P + \nabla K) dx, \tag{8.54}$$

where $H \in BL(\mathbb{R}^2)$ and $K \in BL(\mathbb{R}^2)$ denote the solutions to (8.51) and (8.52), respectively.

Proof. A proof can be found in [70]. □

Before we proceed, the *assumptions* in Theorem 8.3 are discussed. We recall that the reluctivity $\hat{\nu}$ in ferromagnetic material is defined via the B-H-curve, see (8.18), which is based on measurements in practical applications. The B-H-curve, which has been used in this thesis, has been obtained by a suitable interproximation of the measured data points, see [112] for further details on the interproximation technique. As a result, we obtain $\hat{\nu} \in C^2(\mathbb{R}_0^+)$ with $\hat{\nu}'(s) \leq c$ and $\hat{\nu}'' \leq c$ for all $s \in \mathbb{R}_0^+$. Additionally, the conditions (8.28) and (8.29) have been verified.
Furthermore, it can be observed that the right hand side of the magnetostatic problem (8.24) is only supported in the coil and magnet areas and vanishes in the remaining part of the hold-all domain. Consequently, the right hand side is a smooth function on the design domain, which implies $u_\Omega^{\mathrm{em}} \in C^{1,\alpha}(\overline{B_\delta(z)})$ for $\delta > 0$ and $0 < \alpha < 1$, see the monograph [101, Theorem 3.20]. Similarly, we observe that the torque functional (8.19) is defined as an integral over the air gap, which is not contained in the design domain. Hence, the right hand side of the adjoint equation (8.48) is smooth within the design domain, which implies $p_\Omega^{\mathrm{em}} \in C^1(\overline{B_\delta(z)})$ for some $\delta > 0$ by elliptic regularity.

Remark 8.7. *The objective functional T, which is related to $\mathcal{T}$ via $\mathcal{T} = T(S^{em})$, is defined as an integral over the air gap, see (8.19). The topological gradient (8.53), (8.54) has been stated under the assumption that the air gap is not part of the design domain. If, however, the objective functional is defined as an integral over the design domain, the term $\int_{\mathbb{R}^2} |\nabla H|^2 dx$ needs to be added to the topological gradient, see [70].*

We will focus on the term (8.53) of the topological gradient in the following, aiming at obtaining an analytical formula for the practical implementation. It can be observed that the variation of the adjoint state K, which is the solution to (8.52), depends linearly on P. This observation can be exploited to show the existence of a so-called *polarization matrix* $\mathcal{M} = \mathcal{M}(\omega, \partial_u a_0(U), \partial_u a_1(U))$ with the property

$$[a_1(U) - a_0(U)] \cdot \int_\omega P + \nabla K dx = U^T \mathcal{M} P, \tag{8.55}$$

which has been proven in [65]. The following proposition shows that an analytical formula for matrix $\mathcal{M}$ is obtained, if a circular shape of ω is assumed. Note that ω has been allowed to be an open and bounded set of arbitrary shape up to this point.

Proposition 8.2. *Denote $\lambda_1 := \hat{\nu}(|U|)$, $\lambda_2 := \hat{\nu}(|U|) + \hat{\nu}'(|U|)|U|$ and let the rotation matrix $R \in \mathbb{R}^{2\times 2}$ around the angle between U and the x-axis be defined via the relation*

$$U = R \begin{pmatrix} |U| \\ 0 \end{pmatrix}.$$

If $\omega = B_1(0)$, the polarization matrix $\mathcal{M} \in \mathbb{R}^{2\times 2}$, defined by the equality (8.55), can be expressed as follows:

$$\mathcal{M} := \begin{cases} \pi(\nu_0 - \lambda_1) R \begin{pmatrix} \frac{\lambda_2+\sqrt{\lambda_1\lambda_2}}{\nu_0+\sqrt{\lambda_1\lambda_2}} & 0 \\ 0 & \frac{\lambda_1+\sqrt{\lambda_1\lambda_2}}{\nu_0+\sqrt{\lambda_1\lambda_2}} \end{pmatrix} R^T, & \text{if } z \in \Omega, \\ 2\pi\nu_0 R \begin{pmatrix} \frac{\lambda_1-\nu_0}{\lambda_2+\nu_0} & 0 \\ 0 & \frac{\lambda_1-\nu_0}{\lambda_1+\nu_0} \end{pmatrix} R^T, & \text{if } z \in \Omega^d \setminus \bar{\Omega}. \end{cases}$$

Proof. A proof can be found in [65], see Proposition 4.72 and Proposition 4.75. □

Furthermore, we remark that a strategy for an efficient numerical implementation of the term (8.54) has been developed in [65] and [70].

Structural Mechanics

Having treated the torque functional, we proceed with the derivation of the topological gradient of the penalty terms $\mathcal{P}_1$ and $\mathcal{P}_2$, defined in (8.45), by applying Theorem 4.1. As in the previous chapter, we denote the penalty terms for $i \in \{1, 2\}$ by

$$\mathcal{P}_i(\Omega) = P^i_\Omega(\epsilon(u^{\mathrm{sm}}_\Omega)) = \int_{D^{\mathrm{sm}}} j^i_\Omega(\epsilon(u^{\mathrm{sm}}_\Omega))dx,$$

with density function $j^i_\Omega = j^{\mathrm{mat}}_i \chi_\Omega + j^{\mathrm{air}}_i \chi_{D^{\mathrm{sm}}\setminus\Omega}$ as in (4.11) and

$$j^{\mathrm{mat}}_i(d) := \Phi_p(F^i_{\tilde{\sigma}}(\mathbb{C}d)), \qquad j^{\mathrm{air}}_i(d) := \alpha\Phi_p(h(\gamma)^{-1}F^i_{\tilde{\sigma}}(\mathbb{C}d)),$$

for $d \in \mathbb{R}^{2\times 2}$. Further, the *adjoint state* $p^{\mathrm{sm}}_\Omega \in \mathcal{V}$ for the penalty term (8.45) to the state $u^{\mathrm{sm}}_\Omega \in H^1(D^{\mathrm{sm}}, \mathbb{R}^2)$ is the unique solution of the following problem:

$$a_\Omega(v, p^{\mathrm{sm}}_\Omega) = \partial_e P^i_\Omega(\epsilon(u^{\mathrm{sm}}_\Omega))(\epsilon(v)) \quad \forall v \in \mathcal{V}, \tag{8.56}$$

which is the adjoint equation (4.44) for the given specific setting. Note that the bilinear form $a_\Omega(\cdot,\cdot)$ has been defined in (2.8).
Before the topological gradient is stated for a point of perturbation $z \in \Omega^{\mathrm{d}} \setminus \partial\Omega$, the assumptions of Theorem 4.1 are verified. Since the centrifugal forces (8.22) are smooth in the entire rotor domain, the state u^{sm}_Ω is smooth in a neighborhood of the point of perturbation z. Moreover, due to the choice of penalty function Φ_p, the required regularity of the adjoint state p^{sm}_Ω in a neighborhood of z follows as well. Therefore, the application of Theorem 4.1 yields

$$D_T\mathcal{P}_i[\Omega](z) = \pi j_\delta(\epsilon(u_\Omega^{\mathrm{sm}}(z))) - \mathbb{E}\epsilon(u_\Omega^{\mathrm{sm}}(z)) : \epsilon(p_\Omega^{\mathrm{sm}}(z)) + \pi\nabla j_\delta(\epsilon(u_\Omega^{\mathrm{sm}}(z))) : \epsilon(v_X(0)) + \int_{\mathbb{R}^2\setminus\omega} \mathcal{G}^0(z, \epsilon(v_X))dx + \int_\omega \mathcal{G}^1(z, \epsilon(v_X))dx,$$

where j_δ has been defined in (4.23), $\mathbb{E}$ is the elastic moment tensor (4.36), v_X denotes the solution of problem (4.31) and $\mathcal{G}^0, \mathcal{G}^1$ are defined as in (4.46). The computation of the elastic moment tensor $\mathbb{E}$ and the function $\epsilon(v_X)$ is performed analogously to Section 7.2.

8.5. Numerical Experiments

The aim of this section is the numerical solution of the regularized problem (8.44) for the case of an electrical machine. A major point of interest is the effect of the chosen regularization, where the pointwise stress constraints are extended to the entire computational domain, on the level set-based optimization scheme. While, in the previous chapter, this approach showed excellent performance for the solution of the minimum volume problem and the L-beam geometry, it is unclear at this point how the algorithm performs in the case of stress-constrained torque maximization for an electrical machine. Moreover, the effect of two different initial designs, visualized in Figure 8.5, will be examined by numerical experiments.

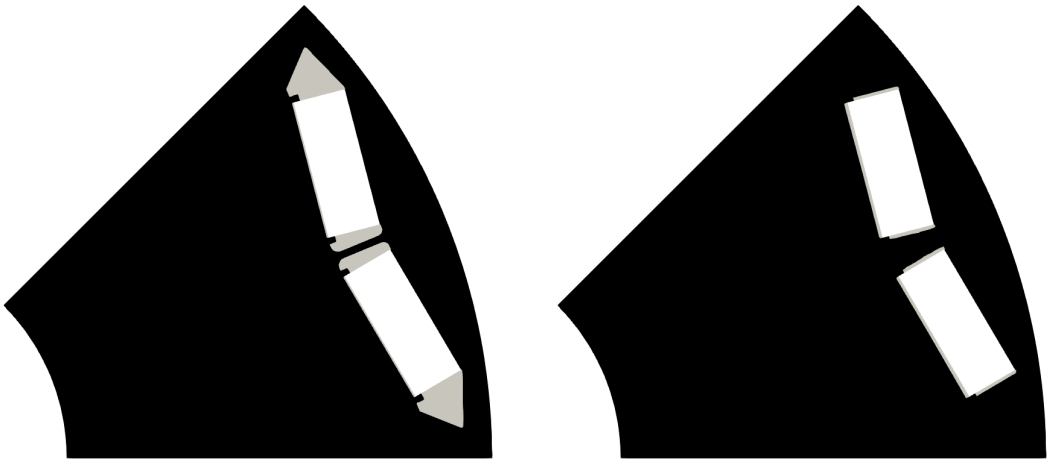

Figure 8.5.: State-of-the-art design (left) and naive design (right) consisting of steel (black), air pockets (gray) and rectangular permanent magnets (white) for numerical experiments.

The left image in Figure 8.5 represents a typical and widely used rotor design of

an interior permanent magnet synchronous machine, which will be referred to as *state-of-the-art design* throughout this section. The reason for its broad use in industrial practice is the good comprise between electromagnetic and structural mechanical criteria. In order to explain this compromise in more detail, we will refer to the air regions, visualized in gray, as *air pockets*. Further, the thin steel region between the permanent magnets as well as the steel parts between the outer air pockets and the air gap will be referred to as *bridges*. One major electromagnetic design criterion is the torque, which is generated in the air gap between rotor and stator, see for instance [29]. We remark that the importance of the air gap in generating the torque is reflected in the definition of functional (8.19). Hence, in order to obtain a high torque, the magnetic flux within the machine needs to be concentrated in the air gap. This insight is precisely the reason for the use of air pockets, which decrease the magnetic flux leakage in the rotor due to the low magnetic permeability of air compared to steel. An entire prevention of rotor flux leakage, however, is impossible due to the steel bridges. This is explained in [100] as follows: "Each bridge effectively creates a magnetic short circuit across the permanent magnets, thereby reducing the magnets' contribution to the overall air-gap flux." Note that an optimal flux behavior is achieved, if the bridges are removed entirely. However, this would clearly be problematic from a structural mechanical point of view due to the lack of stability, especially at high rotational speeds. Therefore, design engineers aim at choosing the bridges as thin as possible in order to obtain high torques while keeping the rotor mechanically stable. Further information on this topic can be found in [100], [141] and [77]. The question, whether fundamentally different shapes of the air pockets and bridges exist, arises naturally at this point. We address this question in the following and investigate, if the level set algorithm is capable of improving the state-of-the-art design in terms of average torque and local stresses.
The second initial design, which will be employed for the numerical experiments, is visualized in the right image of Figure 8.5. Since this design does not contain any air pockets and is, excluding the permanent magnet area, entirely occupied by steel, it will be referred to as *naive design*. In this case, it will be particularly interesting how the algorithm performs, as no prior expert knowledge regarding the shape of the air pockets is provided by the initial design.

Optimization Setup

Before we begin reporting on the numerical investigations, the experimental setup will be fixed. The machine type under investigation is a three-phase permanent magnet

synchronous machine with four pole pairs. The sketch of a two-dimensional cross-section, more precisely a 45°-segment, is shown in Figure 8.2. Note that considering only this part of the entire domain within the optimization procedure is sufficient due to the symmetries of the machine setup. Throughout this section, a constant rotational speed of $\omega = 17000$ revolutions per minute is assumed, which is a typical maximum speed for electrical machines used in battery electric passenger vehicles. We recall that the rotational speed affects directly the mechanical forces within the rotor. Further, the iron parts of the rotor and stator are assumed to consist of steel of the type M330-50A, which is normed by the EN 10106 and standard in the manufacturing of electrical machines in industry. Note that the steel type determines the material characteristics for all physical domains.

Concerning the geometrical setup, an outer and inner stator radius of 116 mm and 79.2 mm as well as an outer and inner rotor radius of 78.6 mm and 26.5 mm is chosen. This results in a diameter of 232 mm for the entire machine and a thickness of 0.6 mm for the air gap between rotor and stator. We mention at this point that the size of the air gap affects the torque significantly. More precisely, the smaller the air gap, the higher the torque, see for instance [136]. Clearly, a certain minimum thickness of the air gap is necessary in order to prevent a collision between rotor and stator at high rotational speeds, caused by centrifugal forces and the resulting material expansion within the rotor. This emphasizes the importance of considering mechanical stability in the rotor design, as it affects directly the allowable diameter of the air gap and thus the maximum torque. Further, the design domain is depicted in Figure 8.4, where the regions around the shaft and the magnets are excluded in order to guarantee physical consistency throughout the optimization, see the discussion in Section 8.2 for details. Moreover, stress constraints are imposed on the entire structural mechanical hold-all domain, which corresponds to the rotor area excluding the permanent magnets. Note that guaranteeing the stress criterion being satisfied in the entire rotor area is crucial in order to obtain a realistic and fail-safe design.

Further, the data concerning the electromagnetic model needs to be set. The B-H-curve of the ferromagnetic material in stator and rotor is depicted in Figure 8.3, determining the reluctivity function $\hat{\nu}$. In air and copper, the reluctivity is given by the constant $\nu_0 = 10^7/4\pi$ m/H. In the permanent magnets, the reluctivity takes the constant value $\nu_m = \nu_0/1.05$ m/H. Moreover, the alternating currents in the coils are represented by a sinusoidal function of amplitude 1556 A and frequency 1133 Hz, where the latter is determined by the number of pole pairs and the rotational speed. Taking the phase shift between the different coils into account, the current density J_3 is chosen accordingly for each rotor position. Further, the magnetization M is assumed to be perpendicular

to the longer edge of the permanent magnets with a magnitude of 1.216 T. For the computation of the mean torque, a total number of $N = 15$ rotor positions is considered with a difference of 1° between the angles of two neighboring rotor positions, which results in the consideration of a 15° rotation. Note that this is sufficient for determining the mean torque, since the torque signal repeats periodically after a 15° rotation due to the 45° periodicity of rotor and stator as well as the use of three-phase currents. The magnetostatic problem (8.24) has been solved using Newton's method, where the linearized equations as well as the adjoint problem (8.48) have been discretized using first order Lagrangian finite elements. Further, an harmonic averaging procedure (cf. Section 6.2) has been employed for computing the reluctivity in intersected mesh elements. Moreover, the second gradient recovery strategy (6.18) from Section 6.3 has been used for the discretization of the topological gradient.
Additionally, the parameters for the structural mechanical model need to be fixed in order to compute the stress criterion. An elastic modulus of $E = 2.0 \times 10^5$ MPa and a Poisson ratio of $\nu = 0.3$ are used for computing the elasticity tensor. Moreover, a weak phase parameter of $\alpha = 10^{-3}$ is employed for considering the difference between steel and air. Together with the rotational speed ω, the density of steel $\rho_{\mathrm{f}} = 7.65 \times 10^3$ kg/m^3 is employed for computing the centrifugal forces (8.22). Further, the magnet replacement load is determined by the density $\rho_{\mathrm{m}} = 8.415 \times 10^3$ kg/m^3 as well as the length and height of 17 mm and 7 mm, respectively, of the permanent magnets. Moreover, a radial displacement with a magnitude of 60 µm is prescribed at the boundary representing the shaft hole. Throughout this chapter, an elastic limit of $\bar{\sigma} = 500$ MPa is chosen in the stress constraints, which represents the yield stress of the specific steel type under consideration.
Concerning the optimization scheme, the same settings as in the previous chapter are employed. This concerns the parameter of the penalty function, the number of integration points within the computation of the topological gradient, the step size control of the algorithm and the choice of $h(\gamma) = \gamma/\gamma_0$. Moreover, the convergence criterion (7.17) is chosen as in the previous chapter. A mesh with 41653 vertices and 76024 elements in the entire machine area as well as 25084 vertices and 48546 elements in the design domain has been used within the optimization.
An important aspect in the implementation of the numerical algorithm is the computation of the topological gradient of the mean torque, which has been addressed in Theorem 8.3. Within this work, we only implemented the first term of the topological gradient (8.53) and neglected the second term (8.54). The reason for this decision is that the second term is small compared to the first term for the application under investigation, see [16]. Moreover, the numerical treatment of the second term (8.54)

requires a lot of technical implementation effort due to the necessity of precomputing look-up tables in an offline stage, see [65] and [16]. This effort is justified by no means compared to the gained numerical accuracy for the topological gradient in a practical application.
Furthermore, a feature for symmetrizing the topological gradient in the entire rotor area along the symmetry axis at 22.5° has been implemented. We performed the symmetrization by averaging the values of the topological gradient in two symmetrically related vertices. Note that the magnetic field, and thus the topological gradient of the torque, is not symmetric along the symmetry axis for a fixed rotor position. Since we simulate rotations only in one direction, which corresponds to motor operation of the machine, the resulting topological gradient of the mean torque remains asymmetric. It follows that the use of this sensitivity within the level set-based optimization algorithm from Chapter 5 leads to asymmetric designs. We mention that the symmetrization is performed for two reasons. First, the enforced symmetry property is common for the machine type under consideration and enables a comparison of our results with existing works from literature. Second, looking at the symmetrization from an engineering point of view, the machine is designed optimally for both rotation directions and hence for motor and generator operation.

State-of-the-art Design

Having described the experimental setup, we turn towards the numerical results. First, we report on the experiments, where the initial guess is provided by the start-of-the-art design. In Figure 8.6, the first principal stress field and the magnitude of the magnetic field of the state-of-the-art design are visualized.
Before we address the numerical solution of the optimal control problem (8.44), the state-of-the-art design is assessed in terms of mean torque and local first principal stresses. Based on the numerical solution of the magnetostatic problem (8.24) and the linear elasticity problem (2.10), a mean torque of 625.3 Nm and a maximum first principal stress of 659.9 MPa is determined. As it can be observed in Figure 8.6, the maximum stress occurs in the bridge between the two permanent magnets. Note that the occurring stress can be reduced by simply increasing the thickness of the bridge. However, as it has been explained in the beginning of this section, an increase of the bridge thickness results in an immediate reduction of the achievable mean torque due to magnetic flux leakage in the rotor. In a first step towards the solution of (8.44), the *unconstrained torque maximization problem*

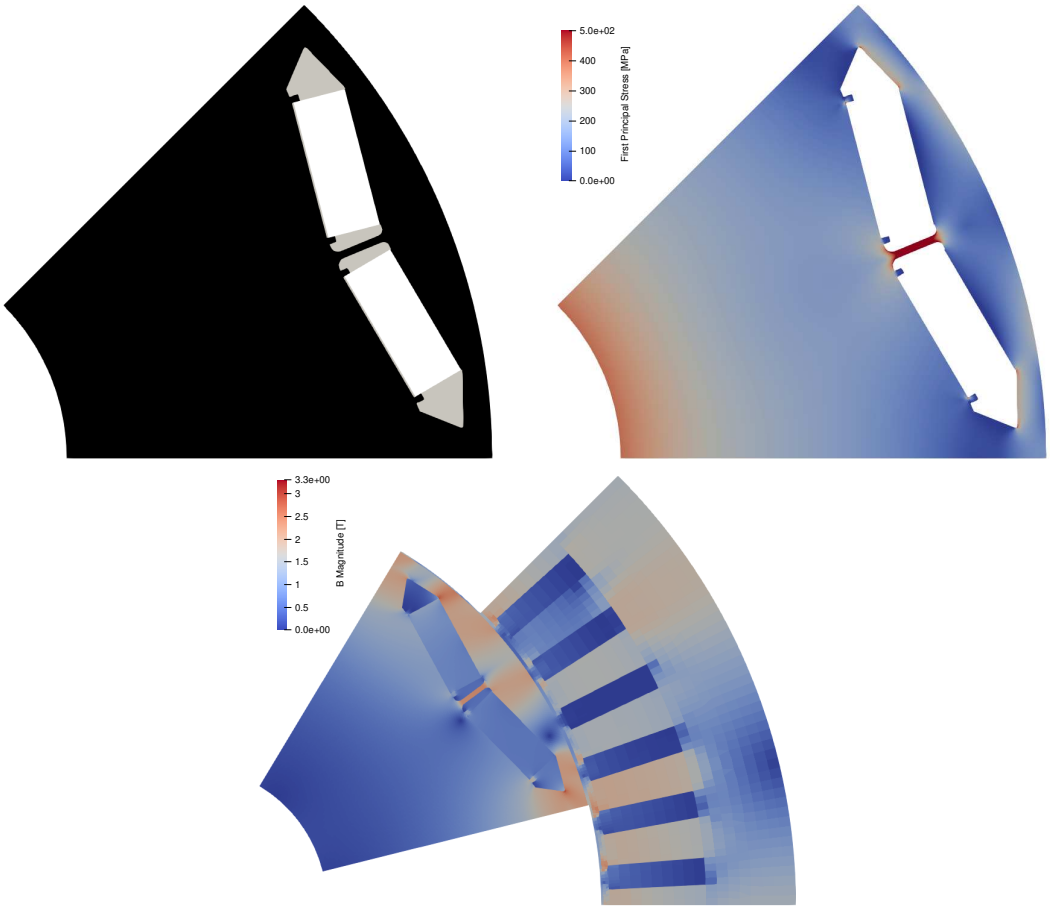

Figure 8.6.: State-of-the-art design with steel in black, air pockets in gray, permanent magnets in white (first row, left), principal stress field (first row, right) and magnetic field (second row).

$$\min_{\Omega \in \mathcal{O}} \quad \mathcal{J}(\Omega)$$

is addressed. We are interested in examining the solution of this problem using the level set-based optimization scheme from Chapter 5 in order to get an idea of an optimal design for the unconstrained case. Furthermore, we can determine the mean torque in the unconstrained case, which provides an upper limit for the stress-constrained case. The numerical scheme converged after 25 iterations with convergence measure $\epsilon_c = 0.0096$ and a mean torque of 737.2 Nm for the final design. In Figure 8.7, the final design along with the corresponding magnetic field is visualized. It can be observed that the algorithm creates air in three main areas. The first major air domain is between the permanent magnets, where the bridge of the initial design has been removed.

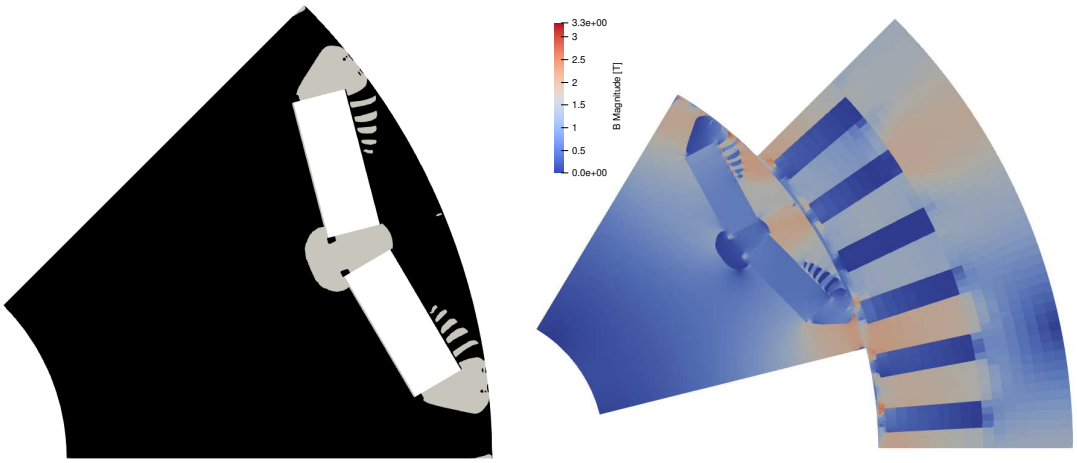

Figure 8.7.: Result of unconstrained torque maximization. Material distribution with steel in black, air pockets in gray, permanent magnets in white (left) and magnetic field (right).

Second, air is created between the outer sides of the magnets and the rotor outer contour in radial direction by removing the outer bridges. Third, feather-shaped air holes are created between the permanent magnets and the rotor outer contour. From an electromagnetic point of view, these design features are highly desirable due to a reduced rotor flux leakage and, consequently, an optimal concentration of the magnetic field in the air gap. From a structural mechanical point of view, however, this design is clearly problematic. It can be observed that the material part between the permanent magnets and the outer contour is barely attached to the remaining part of the rotor. More precisely, the only connections are the small noses at the sides of the permanent magnets. Note that the solution of the elasticity system is unreasonable in this situation, since the assumption of small displacements does not hold anymore. For this reason, a stress analysis is omitted. Summarizing, we can observe that the results for the unconstrained case confirm and illustrate the well-known conflict between electromagnetic and structural mechanical design criteria, which has been discussed in the beginning of this section. In particular, an optimal magnetic flux behavior is achieved by entirely removing the central and outer bridges. For the optimization algorithm, this poses a major challenge with the opportunity of creating novel and inspiring designs. Furthermore, we note that the no-structure problem does not occur for the case of torque maximization. While for the unconstrained minimum volume problem, the trivial and global solution is the empty set, a highly non-trivial result is obtained in the case of unconstrained torque maximization. Nevertheless, the challenge of low design connectivity can be observed for the example under consideration.
We proceed with the results for the *stress-constrained torque maximization problem* (8.44),

where an initial penalty parameter of $\gamma_0 = 2.0 \times 10^7$ has been chosen. The numerical optimization algorithm converged after 54 iterations with convergence measure $\epsilon_c = 0.022$. An electromagnetic analysis reveals a mean torque of 691.5 Nm for the obtained final design, which yields an increase of 10.7 % compared to the initial state-of-the-art design. Furthermore, we observe a maximum first principal stress of 497.6 MPa for the final design and thus a stress reduction of 24.6 % compared to the state-of-the-art design. We emphasize that this excellent result has been obtained without the necessity of applying a continuation strategy since the stress constraints are satisfied already for the initial penalty parameter. In Figure 8.8, the final design is visualized along with the first principal stress field and the magnetic field for a fixed rotor position.

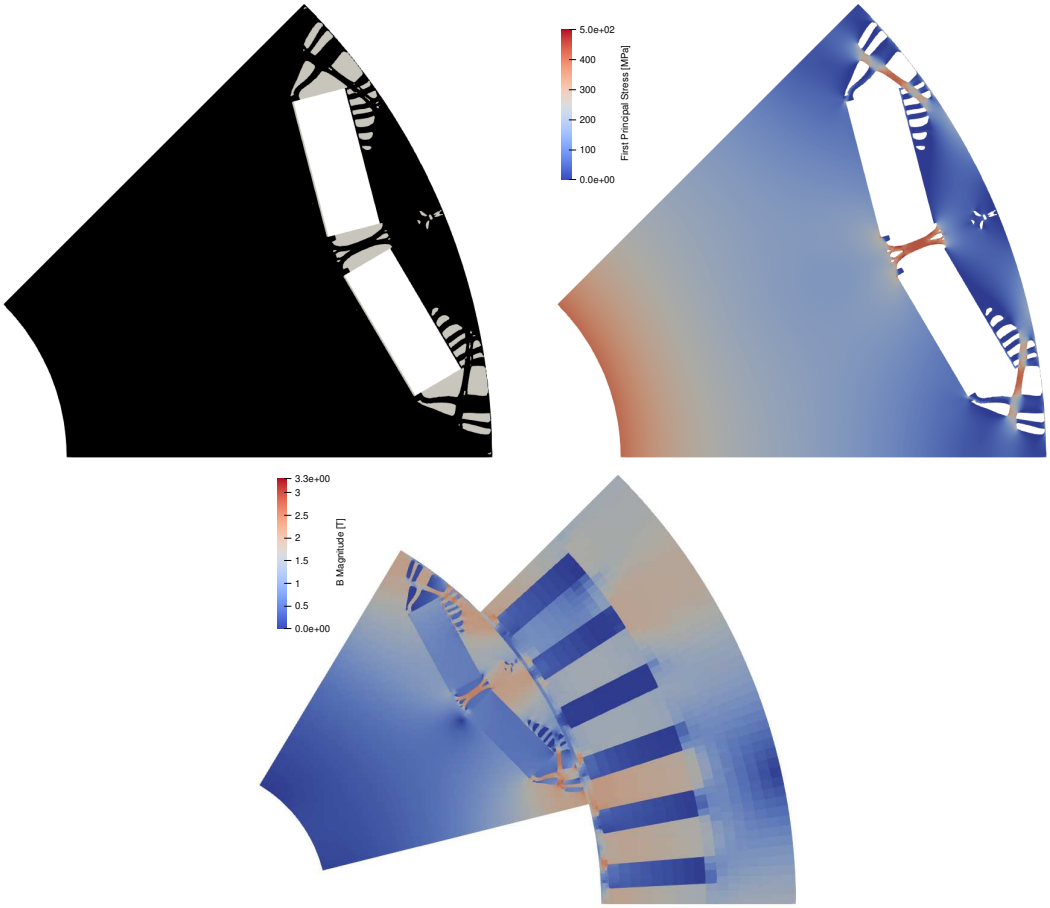

Figure 8.8.: Result of stress-constrained optimization with state-of-the-art design as initial guess. Material distribution with steel in black, air pockets in gray, permanent magnets in white (first row, left), principal stress field (first row, right) and magnetic field (second row).

Analogously to the previous chapter on the minimum volume problem, we performed a realistic stress assessment within the rotor domain by considering only the material

phase and an appropriately refined mesh. As in the previous chapter, this step is conducted in order to eliminate the impact of intersected mesh elements and the surrounding weak phase. Note that only the stress field for the realistic setting is visualized in Figure 8.8 since the corresponding visualization for the original setting, where the weak phase is included, does not contain additional insights. The realistic stress analysis reveals a maximum first principal stress of 646.1 MPa, which occurs at the boundary of the small air holes near the middle bridge between the two permanent magnets. Although this is significantly above the stress limit of 500 MPa, we observe that the constraint violation occurs only in very few vertices. We emphasize that these stress peaks can be eliminated easily by smooth modifications of the boundary or a filling of the small air holes without a significant reduction of the mean torque. Furthermore, we highlight that the critical rotor area, which comprises in particular the bridges, shows stress levels around 500 ± 15 MPa. Moreover, as it could be observed for the minimum volume problem in the previous chapter, a satisfying distribution of the stress levels is achieved by the algorithm and local stress concentrations are prevented. Summarizing, it can be stated that the obtained design satisfies the stress criterion very well and violations of the constraints can be eliminated by minor design modifications. Note that postprocessing routines are commonly used in the practical application of shape and topology optimization methods prior to an actual manufacturing of the optimized design.

Regarding the changes between the initial and the final design, several observations can be made. First, the middle bridge between the permanent magnets is maintained and modified to an X-shape, which is a major difference to the unconstrained case. This modification results in an improved mechanical stability, since the maximum stress within the bridge is decreased due to its curved shape. Second, the outer bridges and air pockets are modified. More precisely, we can observe that the initial shape of the outer air pockets is adapted and additional holes are created within the outer bridges. Furthermore, it can be observed that the initial air pocket, which can still be identified, is divided by a thin steel connection between magnet nose and outer bridge. These modifications result in a complex and non-intuitive structure of the outer bridges and air pockets, which contribute significantly to the gain of mean torque due to a reduced rotor flux leakage. Note that a similarity to the unconstrained case can be observed in this region, where the algorithm entirely removed the outer bridges. For the constrained case, the algorithm keeps as much material as possible in order to guarantee for mechanical stability. Third, as in the unconstrained case, we can observe the creation of feather-shaped air pockets at the magnet boundaries in radial direction.

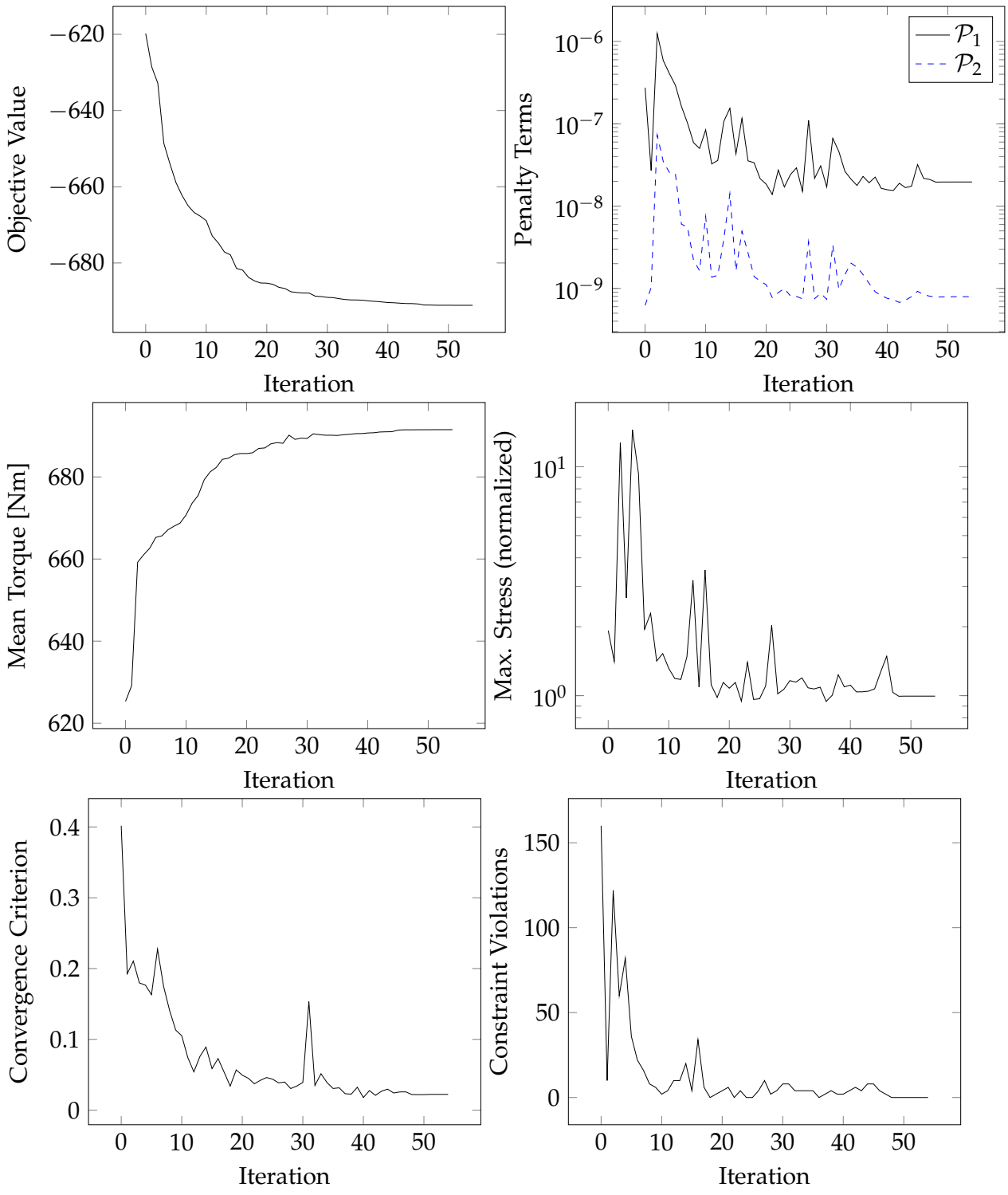

Figure 8.9.: Optimization history for state-of-the-art design with stress constraints.

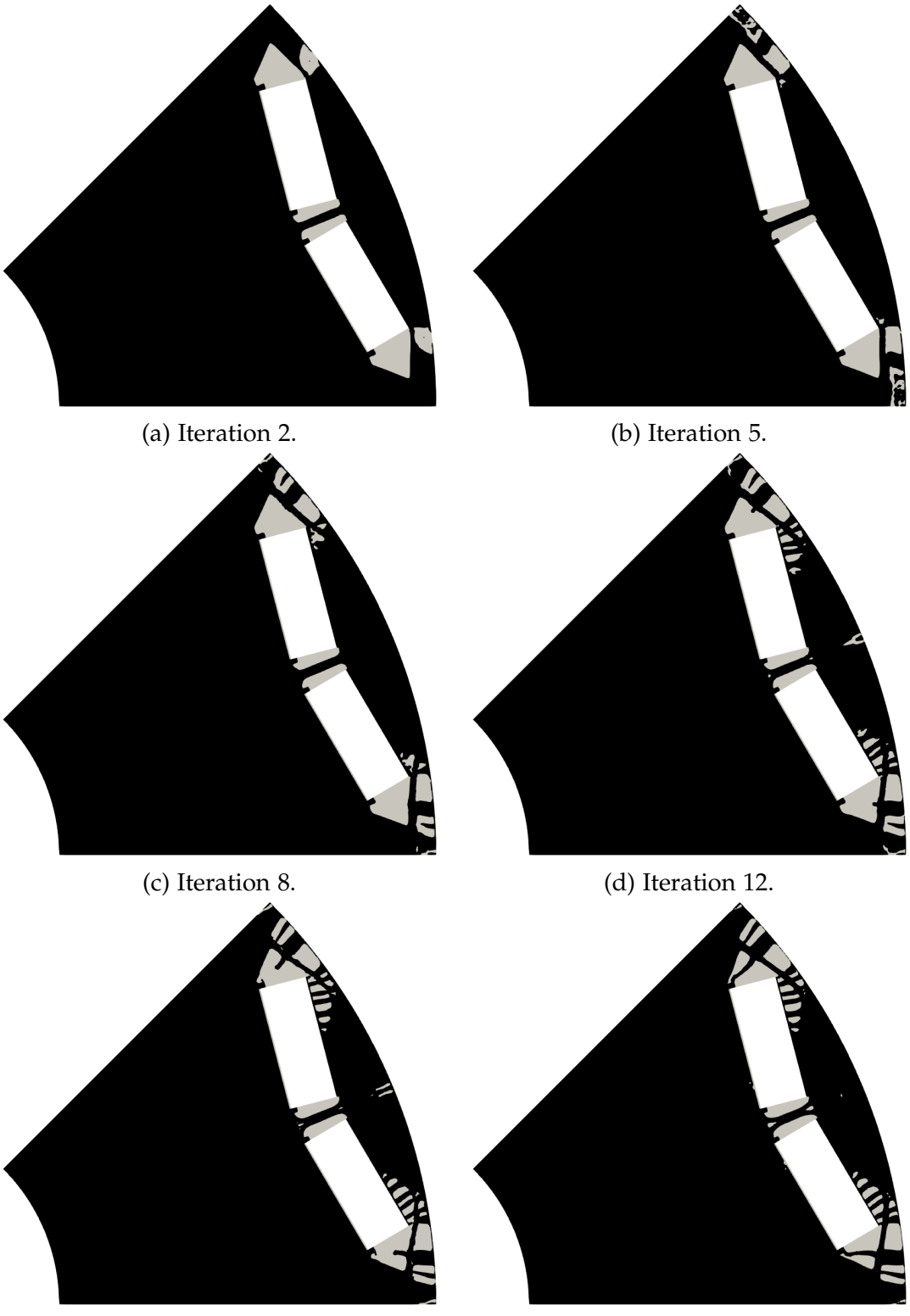

(a) Iteration 2.

(b) Iteration 5.

(c) Iteration 8.

(d) Iteration 12.

(e) Iteration 15.

(f) Iteration 23.

Figure 8.10.: Design evolution for state-of-the-art design as initial guess.

Therefore, we can conclude that this modification leads to an increase of the mean torque and has a rather low effect on the mechanical stability of the rotor, since the stresses are comparably low in this area. Summarizing, it can be stated that the design shows similarities with the unconstrained case and all qualitative differences contribute to mechanical stability.
We highlight at this point that the feather-shaped air pockets represent a design feature, which has been unknown so far in the engineering literature. Therefore, in cooperation with Robert Bosch GmbH, a *patent application* with patent number DE102022203615A1 has been submitted to the German Patent and Trade Mark Office and is currently in the examination process. This result demonstrates the potential and capability of the developed topology optimization method in finding novel and non-intuitive designs.
The optimization history for the stress-constrained problem is shown in Figure 8.9 and, in addition, the design evolution of the optimization process is visualized in Figure 8.10 by means of six different iterations. Both figures demonstrate clearly the connection between variations of the mean torque and the creation of air pockets. In Figure 8.9, a large increase of the mean torque can be observed in the beginning of the optimization process, in particular between iteration 1 and 5 as well as between iteration 10 and 16. In Figure 8.10, we can observe that large air pockets are created in precisely these iterations. Furthermore, a significant increase of the maximum principal stress can be observed for the relevant iterations, which shows that an improvement of the mean torque is performed at the cost of a decrease of the mechanical stability. As it can be observed in the corresponding plot in Figure 8.9, the maximum stress is improved by comparably small design variations after the creation of these large air pockets. Note that, similarly to the minimum volume problem, high fluctuations of the maximum principal stress and the number of constraint violations occur due to the highly nonlinear behavior of the pointwise stress constraints, which means that small design variations can result in a large variation of the maximum stress. Further, it can be observed that a thin steel connection grows through the initial air hole to the magnet nose at the outer side of the permanent magnets. This demonstrates clearly the ability of the optimization algorithm to create material within the air phase.

Observation 8.1. *The regularized design problem (8.44) is solved successfully by the level set-based optimization algorithm. Hence, as it has been observed already in the case of volume minimization, the extension of the pointwise stress constraints to the weak phase has a stabilizing effect on the optimization scheme.*

Naive Design

Let us proceed by investigating the results of the stress-constrained torque optimization for the naive design as initial guess. In the following investigations, the initial penalty parameter has been chosen as $\gamma_0 = 3.0 \times 10^7$. The numerical scheme converged after 43 iterations with convergence measure $\epsilon_c = 0.043$. Further, the mean torque is improved from 557.3 Nm to 688.2 Nm.

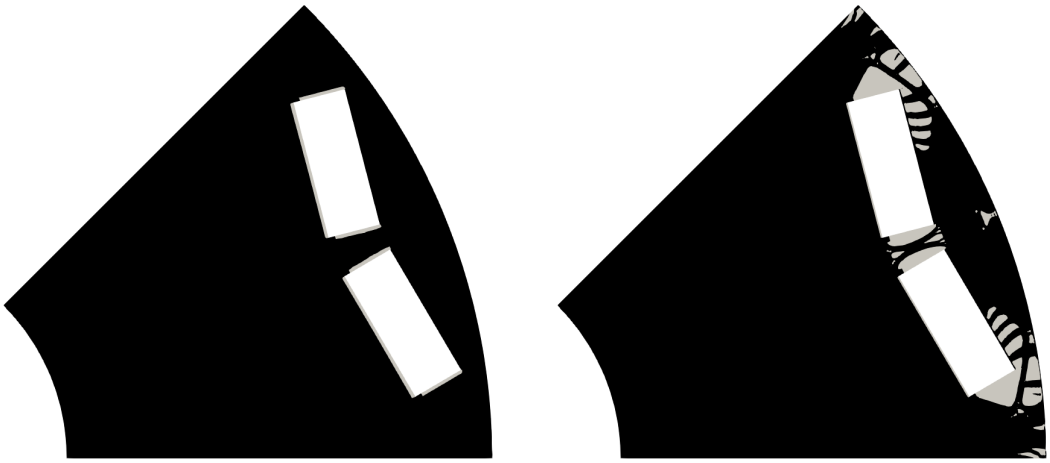

Figure 8.11.: Result of stress-constrained optimization with naive design as initial guess. Initial (left) and final design (right) with steel (black) and air pockets (gray).

In Figure 8.11, the initial design is visualized together with the final design. It can be observed that the result shares many similarities with the design in Figure 8.8, which is the result of the stress-constrained optimization with respect to the state-of-the-art design. The only major qualitative differences are the large air pockets at the outer sides of the permanent magnets, which are not divided by a thin steel component. It is remarkable that all main characteristic features, in particular the X-shaped middle bridge between the magnets, the complex outer bridges and air pockets as well as the feather-shaped air holes can be observed for the naive initial design, where no prior expert knowledge is available.
In Figure 8.12, the first principal stress field for both the initial and the final design is visualized. For the initial design, a maximum first principal stress of 1045.1 MPa is obtained. Unsurprisingly, the stress concentrations occur around the reentrant corners of the magnet pockets, as it is typically observed for geometrically constrained domains. For the final design and the initial penalty parameter, a maximum first principal stress of 492.7 MPa is obtained with respect to the mesh containing the weak phase. The realistic stress assessment, which is conducted only within the material phase with an

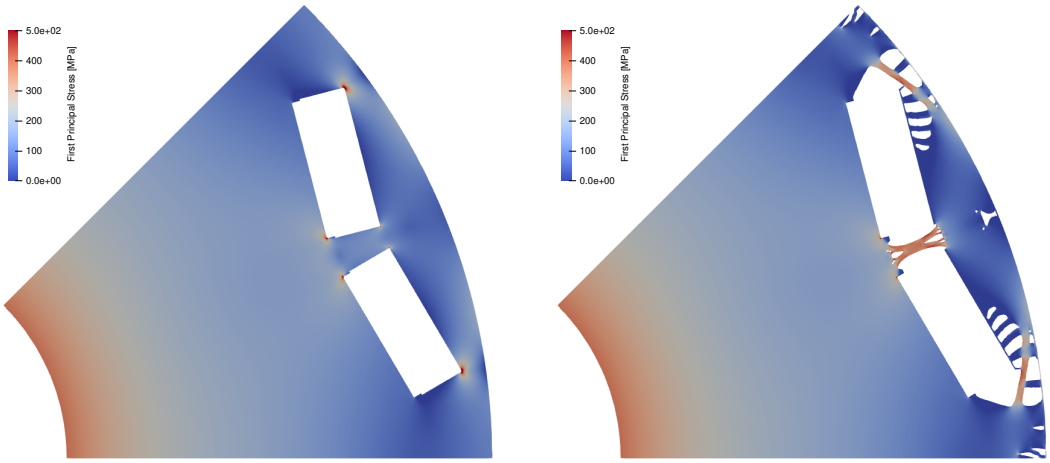

Figure 8.12.: Result of stress-constrained optimization with naive design as initial guess. First principal stress field of the initial (left) and final design (right).

appropriately refined mesh, is depicted in Figure 8.12. We can observe a maximum principal stress of 681.1 MPa, which occurs at the boundary of the small air holes at the middle bridge. As in the previous case, the constraint violation in the realistic stress computation occurs only on very few vertices and can be eliminated by minor design modifications in a postprocessing step. In Figure 8.13, the magnitude of the magnetic flux density is visualized for both the initial and the final design.

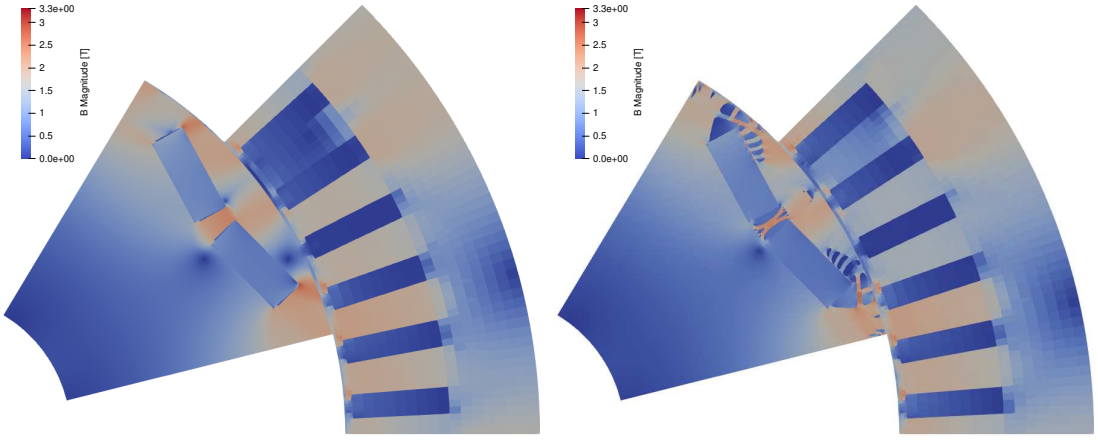

Figure 8.13.: Result of stress-constrained optimization with naive design as initial guess. Magnetic field of the initial (left) and final design (right).

Observation 8.2. *The result of the optimization scheme for the naive design as initial guess can be observed to be qualitatively very similar to the result with respect to the state-of-the-art design. This demonstrates that the developed method is capable of generating complex and non-intuitive structures without the availability of expert knowledge.*

8.6. Discussion

Having reported on the numerical experiments in the previous section, the results will be summarized briefly in the following. As for the stress-constrained minimum volume problem, which has been investigated in the previous chapter, a key in solving the stress-constrained torque maximization problem (8.39) has turned out to be the extension of the pointwise stress constraints to the weak phase. More precisely, combined with the penalty approach from Section 3.3, the level set-based optimization scheme could be observed to converge. In addition to the stabilizing effect on the numerical scheme, it could be observed that the obtained designs are connected and isolated parts are prevented. Furthermore, in contrast to the stress-constrained minimum volume problem, a continuation in the penalty parameter has not been necessary, as the pointwise constraints have been satisfied immediately for the initial penalty parameter. The realistic stress assessment, which has been conducted on a refined and fitted mesh, revealed that the stress levels are around 500 ± 15 MPa in all critical areas. More precisely, the constraints are violated only in very few vertices, which can be resolved easily by minor modifications in a postprocessing step. Regarding the results with the state-of-the-art design as initial guess, the mean torque could be improved and the maximum first principal stress could be decreased significantly. In three main areas within the rotor, in particular in the neighborhood of the steel bridges, the creation of complex and non-intuitive structures could be observed. Moreover, the optimization result for the naive design as initial guess shows large similarities with the result for the state-of-the-art design as initial guess. This demonstrates that the developed method is capable of approximating non-intuitive designs without any prior expert knowledge.

So far, solely topology optimization approaches involving electromagnetic criteria have been investigated for the design of electrical machines in the literature. These works have shown promising results, but do not provide realistic designs. The multiphysical topology optimization method, which has been developed in this chapter, represents a successful extension of the existing works, in particular of the approach in [65], with respect to mechanical stability. The results in this chapter show novel and complex design structures, which represent a sophisticated comprise between the electromagnetic and mechanical design criteria. These results demonstrate the power and potential of topological gradients and level set methods in solving real industrial problems. Furthermore, we highlight that this potential is emphasized by a patent application for a novel rotor design of an interior permanent magnet synchronous machine, which has been submitted to the German Patent and Trade Mark Office.

9. Conclusion and Outlook

Conclusion

In this thesis, a framework for the solution of generic stress-constrained optimal design problems has been developed and applied successfully to the realistic design of an electrical machine.
A key aspect of the approach has turned out to be the regularization of the original optimal design problem. Motivated by the no-structure problem for the specific case of stress-constrained volume minimization, a perturbation of the original problem has been proposed in order to exclude undesirable global solutions from the feasible set. Essentially, this perturbation consists of an extension of the pointwise stress constraints from the material phase to the weak phase. Moreover, a penalty approach has been chosen in order to replace the problem with pointwise constraints by an unconstrained approximation. This regularized problem has been analyzed with respect to the existence of local minima, which is the basis for the development of solution methods.
The topological gradient for the penalty term, resulting from the regularization, has been derived and utilized as the core of a level set-based descent scheme. This approach is particularly well suited for problems with local stress constraints due to the inherent sharp interface between the material and air phase. An emphasis is put on the numerical realization of the optimization scheme, which is defined in the infinite-dimensional setting up to this point. The approximation of the state system with respect to a fixed mesh has been discussed as well as the discretization of the topological gradient. For the latter, the importance of a filtering scheme has been observed, in particular for the case of stress-constrained problems. Further, important aspects concerning the practical implementation of the overall scheme have been provided.
The discretization of the optimization algorithm enables investigating the regularization, more precisely the effect of stress constraints in the weak phase, via numerical experiments. Two penalty terms, the first term with and the second term without constraints in the weak phase, have been examined for the specific case of stress-constrained volume minimization. In a first step, the topological gradient of both functionals has been validated by a comparison with the corresponding finite differ-

ences. Within the validation, significant qualitative differences have been observed between the two terms, in particular for a topological perturbation in the air phase. This observation has been confirmed by the optimization results. In the first case, where only stress constraints in the material phase have been imposed, convergence problems could be observed, resulting in a perforated design with small isolated parts. In contrast, very satisfying results have been obtained for the second case, where the stress constraints are imposed in the entire hold-all domain. Hence, it could be observed that the extension of the stress constraints to the weak phase has a stabilizing effect on the numerical scheme.
We utilized this novel insight for addressing a real industrial application, namely the multiphysical design of the rotor of a permanent magnet synchronous machine. First, we observed that our approach is capable of improving a state-of-the-art rotor design. Second, it was shown that a naive initial guess leads to a very similar design. This is a remarkable result, since no a priori expert knowledge has been available for the optimization process. Finally, our obtained designs have resulted in a patent application, which reflects the potential and novelty of the developed approach.

Future Work

The research in this thesis may be extended and refined in the following directions:

- *Uncertainty quantification and robust optimization*
  The probably most interesting aspect regarding future research addresses the consideration of stochastic effects and robust optimization. This topic is particularly important for the problem class under investigation, since local stress constraints are highly sensitive to design variations. The case of uncertainties in the mechanical loads seems to be a promising approach, especially with regards to the designs with filigree structures, which have been obtained in Chapters 7 and 8. A starting point for this direction, in particular concerning the application to electrical devices, may be the works [116] and [32].

- *3D setting*
  Addressing the three-dimensional case, instead of considering a two-dimensional cross section, can be reasonable in certain applications. The topological gradient of the stress-based penalty term for the three-dimensional setting is covered by Theorem 4.1. Moreover, regarding the application to electrical machines, the topological gradient of the torque functional has been derived in [71] for the three-dimensional case. Using an appropriate modification of the step size control

within the level set-based algorithm, a generalization of the method should be possible immediately.

- *Adaptive mesh refinement*
  A strategy for adaptive mesh refinement with the goal of a resolved material interface during the optimization process is interesting for two reasons. First, a refinement strategy is useful in order to reduce the computational burden. This aspect is of particular interest, if the three-dimensional setting is tackled. Second, a resolved material interface is expected to improve the accuracy of the stress computation at the interface, which may further enhance the reliability of the approach.

- *Additional objectives for rotor design*
  A natural step in the improvement of the topology optimization method for rotor design comprises the consideration of additional objectives from different physical domains. Although the criteria from electromagnetics and structural mechanics in Chapter 8 lead to very satisfying results already, the consideration of thermal and acoustic effects is interesting from an application point of view.

- *Multi-material rotor design*
  In Chapter 8, the permanent magnets in the rotor of the electrical machine have been assumed to be fixed and thus excluded from the design domain. Due to this assumption, the optimal distribution of ferromagnetic material and air has been addressed. It is possible, however, to extend the design domain to the entire rotor area and consider the optimal distribution of three materials. We refer to [66] and [118], where the level set algorithm from Chapter 5 has been extended to the multi-material case.

Bibliography

[1] M. Ainsworth and J. T. Oden. *A Posteriori Error Estimation in Finite Element Analysis*. John Wiley & Sons, Inc., 2000.

[2] G. Allaire. *Shape Optimization by the Homogenization Method*. Springer New York, 2002.

[3] G. Allaire, F. de Gournay, F. Jouve, and A.-M. Toader. Structural optimization using topological and shape sensitivity via a level set method. *Control and cybernetics*, 34(1):59–80, 2005.

[4] G. Allaire and F. Jouve. Minimum stress optimal design with the level set method. *Engineering Analysis with Boundary Elements*, 32(11):909–918, Nov. 2008.

[5] G. Allaire, F. Jouve, and H. Maillot. Topology optimization for minimum stress design with the homogenization method. *Structural and Multidisciplinary Optimization*, 28(2):87–98, 2004.

[6] G. Allaire, F. Jouve, and A.-M. Toader. Structural optimization using sensitivity analysis and a level-set method. *Journal of Computational Physics*, 194(1):363–393, 2004.

[7] G. Allaire, F. Jouve, and N. Van Goethem. Damage and fracture evolution in brittle materials by shape optimization methods. *Journal of Computational Physics*, 230(12):5010–5044, June 2011.

[8] H. W. Alt. *Lineare Funktionalanalysis: Eine anwendungsorientierte Einführung*. Springer Berlin Heidelberg, 2012.

[9] H. Ammari and H. Kang. *Reconstruction of Small Inhomogeneities from Boundary Measurements*. Springer Berlin Heidelberg, 2004.

[10] H. Ammari and H. Kang. *Polarization and Moment Tensors: With Applications to Inverse Problems and Effective Medium Theory*. Springer New York, 2007.

[11] S. Amstutz. Sensitivity analysis with respect to a local perturbation of the material property. *Asymptotic Analysis*, 49(1,2):87–108, 2006.

[12] S. Amstutz. A penalty method for topology optimization subject to a pointwise state constraint. *ESAIM: COCV*, 16(3):523–544, 2010.

[13] S. Amstutz. Analysis of a level set method for topology optimization. *Optimization Methods Software*, 26(4—5):555—-573, Oct. 2011.

[14] S. Amstutz and H. Andrä. A new algorithm for topology optimization using a level-set method. *J. Comput. Phys.*, 216(2):573—-588, Aug. 2006.

[15] S. Amstutz, C. Dapogny, and À. Ferrer. A consistent relaxation of optimal design problems for coupling shape and topological derivatives. *Numerische Mathematik*, 140(1):35–94, Mar. 2018.

[16] S. Amstutz and P. Gangl. Topological derivative for the nonlinear magnetostatic problem. *Electron. Trans. Numer. Anal.*, 51:169–218, 2019.

[17] S. Amstutz and A. A. Novotny. Topological optimization of structures subject to von mises stress constraints. *Structural and Multidisciplinary Optimization*, 41(3):407–420, Apr. 2010.

[18] S. Amstutz, A. A. Novotny, and E. A. de Souza Neto. Topological derivative-based topology optimization of structures subject to drucker-prager stress constraints. *Computer Methods in Applied Mechanics and Engineering*, 233-236:123–136, Aug. 2012.

[19] A. Arkkio. *Analysis of Induction Motors Based on the Numerical Solution of the Magnetic Field and Circuit Equations*. PhD thesis, Helsinki University of Technology, 1987.

[20] I. Babuška. The finite element method for elliptic equations with discontinuous coefficients. *Computing*, 5(3):207–213, Sept. 1970.

[21] J. W. Barrett and C. M. Elliott. Fitted and unfitted finite-element methods for elliptic equations with smooth interfaces. *IMA Journal of Numerical Analysis*, 7(3):283–300, 1987.

[22] S. Bartels. *Numerical Approximation of Partial Differential Equations*. Springer International Publishing, 2016.

[23] O. A. Bauchau and J. I. Craig. *Structural Analysis*. Springer Netherlands, 2009.

[24] T. Belytschko, R. Gracie, and G. Ventura. A review of extended/generalized finite element methods for material modeling. *Modelling and Simulation in Materials Science and Engineering*, 17(4):043001, Apr. 2009.

[25] M. P. Bendsøe. Optimal shape design as a material distribution problem. *Structural Optimization*, 1(4):193–202, Dec. 1989.

[26] M. P. Bendsøe, A. Ben-Tal, and J. Zowe. Optimization methods for truss geometry and topology design. *Structural Optimization*, 7(3):141–159, Apr. 1994.

[27] M. P. Bendsøe and N. Kikuchi. Generating optimal topologies in structural design using a homogenization method. *Computer Methods in Applied Mechanics and Engineering*, 71(2):197–224, Nov. 1988.

[28] M. P. Bendsøe and O. Sigmund. *Topology Optimization*. Springer Berlin Heidelberg, 2004.

[29] A. Binder. *Elektrische Maschinen und Antriebe*. Springer Berlin Heidelberg, 2012.

[30] L. Blank, H. Garcke, M. H. Farshbaf-Shaker, and V. Styles. Relating phase field and sharp interface approaches to structural topology optimization. *ESAIM: Control, Optimisation and Calculus of Variations*, 20(4):1025–1058, Aug. 2014.

[31] M. Bonnet and G. Delgado. The topological derivative in anisotropic elasticity. *The Quarterly Journal of Mechanics and Applied Mathematics*, 66(4):557–586, 2013.

[32] Z. Bontinck. *Simulation and Robust Optimization for Electric Devices with Uncertainties*. PhD thesis, Technische Universität Darmstadt, 2018.

[33] B. Bourdin and A. Chambolle. Design-dependent loads in topology optimization. *ESAIM: Control, Optimisation and Calculus of Variations*, 9:19–48, Jan. 2003.

[34] D. Braess. *Finite Elemente: Theorie, schnelle Löser und Anwendungen in der Elastizitätstheorie*. Springer Berlin Heidelberg, 2007.

[35] S. Brenner and L. R. Scott. *The Mathematical Theory of Finite Element Methods*. Springer New York, 1994.

[36] D. Bucur and G. Buttazzo. *Variational Methods in Shape Optimization Problems*. Birkhäuser Boston, 2005.

[37] M. Burger, B. Hackl, and W. Ring. Incorporating topological derivatives into level set methods. *Journal of Computational Physics*, 194(1):344 – 362, 2004.

[38] M. Burger and S. J. Osher. A survey on level set methods for inverse problems and optimal design. *European Journal of Applied Mathematics*, 16(2):263–301, June 2005.

[39] M. Burger and R. Stainko. Phase-field relaxation of topology optimization with local stress constraints. *SIAM Journal on Control and Optimization*, 45(4):1447–1466, Jan. 2006.

[40] D. J. Cedio-Fengya, S. Moskow, and M. S. Vogelius. Identification of conductivity imperfections of small diameter by boundary measurements. Continuous dependence and computational reconstruction. *Inverse Problems*, 14(3):553–595, 1998.

[41] G. Cheng and Z. Jiang. Study on topology optimization with stress constraints. *Engineering Optimization*, 20(2):129–148, 1992.

[42] G. D. Cheng and X. Guo. ϵ-relaxed approach in structural topology optimization. *Structural optimization*, 13(4):258–266, 1997.

[43] J. Chetboun. *Conception de formes aérodynamiques en présence d'écoulements décollés : contrôle et optimisation*. PhD thesis, Ecole Polytechnique, 2010.

[44] J. S. Choi, K. Izui, S. Nishiwaki, A. Kawamoto, and T. Nomura. Rotor pole design of IPM motors for a sinusoidal air-gap flux density distribution. *Structural and Multidisciplinary Optimization*, 46(3):445–455, Feb. 2012.

[45] P. G. Ciarlet. *Mathematical elasticity*. North-Holland Elsevier Science Publishers, B.V, Amsterdam New York Amsterdam, 1993.

[46] P. G. Ciarlet. *The Finite Element Method for Elliptic Problems*. Society for Industrial and Applied Mathematics, Mar. 2002.

[47] C. D. Coman. *Continuum Mechanics and Linear Elasticity: An Applied Mathematics Introduction*. Springer Netherlands, 2019.

[48] M. A. S. de Troya. *Adaptive mesh refinement in topology optimization*. PhD thesis, University of Illinois at Urbana-Champaign, 2019.

[49] M. A. S. de Troya and D. A. Tortorelli. Adaptive mesh refinement in stress-constrained topology optimization. *Structural and Multidisciplinary Optimization*, 58(6):2369–2386, Oct. 2018.

[50] G. Delgado. *Optimization of composite structures: A shape and topology sensitivity analysis*. PhD thesis, Ecole Polytechnique, June 2014.

[51] G. Delgado and M. Bonnet. The topological derivative of stress-based cost functionals in anisotropic elasticity. *Computers & Mathematics with Applications*, 69(10):1144–1166, May 2015.

[52] J. Deny and J.-L. Lions. Les espaces du type de beppo levi. *Annales de l'institut Fourier*, 5:305–370, 1954.

[53] J. DeWolf, D. Mazurek, F. Beer, and E. Johnston. *Mechanics of Materials*. McGraw-Hill Education, 2014.

[54] J. Dong, Y. Huang, L. Jin, and H. Lin. Comparative study of surface-mounted and interior permanent-magnet motors for high-speed applications. *IEEE Transactions on Applied Superconductivity*, 26(4):1–4, June 2016.

[55] P. Duysinx and M. P. Bendsøe. Topology optimization of continuum structures with local stress constraints. *Int. J. Numer. Meth. Engng.*, 43(8):1453–1478, Dec. 1998.

[56] H. Emmendoerfer and E. A. Fancello. A level set approach for topology optimization with local stress constraints. *International Journal for Numerical Methods in Engineering*, 99(2):129–156, Apr. 2014.

[57] H. Emmendoerfer and E. A. Fancello. Topology optimization with local stress constraint based on level set evolution via reaction–diffusion. *Computer Methods in Applied Mechanics and Engineering*, 305:62–88, June 2016.

[58] H. A. Eschenauer, V. V. Kobelev, and A. Schumacher. Bubble method for topology and shape optimization of structures. *Structural optimization*, 8(1):42–51, Aug. 1994.

[59] J. D. Eshelby. The determination of the elastic field of an ellipsoidal inclusion, and related problems. *Proceedings of the Royal Society of London. Series A. Mathematical and Physical Sciences*, 241(1226):376–396, 1957.

[60] J. D. Eshelby. The elastic field outside an ellipsoidal inclusion. *Proceedings of the Royal Society of London. Series A. Mathematical and Physical Sciences*, 252(1271):561–569, 1959.

[61] L. C. Evans. *Partial Differential Equations*. American Mathematical Society, 1998.

[62] A. Ferrer. *Multi-scale topological design of structural materials: an integrated approach.* PhD thesis, Universitat Politècnica de Catalunya, 2017.

[63] S. Frei. *Eulerian finite element methods for interface problems and fluid-structure interactions*. PhD thesis, Ruprecht-Karls-Universität Heidelberg, 2016.

[64] S. Frei and T. Richter. A locally modified parametric finite element method for interface problems. *SIAM J. Numer. Anal.*, 52(5):2315–2334, Apr. 2014.

[65] P. Gangl. *Sensitivity-Based Topology and Shape Optimization with Application to Electrical Machines*. PhD thesis, Johannes Kepler University Linz, 2016.

[66] P. Gangl. A multi-material topology optimization algorithm based on the topological derivative. *Computer Methods in Applied Mechanics and Engineering*, 366:113090, 2020.

[67] P. Gangl, S. Amstutz, and U. Langer. Topology optimization of electric motor using topological derivative for nonlinear magnetostatics. *IEEE Transactions on Magnetics*, 52(3):1–4, 2016.

[68] P. Gangl and U. Langer. Topology optimization of electric machines based on topological sensitivity analysis. *Computing and Visualization in Science*, 15(6):345–354, Dec. 2012.

[69] P. Gangl, U. Langer, A. Laurain, H. Meftahi, and K. Sturm. Shape optimization of an electric motor subject to nonlinear magnetostatics. *SIAM Journal on Scientific Computing*, 37(6):B1002–B1025, Jan. 2015.

[70] P. Gangl and K. Sturm. A simplified derivation technique of topological derivatives for quasi-linear transmission problems. *ESAIM: Control, Optimisation and Calculus of Variations*, 26:106, 2020.

[71] P. Gangl and K. Sturm. Asymptotic analysis and topological derivative for 3d quasi-linear magnetostatics. *ESAIM: M2AN*, 55:S853–S875, 2021.

[72] S. Garreau, P. Guillaume, and M. Masmoudi. The topological asymptotic for pde systems: The elasticity case. *SIAM Journal on Control and Optimization*, 39(6):1756–1778, 2001.

[73] P. L. Gould. *Introduction to Linear Elasticity*. Springer New York, 2013.

[74] P. Grisvard. *Elliptic problems in nonsmooth domains*. Pitman Advanced Pub. Program, Boston, 1985.

[75] N. Gunduz, N. Akbulut, and F. O. Sonmez. Generating optimal 2d structural designs using simulated annealing. *S. Hernandez, C. A. Brebbia (Eds.), Computer Aided Optimum Design of Structures, WIT Press*, VII:347–356, 2001.

[76] J. Haslinger and R. A. E. Mäkinen. *Introduction to Shape Optimization*. Society for Industrial and Applied Mathematics, Jan. 2003.

[77] T. He, Z. Zhu, F. Eastham, Y. Wang, H. Bin, D. Wu, L. Gong, and J. Chen. Permanent magnet machines for high-speed applications. *World Electric Vehicle Journal*, 13(1):18, Jan. 2022.

[78] J. Hemsen, T. Negri, C. Trost, and L. Eckstein. Comparison of permanent magnet rotor designs for different vehicle classes and driving scenarios: A simulation study. *SAE International Journal of Alternative Powertrains*, 7(2), June 2021.

[79] A. Henrot and M. Pierre. *Variation et optimisation de formes*. Springer Berlin Heidelberg, 2005.

[80] M. Hintermüller. Fast level set based algorithms using shape and topological sensitivity information. *Control and Cybernetics*, 34(1):305–324, 2005.

[81] M. Hintermüller and K. Kunisch. PDE-constrained optimization subject to pointwise constraints on the control, the state, and its derivative. *SIAM J. Optim.*, 20(3):1133–1156, Aug. 2009.

[82] M. Hintermüller and A. Laurain. Where to create a hole? European Consortium for Mathematics in Industry, ECMI Newsletter 41, 2007.

[83] M. Hintermüller and A. Laurain. Electrical impedance tomography: from topology to shape. *Control and Cybernetics*, 37(4), 2008.

[84] M. Hintermüller and A. Laurain. A shape and topology optimization technique for solving a class of linear complementarity problems in function space. *Computational Optimization and Applications*, 46(3):535–569, Sept. 2008.

[85] M. Hintermüller and A. Laurain. Multiphase image segmentation and modulation recovery based on shape and topological sensitivity. *Journal of Mathematical Imaging and Vision*, 35(1):1–22, Apr. 2009.

[86] M. Hintermüller and A. Laurain. Optimal shape design subject to elliptic variational inequalities. *SIAM Journal on Control and Optimization*, 49(3):1015–1047, Jan. 2011.

[87] M. Hintermüller, A. Laurain, and A. A. Novotny. Second-order topological expansion for electrical impedance tomography. *Advances in Computational Mathematics*, 36(2):235–265, Oct. 2011.

[88] M. Hintermüller and W. Ring. A second order shape optimization approach for image segmentation. *SIAM Journal on Applied Mathematics*, 64(2):442–467, 2004.

[89] M. Hinze, R. Pinnau, M. Ulbrich, and S. Ulbrich. *Optimization with PDE Constraints*. Springer Netherlands, 2008.

[90] N. Ida and J. P. A. Bastos. *Electromagnetics and Calculation of Fields*. Springer New York, 1997.

[91] J.-W. Jung, B.-H. Lee, D.-J. Kim, J.-P. Hong, J.-Y. Kim, S.-M. Jeon, and D.-H. Song. Mechanical stress reduction of rotor core of interior permanent magnet synchronous motor. *IEEE Transactions on Magnetics*, 48(2):911–914, Feb. 2012.

[92] M. Kaltenbacher. *Numerical Simulation of Mechatronic Sensors and Actuators*. Springer Berlin Heidelberg, 2015.

[93] D. Knees and A.-M. Sändig. Regularity of elastic fields in composites. *Multifield Problems in Solid and Fluid Mechanics, R. Helmig, A. Mielke, B. Wohlmuth (Eds.), vol. 28 of Lecture Notes in Applied and Computational Mechanics*, pages 331–360, 2006.

[94] A. Kost. *Numerische Methoden in der Berechnung elektromagnetischer Felder*. Springer Berlin Heidelberg, 1994.

[95] E. Kuci, F. Henrotte, P. Duysinx, and C. Geuzaine. Combination of topology optimization and lie derivative-based shape optimization for electro-mechanical design. *Structural and Multidisciplinary Optimization*, 59(5):1723–1731, Nov. 2018.

[96] C. Le, J. Norato, T. Bruns, C. Ha, and D. Tortorelli. Stress-based topology optimization for continua. *Structural and Multidisciplinary Optimization*, 41(4):605–620, Oct. 2009.

[97] S. Li, R. Sauer, and G. Wang. A circular inclusion in a finite domain i. the dirichlet-eshelby problem. *Acta Mechanica*, 179(1):67–90, Sept. 2005.

[98] Z. Li. The immersed interface method using a finite element formulation. *Applied Numerical Mathematics*, 27(3):253–267, July 1998.

[99] C. G. Lopes and A. A. Novotny. Topology design of compliant mechanisms with stress constraints based on the topological derivative concept. *Structural and Multidisciplinary Optimization*, 54(4):737–746, Oct. 2016.

[100] E. Lovelace, T. Jahns, T. Keim, and J. Lang. Mechanical design considerations for conventionally laminated, high-speed, interior PM synchronous machine rotors. *IEEE Transactions on Industry Applications*, 40(3):806–812, May 2004.

[101] J. Malý and W. P. Ziemer. *Fine Regularity of Solutions of Elliptic Partial Differential Equations*. American Mathematical Society, 1997.

[102] M. Merkel, P. Gangl, and S. Schöps. Shape optimization of rotating electric machines using isogeometric analysis. *IEEE Transactions on Energy Conversion*, 36(4):2683–2690, Dec. 2021.

[103] T. Mura. *Micromechanics of Defects in Solids*. Springer Netherlands, 1987.

[104] J. Nocedal and S. Wright. *Numerical Optimization*. Springer New York, 2006.

[105] A. A. Novotny and J. Sokołowski. *Topological Derivatives in Shape Optimization*. Springer Berlin Heidelberg, 2013.

[106] A. A. Novotny, J. Sokołowski, and A. Żochowski. *Applications of the Topological Derivative Method*. Springer International Publishing, 2019.

[107] Y. Okamoto and N. Takahashi. A novel topology optimization of nonlinear magnetic circuit using ON/OFF method. *IEEJ Transactions on Fundamentals and Materials*, 125(6):549–553, 2005.

[108] S. Osher and J. A. Sethian. Fronts propagating with curvature-dependent speed: Algorithms based on hamilton-jacobi formulations. *Journal of Computational Physics*, 79(1):12–49, 1988.

[109] S. J. Osher and F. Santosa. Level set methods for optimization problems involving geometry and constraints. *Journal of Computational Physics*, 171(1):272–288, July 2001.

[110] C. Pechstein. Multigrid-newton-methods for nonlinear magnetostatic problems. Master's thesis, Johannes Kepler University Linz, 2004.

[111] C. Pechstein. *Finite and Boundary Element Tearing and Interconnecting Methods for Multiscale Elliptic Partial Differential Equations*. PhD thesis, Johannes Kepler University Linz, 2008.

[112] C. Pechstein and B. Jüttler. Monotonicity-preserving interproximation of b-h-curves. *J. Comput. Appl. Math.*, 196(1):45–57, 2006.

[113] M. Petzoldt. Regularity results for laplace interface problems in two dimensions. *Zeitschrift für Analysis und ihre Anwendungen*, 20(2):431–455, 2001.

[114] R. Picelli, S. Townsend, C. Brampton, J. Norato, and H. A. Kim. Stress-based shape and topology optimization with the level set method. *Computer Methods in Applied Mechanics and Engineering*, 329:1–23, 2018.

[115] R. Picelli, S. Townsend, and H. A. Kim. Stress and strain control via level set topology optimization. *Structural and Multidisciplinary Optimization*, 58(5):2037–2051, July 2018.

[116] P. Putek, R. Pulch, A. Bartel, E. J. W. ter Maten, M. Günther, and K. M. Gawrylczyk. Shape and topology optimization of a permanent-magnet machine under uncertainties. *Journal of Mathematics in Industry*, 6(1), Nov. 2016.

[117] L. Rakotondrainibe, J. Desai, P. Orval, and G. Allaire. Coupled topology optimization of structure and connections for bolted mechanical systems. *European Journal of Mechanics - A/Solids*, 93:104499, 2022.

[118] A. A. Romero Onco and S. M. Giusti. A robust topological derivative-based multi-material optimization approach: Optimality condition and computational algorithm. *Computer Methods in Applied Mechanics and Engineering*, 366:113044, 2020.

[119] G. I. N. Rozvany. A critical review of established methods of structural topology optimization. *Structural and Multidisciplinary Optimization*, 37(3):217–237, Feb. 2008.

[120] R. B. Santos, C. G. Lopes, and A. A. Novotny. Structural weight minimization under stress constraints and multiple loading. *Mechanics Research Communications*, 81:44–50, Apr. 2017.

[121] M. Schneider and H. Andrä. The topological gradient in anisotropic elasticity with an eye towards lightweight design. *Mathematical Methods in the Applied Sciences*, 37(11):1624–1641, 2014.

[122] A. Schumacher. *Topologieoptimierung von Bauteilstrukturen unter Verwendung von Lochpositionierungskriterien*. PhD thesis, University Siegen, 1995.

[123] J. A. Sethian. *Level Set Methods and Fast Marching Methods: Evolving Interfaces in Computational Geometry, Fluid Mechanics, Computer Vision, and Materials Science*. Cambridge University Press, 1999.

[124] P. Y. Shim and S. Manoochehri. Generating optimal configurations in structural design using simulated annealing. *Int. J. Numer. Meth. Engng.*, 40(6):1053–1069, Mar. 1997.

[125] O. Sigmund. On the usefulness of non-gradient approaches in topology optimization. *Structural and Multidisciplinary Optimization*, 43(5):589–596, Mar. 2011.

[126] O. Sigmund and K. Maute. Topology optimization approaches. *Structural and Multidisciplinary Optimization*, 48(6):1031–1055, 2013.

[127] J. Sokołowski and A. Żochowski. On the topological derivative in shape optimization. *SIAM Journal on Control and Optimization*, 37(4):1251–1272, 1999.

[128] J. Sokołowski and A. Żochowski. Topological derivatives of shape functionals for elasticity systems. *Mechanics of Structures and Machines*, 29(3):331–349, June 2001.

[129] J. Sokołowski and J.-P. Zolésio. *Introduction to Shape Optimization*. Springer Berlin Heidelberg, 1992.

[130] R. Stainko. *Advanced Multilevel Techniques to Topology Optimization*. PhD thesis, Johannes Kepler University Linz, 2006.

[131] M. Stolpe and M. P. Bendsøe. Global optima for the zhou-rozvany problem. *Structural and Multidisciplinary Optimization*, 43(2):151–164, 2011.

[132] M. Stolpe and K. Svanberg. Modelling topology optimization problems as linear mixed 0-1 programs. *International Journal for Numerical Methods in Engineering*, 57(5):723–739, 2003.

[133] E. Süli and D. F. Mayers. *An Introduction to Numerical Analysis*. Cambridge University Press, Aug. 2003.

[134] K. Svanberg and M. Werme. Sequential integer programming methods for stress constrained topology optimization. *Structural and Multidisciplinary Optimization*, 34(4):277–299, May 2007.

[135] N. Takahashi, T. Yamada, and D. Miyagi. Optimization of rotor of actual IPM motor using ON/OFF method. In *Digests of the 2010 14th Biennial IEEE Conference on Electromagnetic Field Computation*. IEEE, May 2010.

[136] A. Tenconi, S. Vaschetto, and A. Vigliani. Electrical machines for high-speed applications: Design considerations and tradeoffs. *IEEE Transactions on Industrial Electronics*, 61(6):3022–3029, June 2014.

[137] F. Tröltzsch. *Optimale Steuerung partieller Differentialgleichungen: Theorie, Verfahren und Anwendungen*. Vieweg+Teubner Verlag, 2010.

[138] M. Ulbrich and S. Ulbrich. *Nichtlineare Optimierung*. Springer Basel, 2012.

[139] Y. M. Xie and G. P. Steven. *Evolutionary Structural Optimization*. Springer London, 1997.

[140] E. Zeidler. *Nonlinear Functional Analysis and its Applications: II/B: Nonlinear Monotone Operators*. Springer New York, 1990.

[141] J. Zhang, W. Chen, X. Huang, Y. Fang, J. Zhang, J. Ma, and W. Cao. Evaluation of applying retaining shield rotor for high-speed interior permanent magnet motors. *IEEE Transactions on Magnetics*, 51(3):1–4, Mar. 2015.

[142] O. C. Zienkiewicz, R. L. Taylor, and J. Z. Zhu. *The Finite Element Method: Its Basis and Fundamentals*. Elsevier Science, 2005.

List of Figures

Selbständigkeitserklärung

Ich erkläre, dass ich die Dissertation selbständig und nur unter Verwendung der von mir gemäß §7 Abs. 3 der Promotionsordnung der Mathematisch-Naturwissenschaftlichen Fakultät, veröffentlicht im Amtlichen Mitteilungsblatt der Humboldt-Universität zu Berlin Nr. 42/2018 am 11.07.2018 angegebenen Hilfsmittel angefertigt habe.

Stuttgart, den 2. August 2022